New Physics at Colliders and in Space

Glenn Robbins

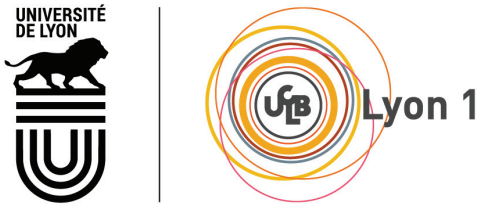

N° d'ordre NNT : xxx

THÈSE DE DOCTORAT DE L'UNIVERSITÉ DE LYON

opérée au sein de

l'Université Claude Bernard Lyon 1

École Doctorale ED52
de Physique et d'Astrophysique

Spécialité de doctorat : Physique Théorique / Physique des Particules

Soutenue publiquement le 24/09/2018, par :

Glenn Robbins

New Physics at Colliders and in Space

Devant le jury composé de :

AUGIER Corinne, Professeure, Université Lyon 1, IPNL	Présidente
BELANGER Geneviève, Directrice de recherche CNRS, LAPTh, Annecy	Rapporteure
COVI Laura, Professeure, Goettingen University	Rapporteure
CIRELLI Marco, Directeur de recherche CNRS, LPTHE, Paris	Examinateur
ELLIS John, Professeur, King's College London	Examinateur
KAHLHOEFER Felix, Professeur associé, RWTH Aachen University	Examinateur
MAHMOUDI Farvah, Maître de conférences, Université Lyon 1, IPNL	Directrice de thèse

Résumé

Nouvelle Physique aux Collisionneurs et dans l'Espace

La quête de la nouvelle physique est un défi impliquant à la fois la recherche de particules de matière noire dans les halos galactiques, et celle, aux collisonneurs, de particules dont l'existence est prédite par des théories au-delà du Modèle Standard, telles que la supersymétrie. Alors que les contraintes expérimentales sur ces particules s'intensifient, il devient capital de combiner les limites provenant de ces deux volets afin de guider la suite des recherches. Pour ce faire, il est indispensable d'évaluer et de tenir compte correctement des incertitudes astrophysiques, cosmologiques et nucléaires, pourtant souvent ignorées. La première partie de cette thèse est dédiée à l'étude de ces incertitudes et leur impact sur les contraintes obtenues en supersymétrie, ainsi que la complémentarité entre les contraintes des collisionneurs et de matière noire pour la recherche de nouvelle physique. La deuxième partie est consacrée au développement d'outils de calculs pour les détections directe et indirecte de matière noire, conçus afin de prendre correctement en compte les incertitudes astrophysiques et nucléaires, et à leur implémentation dans le code public SuperIso Relic. Enfin la troisième partie du travail concerne l'étude des implications cosmologiques d'une éventuelle découverte de nouvelles particules aux collisionneurs. Nous avons montré qu'il serait possible de tester les hypothèses du modèle cosmologique standard et d'obtenir des informations sur les propriétés de l'Univers primordial à une époque observationnellement inaccessible.

Mots-clefs: *Matière noire, Supersymétrie, Astroparticules, Physique des particules*

Abstract

New Physics at Colliders and in Space

The quest for new physics is a challenging task which involves, on the one hand, the search for dark matter particles from space, and on the other hand, the search at colliders for particles predicted by theories beyond the Standard Model, such as supersymmetry. With the experimental constraints on new particles getting stronger, it becomes crucial to combine the limits from both sectors in order to guide future searches. To this end, it is essential to estimate and take into account correctly the astrophysical, nuclear and cosmological uncertainties, which are most often ignored.

The first part of this thesis is dedicated to the study of such uncertainties and to their impact on the constraints applied on supersymmetry. Moreover, we investigate the interplay between the constraints from colliders and dark matter searches in some detail. The second part concerns the development and the implementation in the public code SuperIso Relic of numerical tools for the calculation of direct and indirect dark matter detection constraints which were designed specifically to take correctly into account the astrophysical and nuclear uncertainties. Finally, in the third part of this work, we consider the cosmological implications of a hypothetical discovery of new particles at colliders. We show that it would be possible to test the assumptions of the standard cosmological model and to obtain information on the properties of the primordial Universe at an epoch which is beyond observational reach.

Keywords: *Dark matter, Supersymmetry, Astroparticles, Particle physics*

Acknowledgements

J'aimerais d'abord remercier l'équipe du CRAL et du groupe Théorie de l'IPNL pour m'avoir chaleureusement accueilli durant mes trois années de doctorat. En particulier, un grand merci à Nazila Mahmoudi qui a dirigé ma thèse. Ta motivation au travail est très inspirante et tu as toujours su me pousser et m'écouter lorsqu'il y en avait besoin. De même, merci à Alexandre Arbey qui a su être très présent et avec qui j'ai eu un grand plaisir à travailler. Je suis aussi très reconnaissant envers le groupe Matière Noire qui m'a accueilli à l'IPNL dans un premier temps et avec qui j'ai eu des discussions très enrichissantes. Plus particulièrement, je remercie Corinne Augier qui m'a offert l'occasion d'enseigner l'optique à l'Université. Je remercie aussi les doctorants du CRAL et de l'IPNL, notamment mes chères co-bureau Emeline et Solène sans qui cette expérience aurait été beaucoup moins drôle.
Je tiens aussi à remercier sincèrement Mathieu Boudaud et John Ellis avec qui j'ai eu un très grand plaisir à collaborer pour les deux projets principaux de cette thèse.
Je remercie ensuite tous les membres de mon jury pour avoir participé à ma soutenance malgré des transports capricieux, et en particulier Geneviève Belanger et Laura Covi qui ont pris le temps de rapporter ma thèse.
Je remercie également le LABEX Institut Lyonnais des Origines (ANR-10-LABX-0066) de l'Université de Lyon pour son soutien financier dans le cadre du programme "Investissements d'Avenir" (ANR-11-IDEX-0007) de l'Etat Français géré par l'Agence Nationale de la Recherche (ANR).
Plus personnellement, je tiens à remercier ma famille qui m'a toujours apporté le soutien nécessaire. Merci aussi à Mourtaza avec qui nous avons pu nous plaindre longuement de la vie autour d'une tasse de thé et mes deux Pô pour ces inoubliables soirées pizza du lundi soir. Un grand merci à Chaton (mon chat) pour tous ses câlins réconfortants et pour avoir chassé les souris. Et évidemment, merci à Loutron (non, lui ce n'est pas une vraie loutre), pour être apparu dans ma vie, l'avoir rendue tellement plus douce, et pour m'avoir cuisiné de bons petits plats pendant que je rédigeais.

Table of Contents

List of Tables

List of Figures

Figure **Page**

We grow accustomed to the Dark

We grow accustomed to the Dark -
When Light is put away -
As when the Neighbor holds the Lamp
To witness her Goodbye -

A Moment - We uncertain step
For newness of the night -
Then - fit our Vision to the Dark -
And meet the Road - erect -

And so of larger - Darknesses -
Those Evenings of the Brain -
When not a Moon disclose a sign -
Or Star - come out - within -

The Bravest - grope a little
And sometimes hit a Tree
Directly in the Forehead -
But as they learn to see -

Either the Darkness alters -
Or something in the sight
Adjusts itself to Midnight -
And Life steps almost straight.

Emily Dickinson (1830–1886)

Introduction

We grow accustomed to the dark, as Emily Dickinson once wrote. At least, I really hope so. This poem stroke me by its perfect connection with the research I have carried out during my Ph.D., though it can certainly apply to any research in general. The existence of dark matter has been suggested for more than eighty years and, yet, its nature in terms of particle content is still completely unknown. Contrary to ordinary matter, dark matter does not emit nor absorb light, which makes it incredibly difficult to detect. Currently, the only way to probe its existence is through the study of its gravitational interaction with astrophysical objects. Dark matter is thus known to constitute 85% of the matter in the Universe. In particular, every galaxy, including the Milky way, is embedded in a dark matter halo. One may therefore say that we all live in the dark. Several experiments were designed to detect either the products of the annihilation of dark matter particles in the galactic haloes, or the collision of a dark matter particle with ordinary matter. However, no convincing signal has been detected yet.

The light could arise from particle physics, as a large panel of theories proposes candidate particles for dark matter. These theories emerged from the quest for "New Physics", which is, in simple words, the search for the missing pieces of the puzzle which will reveal to us the very foundations of the Universe. One of the theories which have been regarded with the most interest by the particle physics community for the last decades is *Supersymmetry*. It postulates the existence of a whole set of particles which have not been detected yet, the lightest of these particles possibly being the dark matter. Unfortunately, experimental collaborations are still struggling to detect any of these supersymmetric particles at colliders. Great expectations were placed, in particular, on the Large Hadron Collider at CERN which was crowned with success for the discovery of the Higgs boson in 2012. However, superparticles, if they do exist, seem to be extremely good at hiding.

Nevertheless, the discovery of nothing is still a discovery. Exactly like when you search your keys in the night, you grope around, finding nothing, but thus knowing where not to look anymore, until you finally have a catch. You will probably hit a few trees directly in the forehead during the process, but you will eventually have the pleasure to go home. This is precisely the same here, as we are able to derive constraints on dark matter and superparticle properties. Little by little, we restrain the possibilities of where to find these particles, and someday, hopefully, a signal will be detected. Perhaps we will first detect a dark matter particle from the galactic halo, which will allow us to confirm or not the supersymmetric theory. Or vice-versa, we could first produce a new kind of particle at colliders, which will unveil the key to dark matter.

The work I will present here focuses on the uncertainties related to the search for dark matter.

It certainly caused me, at first, serious “evening of the brains”, but I hope that, in three years, I have grown a little accustomed to the dark.
I will begin with a short historical introduction to dark matter and then I will introduce the theoretical bases of supersymmetry.
In a second part, I will present the study I have carried out, in collaboration with Prof. Alexandre Arbey, Dr. Mathieu Boudaud and Prof. Nazila Mahmoudi, on the constraints derived from dark matter and collider searches applied to the Minimal Supersymmetric Standard model. The stress will be put on the astrophysical and nuclear uncertainties related to dark matter detection limits. This part will conclude on the description of the numericals tools I have implemented in the public code SuperIso Relic for the calculation of dark matter detection constraints.
The third and last part will take place in the hypothetical context where a dark matter particle has been detected. In this case, it would be possible to calculate the average density of this particle from its annihilation rate, within the standard cosmological model. But what if this density does not match with the measured dark matter density? It would inform us that the particle content at the beginning of the Universe differs from the one assumed in the standard cosmological model. In fact, little is known on the Universe content before the primordial nucleosynthesis and the discovery of a dark matter particle could allow us to deduce constraints on alternative cosmological models. We will perform this exercise for a couple of models including the presence of a scalar field before Big Bang nucleosynthesis. This work was carried out in collaboration with Prof. Alexandre Arbey, Prof. John Ellis and Prof. Nazila Mahmoudi.

Part I

Introduction to Dark Matter and Supersymmetry

CHAPTER 1

THE QUEST FOR DARK MATTER PARTICLES

Dark matter is a hypothetical kind of matter which represents 85% of the mass of matter in the Universe. By its nature, dark matter (DM) does not emit any light, which makes its detection difficult. However, it is possible to detect its gravitational interaction with ordinary "baryonic" matter. In this first chapter, I will start with a short historical review of the observational evidences of the existence of dark matter, then I will present a few dark matter models. Finally, I will describe the various types of experiment aiming at detecting dark matter particles.

1.1 Evidences for dark matter

The idea that a part of the matter in the Universe may escape the observations because they do not emit light or are just too dim to see was already seriously considered at the beginning of the twentieth century. In 1904, Lord Kelvin hypothesized the existence of dark stars in the Milky Way possibly not bright enough to be directly observable. Considering that the stars in our galaxy are acting like molecules in a gas, Kelvin realized there was a way to calculate the total mass of luminous and non-luminous matter from the velocity dispersion of the stars [1]. This method was, however, later reconsidered by Henri Poincaré whose final calculation showed that the observed velocity dispersion was in agreement with the mass of luminous matter [2]. It wasn't until the beginning of the 1930's that a real discrepancy between the total mass and the luminous mass of an astrophysical system was measured. From this point, the observational evidences for dark matter multiplied at various astrophysical and cosmological scales.

1.1.1 Local Dark Matter

The first attempts to probe the existence of a population of dark astrophysical objects via their gravitational interactions with luminous matter were, in fact, not the most successful. They were, nevertheless, the first steps to great discoveries. It began with the observations of the stars in the

sun vicinity (i.e. stars at a distance $\lesssim 0.1 - 1$ kpc from the sun). In 1915, Estonian astronomer Ernst Öpik calculated the total local mass density by measuring the vertical oscillations of those stars [3]. He eventually found that the motion of the stars could be explained by the mass of luminous matter alone and that there were no need to assume the existence of dark matter. Improved analyses were later carried out by Kapteyn [4] and Jeans [5] who found a total local density of 0.099 $M_\odot pc^{-3}$ and 0.143 $M_\odot pc^{-3}$. Similarly, in 1932, Jan Hendrick Oort, Kapteyn's student, found a local density of 0.092 $M_\odot pc^{-3}$ [6]. None of them found an excessive amount of dark matter and Oort argued that by taking into account the expected number of white dwarves, his result was coherent with the contribution of ordinary matter alone.

It appears, actually, that the main source of uncertainties in the calculation of the amount of dark matter does not come from the total density measurement, which is quite coherent between the various analyses, but comes from the estimation of the amount of luminous matter. More precise estimations were recently done and the local density of dark matter is now believed to be around 0.008 $M_\odot pc^{-3}$ (0.3 GeV cm^{-3}), with large uncertainties. One can refer to the review on local dark matter density by J.I. Read for further information [7].

While the study of vertical oscillations of stars in the Sun's vicinity is not the most convincing evidence of the existence of dark matter, the precise measurement of local DM density is crucial for DM direct detection (see Section 1.3.2). The first really challenging measurements came, in fact, from the observations of galaxy clusters.

1.1.2 Galaxy clusters

One of the first striking evidences for dark matter came from the Swiss astronomer Fritz Zwicky in 1933 [8]. At that time, Zwicky was carrying out a project in Mount Wilson concerning the measurement of galaxy cluster distances via the spectral red-shift related to the expansion of the Universe. While observing the Coma galaxy cluster, he measured the velocity of eight galaxies and deduced an approximate value of the total mass of the cluster using the virial theorem. This value was 400 times greater than the one expected by summing the masses of luminous objects. The discrepancy between the mass of luminous objects and the mass calculated via the Newtonian law of gravity lead him to suggest the existence of a non-luminous type of matter composing the cluster which he referred to as *dunkle Materie* or "dark matter". His calculations should, however, be reviewed as he took a value of the Hubble constant $H_0 = 558$ km s^{-1} Mpc^{-1}. The current value of H_0 is now ≈ 70 km s^{-1} Mpc^{-1}, therefore the overdensity of 400 should be reduced to 50. Nevertheless, the conclusion that the majority of the matter in the cluster must be dark remains relevant.

Three years later, a similar study lead by Sinclair Smith showed that the mass of the Virgo cluster was 200 times larger than expected [9], giving weight to Zwicky's hypothesis. In 1959, Kahn and Woltjer calculated the mass of the Local Group from the motion of Andromeda towards the Milky Way [10]. They found that the Local Group was six times more massive than the observed luminous matter and suggested that the missing mass was composed of very hot gas in the intergalactic medium. At this time, it was not yet considered that dark matter cannot be composed of ordinary particles.

Figure 1.1: A purple haze shows dark matter flanking the "Bullet Cluster." X-rays observations of hot gas is represented in pink. **Image Credit**: X-ray: NASA/CXC/M.Markevitch et al. Optical: NASA/STScI; Magellan/U.Arizona/D.Clowe et al. Lensing Map: NASA/STScI; ESO WFI; Magellan/U.Arizona/D.Clowe et al.

Today, the most convincing evidence of the existence of dark matter is based on the observation of the Bullet Cluster (1E 0657-558), which consists in two colliding galaxy clusters at a co-moving radial distance of approximately one giga-parsec from us [11]. Its observation in X-rays reveals hot gas, represented in pink in figure 1.1, which forms a distinct arc characteristic of a shock-wave. It is also possible to map the distribution of mass in the cluster by studying gravitational lensing. Gravitational lensing is a phenomenon related to General Relativity. The bullet cluster, thanks to its mass, deforms space-time around it. If a luminous object, such as a galaxy, is located behind the Bullet Cluster in the line of sight, the space-time deformation bends the trajectory of the light emitted by the galaxy. This effect allows us to observe the galaxy, but its image is slightly curved. The study of this curvature is key to calculate the mass distribution of the Bullet Cluster, which is represented by a purple haze in figure 1.1. One can notice that the location of mass is clearly decorrelated from the position of hot gas in the Bullet Cluster. That can be easily explained if one considers that the cluster is mainly composed of gas and dark matter. Ordinary matter, such as the gas suffers from friction due to electromagnetic interaction. Therefore, when the two clusters collided, ordinary matter tended to stay at the position of collision. This is not the case for dark matter, which is not stopped by frictions. When the two clusters collided, dark matter continued its motion by inertia. This explains why the mass, mainly carried by dark matter, is separated from the gas in the Bullet Cluster. This observation was extremely important as it challenged significantly models of modified gravity.

1.1.3 Spiral galaxies

Another remarkable evidence that dark matter exists comes from the study of the motion of luminous matter in the periphery of spiral galaxies. The first obvious specimen for this kind of observations is our neighbour, the Andromeda galaxy (M 31). In 1939, American astronomer Ho-

race W. Babcock obtained the spectra of M31 and deduced the rotational velocity of the different regions of the galaxy, up to ≈ 20 kpc from the center of the galaxy [12]. He found that outer regions had an unexpectedly high velocity compared to the Keplerian velocity calculated from the luminous mass of the galaxy. He explained this either by the presence of poorly luminous matter in the outer region of the galaxy or by strong dust absorption. Similar unexpected results were obtained by Oort when studying galaxy NGC 3115 [13].
Results on the Andromeda galaxy were improved after WWII, when Oort and his team realized that German radars could be rehabilitated into radio-telescopes. They discovered that neutral hydrogen gas emitted interesting radio waves at 21 cm wavelength. The 21-cm line is now one of the most important astrophysical probe. Oort's student, Van de Hulst, was then able to measure the rotational velocity of hydrogen gas up to 30 kpc from the center of Andromeda galaxy, improving previous analyses [14].
Important optical and radio measurements followed in the next years, including the remarkable works of Roberts [15], Rubin & Ford [16] and Roberts & Rots [17]. They all point towards the fact that rotation velocity curves of spiral galaxies become flat at large radii from the center of the galaxies, as can be seen in figure 1.2. In classical Newtonian dynamics, this velocity can be written as $v(r) = \sqrt{\frac{GM(r)}{r}}$ for a radius r from the galactic center, with $M(r)$ the total mass contained within a sphere of radius r. At large radii, where luminous matter becomes scarce, $M(r)$ should become constant and $v(r)$ should then drop-off as $r^{-1/2}$. The fact that $v(r)$ becomes constant may show that there is a large amount of dark matter at large radii, so that $M(r) \propto r$. Today, it is believed that every galaxy is surrounded by a large spherical dark matter halo.

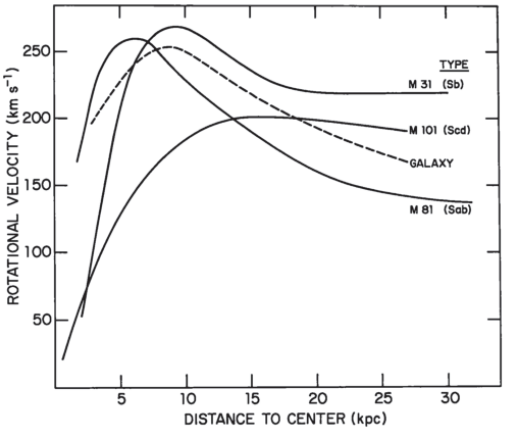

Figure 1.2: Rotation curves for the galaxies M 31, M 101 and M 81 are shown as solid lines. The rotation curve for our galaxy is shown as a dashed line. Figure from [17].

1.1.4 Cosmological Scale

According to the Big Bang model, the Universe starts with an extremely hot and dense state of matter. During the first seconds of the Universe, the very high temperatures prevent any group of particles from bonding. For instance, helium nuclei formed through the fusion of two protons

and one or two neutrons are immediately destroyed by collisions with high energetic photons. However, as the Universe expands, the photons lose energy and are not able to break the nuclei anymore. The first light nuclei (helium-3, helium-4, lithium and beryllium), can thus be stably produced. Approximatively 20 minutes after the Big Bang, the production of light nuclei freezes-out as the temperature becomes too low for the production process to occur. The abundances of light elements have not evolved since and remain observable today. This phenomenon is called Big Bang Nucleosynthesis (BBN) and first was described by Alpher, Bethe and Gamow in 1948 [18]. It constitutes a crucial source of information in cosmology and allows us to constrain the nature of dark matter, as we will see in section 1.2.1.

After BBN, the electrons and nuclei are still decoupled because of the photo-dissociation. Thus, photons have very short mean free paths as they scatter on electrons and nuclei and are trapped in the very hot and dense gas. It is only around 380 000 years after the Big Bang that the Universe becomes cool enough for the electrons and the nuclei to finally couple. This is the recombination. Atoms are formed and photons can eventually escape and propagate through the whole Universe. This light is still observable as a nearly-perfect black body radiation with a temperature of 2.7K, homogeneous and isotropic through the Universe. The Cosmic Microwave Background (CMB), as it is called, was first observed by Penzias and Wilson in 1965 [19] and is now a pillar of cosmology. Three main space telescopes were launched in order to study the CMB, starting with the Cosmic Background Explorer (COBE) in 1989. It revealed tiny fluctuations in the CMB which can be explained by overdensities at the epoch of recombination [20]. Those overdensities are believed to be quantum fluctuations appearing at the very beginning of the Universe which grew into large structures, such as clusters of galaxies and galaxies, by attracting matter thanks to their gravitational potential. High precision measurements of the fluctuations followed with space-telescopes WMAP [21] and Planck [22]. The analysis of the angular correlation of these fluctuations is key to constraining cosmological parameters. The power spectrum associated to these correlations displays multiple peaks (see figure 1.3). While the position of the first peak reveals information on the total energy density ρ_{tot} of the Universe, the position of the second peak allows us to constrain non-baryonic dark matter density ρ_{DM}.

Within the framework of the standard model of cosmology ΛCDM, the Universe is composed of radiation, baryonic matter, non-relativistic (“cold”) dark matter and dark energy, which accounts for the accelerated expansion of the Universe. The total density can then be written :

$$\rho_{tot} = \rho_{rad} + \rho_b + \rho_{DM} + \rho_\Lambda \quad . \tag{1.1}$$

In cosmology, it is however convenient to use density parameters defined as $\Omega_{(i)} = \frac{\rho_{(i)}}{\rho_c}$ where $\rho_c = \frac{3H^2}{8\pi G}$ is the critical density. By definition, if $\rho_{tot} = \rho_c$ ($\Omega_{tot} = 1$) then the Universe is flat.

The last results from Planck mission showed that $1 - \Omega_{tot} = 0.000 \pm 0.005$, that is to say that the Universe is measured to be flat with a good precision. It also showed that $\Omega_b h^2 = 0.02230 \pm 0.00014$ and $\Omega_{DM} h^2 = 0.1188 \pm 0.0010$ where h is the reduced Hubble constant $h = \frac{H}{100\,\mathrm{km/s/Mpc}}$. Thus, there should be five times more dark matter than ordinary matter to explain CMB fluctuations.

Such observations are directly related to the formation of large structures of the Universe. In 1982, the CfA survey, which was the first extensive survey of galaxies in the local Universe showed that galaxies were grouped into clusters and super-clusters connected by long filaments

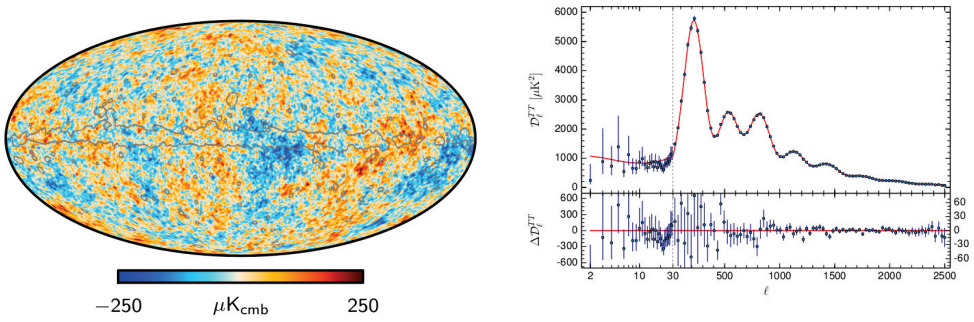

Figure 1.3: **Left**: CMB fluctuations from [25]. **Right**: Planck 2015 temperature power spectrum from [22] is shown in the upper panel along with the best-fit base ΛCDM theoretical spectrum in red plain line. Residuals with respect to this model are shown in the lower panel. The error bars show $\pm 1\sigma$ uncertainties.

[23]. Without dark matter, the matter could not have collapsed in time to form these current structures. As baryonic matter interacts through electromagnetism, the resulting pressure in the hot primordial gas slows down gravitational collapse. This is not the case for cold dark matter which can easily form clusters and then accrete ordinary matter. In order to reproduce all the features of large structures in numerical simulations, it is also needed that dark matter be non-relativistic at the time of the formation of large structures. From this result, it is possible to rule out neutrinos as dark matter candidates [24].
In the next section, we will see more specifically what are the possible candidates for dark matter.

1.2 Dark matter candidates

Numerous models have been built over the past decades in order to describe the nature of dark matter. As it would be too long and tedious to describe them all, I will focus only on two types of model and present a few examples at the end of this section. The first model is the most natural approach as it postulates that dark matter consists in feebly luminous astrophysical objects, named *MACHOs*. This model is, however, severely constrained. The second one, the WIMP hypothesis, is one of the most popular models in particle physics. In this model, dark matter is described as a weak interacting massive particle (WIMP) beyond the Standard Model. It will be at the center of the rest of my Ph.D. thesis.

1.2.1 Massive Astrophysical Compact Halo Objects (MACHOs)

One of the most immediate answers to the question of the nature of dark matter is that it should be composed of ordinary matter too dim to be observed. Compact astrophysical objects such as brown dwarves, red dwarves, white dwarves, neutron stars or black holes are very difficult to observe via their emission of light and could be excellent candidates for dark matter. Those kinds of objects are commonly named Massive Astrophysical Compact Halo Objects (MACHOs). Several evidences are, however, suggesting that MACHOs could only compose a small fraction of dark

matter.

The first evidence involves micro-gravitational lensing. This phenomenon occurs when a massive object lies in the line of sight of a star. If the massive object is compact enough, its gravitational field will have for effect to enhance the apparent luminosity of the star behind it. In 1986 Bohdan Paczyński proposed a method to detect MACHOs in the halo of the Milky Way [26], which was, one year later, used with more detailed calculations in the Ph.D. thesis of Robert Nemirof [27]. The method involves the observation of a nearby galaxy, such as the Magellanic Clouds. If the halo of the Milky Way is entirely composed of MACHOs, they calculated that at any time, any star in the Magellanic Clouds would have a probability of about one out of a million to be magnified by the gravitational field of a MACHO. If a large amount of stars are monitored in the Magellanic Clouds, it would therefore be possible to estimate the number of MACHOs in the Milky Way halo. In addition, it would give limits on the mass of the compact objects as the duration of a microlensing event is a function of the mass $t \sim 130\text{days} \times \sqrt{\frac{M}{M_\odot}}$. From this relation, one can deduce that with such a method, only MACHOs with masses ranging from $\sim 10^{-7} M_\odot$ to $\sim 10^{2} M_\odot$ would be easily observable, which corresponds to times of observation ranging from a couple of hours to a few years.

A project, simply called MACHO, was dedicated to this task. In 2000, after 5.7 years of observations of the Large Magellanic Cloud (LMC), using the 1.27-meter telescope at Mount Stromlo Observatory, the MACHO Collaboration published their results. From the monitoring of 40 million stars in the LMC, only between 14 and 17 candidate microlensing events were identified. They concluded that between 8% and 50% of the mass the Milky Way's halo consisted of MACHOs [28]. Six years later, a similar project, EROS (Experience pour la Recherche d'Objets Sombres), published the results of 6.7 years of monitoring of both Magellanic Clouds and showed that MACHOs could not make more than 8% of the halo [29].

The second evidence showing that MACHOs can only account for a small fraction of dark matter comes from cosmology. As seen in section 1.1.4, the study of the CMB shows that there is, in mass, five times more non-baryonic dark matter than baryonic matter in the Universe. As MACHOs count as baryonic matter, this would leave a large fraction of non-baryonic dark matter whose nature remains unknown and would also severely constrain the density of MACHOs. It is also possible to draw constraints on baryonic matter density from BBN. By observing the abundance of light elements in the Universe, one can deduce the values of cosmological parameters such as Ω_b. In 1973, Reeves et al., managed to calculate an upper limit on the baryon density parameter $\Omega_b < 0.1$ from the deuterium abundance fraction D/H [30]. Deuterium is a good indicator, as it is believed to be only produced during BBN and not in stellar processes. Several studies measured more precisely the deuterium abundance and showed that $\Omega_b \approx 0.02$ with 10% precision, which is coherent with CMB analyses [31–35]. Such a baryonic density leaves little room for MACHO dark matter.

Recently, there has been a renewed interest for MACHOs with the observation of black hole mergers by gravitational-wave interferometers LIGO and VIRGO [36]. The unexpectedly high masses of the observed black holes may suggest that they were not created by the gravitational collapse of a star but were produced at the very beginning of the Universe, during inflation, from small overdensities. Primordial black holes could make a credible candidate for dark matter as they evade cosmological constraints and also micro-lensing constraints, depending on their mass dis-

tribution [37].
The hypothesis which draws the most the attention in particle physics remains, nevertheless, that dark matter consists of weakly interacting massive particles.

1.2.2 The WIMPs

After the 70s, it was becoming clear that dark matter consists of exotic kinds of particles. Several models in particle physics were proposed in order to find a candidate for dark matter particles. Those candidates had features in common and a category of particles emerged from those models: the WIMPs, standing for Weakly Interacting Massive Particles [38]. The WIMPs consist in particles heavy enough ($m \gtrsim 1-100$ keV) to be non-relativistic and in thermal equilibrium at the beginning of the Universe. As the Universe expands, those particles have the particular feature of leaving thermal equilibrium and ceasing to annihilate at a co-moving density still observable at present time. This is done via the freeze-out mechanism described below.
At thermal equilibrium, dark matter particles annihilate into Standard Model (ordinary) particles, and conversely, Standard Model particles annihilate into dark matter particles.

$$\chi\chi \rightleftarrows \mathrm{SM\,SM}$$

Both processes equilibrate so that dark matter keeps an equilibrium density $n = n_{eq}(T)$ which decreases with temperature (steps (1) and (2) in figure 1.4). However, when the expansion rate of the Universe becomes as large as the annihilation rate of dark matter, this decrease stops. Dark matter density becomes too small for annihilation to occur and the dark matter co-moving density "freezes-out" (step (3)). This remaining density is named the relic density.
The detailed calculation of the relic density from Boltzmann equation is done in Appendix A. For a dark matter particle featuring weak interaction characteristics ($m \sim 100$ GeV, $\langle\sigma v\rangle \sim 10^{-26}$ $\mathrm{cm^3 s^{-1}}$), one ends up with a cosmological dark matter density of the same order of magnitude as the one observed by Planck satellite $\Omega_{DM}h^2 = 0.1188 \pm 0.0010$. This is called the WIMP miracle.
It is also important to notice that dark matter relic density is inversely proportional to its annihilation cross section:

$$\Omega^0_\chi h^2 \sim \frac{3\times10^{-27}\,\mathrm{cm^3\,s^{-1}}}{\langle\sigma v\rangle}\ .$$

WIMPs are currently the subjects of a large variety of experiments around the world, which will be described in section 1.3.

1.2.3 Examples of particle candidates

One of the most studied WIMPs in the literature is the neutralino, which will be described in details in chapter 2 on supersymmetry. However, other models of particle physics exhibit some WIMPs. This is the case of extra-dimension theories in which new spatial dimensions are introduced in addition to the three dimensions that we all know. Those extra-dimensions are usually compact so that they remain unnoticed at large scale. They can, however, have some importance at a particle level. In particular, they may resolve the hierarchy problem [40], which will be described in section 2.2.3. Moreover, to the particles of the Standard Model are attributed some modes in relation to the extra-dimension. Those modes are assimilated to particles commonly

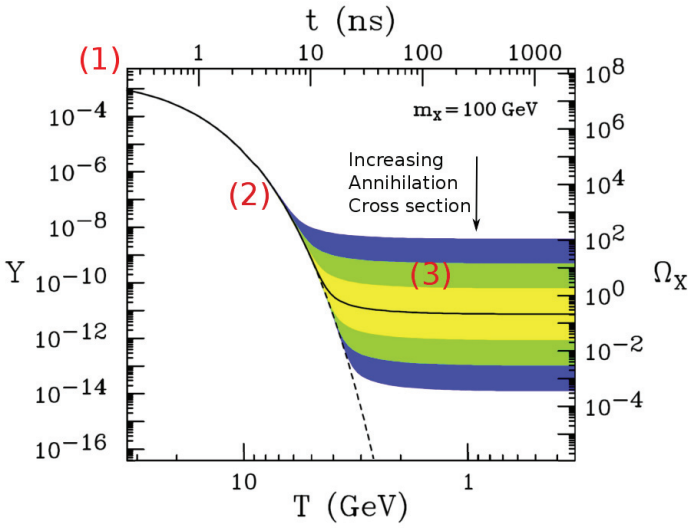

Figure 1.4: Evolution of WIMPs density.The comoving number density Y (left) and resulting thermal relic density (right) of a 100 GeV, P-wave annihilating dark matter particle as a function of temperature T (bottom) and time t (top). The solid contour is for an annihilation cross section that yields the correct relic density, and the shaded regions are for cross sections that differ by 10, 10^2, and 10^3 from this value. The dashed contour is the number density of a particle that remains in thermal equilibrium. From [39].

named Kaluza-Klein (KK) particles. A KK-parity may preserve the lightest KK-particle from decay, which would make it a viable candidate for dark matter.

Another plausible candidate to dark matter, which is not a WIMP this time, is the axion, a pseudo-scalar boson appearing through the breaking of the U(1) Peccei-Quinn symmetry which is invoked to solve the strong CP problem. From astrophysical observations, it is possible to set an upper limit to the axion mass of ~ 16 MeV [41]. More recently, in 2016, the calculation of the formation of axions during the post-inflation from lattice QCD [42] allowed us to define a range of possible masses between 50 and 1500 μeV, which makes it a very light particle compared to WIMPs. Moreover, axions are expected to interact extremely weakly with baryonic matter and thus should not be in thermal equilibrium at the beginning of the Universe. Its density does not "freeze-out" like a WIMP, but "freeze-in". When propagating through a strong magnetic field, axions have the property to be able to convert into photons. This particularity opens up the opportunity to detect them and is at the basis of experiments such as ADMX [43].

The panel of candidates is in fact very wide and it would be beyond the scope of this introduction to make an exhaustive list. I could only name a few other models such as superheavy candidates called "wimpzillas", right-handed neutrinos, sterile neutrinos, etc..

1.3 Dark matter particle detection

The experiments aiming at detecting WIMPs, and more generally at discovering hints of new physics, can be grouped into three categories which correspond to the three different ways of reading diagram 1.5: indirect detection (WIMP annihilation), direct detection (WIMP scattering on ordinary matter) and collider experiments (WIMP production). In this section, I will describe indirect and direct detection of dark matter. Collider experiments, more closely related to Supersymmetry, will be treated in the next chapter.

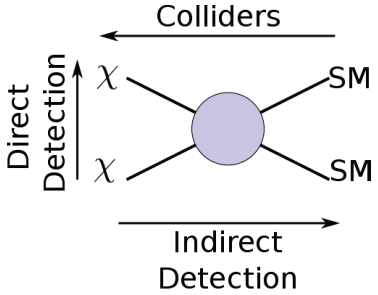

Figure 1.5: The three different types of dark matter particle detection experiments.

1.3.1 Indirect detection

Indirect detection experiments focus on the annihilation of dark matter particles in galactic halos. The annihilation of dark matter particles would produce high-energetic cosmic-rays which could be detectable on Earth. For instance, dark matter could annihilate into gamma-rays, a pair of electron/positrons, or quark/antiquarks which would then hadronize into protons/antiprotons. It is possible to estimate the cosmic-ray spectra expected from ordinary astrophysical events and then to compare it to experimental measurements to search for any deviation. An excess of cosmic-rays in the measurements could be interpreted as a signal of dark matter particle annihilation.

Gamma-rays: Among the cosmic-rays, gamma-rays have the advantage of propagating straightly through the galactic halo, while charged cosmic-rays are diffused by magnetic fields. Several experiments are currently designed to detect gamma-rays, such as the space-telescope Fermi-LAT, sensitive to GeV-scale energies, and ground-based Cherenkov telescopes H.E.S.S. [44], MAGIC [45], VERITAS [46] and HAWC [47], which cover TeV-scale energies. Two types of targets are privileged for gamma-rays: the center of the Milky Way and dwarf spheroïdal galaxies (dSphs). It is expected that dark matter density is peaked at the center of our galaxy, which makes it an ideal target for dark matter annihilation signal. In fact, a gamma-ray excess in the galactic center has been measured by Fermi-LAT [48–53]. However, this excess could be explained either by a dark matter signal or by the presence of milli-second pulsars [54] or even by the past activity of the super-massive black-hole in the galactic center [55]. The second type of targets is dwarf spheroïdal galaxies. These objects are particularly interesting as they are dominated by dark matter and have a low astrophysical background emission of gamma-rays. No significant excess have been detected in dSphs, but one can deduce, from their observations, severe limits on dark

matter annihilation cross section as a function of its mass and annihilation channel.

Antimatter: Contrary to gamma-rays, charged cosmic-rays are diffused by the galactic magnetic field. Therefore, it is not possible to point telescopes towards a specific target and experiments are sensitive to cosmic-rays produced by the entire galactic halo. However, the measurement of their fluxes allows us to draw strong constraints on dark matter. The observation of antiparticles is particularly interesting as their astrophysical background is expected to be very small.
In particular, antiprotons, measured by space telescopes PAMELA [56] and AMS-02 [57], are regarded with great interest. Antiprotons can be divided in two categories according to the way they were produced. *Primary antiprotons* are produced by dark matter annihilation in pair with protons, whereas *secondary antiprotons* are created through the collision of high-energetic protons produced in supernovae with the galactic medium. The theoretical flux of *secondary antiprotons*, which constitutes the astrophysical background, can be summed to the flux of *primary antiprotons*, and then be compared to the flux measured experimentally. An excess has been claimed from AMS-02 data corresponding to a WIMP with a mass around 100 GeV [58, 59]. However, the significance of this excess is questionable considering the large theoretical uncertainties related to the density profile of the dark matter halo, to the propagation of antiprotons through the galactic medium and to the antiproton production cross section from proton-proton and proton-helium interactions.
An excess of positrons has also been observed [60]. However, the lack of knowledge on positron astrophysical background above a few GeV, makes any analysis challenging. As a matter of fact, this excess can also be explained by the presence of young nearby pulsars.

Neutrinos: Dark matter particles are expected to be captured in the Sun through consecutive scatterings on the hydrogen nuclei. The captured dark matter would then annihilate and produce neutrinos that would be detected by experiments such as IceCube [61] or Super-Kamiokande [62]. Assuming equilibrium between dark matter capture and its annihilation, it is possible to draw constraints on dark matter - proton scattering cross sections. These limits are in competition with the spin-dependent cross-section limits obtained from dark matter direct detection, but have the disadvantage of depending strongly on dark matter annihilation channel.

1.3.2 Direct detection

Considering the standard dark matter halo model in which the halo is described as a non-rotating isothermal sphere, the mean dark matter particle velocity in Earth rest frame is the rotational velocity of the sun around the Milky Way $v_{rot} \approx 220$ km/s. If dark matter has a local density around 0.3 GeV/cm^3, as seen in section 1.1.1, and a typical mass for a WIMP $m = 100$ GeV then the flux of dark matter on Earth would be ~ 66000 particles/cm^2/s or ~ 10 million particles per second through one hand. In view of this number, and assuming dark matter couples, though weakly, with baryonic matter, one could expect to observe frequent interactions between dark matter and ordinary particles. The principle of dark matter direct detection is to store a large quantity of baryonic target material and to wait to observe tiny recoil energy deposits when DM particles

scatter off target atomic nuclei. The larger is the time of exposure and the quantity of target material, the larger will be the number of observed events. However, cosmic rays and radioactive emissions, when interacting with the target material, can be mistaken with dark matter. For this reason, direct detection experiments are based underground in order to block cosmic rays and every components, including the target material, are cautiously selected to reduce radioactive background. So far, no convincing signal has been detected, but stringent limits can be derived on the WIMP-nucleon scattering cross sections (see figure 1.6).

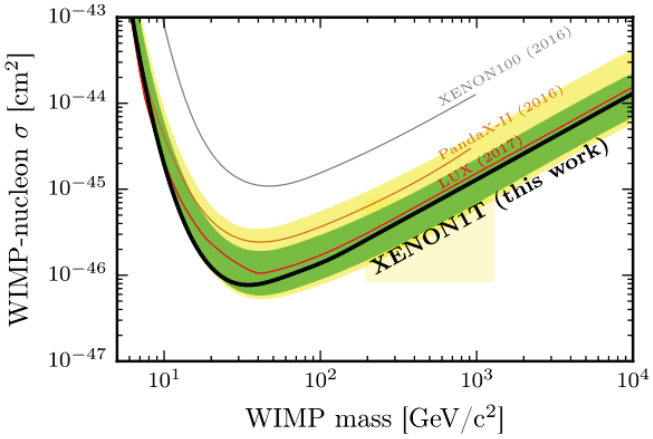

Figure 1.6: Spin-independent WIMP-nucleon cross section limits as a function of WIMP mass at 90% confidence level for XENON1T, LUX, PANDAX-II and XENON100. Figure from [63].

The various direct detection experiments can be differentiated following several criteria:

Low or high WIMP mass: First, they are not all designed to observe WIMPs with the same masses. Some experiments such as EDELWEISS [64], CDMS [65], or CRESST [66], were designed to detect low-mass WIMPs ($m < 10$ GeV). In this specific case, the challenge is to reduce the energy threshold to which the detector starts to be sensitive in order to detect even lower masses. Other experiments such as LUX [67], PANDAX II [68] and XENON1T [63] are dedicated to the search of high-mass WIMPs (10 GeV $\lesssim m \lesssim$ 1 TeV), the latest giving the strongest constraints on the nucleon-WIMP scattering cross section.

Spin-dependent and spin independent interactions: Second, the WIMP-nucleus cross-section is usually decomposed in a spin-independent (SI) and a spin-dependent (SD) contributions in the zero momentum transfer limit. The choice of the target nuclei depends strongly on the type of interactions (SI and/or SD) to which the experiment is designed to be sensitive. The SI WIMP-nucleus cross-section can be written as

$$\sigma^{SI}_{\chi-N} = \frac{4\mu^2}{\pi}[Zf_p + (A-Z)f_n]^2\,, \tag{1.2}$$

where Z and $(A-Z)$ are the number of protons and neutrons in the nucleus, μ is the WIMP-nucleus reduced mass and f_p and f_n are the effective SI WIMP-proton and WIMP-neutron couplings. Using

the common approximation $f_p \approx f_n$, the WIMP-proton and WIMP-neutron SI cross sections are equal and proportional to A^2. In this context, the larger is the nucleon number, the stronger are the interactions. Currently, the most stringent constraints are given by xenon experiments. Argon target experiments, such as DarkSide-50 [69], give limits two orders of magnitude weaker. The SD WIMP-nucleus cross-section can been written as

$$\sigma^{SD}_{\chi-N} = \frac{32\mu^2 G_F^2}{\pi} \frac{J+1}{J} [a_p \langle S_p \rangle + a_n \langle S_n \rangle]^2 , \tag{1.3}$$

where G_F is the Fermi constant, J is the total spin of the nucleus, f_p and f_n are the effective SI WIMP-proton and WIMP-neutron couplings and $\langle S_{p,n} \rangle$ are the average spin contributions from the protons and neutrons in the nucleus. a_p and a_n are the WIMP-proton and WIMP-neutron SD effective scattering amplitudes. If the number of protons and neutrons in the nucleus are even, then the nucleus spin will be zero and there will be no way to detect a WIMP SD interaction. Hence, argon experiments are not sensitive to spin-dependent interactions, since its atomic number is 18 and each of its stable isotope possesses an even number of neutrons. The target nucleus needs to have an odd-number of protons to be sensitive to WIMP-proton SD interactions or an odd-number of neutrons to be sensitive to WIMP-neutron SD interactions. In xenon target experiments, for instance, the spin is carried by neutrons in neutron-odd isotopes (^{129}Xe, ^{131}Xe). The best SD WIMP-neutron cross section limits are currently given by LUX [70] and PANDAX-2 [71]. Regarding the constraints on WIMP-proton SD cross sections, one of the strongest limits is obtained by the PICO-60 experiment, using C_3F_8 target [72].

Method of detection: Finally, the experiments can be differentiated by their method of detection. In fact, the nuclear recoil generated by the scattering of a dark matter particle can be detected via a phonon, scintillation or ionization signal or a combination of these. For instance, most of the xenon experiments, which will be of great interest for us, use a combination of scintillation and ionization signals.

One special feature of a dark matter signal is its annual modulation. As the Earth orbits around the sun, the flux of dark matter is expected to vary according to the velocity of Earth with regard to the dark matter "wind". Thus, the number of events per unit of time is expected to be modulated by ~ 7% along a year. The DAMA/LIBRA collaboration, who used a matrix of NaI(Tl) scintillation detectors, claimed to have observed a signal featuring 7 annual modulations with 8.2σ [73, 74]. However, this signal is very controversial as it was in conflict with XENON 10, XENON 100, and CDMS [75], and its pertinence is still under investigation. The CoGeNT collaboration also claimed to have observed a signal coherent with DAMA/LIBRA [76] but realized, shortly after, that they simply underestimated surface events [77].

The constraints on WIMP-nucleon scattering cross sections are expected to be remarkably improved by experiments that will increase their total target mass and time of exposure, starting with XENONnT [78], LZ [79] and DARWIN [80]. In ten years or so, the detectors should be sensitive enough to reach the neutrino threshold, under which neutrinos will also be detected and will become a problematic background. If no dark matter particle is discovered by then, directional

detection will be key to pursue the search for DM particles [81].

CHAPTER 2

SUPERSYMMETRY

While the concept of dark matter was born from observations and now lacks a consistent theory from a particle point of view, supersymmetry is conversely a purely theoretical formalism lacking observational evidences. Fortunately, both problems may be connected as supersymmetry offers us candidates for dark matter. Any new advances on one side could thus hopefully give further information on the other one.
In this chapter, I will discuss the main limitations of the Standard Model of particle physics and will introduce the fundamental bases of supersymmetry, along with its most simple versions. I will conclude by describing the principles of supersymmetric particle detection at colliders. This chapter is inspired by the *Supersymmetry* book by Pierre Binetruy [82] and *A Supersymmetry Primer* by Stephen P. Martin [83].

2.1 The Standard Model

The Standard Model (SM) of particle physics is built based on gauge symmetry classifies the elementary particles discovered so far and describes electromagnetic, weak and strong interactions. It is, to this day, the most consistent and predictive model in particle physics.

2.1.1 Particle content

In the Standard Model, ordinary matter is composed of fermions of spin 1/2 which interact via gauge bosons of spin 1: photons (electromagnetic interaction), W and Z bosons (weak interaction) and gluons (strong interaction) (see figure 2.1). There are two main types of fermions: quarks and leptons. The *quarks* interact through the strong interaction to form protons and neutrons. Protons, for instance, are composed of two quarks of type *up* (electric charge $Q_{em} = 2/3$) and one quark *down* ($Q_{em} = -1/3$). The *leptons*, contrary to the quarks, do not interact through the strong interaction. However, there are similarly two types of leptons: charged leptons (electrons) and neutral leptons (neutrinos) ν_e. Quarks and leptons exist in three different versions, or *genera-*

tions, differing only by their mass. In other words, it exists two heavier versions of the ordinary fermions (up, down , electron, ν_e), named (charm, strange, μ, ν_μ) and (top, bottom, τ, ν_τ). Finally, fermions present two chiralities: left-handed or right-handed, except for neutrinos which are observed exclusively with a left-handed chirality.
The only scalar field in the SM is the Higgs field, which couples to every quark and charged lepton. Through the Brout-Englert-Higgs-Hagen-Guralnik-Kibble mechanism [84–89], related to electroweak symmetry breaking, the Higgs field acquires a non-zero vacuum expectation value (vev), and is thus responsible of the mass of the particles.

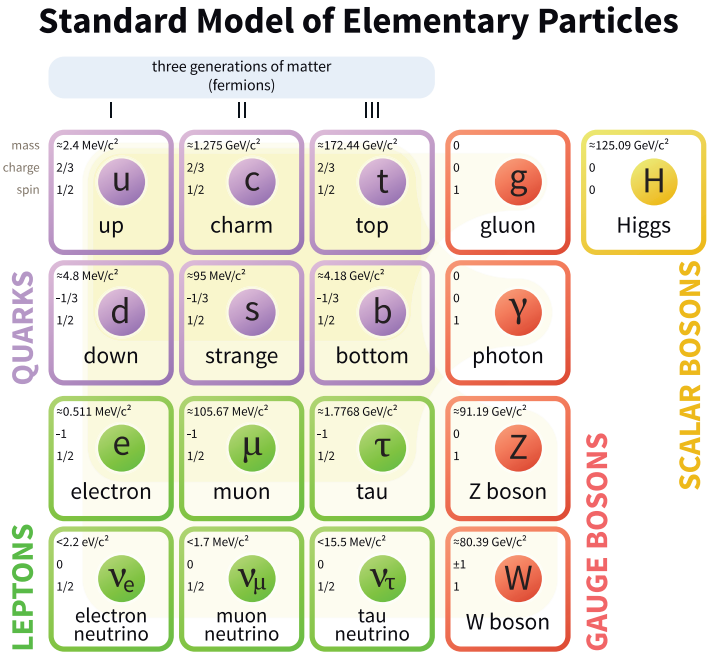

Figure 2.1: Elementary particles in the Standard Model

2.1.2 Symmetry groups

The essential tool in quantum field theory is the Lagrangian, which is an expression depending on the various fields of the model and their derivatives. It defines the dynamics and the couplings of the fields. In order to make the Lagrangian invariant under certain transformations of the fermionic fields, one has to introduce vector (gauge) fields in the model. In this way, one can retrieve naturally the three fundamental gauge interactions.
In the Standard Model, the Lagrangian must be invariant under three symmetries:

$$U_Y(1) \otimes SU_L(2) \otimes SU_c(3).$$

The transformations of a field Ψ corresponding to these symmetries can be written in the general form:

$$\Psi(x) \rightarrow e^{-\alpha_i(x)T^i}\Psi(x) \tag{2.1}$$

where T^i are the generators of the symmetry group and $\alpha_i(x)$ are space-dependent angles.
In the case of $U_Y(1)$, only one generator $\frac{Y}{2}$ exists. Y is a constant, named the hypercharge, which is a property of the field. One gauge boson B_μ is associated to this generator.
The $SU_L(2)$ symmetry possesses three generators $\tau^i = \frac{\sigma^i}{2}$ with σ^i the Pauli matrices, and three corresponding gauge bosons $W^{i=1,2,3}$. Left-handed fermions transform under $SU_L(2)$ in pairs called "doublets": $Q = \begin{pmatrix} u_L \\ d_L \end{pmatrix}$ and $L = \begin{pmatrix} e_L \\ \nu_L \end{pmatrix}$, whereas right-handed fermions are singlets of the $SU_L(2)$ symmetry and do not transform. Each component of a doublet differs by a quantity t_3, namely the third-component of the weak isospin. $t_3 = +1/2$ for up-quarks and electrons and $t_3 = -1/2$ for down-quarks and neutrinos.
Finally, $SU_c(3)$ necessitates eight generators $\lambda^a/2$ where λ^a are the Gell-Mann matrices. Eight gauge bosons, the gluons G^a_μ, $a = 1,2,...8$, are associated to these generators. Quarks are triplets of the SU(3) symmetry. Each representation of a quark with regards to this symmetry differs by a quantum number named the *color* (green, blue, red).

These groups of symmetry are the basis for building the Standard Model Lagrangian, which I will detail in the following.

2.1.3 Standard Model Lagrangian

The Lagrangian of the Standard Model can be divided in four parts:

$$\mathscr{L}_{SM} = \mathscr{L}_{Yang\ Mills} + \mathscr{L}_{Gauge\ interactions} + \mathscr{L}_{Higgs} + \mathscr{L}_{Yukawa}. \tag{2.2}$$

Gauge boson propagation
The first term, the Yang-Mills Lagrangian describes the propagation of the gauge bosons:

$$\mathscr{L}_{Yang\ Mills} = -\frac{1}{4}\left(B_{\mu\nu}B^{\mu\nu} + \sum_{i=1}^{3} W^i_{\mu\nu}W^{i\,\mu\nu} \sum_{i=1}^{8} G^i_{\mu\nu}G^{i\,\mu\nu}\right). \tag{2.3}$$

Here, the objects $B_{\mu\nu}$, $W^i_{\mu\nu}$ and $G^i_{\mu\nu}$ are defined by replacing F by B, W or G in the following general equation:

$$F^i_{\mu\nu} = \partial_\mu F^i_\nu - \partial_\nu F_\mu + g\epsilon_{ijk}F^j_\mu F^k_\nu\ , \tag{2.4}$$

where g is the coupling strength of the gauge symmetry and ϵ_{ijk} is the structure function of the corresponding group. The structure function occurs in the anti-commuting relation $[T^i, T^j] = i\epsilon^{ijk}T^k$, where T^i are the group generators.

Gauge interactions
The second term describes the propagation of fermions and their interactions with gauge fields:

$$\begin{aligned}\mathscr{L}_{Gauge\ interactions} = \sum_{i=1}^{3} &\overline{L}_{i,L}\gamma_\mu D^\mu L_{i,L} + \overline{e}_{i,R}\gamma_\mu D^\mu e_{i,R} \\ &+ \overline{Q}_{i,L}\gamma_\mu D^\mu Q_{i,L} + \overline{u}_{i,R}\gamma_\mu D^\mu u_{i,R} + \overline{d}_{i,R}\gamma_\mu D^\mu d_{i,R}\,,\end{aligned} \tag{2.5}$$

where the covariant derivative D_μ is defined as

$$D_\mu = \partial_\mu + ig' B_\mu \frac{y}{2} + ik_2 g \sum_{i=1}^{3} W_\mu^i \frac{\sigma^i}{2} + ik_3 g_s \sum_{a=1}^{8} G_\mu^a \frac{\lambda^a}{2} \,, \tag{2.6}$$

where g', g and g_s are the coupling strengths of $U_Y(1)$, $SU_L(2)$ and $SU_c(3)$ respectively. k_2 is set to 1 for SU(2) doublets L and Q, and to 0 for other fields, while $k_3 = 1$ for quarks, $k_3 = 0$ otherwise. This covariant derivative ensures the Lagrangian to be invariant under $U_Y(1) \otimes SU_L(2) \otimes SU_c(3)$.

Higgs mechanism

It is not possible to write directly a mass term for the fermions in the Lagrangian without breaking the gauge symmetries. A solution is to introduce a doublet defined as:

$$\phi = \frac{1}{\sqrt{2}} \begin{pmatrix} \phi^+ \\ \phi^0 \end{pmatrix}, \tag{2.7}$$

where ϕ^+ is a complex charged scalar field and ϕ^0 is a neutral complex scalar field.
Its propagation is defined by the Lagrangian:

$$\mathscr{L}_{Higgs} = (D_\mu \phi)^\dagger (D^\mu \phi) - V(\phi), \tag{2.8}$$

where $V(\phi)$ is a potential containing mass terms

$$V(\phi) = -\mu^2 \phi^\dagger \phi + \lambda (\phi^\dagger \phi)^2, \tag{2.9}$$

with μ and λ complex constants.
The minimization of $V(\phi)$ with respect to $|\phi|$ shows that the value of ϕ in the vacuum is non-zero $\phi = \frac{1}{\sqrt{2}} \begin{pmatrix} 0 \\ v \end{pmatrix}$. If μ^2 is chosen to be negative and λ positive, $v = \sqrt{\frac{-\mu^2}{\lambda}}$.
With an appropriate redefinition of the fields and gauge fixing, we are left with a neutral massive scalar field h called the Higgs field, while the three other degrees of freedom of the Higgs doublet are absorbed by the longitudinal components of W and Z bosons.
This mechanism breaks the electroweak $U_Y(1) \otimes SU_L(2)$ symmetry, which is replaced by $U_{em}(1) \otimes SU(2)$ at low energy. $U_{em}(1)$ is the symmetry which describes the usual electromagnetic interaction with $Q_{em} = t^3 + \frac{Y}{2}$.
In this context, B_μ and W_μ^i are not mass eigenstates. They mix to form the photon A_μ, $W^\pm$ and Z^0 bosons:

$$\begin{aligned} W_\mu^+ &= \frac{W_\mu^1 - iW_\mu^2}{\sqrt{2}} \,, & W_\mu^- &= \frac{W_\mu^1 + iW_\mu^2}{\sqrt{2}} \,, \\ Z_\mu^0 &= \frac{g' B_\mu - g W_\mu^3}{\sqrt{g^2 + g'^2}} \,, & A_\mu &= \frac{g' B_\mu + g W_\mu^3}{\sqrt{g^2 + g'^2}} \,. \end{aligned} \tag{2.10}$$

Yukawa couplings

The Higgs doublet couples with the quarks and charged leptons following the Lagrangian:

$$\mathscr{L}_{Yukawa} = -\sum_{i,j=1}^{3} y^u_{i,j}\overline{Q}_i\widetilde{\phi}u_{j,R} + y^d_{i,j}\overline{Q}_i\widetilde{\phi}d_{j,R} + y^l_{i,j}\overline{L}_i\widetilde{\phi}e_{j,R}\,, \tag{2.11}$$

with $\widetilde{\phi} = i\sigma^2\phi^*$, σ^2 being the second Pauli matrix and $\mathbf{y^u}$, $\mathbf{y^d}$, $\mathbf{y^l}$ are 3×3 matrices defining the Yukawa Higgs couplings to fermions. As the Higgs doublet gets a non-zero vacuum expectation value, these terms generate a mass for the fermions.

2.1.4 Beyond the Standard Model

The Standard Model proved to be successful in providing numerous experimental predictions, the latest being the discovery of the Higgs boson at the LHC in 2012 [90, 91]. However, the SM has some theoretical limits and is most probably the effective model at low energy of a more fundamental theory. For instance, it does not provide a satisfying explanation for the matter/antimatter asymmetry, nor why only left-handed neutrinos are observed, and does not describe neutrino masses and oscillation. This model also fails unifying gravitation with the three other fundamental interactions, and even more important for us, does not provide any good candidate for dark matter. It is therefore necessary to build models beyond the Standard Model.
The recurrent idea when building a new model in particle physics is to assume the existence of a new symmetry, similarly to the way the Standard Model was constructed. One of the theories which have been regarded as the most promising for the last decades is supersymmetry and is precisely based on the idea that a symmetry exists between fermions and bosons.

2.2 The supersymmetric hypothesis

The idea of supersymmetry (SUSY) was developed and formalized at the beginning of 70's from independent and very diverse studies [92–95]. It states that a symmetry exists between fermions (particles with half-integer spins) and bosons (particles with integer spins). Formally, there should be an operator allowing us to pass from a fermionic field to a bosonic field and vice-versa. The fields could thus be grouped into families of at least two members (one fermion and one boson) called supermultiplets, of same electric charge and colors. This theory involves unavoidably the existence of undiscovered particles, "superpartners" of the particles already known. These superparticles should not have the same mass as their partners, otherwise they would have already been detected. Therefore, supersymmetry must be broken via some unknown mechanism. Nevertheless, supersymmetry opens up the way to new exciting discoveries and allows us to solve fundamental problems.

2.2.1 Grand Unified Theory

The unification of the three gauge fundamental interactions into one larger gauge symmetry is a long-term problem. In the SM, the coupling constants of electromagnetism, strong and weak interactions differ by several orders of magnitude at low energy and cannot be renormalized to a

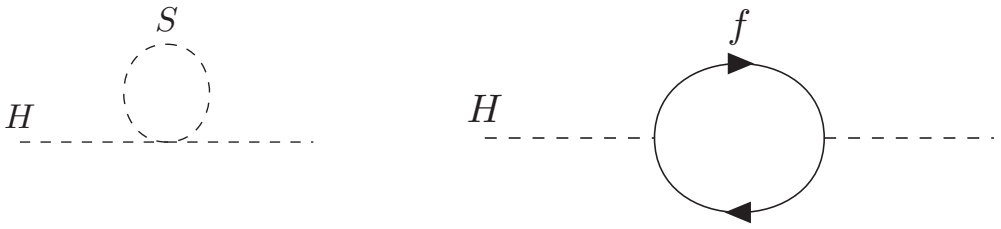

Figure 2.2: One-loop quantum corrections to the Higgs squared mass parameter due to a scalar (left) and a fermion (right).

unified constant at a higher energy. In supersymmetry, the three coupling constants unify naturally at an energy of $\sim 10^{16}$ GeV.

2.2.2 Supergravity and theory of everything

The next step would be to unify gravitation with the three gauge interactions. It appears that when supersymmetry is made local, one can naturally retrieve Einsteins's equations of General Relativity. That is what is called Supergravity [96–98]. This theory is still non-renormalizable, but could lead to a more fundamental theory. Moreover, it comes out that supersymmetry may be necessary for the string theory to be consistent. Finally, supersymmetry is demonstrated to be the only way to merge Poincaré's group and internal symmetries such as the spin into one larger group. It constitutes, in fact, the only loophole to the Coleman-Mandula no-go theorem.

2.2.3 Hierarchy problem

Another problem, more subtle but also more fundamental for particle theorists is related to the calculation of the Higgs mass. The Higgs mass suffers indeed from quadratically divergent quantum corrections from its interaction with scalars and fermions, as represented in figure 2.2.
The quantum loop corrections due to a scalar and a fermion can be written as:

$$\Delta M_H^2 = +\frac{\lambda_S}{16\pi^2}\Lambda_{\mathrm{UV}}^2 + \ldots \tag{2.12}$$

and

$$\Delta M_H^2 = -\frac{|\lambda_f|^2}{8\pi^2}\Lambda_{\mathrm{UV}}^2 + \ldots, \tag{2.13}$$

with Λ_{UV} a finite cut-off in the loop integrals, which is not necessarily the same from one correction to another.

In the SM, the different contributions to the quantum corrections do not compensate, except if invoking a large fine-tuning between the parameters, and the corrections to the bare mass diverge abnormally compared to the observed mass of the Higgs boson $M_H \approx 125$ GeV. Supersymmetry gives a very natural mechanism to avoid those divergences. For every fermion, composed of a left-handed and right-handed part, exists two superpartner scalars corresponding to each chirality. If

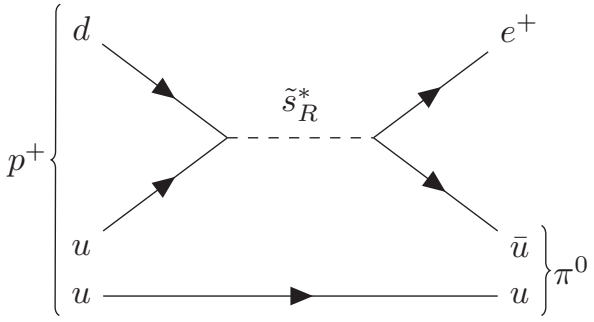

Figure 2.3: Proton decay into a pion and a positron in supersymmetry.

$|\lambda_f|^2 = \lambda_s$, then the corrections due to the fermion and its superpartners compensate. Therefore, no fine-tuning needs to be invoked.
However, this mechanism works well only if the masses of the superpartners are of the order of the TeV. Beyond, higher order corrections become important and the *naturalness* is lost.

2.2.4 R-Parity and dark matter

Supersymmetry also provides candidate particles for dark matter. In fact, this feature arises from the solution to another problem. Assuming supersymmetry exists, the proton should be able to decay into a pion and a positron via a quark superpartner (squark), as shown in diagram 2.3.

However, the proton must have a half-life longer than the age of the Universe. Therefore, this decay should be forbidden. By invoking a new discrete symmetry called R-parity [99], it is possible to find a solution to this problem. If one notes

$$R_p = (-1)^{2S+3(B-L)}\,, \tag{2.14}$$

with S the spin of the particle, B its baryonic number and L its leptonic number, $R_p = +1$ for ordinary particles and $R_p = -1$ for superparticles. If this multiplicative parity is conserved during an interaction, vertices with an odd number of superparticles should be forbidden. This symmetry would thus prevent proton decay.
Moreover, R-parity would also force superparticles to decay into one lighter superparticle and some baryonic particles. Hence, the lightest supersymmetric particle (LSP) is preserved from decay.
If the LSP is neutral and interacts weakly with baryonic matter, it can be considered as an obvious candidate for dark matter.

Numerous models of supersymmetry exist and differ essentially by the number $\mathcal{N}+1$ of fields contained in a supermultiplet. In the following, we will build the Lagrangian in the case $\mathcal{N} = 1$ for the chiral and vector supermultiplets.

2.3 Supersymmetric Lagrangian

In the model $\mathcal{N} = 1$, in the absence of graviton, only two kinds of supermultiplets exist: chiral and vector supermultiplets.

2.3.1 Chiral supermultiplet

The chiral supermultiplet is composed of a Weyl fermion ψ and a complex scalar superpartner ϕ. In the case of massless fields, the most simple Lagrangian is the Wess-Zumino Lagrangian [94] consisting only of kinetic terms

$$\mathcal{L}_{WZ} = -\partial^\mu \phi^* \partial_\mu \phi + i\overline{\psi}\overline{\sigma}^\mu \partial_\mu \psi + F^* F \,. \tag{2.15}$$

Here, F is a scalar auxiliary field added in order to make the Lagrangian invariant under supersymmetry. F is indeed chosen to transform under supersymmetry in such a way that it compensates exactly the transformation terms of the other fields. Infinitesimal transformations can thus be written:

$$\begin{aligned} \delta\phi &= \epsilon\psi, & \delta\phi^* &= \bar{\epsilon}\overline{\psi}, \\ \delta\psi &= -i\sigma^\mu \bar{\epsilon}\partial_\mu \phi + \epsilon F, & \delta\overline{\psi} &= i\epsilon\sigma^\mu \partial_\mu \phi^* + \bar{\epsilon} F^*, \\ \delta F &= -i\bar{\epsilon}\overline{\sigma}^\mu \partial_\mu \psi & \delta F &= i\partial_\mu \overline{\psi}\overline{\sigma}^\mu \epsilon. \end{aligned} \tag{2.16}$$

where ϵ is an anticommuting Weyl spinor, invariant under space-time transformations, which characterizes the supersymmetric infinitesimal transformation.

Chiral supermultiplets $\Psi_i = (\psi_i, \phi_i, F_i)$ can interact between each other according to the interacting Lagrangian

$$\mathcal{L}_{int} = -\frac{1}{2}\mathcal{W}^{ij}\psi_i\psi_j + \mathcal{W}^i F_i + h.c. \tag{2.17}$$

where $\mathcal{W}$ is the *superpotential* defined as

$$\mathcal{W} = \frac{1}{2}M^{ij}\phi_i\phi_j + \frac{1}{6}y^{ijk}\phi_i\phi_j\phi_k. \tag{2.18}$$

I omitted in this last equation a term which appears only when a singlet exists in the model, which will not be the case in the Minimal Supersymmetric Standard Model described in next section.
The superscripts i and j in $\mathcal{W}^{ij}$ and $\mathcal{W}^i$ refer to the partial derivatives with respect to the scalar fields ϕ_i and ϕ_j.

$$\mathcal{W}^i = \frac{\partial \mathcal{W}}{\partial \phi_i}, \qquad \mathcal{W}^{i,j} = \frac{\partial^2 \mathcal{W}}{\partial \phi_i \partial \phi_j} \,. \tag{2.19}$$

The form of $\mathcal{L}_{int}$ is, in fact, specifically chosen in order to be invariant under supersymmetry. It is important to note, for instance, that the superpotential cannot depend on ϕ^*. This feature is important in the Higgs sector as the Standard Model Yukawa couplings is thus not allowed. In order to get a Higgs mechanism consistent with supersymmetry, two Higgs doublets H_u and H_d

will be required.

The auxiliary field can then be eliminated by making use of its equation of motion:

$$F_i = -\mathcal{W}_i^*, \qquad F^{*i} = -\mathcal{W}^i. \tag{2.20}$$

The Wess-Zumino and interacting Lagrangians can finally be summed to form the total chiral Lagrangian :

$$\mathcal{L}_{chiral} = -\partial^\mu \phi^{i\,*} \partial_\mu \phi_i + i\overline{\psi}^i \overline{\sigma}^\mu \partial_\mu \psi_i - \frac{1}{2}\left(\mathcal{W}^{ij}\psi_i\psi_j + \mathcal{W}^8_{ij}\overline{\psi}^i\overline{\psi}^j\right) - \mathcal{W}^i\mathcal{W}_i^*. \tag{2.21}$$

2.3.2 Gauge supermuliplet

The second basic supermultiplet is the gauge (or vector) supermultiplet. It is composed of a massless gauge boson A^a_μ and a two-component Weyl fermion gaugino ξ^a. The propagations and interactions between these two fields are described by the Lagrangian:

$$\mathcal{L}_{gauge} = -\frac{1}{4}F^a_{\mu\nu}F^{a\,\mu\nu} + i\overline{\xi}^a\overline{\sigma}^\mu D_\mu \xi^a + \frac{1}{2}D^a D^a \ , \tag{2.22}$$

where $a = 1,2,...n$ with $n = 8$ for SU(3), $n = 3$ for SU(2) and $n = 1$ for U(1). $F^a_{\mu\nu}$ is defined as in equation 2.4 for the vector field A_μ, and the covariant derivative D_μ describes the interaction of the fermion with gauge field.
One real bosonic field D^a needs to be added to the Lagrangian for the sake of supersymmetry invariance, similarly to the auxiliary field F of the chiral supermultiplet. The supersymmetric transformations of the fields counterbalance in the Lagrangian according to:

$$\delta A^a_\mu = -\frac{1}{\sqrt{2}}\left(\overline{\epsilon}\overline{\sigma}_\mu \xi^a + \overline{\xi}^a\overline{\sigma}_\mu\epsilon\right) \ , \tag{2.23}$$

$$\delta\xi^a = \frac{i}{2\sqrt{2}}\left(\sigma^\mu\overline{\sigma}^\nu\epsilon\right)F^a_{\mu\nu} + \frac{1}{\sqrt{2}}\epsilon D^a \ , \tag{2.24}$$

$$\delta D^a = \frac{i}{\sqrt{2}}\left(\ \overline{\epsilon}\overline{\sigma}^\mu D_\mu\xi^a + D_\mu\overline{\xi}^a\overline{\sigma}^\mu\epsilon\right). \tag{2.25}$$

2.3.3 Gauge interactions

Additional interactions can exist between the vector boson of a gauge supermultiplet A^a_μ and the other fields. First, it is sufficient to replace partial derivatives by covariant derivatives in equation 2.15 to couple A^a_μ to the scalar and fermionic components of chiral multiplets. Then, A^a_μ can also couple to the fermionic and auxiliary fields of the gauge multiplets via three types of couplings which respect renormalizability: $(\phi^* T^a \psi)\xi^a$, $\overline{\xi}(\overline{\psi}T^a\phi)$ and $(\phi^* T^a\phi)D^a$ where T^a are the generators of the gauge symmetry related to A^a_μ.

The total supersymmetric Lagrangian can finally be written under the form

$$\mathcal{L} = \mathcal{L}_{chiral} + \mathcal{L}_{gauge} \tag{2.26}$$

$$- \sqrt{2}g(\phi^* T^a\psi)\lambda^a - \sqrt{2}g\overline{\lambda}(\overline{\psi}T^a\phi) + g(\phi^* T^a\phi)D^a. \tag{2.27}$$

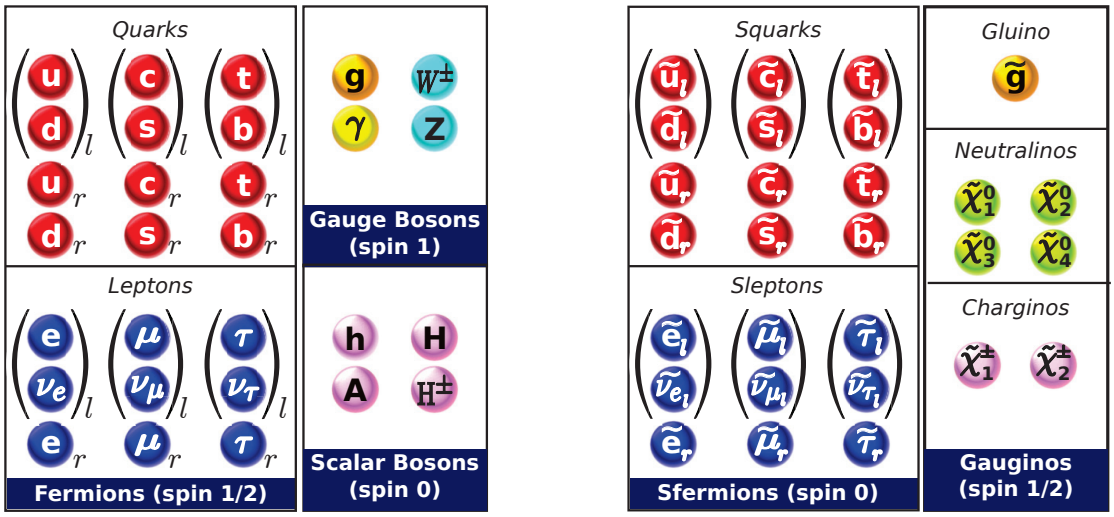

Figure 2.4: The Minimal Supersymmetric Standard Model

The most simple version of this model is the Minimal Supersymmetric Standard Model, which contains the minimal number of fields. In the next section, I will describe this model from a phenomenological point of view.

2.4 The Minimal Supersymmetric Standard Model

The Minimal Supersymmetric extension of the Standard Model (MSSM) was developed by Pierre Fayet in the late 70's [100–102]. He showed that within the Standard Model, no particle could be the superpartner of another. He was then able to built the supersymmetric model with the minimum number of particles (see figure 2.4). The SM fermions are contained in chiral supermultiplets along with their scalar partners named *sfermions*, while SM vector bosons are in gauge supermultiplets with Weyl fermion superpartners called *gauginos*.

As mentioned previously, supersymmetry needs to be broken to explain the difference in mass between SM particles and their supersymmetric partners. The mechanism of symmetry breaking is still under debate. However, it is possible to introduce an ad-hoc additional term to the supersymmetric Lagrangian to study the phenomenology of the model at low energy. This term, qualified as "soft" contains the mass terms for the superpartners.

$$\begin{aligned}\mathscr{L}_{soft} = &-\frac{1}{2}(M_1\widetilde{B}\widetilde{B} - M_2\widetilde{W}^i\widetilde{W}_i - M_3\widetilde{G}^\alpha\widetilde{G}_\alpha + h.c.)\\ &- m^2_{H_u}H_u^\dagger H_u - m^2_{H_d}H_d^\dagger H_d - (bH_uH_d + h.c.)\\ &- (\widetilde{u}^*_R\mathbf{a_u}\widetilde{Q}H_u - \widetilde{d}^*_R\mathbf{a_d}\widetilde{Q}H_d - \widetilde{e}^*_R\mathbf{a_e}\widetilde{L}H_d + h.c.)\\ &- \widetilde{Q}^\dagger\mathbf{m^2_{\tilde{Q}}}\widetilde{Q} - \widetilde{L}^\dagger\mathbf{m^2_{\tilde{L}}}\widetilde{L} - \widetilde{u}^*_R\mathbf{m^2_{\tilde{u}_R}}\widetilde{u}_R - \widetilde{d}^*_R\mathbf{m^2_{\tilde{d}_R}}\widetilde{d}_R - \widetilde{e}^*_R\mathbf{m^2_{\tilde{e}_R}}\widetilde{e}_R\ .\end{aligned} \tag{2.28}$$

When a tilde is drawn over a field, we refer to its superpartner. For instance, $\widetilde{u_R}$ refers to the superpartner of the right-handed up-quark. The terms in $\mathbf{a_f}$ are trilinear coupling matrices and

those in $\mathbf{m}_{\tilde{\mathbf{f}}}$ are soft squared mass matrices.

In the following, we will describe the phenomenology of the Higgs, sfermion, and gaugino sectors.

2.4.1 Higgs sector

To get a consistent supersymmetric Higgs mechanism for the electroweak symmetry breaking, it is necessary to assume the existence of two Higgs doublets $H_u = \left(H_u^+, H_u^0\right)$ and $H_d = \left(H_d^0, H_d^-\right)$, while there is only one doublet in the SM. The interactions between the two Higgs doublets H_u and H_d are contained in the superpotential

$$\mathcal{W}_{MSSM} = \tilde{u}_R^* \mathbf{y_u} \tilde{Q} H_u - \tilde{d}_R^* \mathbf{y_d} \tilde{Q} H_d - \tilde{e}_R^* \mathbf{y_e} \tilde{L} H_d + \mu H_u H_d \,. \tag{2.29}$$

H_u couples to up-type quarks and H_d to down-type quarks and charged leptons. Those two complex doublets represent eight degrees of freedom. After electroweak symmetry breaking, three of them become the longitudinal modes of the W and Z bosons, leaving five physical mass-eigenstate Higgs bosons: two neutral CP-even scalars h^0 and H^0, with $m_{h^0} < m_{H^0}$, two charged CP-even scalar $H^\pm$, and one neutral pseudo-scalar A^0. The two neutral component of the Higgs doublet acquire a vev:

$$\langle H_u^0 \rangle = \frac{v\, sin\beta}{\sqrt{2}} \,, \qquad \langle H_d^0 \rangle = \frac{v\, cos\beta}{\sqrt{2}} \,, \tag{2.30}$$

with v the vev in the Standard Model and β a free parameter of the model, usually used in the form of

$$tan\beta = \frac{\langle H_u^0 \rangle}{\langle H_d^0 \rangle} \,. \tag{2.31}$$

This angle β, along with another mixing angle α, also appears in the matrix allowing us to pass from the Higgs doublet elements to the mass eigenstates:

$$\begin{pmatrix} H_d^0 \\ H_u^0 \end{pmatrix} = \frac{1}{\sqrt{2}} \begin{pmatrix} cos\,\alpha & -sin\,\alpha \\ sin\,\alpha & cos\,\alpha \end{pmatrix} \begin{pmatrix} H^0 \\ h^0 \end{pmatrix} + i \frac{1}{\sqrt{2}} \begin{pmatrix} cos\,\beta & sin\,\beta \\ -sin\,\beta & cos\,\beta \end{pmatrix} \begin{pmatrix} Z_L^0 \\ A^0 \end{pmatrix} \,, \tag{2.32}$$

$$\begin{pmatrix} H_d^\pm \\ H_u^\pm \end{pmatrix} = \frac{1}{\sqrt{2}} \begin{pmatrix} cos\,\beta & sin\,\beta \\ -sin\,\beta & cos\,\beta \end{pmatrix} \begin{pmatrix} W_L^\pm \\ H^\pm \end{pmatrix} \,. \tag{2.33}$$

The masses of the different Higgs bosons can be expressed at tree level in terms of β, the mass of the lightest Higgs m_{h^0} and the masses of Z and $W^\pm$ bosons. Simple relations between these masses can then be written, such as:

$$m_{H^0}^2 + m_{h^0}^2 = m_{A^0}^2 + m_Z^2 \,, \tag{2.34}$$

$$m_{H^\pm}^2 = m_{A^0}^2 + m_W^2 \,, \tag{2.35}$$

which assure that all the heavy Higgs bosons are of equal order of magnitude in mass.

2.4.2 Sfermion sector

In the MSSM, every fermion has one or two superpartners called *sfermions* depending on its number of degrees of freedom, the *s* at the beginning of the name referring to *scalar*. For instance, the left-handed and right-handed chiral component of quarks and charged leptons are each associated to one sfermion. The squarks and sleptons are commonly denoted by a r or a l according to the chirality of their superpartners, but do not have a chirality on their own, as they are scalars. One should be aware of this subtility when we will talk in the following of left/right-handed sfermions. Neutrinos, however, are only observed with a left-handed chirality, and only have one superpartner.
The superpartners of the left-handed and right-handed sfermions may mix according to the mass matrices for up-type squarks, down-type squarks and charged leptons of the i^{th} generation.

$$\begin{aligned}\widetilde{M}^2_{u_i} &= \begin{bmatrix} \widetilde{m}^2 u_i LL & \widetilde{m}^2 u_i LR \\ \widetilde{m}^2 u_i RL & \widetilde{m}^2 u_i RR \end{bmatrix} \\ &= \begin{bmatrix} m^2_{Q_i} + m^2_{u_i} + \frac{1}{6}(4M^2_W - M^2_Z)cos\,2\beta & m_{u_i}(A^*_{u_i} - \mu cot\,\beta) \\ m_{u_i}(A_{u_i} - \mu^* cot\,\beta) & m^2_{U_i} + m^2_{u_i} + \frac{2}{3}(-M^2_W + M^2_Z)cos\,2\beta \end{bmatrix},\end{aligned} \tag{2.36}$$

$$\begin{aligned}\widetilde{M}^2_{d_i} &= \begin{bmatrix} \widetilde{m}^2 d_i LL & \widetilde{m}^2 d_i LR \\ \widetilde{m}^2 d_i RL & \widetilde{m}^2 d_i RR \end{bmatrix} \\ &= \begin{bmatrix} m^2_{Q_i} + m^2_{d_i} + \frac{1}{6}(4M^2_W - M^2_Z)cos\,2\beta & m_{d_i}(A^*_{d_i} - \mu cot\,\beta) \\ m_{d_i}(A_{d_i} - \mu^* cot\,\beta) & m^2_{D_i} + m^2_{d_i} + \frac{2}{3}(-M^2_W + M^2_Z)cos\,2\beta \end{bmatrix},\end{aligned} \tag{2.37}$$

$$\begin{aligned}\widetilde{M}^2_{e_i} &= \begin{bmatrix} \widetilde{m}^2 e_i LL & \widetilde{m}^2 e_i LR \\ \widetilde{m}^2 e_i RL & \widetilde{m}^2 e_i RR \end{bmatrix} \\ &= \begin{bmatrix} m^2_{L_i} + m^2_{e_i} + \frac{1}{6}(4M^2_W - M^2_Z)cos\,2\beta & m_{e_i}(A^*_{e_i} - \mu cot\,\beta) \\ m_{e_i}(A_{e_i} - \mu^* cot\,\beta) & m^2_{E_i} + m^2_{e_i} + \frac{2}{3}(-M^2_W + M^2_Z)cos\,2\beta \end{bmatrix},\end{aligned} \tag{2.38}$$

where m_{u_i}, m_{d_i} and m_{e_i} are the fermion masses, μ the Higgs-Higgsino mass term, A_{u_i}, A_{d_i} and A_{e_i} trilinear soft couplings. m_{Q_i} is the soft mass term associated to the SU(2) doublet formed by the superpartners of the left-handed up-type and down-type quarks and m_{U_i} and m_{D_i} are the mass terms of the right-handed up-squarks and down-squarks. Identically, m_{L_i} is the mass term of the doublet formed by the left-handed selectron/sneutrino and m_{E_i} the mass term of the right-handed charged lepton.
One can note that the non-diagonal terms are all proportional to the fermion mass. Hence, these terms will be negligible for the first and second generation of sfermions, but mixings will occur for the third generation. In the latter case, the trilinear couplings A_b, A_t and A_τ may have some phenomenological importance. The right-handed and left-handed sbottoms, stops and staus will respectively mix to form mass eigenstates $\{\widetilde{b}_1, \widetilde{b}_2\}$, $\{\widetilde{t}_1, \widetilde{t}_2\}$ and $\{\widetilde{\tau}_1, \widetilde{\tau}_2\}$ with indices 1,2 denoting a classification in mass ($m_{\widetilde{b}_1} < m_{\widetilde{b}_2}$, ...).

2.4.3 Gaugino-Higgsino sector

As for ordinary bosons, their superpartners are named by adding -ino at the end of the word. The superpartner of the Higgs boson is, for instance, named higgsino. The superpartners of the Higgs bosons are not mass eigenstates and mix with the superpartners of the photon, Z and $W^{\pm}$ bosons. This gives four neutral gauginos called neutralinos $\tilde{\chi}_1^0$, $\tilde{\chi}_2^0$, $\tilde{\chi}_3^0$, $\tilde{\chi}_4^0$ and two charged gauginos simply named charginos $\tilde{\chi}_1^{\pm}$, $\tilde{\chi}_2^{\pm}$. The indices attributed to neutralinos and charginos refer to the hierarchy in mass $m_{\tilde{\chi}_1^0} < m_{\tilde{\chi}_2^0} < m_{\tilde{\chi}_3^0} < m_{\tilde{\chi}_4^0}$. In the following, if no index is mentioned, it will refer to the lightest neutralino. The lightest neutralino will be of the greatest interest to us as it constitutes the most promising candidate for dark matter. Sneutrinos, in the case they are the LSP, could also be eligible candidates. However, they interact too strongly with baryonic matter and are already excluded by direct detection constraints [103].
When discussing the nature of the neutralino, we will refer to its fraction in higgsinos, and in photon and Z superpartners. In fact, instead of considering the photon and Z superpartners, we will refer to the gauge eigenstates before electroweak symmetry breaking B^0 and W^3. The neutralino can thus be considered as a superposition of a *bino*, a *wino* and a *higgsino* and we will use the basis $\Psi^0 = \{\widetilde{B}^0, \widetilde{W}^3, \widetilde{H}_d^0, \widetilde{H}_u^0\}$. The mass eigenstates can then be calculated via the mixing matrix N:

$$\tilde{\chi}_i^0 = N_{i,j}\Psi_j^0 \,, \qquad \text{with } j \in \{1,2,3,4\} \,. \tag{2.39}$$

Using this notation, we will consider that the lightest neutralino is:

- **Bino-like** if $N_{1,1}^2 \approx 1$
- **Wino-like** if $N_{1,2}^2 \approx 1$
- **Higgsino-like** if $N_{1,3}^2 + N_{1,4}^2 \approx 1$
- **Mixed** otherwise.

The neutralino nature is important as each type presents different phenomenological properties. For instance, bino-like neutralinos are known to have small annihilation cross sections and for this reason, a large relic density. The different types of neutralino also behave differently in the context of direct and indirect detection, as we will see in Part II. For instance, among the 13 different tree level neutralino annihilation channels enumerated in figure 2.5, wino-like neutralinos will privilege the $\chi\chi \to WW$ channel, while higgsino-like neutralinos will mostly annihilate into a pair of Z bosons.
As for direct detection, the neutralino interacts with the quark content of atoms through four types of channel at tree level (see figure 2.6). The interaction through a CP-even Higgs boson is spin-independent in the zero-momentum transfer approximation, while the interaction via a Z boson is spin-dependent. The scattering via a squark in s-channel or t-channel has at the same time a spin-dependent and spin-independent component.
As we will see in part II, the phenomenology of the different neutralino types can be substantially different in the context of direct detection.

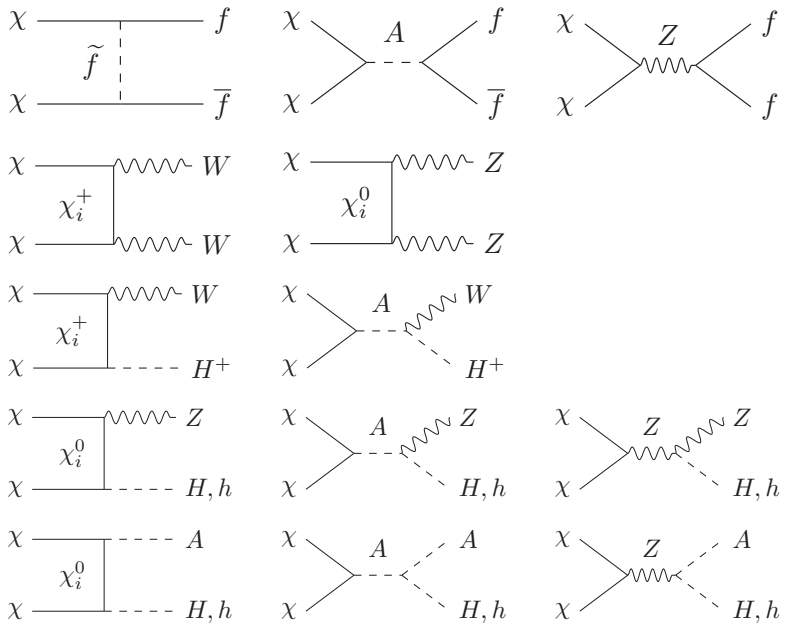

Figure 2.5: Neutralino annihilation channels.

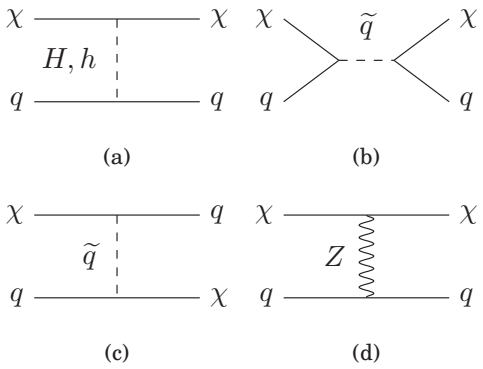

Figure 2.6: Scattering channels of the lightest neutralino on a quark.

2.4.4 Constrained Models

The MSSM, though the simplest model of supersymmetry, presents more than one hundred free parameters consisting essentially in superparticle masses, couplings and the ratio of the two Higgs vacuum expectation values $\tan\beta$. This large number of free parameters does not allow to perform any relevant scan in order to test the validity of the model. However, several ways were thought to reduce the number of free parameters:

Constrained MSSM (CMSSM): The CMSSM [104] is directly related to the minimal model of supergravity mSUGRA, which describes a mechanism of gravitation-mediated supersymmetry breaking. Knowing how supersymmetry was broken allows us to reduce considerably the number of free parameters. In the CMSSM, only four free parameters remain at the GUT scale: the

$\tan\beta$	the ratio of the vevs of the two Higgs doublet
M_A	Mass of pseudo-scalar Higgs
M_1, M_2, M_3	Bino, wino and gluino mass parameters
μ	Higgs-Higgsino mass parameter
$M_{\tilde{q}}, M_{\tilde{u}_R}, M_{\tilde{d}_R}, M_{\tilde{l}}, M_{\tilde{e}_R}$	first/second generation sfermion masses
$M_{\tilde{Q}}, M_{\tilde{t}_R}, M_{\tilde{b}_R}, M_{\tilde{L}}, M_{\tilde{\tau}_R}$	third generation sfermion masses
A_t, A_b, A_τ	third generation trilinear coupling

Table 2.1: pMSSM 19 free parameters.

universal scalar mass m_0, the gaugino mass parameter $m_{1/2}$, the universal trilinear coupling A_0, the ratio of the two Higgs vacuum expectation values $\tan\beta$. The sign of the higgsino mass parameter μ is also to be chosen. The CMSSM constitutes a benchmark model tested by the various experimental analyses. It is however already tightly constrained by the LHC, direct detection and the measurement of the relic density.

The phenomenological MSSM (pMSSM) [105]: A more general set-up without the GUT scale unification assumption is the phenomenological MSSM. By imposing natural constraints in regards to the observed particle phenomenology, it is possible to reduce the number of free parameters. In the case of the phenomenological MSSM, it is imposed that no new source of CP violation and no Flavour Changing Neutral Current (FCNC) can emerge from supersymmetry, and that there is a universality between the first and second generations of fermions. The number of free parameters is thus reduced to only 19. For instance, in order to remove all new sources of CP-violation, one can simply set all phases in the soft-SUSY breaking potential to zero, and it is necessary to impose that the matrices for the sfermion masses and for the trilinear couplings are diagonal in order to avoid FCNCs. Moreover, the first and second generation universality involves that the sfermion masses are equal between the two first generations: $m_{\tilde{u}} = m_{\tilde{c}}$, $m_{\tilde{d}} = m_{\tilde{s}}$, $m_{\tilde{e}} = m_{\tilde{\mu}}$... A complete list of the parameters is given in table 2.1 with their meanings.

2.4.5 Extensions of the MSSM

As we will see in the following, the MSSM is tightly constrained by current experiments. It is therefore interesting to study other models of supersymmetry, and in particular, simple extensions of the MSSM. The easiest way to extend the MSSM is to add a new kind of particle to the SM, such as the axion and the graviton. The superpartners of these particles, the axino and the gravitino can have interesting phenomenologies and could be a dark matter particle if they are the LSP.
Another way to extend the MSSM is to add a gauge singlet. That is what is done in the next-to-minimal supersymmetric standard model (NMSSM). This model has the advantage to solve the so-called μ-problem. In the supersymmetric Lagrangian, in the term $\mu H_u H_d$, μ should be of the order of magnitude of the electroweak scale in order to obtain non-zero vevs. This feature has

no natural explanation in the MSSM, but find a straightforward solution in the NMSSM. The singlet gives two additional Higgs scalar bosons compared to the MSSM: one CP-even scalar and one CP-odd scalar. The supersymmetric counterparts of those particles form a fifth neutralino.

2.5 SUSY searches at colliders

Superparticles are the subject of active searches at colliders, even if no significant excess has been measured yet. Though the 750 GeV excess at ATLAS [106] and CMS [107] made quite a fuss, it eventually happened to be just a simple statistical fluctuation. Nevertheless, collider results lead to strong constraints on the MSSM. Two types of colliders will be of interest for us: electron/positron and proton/antiproton colliders.

2.5.1 Electron/positron Colliders

The Large Electron-Positron collider (LEP) at CERN, Geneva, is the largest electron-positron circular collider ever constructed with 27km in circumference. During its period of activity (1989-2000), the LEP reached a center of mass energy of 209 GeV and led to high-precision measurements of the W and Z bosons.
Electron/positron collisions should produce all types of superparticle, except gluinos because of colour conservation.

$$e^+e^- \to \widetilde{\chi}_i^+\widetilde{\chi}_j^-, \quad \widetilde{\chi}_i^0\widetilde{\chi}_j^0, \quad \widetilde{l}^+\widetilde{l}^-, \quad \widetilde{\nu}\widetilde{\nu}^*, \quad \widetilde{q}\widetilde{q}^* \,.$$

Even if none of those processes has been observed, strong limits on the superparticle masses were drawn. In 2001, the LEP was dismantled to leave place to the construction of the LHC.

2.5.2 Hadron Colliders

One of the most important hadron colliders and the largest before the LHC is the Tevatron. This circular proton/antiproton collider of 1 km in diameter was in use at Fermilab from 1987 to 2011 and reached a center of mass energy of 1.96 TeV without detecting any superparticle.
The Large Hadron Collider (LHC), at CERN, Geneva, took over this search in 2010. It is the most powerful hadron collider in the world with 27 km in circumference. Its activity can be divided in two periods. From 2010 to 2013, the first run was performed with a center mass energy of 8 TeV, leading to the detection of the Higgs boson in 2012. The LHC started its second run in 2015 with an energy of 13 TeV, confirming the mass of the Higgs boson at ~ 125 GeV.
Four detectors are built on the LHC ring:

- **ATLAS and CMS** are dedicated to high-precision measurements of SM observables and to the search for new physics,
- **LHCb** is dedicated to flavour physics measurements,
- **ALICE** is designed for the study of heavy ions.

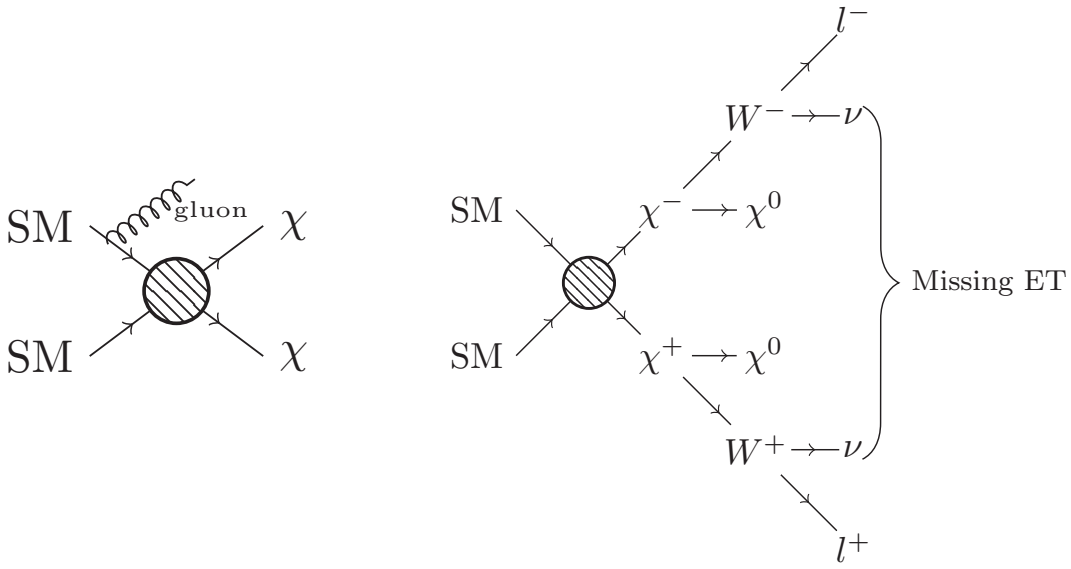

Figure 2.7: **Left:** Monojet. **Right:** Example of SUSY direct searches with two leptons and missing transverse energy in the final state.

Superparticles can be produced from the interaction of quarks and gluons at the electroweak strength via the processes:

$$q\overline{q} \to \widetilde{\chi}_i^+ \widetilde{\chi}_j^-, \quad \widetilde{\chi}_i^0 \widetilde{\chi}_j^0 \qquad u\overline{d} \to \widetilde{\chi}_i^+ \widetilde{\chi}_j^0, \qquad \overline{u}d \to \widetilde{\chi}_i^- \widetilde{\chi}_j^0,$$

$$q\overline{q} \to \widetilde{l}_i^+ \widetilde{l}_j^-, \quad \widetilde{\nu}_l \widetilde{\nu}_l^* \qquad u\overline{d} \to \widetilde{l}_L^+ \widetilde{\nu}_l, \qquad \overline{u}d \to \widetilde{l}_L^- \widetilde{\nu}_l^*,$$

and at QCD strength via:

$$g\overline{g} \to \widetilde{g}\widetilde{g}, \quad \widetilde{q}_i \widetilde{q}_j^* \qquad gq \to \widetilde{g}\widetilde{q}_i,$$

$$q\overline{q} \to \widetilde{g}\widetilde{g}, \quad \widetilde{q}_i \widetilde{q}_j^* \qquad qq \to \widetilde{q}_i \widetilde{q}_j.$$

As superparticles are expected to decay quickly, except for the LSP, one can only search for their decay products composed of SM particles and LSP. The LSP, as well as neutrinos, cannot be directly detected as they interact too weakly with matter. However, it is possible to calculate the corresponding missing energy at the end of a reaction. As only particles with a momentum transverse to the beam direction are detected, it is in fact only the energy $\not{E}_T$ corresponding to the transverse momentum which is measured. As for quarks and gluons, they hadronize into jets because of QCD confinement. Eventually, any process in which superparticles are created leads to a final state of the type $\{n \text{ leptons} + m \text{ jets} + \not{E}_T \text{ with } n\, m \in \mathbb{N}\}$. The search for this type of signals is commonly named *SUSY direct searches*.

The emission of a gluon by a particle in the initial state followed by the production of two neutralinos in the final state is another kind of processes named *monojet* which leads to the signal jet + $\not{E}_T$ specific to the production of neutralinos (see figure 2.7).

However, those signals have a large background from Standard Model processes. In particular, the production of W or Z bosons, which decay into charged leptons and neutrinos, leads to large

	WW	ZZ	$\gamma\gamma$	$\tau\tau$	bb	Total decay width (GeV)
BR	0.2137	0.02619	0.002270	0.06272	0.5824	4.088×10^{-3}

Table 2.2: SM Higgs branching ratios at $m_h = 125$ GeV [108].

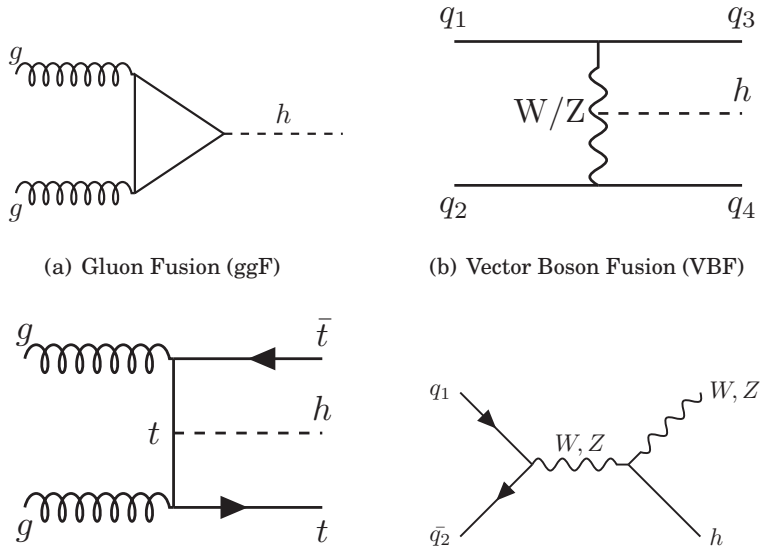

(a) Gluon Fusion (ggF)

(b) Vector Boson Fusion (VBF)

(c) Production associated with top quarks (tth)

(d) Production associated with vector boson production (VH)

Figure 2.8: The four main production processes of the Standard Model Higgs Model

missing transverse energy which can be mistaken with the production of a neutralino. It is therefore necessary to apply energy cuts in the analyses to reduce the background.

Another way of searching for hints of supersymmetry is to detect the production and decay of Higgs bosons. First, one can measure the SM Higgs signal strength, which is the quantity comparing the experimental signal of the production and decay of the Higgs bosons to the one calculated in the Standard Model. It can be written in the general form :

$$\mu^{exp}_{XX\to h\to YY} = \frac{\sigma^{exp}_{XX\to h} \times BR^{exp}_{h\to YY}}{\sigma^{SM}_{XX\to h} \times BR^{SM}_{h\to YY}}. \tag{2.40}$$

In the case of no sign of new physics, $\mu^{exp}_{XX\to h\to YY} = 1$. Otherwise, the production cross section $\sigma^{exp}_{XX\to h}$ or the branching ratio $BR^{exp}_{h\to YY}$ can get contribution from superparticle exchanges and the signal strength deviates from 1. The main decay channels of interest for CMS and ATLAS are into WW, ZZ, $\gamma\gamma$,$\tau\tau$ and bb, with predicted branching ratios reported in table 2.2.
There are also different processes of production of the Higgs boson: by gluon fusion (ggF), vector boson fusion (VBF), and two additional processes associated with a production of a vector boson or top quarks (VH) and (tth) (see figure 2.8).
Second, the search of heavy Higgs decay can also bring important constraints in the MSSM. The neutral heavy Higgs bosons, for instance, are expected to decay into a pair of charged leptons or

quarks or into light Higgs bosons h^0:

$$\begin{aligned} A^0/H^0 &\to \tau^+\tau^-, \quad \mu^+\mu^-, \quad b\bar{b}, \quad t\bar{t}\,, \\ H^0 &\to h^0 h^0\,, \\ A^0 &\to Z h^0\,. \end{aligned}$$

Finally, measurements in flavour physics, in particular of the B meson decays, can bring indirect constraints on supersymmetric models. The measurement of those processes can probe, indeed, higher energy levels than direct searches, as superparticles do not need to be produced on-shell but can possibly appear only at loop-level. The branching ratios $BR(B_s \to \mu^+\mu^-)$, $BR(B \to X_s\gamma)$ and $BR(B^+ \to \tau\nu_\tau)$. for instance, do not show a significant deviation from their SM value, but put strong constraints on the MSSM. The quark content of B mesons and kaons are listed in table 2.3. The process $B \to X_s\gamma$ refers to de decay of any B meson into a photon and any kind of composite particle containing a strange quark.

Meson	B^0	B^+	B_s^0	K^+	K^{0*}
Quark content	$d\bar{b}$	$u\bar{b}$	$s\bar{b}$	$u\bar{s}$	$d\bar{s}$

Table 2.3: Quark content of B mesons and Kaons.

Other observables in flavour physics, however, show some anomalies which are still under investigation. In particular, for the $B^0 \to K^{0*}\mu^+\mu^-$ process, the quantity $P_5^{'}$ shows an anomaly of $\sim 3\sigma$ [109] and the ratios $R_K = \frac{BR(B^+\to K^+\mu^+\mu^-)}{BR(B^+\to K^+e^+e^-)}$ and $R_{K^*} = \frac{BR(B^0\to K^{*0}\mu^+\mu^-)}{BR(B^0\to K^{*0}e^+e^-)}$ show deviations with lepton generation universality of about 2.5σ [110, 111]. If confirmed, those anomalies will constitute a breakthrough in the search for new physics.
For the moment, however, we will restrain ourselves in applying constraints to the MSSM from measurements of colliders which do not show any anomaly and we will investigate their interplay with dark matter direct and indirect detection constraints.

Part II

Astrophysical and nuclear uncertainties of dark matter direct an indirect detection constraints

CHAPTER 3

ROBUSTNESS OF DARK MATTER CONSTRAINTS AND INTERPLAY WITH COLLIDER SEARCHES FOR NEW PHYSICS

3.1 Objectives of the analysis

With the increasing precision of collider measurements and dark matter searches, it is important to assess carefully the constraining power of both sectors on supersymmetric models in order to guide future searches. Several studies have been carried out on the subject, focusing either on the excluded parameter space regions or on preferred regions determined from global fits (see e.g. [112–119]). However, while collider constraints are obtained in environments under control, which therefore lead to relatively hypothesis-free limits, it is well known that dark matter direct and indirect detection constraints suffer from large astrophysical and nuclear uncertainties which are rarely taken into account in this kind of analyses.
In this work, we aimed at studying the regions in the MSSM excluded by collider constraints and dark matter searches, taking a special care to assess the robustness of dark matter constraints with respect to astrophysical sources of uncertainties, namely the dark matter density halo profile, dark matter velocity profile and cosmic-ray propagation through the galactic medium. Nuclear uncertainties will be considered in next chapter.
This work was carried out in collaboration with Prof. Farvah Nazila Mahmoudi, Prof. Alexandre Arbey and Dr. Mathieu Boudaud. It resulted in a publication in the Journal of High Energy Physics [120].

3.2 Method

3.2.1 MSSM Scans

In order to define the excluded regions of the MSSM, it is necessary to perform a scan over its parameters, or in other words, to choose randomly several sets of numerical values for the free parameters. Each set of values is called a *model point* or a *point* in short. Then, we test the valid-

ity of each point under the various experimental constraints. However, the most general MSSM scenario presents more than one hundred free parameters. Considering this large number of parameters, one would need to generate an enormous amount of points in order to probe correctly the entire parameter space, which requires gigantic computational resources. To cope with this problem, we consider the pMSSM in this analysis, which was described in section 2.4.4. As only a small part of those parameters, namely $tan\,\beta$, M_A, M_1, M_2 and μ, plays a significant role in the phenomenology that we consider, it is possible to perform an exhaustive scan. Moreover, the conclusions we draw in the pMSSM are expected to be valid in more general scenarios. In particular, it was shown in [121, 122] that CP violation does not have important consequences on the dark matter sector after imposing the experimental constraints from the electric dipole moments and the Higgs coupling measurements. The results presented in the following thus remain valid also for CP violating scenarios.

20 million points are generated with SOFTSUSY [123], with a flat random sampling using the ranges given in Table 3.1 for the 19 pMSSM parameters. After checking the theoretical validity of each point, we impose a few pre-constraints.
First, we impose the lightest neutralino to be the lightest supersymmetric particle using the set-up presented in [124, 125]. This particle therefore constitutes dark matter. This choice is not as restrictive as it may first appear since the neutralino can take different natures, namely bino-like, wino-like, Higgsino-like and mixed-state, depending on the free-parameter values. Thereby, it gives us the opportunity to study very different phenomenologies which could be relevant to other dark matter models. We only consider here neutralinos with a mass $m_\chi \gtrsim 10$ GeV. The case of very light neutralinos was already studied in detail in [126–129].
Second we impose constraints on the light Higgs mass. The combined measurements of the Higgs mass by ATLAS and CMS from Run 1 gives [130]

$$M_{h_{\rm SM}} = 125.09 \pm 0.21(\text{stat.}) \pm 0.11(\text{syst.})\,\text{GeV}\,. \tag{3.1}$$

While this measurement is very precise, the calculation of the Higgs mass in the MSSM is still subject to larger uncertainties (see for example [131]). For this reason, we adopt the constraint:

$$122\,\text{GeV} < M_{h_{\rm SM}} < 128\,\text{GeV}\,. \tag{3.2}$$

At leading order, the light Higgs mass can be written in the MSSM as:

$$\begin{aligned} M_h^2 &\approx M_Z^2 \cos^2 2\beta \left[1 - \frac{M_Z^2}{{M_A}^2} \sin^2 2\beta\right] \\ &+ \frac{3m_t^4}{2\pi^2 v^2}\left[\log\frac{{M_S}^2}{m_t^2} + \frac{{X_t}^2}{{M_S}^2}\left(1 - \frac{{X_t}^2}{12{M_S}^2}\right)\right], \end{aligned} \tag{3.3}$$

where $M_S = \sqrt{M_{\tilde{t}_1} M_{\tilde{t}_2}}$ and $X_t = A_t - \mu \cot\beta$. Thereby, it limits in particular the stop masses and mixing.
400 000 points remain after imposing those pre-constraints.
Next, we apply the constraints from dark matter searches, including the measurement of DM relic density, and direct and indirect detection limits, which are described in detail below. Finally,

Parameter	Range (in GeV)
M_A	[50, 2000]
M_1	[-3000, 3000]
M_2	[-3000, 3000]
M_3	[50, 3000]
$A_d = A_s = A_b$	[-10000, 10000]
$A_u = A_c = A_t$	[-10000, 10000]
$A_e = A_\mu = A_\tau$	[-10000, 10000]
μ	[-3000, 3000]
$M_{\tilde{e}_L} = M_{\tilde{\mu}_L}$	[0, 3000]
$M_{\tilde{e}_R} = M_{\tilde{\mu}_R}$	[0, 3000]
$M_{\tilde{\tau}_L}$	[0, 3000]
$M_{\tilde{\tau}_R}$	[0, 3000]
$M_{\tilde{q}_{1L}} = M_{\tilde{q}_{2L}}$	[0, 3000]
$M_{\tilde{q}_{3L}}$	[0, 3000]
$M_{\tilde{u}_R} = M_{\tilde{c}_R}$	[0, 3000]
$M_{\tilde{t}_R}$	[0, 3000]
$M_{\tilde{d}_R} = M_{\tilde{s}_R}$	[0, 3000]
$M_{\tilde{b}_R}$	[0, 3000]
$\tan\beta$	[1, 60]

Table 3.1: pMSSM scan ranges.

we consider the limits from collider searches. As we do not intend to define a preferred parameter region, there is no need to calculate some global likelihood. Instead, it is more straightforward to apply the constraints separately at the 2σ level, apart from for the Higgs sector where a likelihood analysis is used. This choice should not affect the conclusions of our study.

3.2.2 Dark matter constraints

3.2.2.1 Relic density

The dark matter abundance has been measured in the framework of the standard cosmological model, and the Planck Collaboration has provided a precise evaluation of the cold dark matter density [22]:

$$\Omega_c h^2 = 0.1188 \pm 0.0010\,. \tag{3.4}$$

Constraints on new physics scenarios which propose dark matter candidates can therefore be obtained by comparing the computed dark matter density to the Planck value. SuperIso Relic [132, 133] is used to calculate the relic density for our sample of points.
Several assumptions can nevertheless limit the constraining power of the relic density.

The first uncertainties arise from the numerical calculations of the annihilation and co-annihilation cross sections. Whereas in the simplest cases the calculation of the relic density relies on a few decay channels, in the most compressed scenarios of the MSSM, more than 3000 channels can get involved, severely limiting the calculation speed of the relic density. For this reason, the cross sections are generally considered at tree-level. Yet, in individual channels, higher-order corrections can lead to 30% modifications or more [134]. However, in most cases, the relic density calculated at tree-level differs by less than 10% from the one calculated at one-loop [135, 136]. Therefore, in the general case, about 10% uncertainty can be associated to tree-level calculations of the relic density.

A second limitation comes from QCD equations of state. Indeed, computing the relic density requires the knowledge of the number of effective degrees of freedom of radiation density and entropy. While it was originally thought that the primordial plasma could be treated as an ideal gas above the QCD phase transition temperature, non-perturbative studies showed that at high temperature, the ideal gas approximation does not work, and different models for this plasma have been studied [137–139], leading to different sets of QCD equations of state. The consequences on the relic density are however rather mild and can modify it by a few percent.
For these two reasons, we add to the Planck measurement error a theoretical uncertainty of 10% in order to be conservative, and consider the 3.5σ interval

$$0.0772 < \Omega h^2 < 0.1604\,. \tag{3.5}$$

However, we will disregard the lower dark matter density limit. Indeed, in the usual calculation of relic density, the expansion of the Universe is considered to be dominated purely by the radiation density. This hypothesis can however be falsified in many extensions of the standard model of cosmology [140–144]. Similarly, entropy injection or non-thermal production of dark matter particles can modify the relic density [145–149]. These modifications of the standard model of cosmology can result in a change of the relic density by orders of magnitude, but are more likely to increase it. Some of these alternative scenarios will be studied in Chapter 5.

3.2.2.2 Indirect detection

We calculate indirect detection constraints from AMS-02 antiproton and Fermi-LAT gamma-ray data. The annihilation cross sections necessary for the interpretation of indirect detection data are calculated with MicrOMEGAs [150–152], and PPPC4DMID [153] is used for the antiproton and gamma spectra.

Antiprotons We derive constraints on the dark matter annihilation cross section $\langle\sigma v\rangle$ from the cosmic ray antiproton flux measured by PAMELA [56] as well as AMS-02 [57]. We apply the same procedure described in [154] to derive the 95% C.L. upper limit on the annihilation cross section $\langle\sigma v\rangle$. The procedure was also implemented in SuperIso Relic and is detailed in section 4.3. Practically, we solve the differential equation describing the propagation of antiproton through the galactic medium, using a semi-analytical method, to calculate the primary and secondary antiproton spectra at the Earth position. This calculation suffers from two sources of uncertainties, namely on the propagation parameters, which account, in particular, for the diffusion and

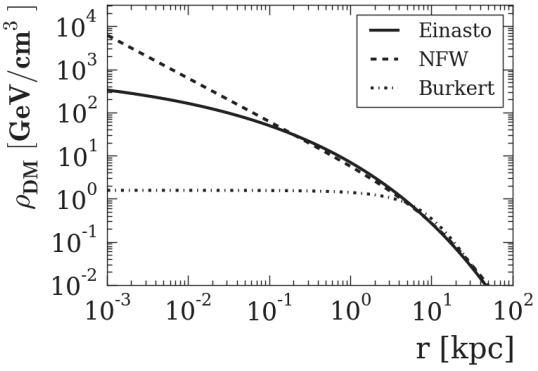

Figure 3.1: Dark matter density as a function of the distance from the galactic center for Einasto, NFW and Burkert profiles.

Halo profile	r_s [kpc]	ρ_s [GeV/cm^3]	$R_\odot$ [kpc]	$\rho_\odot$ [GeV/cm^3]
NFW	19.6	0.32	8.21	0.383
Einasto ($\alpha = 0.22$)	16.07	0.11	8.25	0.386
Burkert	9.26	1.57	7.94	0.487

Table 3.2: Dark matter mass model parameters for NFW [164], for Einasto [165] and for Burkert [166] profiles.

convection of antiprotons through the galaxy, and also on the dark matter density profile of the galactic halo. Therefore, we calculate the limits on the annihilation cross section for two sets of propagation parameters and three different density profiles in order to estimate the error on our constraints.

Three benchmark sets of propagation parameters MIN, MED, and MAX were proposed in [155]. These models are meant to be consistent with the boron over carbon (B/C) ratio. The MED model corresponds to the best fit to the (B/C) ratio, whereas the MIN and MAX sets of parameters define the lower and upper bounds for the primary $\bar{p}$ flux. However, it was found recently from studies based on synchrotron radio emission [156–159], on cosmic ray positrons [160] as well as on gamma rays [161], that the thin halo predicted by MIN is disfavoured. The study of secondary positrons [162, 163] points towards the same conclusion. As a result, the MED model provides a conservative lower bound to the dark matter antiproton signal. We thus calculate the limits only for the MED and MAX models. The recent B/C data reported by AMS-02 and their future studies would result in an improved determination of the parameters of the propagation models.

Concerning the DM density profiles, we use three different halo models, namely Navarro-Frenk-White (NFW) [164], Einasto [165] and Burkert [166] profiles, in which dark matter particles are isotropically distributed around the galactic center.
The NFW profile was defined from cosmological simulations [167] as

$$\rho_{\mathrm{NFW}}(r) = \rho_s \frac{r_s}{r}\left(1+\frac{r}{r_s}\right)^{-2}, \tag{3.6}$$

where r_s is the radius at which the logarithmic slope of the profile is -2 and ρ_s the dark mater density normalization.
The Einasto profile on the other hand is defined as

$$\rho_{\mathrm{Ein}}(r) = \rho_s \exp\left\{-\frac{2}{\alpha}\left[\left(\frac{r}{r_s}\right)^{\alpha}-1\right]\right\}, \tag{3.7}$$

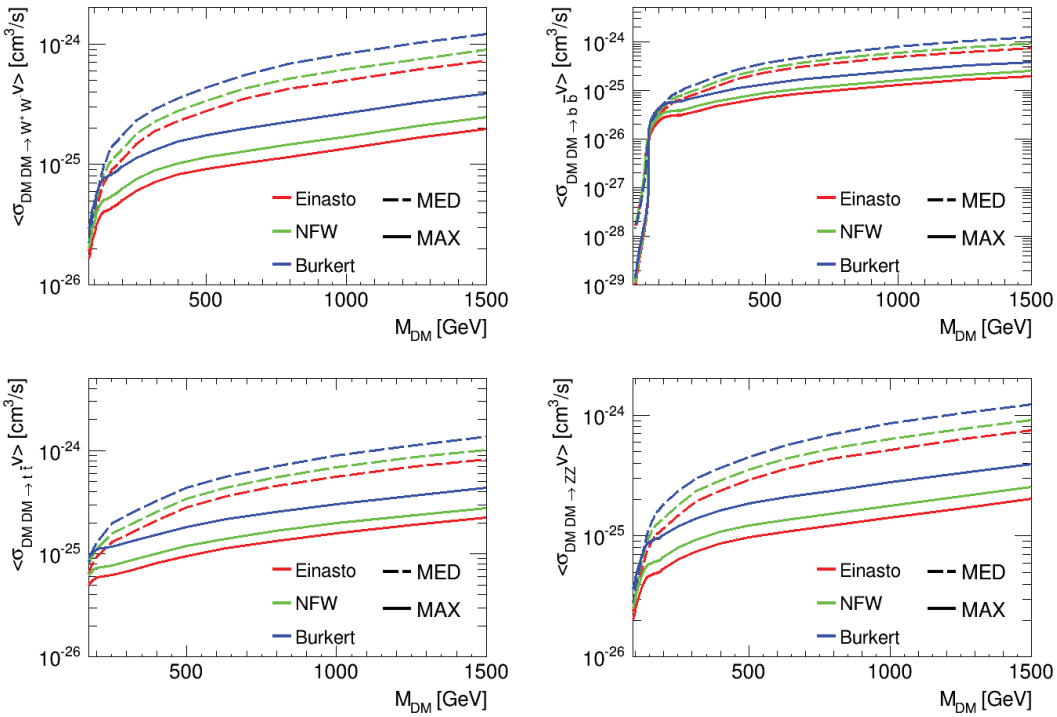

Figure 3.2: 95% C.L. upper limit of the neutralino annihilation cross section into W^+W^- (upper left), $b\bar{b}$ (upper right), $t\bar{t}$ (lower left) and ZZ (lower right), derived from AMS-02 antiproton data.

and provides a better agreement with the latest simulations [168] and does not suffer from the central divergence of the NFW profile (equation 3.6).
The Burkert profile arises from the study of the star activity occurring in the inner galaxy [169]. It could sweep dark matter particles from the inner region, resulting in a core profile as observed in many galaxies. Such profiles are parametrized by:

$$\rho_{\mathrm{Bur}}(r) = \frac{\rho_s}{\left(1+\frac{r}{r_s}\right)\left(1+\left(\frac{r}{r_s}\right)^2\right)}\,. \tag{3.8}$$

The parameters r_s and ρ_s as well as the distance of the Solar system to the galactic center are determined by dynamical observations of the Galaxy. We use the values determined by [164] for NFW, by [165] for Einasto and by [166] for Burkert profile as reported in Table 3.2.

The 95% C.L. upper limits on the annihilation cross section derived from the AMS-02 data are shown in Fig. 3.2 with respect to the dark matter mass for the W^+W^-, $b\bar{b}$, $t\bar{t}$ and ZZ annihilation channels.
One can note that the DM density is much larger in the Galactic center for the cuspy Einasto and NFW profiles than for the Burkert one (see figure 3.1). The DM annihilation rate is thus enhanced at the galactic center for the two cuspy profiles, which leads to stronger constraints than for the Burkert profile. Another important feature is that the limits derived using the MED model are weaker than for the MAX model. The MAX model was indeed defined to give a maximum flux

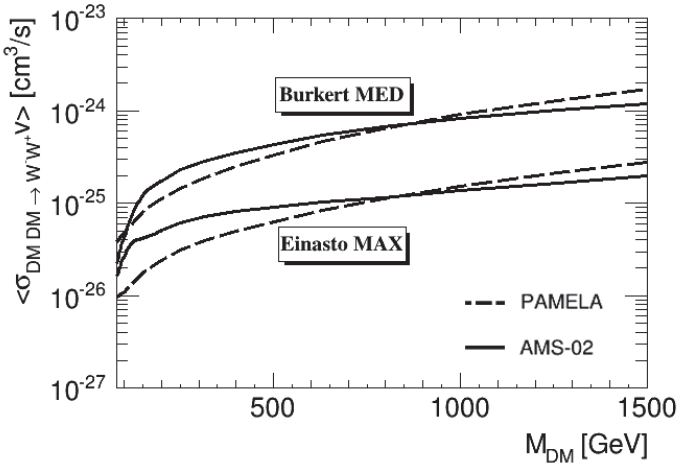

Figure 3.3: Compared DM annihilation cross section upper limit from PAMELA (dashed) and AMS-02 (solid) antiproton data for the W boson channel with Burkert-MED and Einasto-MAX.

of antiprotons at the Earth position, so the constraints calculated using this model are logically stronger. In any case, the theoretical uncertainties coming from the poor knowledge of the propagation parameters is larger (up to a factor 4 on $\langle\sigma v\rangle$) than the one arising from the choice of the DM profile (up to a factor 2). For all annihilation channels, we find that the strongest constraint is obtained using the Einasto profile and the MAX propagation model and the weakest constraint is given by the Burkert profile and MED model. In the following, we will therefore use these two cases to probe the uncertainties on indirect detection limits. Note also that the constraints for the b quark channel become very stringent when m_{DM} falls below 50 GeV, excluding the thermal relic cross sections down to $\sim 10^{-29}$ cm^3/s at 10 GeV.

For the sake of consistency, we perform the same analysis using PAMELA antiproton data. The comparison between the results for the W boson channel obtained with AMS-02 and PAMELA data are given in Fig. 3.3 for the Burkert-MED and Einasto-MAX cases. For $m_{DM} \lesssim 1$ TeV, the constraints derived from PAMELA data are more stringent than the AMS-02 ones. This can be understood by the fact that below ~1 TeV, the proton flux measured by PAMELA is larger than the one reported by AMS-02 by a factor of up to 10%, leading to a larger yield of secondary antiprotons and thus a smaller room left for the primary component. The proton fluxes reported by the two experiments become similar above ~1 TeV and in this regime, the experimental errors of AMS are much smaller than the PAMELA ones, leading to slightly stronger constraints for the more recent experiment. In the following of this paper, we consider only the results obtained using the AMS-02 data since they are more recent and they provide globally more conservative results.

Gamma rays We now turn to a combined analysis of the 19 confirmed dwarf spheroidal galaxies (dSphs) recently observed by Fermi-LAT [170].

We compute a delta-log likelihood for each of the points using the tabulated bin-by-bin likelihoods released by the Fermi-LAT Collaboration for each target [171] and we exclude points at the 95%

C.L. This procedure will be described in detail in section 4.3.2. We include statistical uncertainties on the J-factors of each dwarf spheroidal galaxy by adding an additional J-factor likelihood term, as prescribed by the Fermi-LAT collaboration in their study. J-factors probe the DM content of the dSphs and the gamma-ray flux produced by dark matter is proportional to this quantity. It is defined as the integral of the squared dark matter density along the line of sight:

$$J = \int_{\Delta\Omega} \int_{l.o.s} \rho^2_{DM}(r(l)) dl d\Omega \, . \tag{3.9}$$

Those J-factors were calculated assuming a NFW profile, but previous work showed that the limits calculated with other halo profiles differed only by ~30%, the strongest difference being for Burkert halo profile [172]. One of the largest uncertainties on these limits seems to reside in the choice of the dSphs sample used in the analysis. As pointed out in [170], adding galaxies with low-significance excesses, such as Reticulum II and Tucana III, can weaken significantly these limits. Assessing the effects of such uncertainties seems to be very delicate and we will use these limits only for comparison with the constraints coming from antiprotons.

In addition, we considered the limits given by the HESS Collaboration [44]. As they do not use the same set of parameter values for the DM halo profiles as ours, we renormalized their limits following the J-Factors calculated for our different halo profiles NFW, Einasto and Burkert to be consistent with the rest of our study. The strongest limit being obtained for the NFW profile, we noticed that it barely reaches the distribution of our points without excluding any.

3.2.2.3 Direct detection

Calculation of constraints The standard method to apply the constraints from direct detection is to calculate the differential recoil rate $\frac{dR}{dE}$ expected from each neutralino in our sample of points and compare it to experimental results. This quantity is defined as the number of collisions of a WIMP and a nucleus per unit of target material mass, per unit of time and per unit of nuclear recoil energy:

$$\frac{dR}{dE} = \frac{n_\chi}{M} \left\langle v \frac{d\sigma}{dE} \right\rangle = \frac{2\rho_\chi}{m_\chi} \int d^3v \, v f(\mathbf{v},t) \frac{d\sigma_i}{dq^2}(q^2,v), \tag{3.10}$$

where $n_\chi = \rho_\chi / m_\chi$ is the number density of WIMPs, with ρ_χ the local DM mass density; $f(\mathbf{v},t)$ is the WIMP velocity distribution and $\frac{d\sigma_i}{dq^2}(q^2,v)$ is the differential WIMP/nucleus cross section, with $q^2 = 2ME$ the momentum exchanged in the scatter. Using the form of the differential cross section for the most commonly assumed couplings, equation 3.10 can be simplified as

$$\frac{dR}{dE} = \underbrace{\frac{1}{2m_\chi \mu^2} \sigma(q)}_{\text{Particle physics}} \underbrace{\rho_\chi \eta(v_{min}(E),t)}_{Astrophysics}, \tag{3.11}$$

where $\sigma(q)$ is an effective scattering cross-section and

$$\eta(v_{min},t) \equiv \int_{v>v_{min}} d^3v \frac{f(\mathbf{v},t)}{v} \tag{3.12}$$

is the mean inverse speed. v_{min} can be written as

$$v_{min} = \sqrt{\frac{ME}{2\mu^2}} \ , \tag{3.13}$$

where μ is the reduced mass $\mu = m_\chi M/(m_\chi + M)$. The complete procedure have been implemented in SuperIso Relic and will be described in chapter 4. At the time of this study, however, these numerical tools were not finalized and we had to use a more direct approach. Direct detection experimental collaborations release upper limits on the WIMP-nucleon cross sections with respect to the WIMP mass and it is thus possible to exclude points only from the calculation of the neutralino scattering cross sections. This approach is limited by the fact that the limits on the spin-independent (SI) and spin-dependent (SD) cross sections have to be applied independently, whereas a complete approach would have taken all types of interaction at once and would have thus led to stronger constraints. In any case, our method remains conservative and we benefit from the limits directly calculated by the different collaborations, which are difficult to retrieve exactly.

All the scattering cross sections are calculated using MicrOMEGAs [152, 173]. For the SI constraint, however, one cannot compare directly these cross sections to the experimental upper limits. Indeed, the limits are derived under the assumption that the WIMP-proton and WIMP-neutron effective couplings f_p and f_n are equal in the WIMP-nucleus cross section formula $\sigma^{SI}_{\chi-N} = \frac{4\mu^2}{\pi}[Zf_p + (A-Z)f_n]^2$, where A and Z are respectively the nucleon and proton number in the nucleus. In our sample of points, this approximation is reasonable for Higgsino-like neutralinos, but is not necessarily correct for other neutralino types. However, there is a simple way to cope with this problem. The experimental WIMP-nucleon limits can be described more generally in terms of WIMP-nucleus cross section limits, averaged over all the target isotopes, and renormalized to a WIMP-nucleon limit in the case $f_p = f_n$. Consequently, for a given point, the appropriate quantity to compare with the experimental limit is:

$$\sigma^{SI}_{\chi-nucleon}(A) = \sigma^{SI}_{\chi-p} \frac{\sum_i \eta_i \mu^2_{A_i}[Z + (A_i - Z)f_n/f_p]^2}{\sum_i \eta_i \mu^2_{A_i} A_i^2} \ , \tag{3.14}$$

where the subscript i stands for the various isotopes present in the experiment and η_i is their corresponding abundance. These quantities depend on the target nucleus and are, a priori, different for xenon and argon. However, in our sample of points, we noticed that the relative difference $\delta = \left| \frac{\sigma^{SI}_{\chi-nucleon}(Xe) - \sigma^{SI}_{\chi-nucleon}(Ar)}{\sigma^{SI}_{\chi-nucleon}(Xe)} \right|$ was quite small, verifying $\delta \lesssim 10\%$ ($\delta \lesssim 1\%$ for the great majority of the points). The limits coming from xenon and argon experiments can then be easily compared, the XENON1T limit being the strongest one for our points [63].
Concerning the SD cross section limits, such problems do not exist. For the WIMP-neutron cross section, we apply the limit given by the LUX experiment [70] on our sample of points and for the WIMP-proton cross section, we use the one given by the PICO-60 experiment [72]. We also tested the limits given by IceCube [61], using the W^+W^- channel which is dominant for the wino-like and Higgsino-like neutralinos, and verified that the points excluded by the IceCube limit were already excluded by XENON1T or PICO-60.

In addition, we examine how the uncertainties on the local dark matter density and on the disc rotation velocity impact these limits.

Local dark matter density All the experimental limits are calculated using the benchmark value $\rho_0 = 0.3$ GeV/cm^3 for the local DM density, but recent studies give a best fit value closer to 0.4 GeV/cm^3 [165, 166, 174]. The uncertainties on the local density value are still quite large, one of the main sources residing in the knowledge of the baryon density in the galaxy. There may also be a discrepancy between the value calculated from the study of the motion of nearby stars and the one calculated from a global fit of stellar dynamics over the galaxy, assuming a spherical dark matter halo. In our study, we consider that the local DM density lies between 0.2 and 0.6 GeV/cm^3 (see [7] for a complete review) and we choose three different values to test the impact of those uncertainties on the exclusions in our sample of points: $\rho_0 = 0.2$, 0.4 and 0.6 GeV/cm^3. By rescaling the cross section coordinates, we obtain the limits for these three densities.

Velocity distribution Customarily, an isotropic Maxwellian distribution is assumed for the WIMP velocity distribution $f(\mathbf{v})$, with the galactic disk rotation velocity v_{rot} being the most probable speed. It corresponds to the Standard Halo Model describing the dark matter halo as a non-rotating isothermal sphere [175, 176]. The canonical value for v_{rot} is 220 km/s but it is believed that it can range from 200 to 250 km/s [177–179].

This velocity distribution is truncated at the escape velocity v_{esc} at which a WIMP can escape the galaxy potential well. Its value is subject to large uncertainties, $v_{esc} = 500 - 600$ km/s, with a benchmark value $v_{esc} = 544$ km/s [180]. However, for WIMP masses $m_{DM} > 10$ GeV, v_{min} is relatively low. The velocity distribution is then integrated over a large range of velocities and dR/dE_R is not sensitive to the tail of the distribution. Thus, the uncertainties on v_{esc} should not impact our analysis.

Other halo models have been proposed, such as the King Model which describes the finite size of the halo and the gravitational interaction with ordinary matter in a more realistic way [181, 182] or such as triaxial halo models [183]. In this study, we focus only on the uncertainties related to the Standard Halo Model, which is the most widely used in the literature.

In order to test the impact of v_{rot} uncertainties, we proceeded to a variable substitution in the integral of the velocity distribution appearing in the calculation of the differential recoil rate per unit detector mass (equation 3.10). To perform such a calculation, it was necessary to consider that $v_{esc} \approx \infty$. This approximation induces errors only for low WIMP masses, which are not concerned by our study. We were then able to rescale the upper limits originally calculated with $v_{rot} = 220$ km/s for two other values $v_{rot} = 200$ and 250 km/s. Basically, taking smaller values for v_{rot} shifts the limit to the right relative to m_{DM}, and taking larger values shifts it to the left. The impact of ρ_0 and v_{rot} uncertainties on the XENON1T 90% C.L. upper limit is shown in Fig. 3.4. The uncertainties on v_{rot} within the considered values have a small impact compared to the local density uncertainties. Moreover, the uncertainties on v_{rot} have a mild influence on the neutralino type of the excluded points and change the fraction of excluded points by less than 1%. For these reasons, and for the sake of simplicity, we keep, in the rest of this study, the benchmark value $v_{rot} = 220$ km/s and vary only the local dark matter density value.

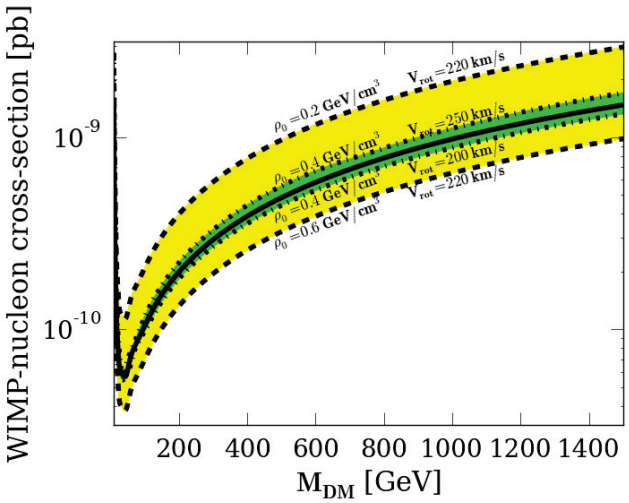

Figure 3.4: XENON1T 90% C.L. spin-independent WIMP-nucleon cross section upper limit for $\rho_0 = 0.4$ GeV/cm^3 and $v_{rot} = 220$ km/s (black plain line). Uncertainties on these values are shown by varying independently the DM local density (yellow band) and the disc rotation velocity (green band).

3.2.3 Collider constraints

To the set of points in our analysis we apply constraints from LEP and Tevatron, from flavour physics, as well as the LHC constraints from the Higgs sector and supersymmetry and monojet direct searches.

3.2.3.1 LEP and Tevatron constraints

LEP and Tevatron have provided strong constraints on the supersymmetric particle masses [184], which can be, in some cases, complementary to the constraints from the LHC. We apply to our set of points the limits summarized in Table 3.3. The limits from the LEP on the mass of the lightest neutralino will, however, not be considered here as it has been highlighted that they can be evaded in specific cases [126–129]. As our study is focussed on neutralino dark matter, we aimed at remaining as conservative as possible. The neutralino mass will nevertheless be constrained by the light Higgs signal strength measurements, which can lead to stronger limits than LEP [185–190].

3.2.3.2 Flavour constraints

Flavour constraints are complementary to dark matter and direct SUSY searches. They can probe in fact higher energy levels as supersymmetric particles appear at loop level in the processes of interest.
We will focus here on three major decays, namely $B_s \to \mu^+\mu^-$, $B \to X_s\gamma$ and $B_u \to \tau\nu$ which capture the main constraints in the MSSM.

Particle	Limits	Conditions
$\tilde{\chi}_2^0$	62.4	$\tan\beta < 40$
$\tilde{\chi}_3^0$	99.9	$\tan\beta < 40$
$\tilde{\chi}_4^0$	116	$\tan\beta < 40$
$\tilde{\chi}_1^\pm$	94	$\tan\beta < 40$, $m_{\tilde{\chi}_1^\pm} - m_{\tilde{\chi}_1^0} > 5$ GeV
$\tilde{e}_R$	73	
$\tilde{e}_L$	107	
$\tilde{\tau}_1$	81.9	$m_{\tilde{\tau}_1} - m_{\tilde{\chi}_1^0} > 15$ GeV
$\tilde{u}_R$	100	$m_{\tilde{u}_R} - m_{\tilde{\chi}_1^0} > 10$ GeV
$\tilde{u}_L$	100	$m_{\tilde{u}_L} - m_{\tilde{\chi}_1^0} > 10$ GeV
$\tilde{t}_1$	95.7	$m_{\tilde{t}_1} - m_{\tilde{\chi}_1^0} > 10$ GeV
$\tilde{d}_R$	100	$m_{\tilde{d}_R} - m_{\tilde{\chi}_1^0} > 10$ GeV
$\tilde{d}_L$	100	$m_{\tilde{d}_L} - m_{\tilde{\chi}_1^0} > 10$ GeV
$\tilde{b}_1$	248	$m_{\tilde{\chi}_1^0} < 70$ GeV, $m_{\tilde{b}_1} - m_{\tilde{\chi}_1^0} > 30$ GeV
	220	$m_{\tilde{\chi}_1^0} < 80$ GeV, $m_{\tilde{b}_1} - m_{\tilde{\chi}_1^0} > 30$ GeV
	210	$m_{\tilde{\chi}_1^0} < 100$ GeV, $m_{\tilde{b}_1} - m_{\tilde{\chi}_1^0} > 30$ GeV
	200	$m_{\tilde{\chi}_1^0} < 105$ GeV, $m_{\tilde{b}_1} - m_{\tilde{\chi}_1^0} > 30$ GeV
	100	$m_{\tilde{b}_1} - m_{\tilde{\chi}_1^0} > 5$ GeV
$\tilde{g}$	195	

Table 3.3: Constraints on the SUSY particle masses (in GeV) from searches at LEP and the Tevatron [184].

First, $B_s \to \mu^+\mu^-$ has a very strong constraining power in the MSSM. Indeed, this rare decay has a very low Standard Model background, but can receive large scalar and pseudoscalar contributions in supersymmetric scenarios. As those contributions enhance the branching ratio proportionally to a factor $\tan^6\beta/M_A^4$, small M_A parameter regions and large $\tan\beta$ are strongly constrained [191–195].

Second, the inclusive decay $B \to X_s\gamma$ receives contributions from charged Higgs-top and chargino-stop loops, which also restrict the charged Higgs, stop and chargino masses in the large $\tan\beta$ regions. As noted in section 2.4.1, the pseudoscalar and charged Higgs masses are connected at tree level by the relation

$$M_{H^+}^2 = M_A^2 + M_W^2 \,, \tag{3.15}$$

so that the pseudoscalar masses are also restricted.

Finally, the third transition, $B_u \to \tau\nu$ is a tree-level leptonic decay which can be mediated by a W-boson or a charged Higgs. It also restricts the small M_{H^+} and large $\tan\beta$ region. The value of the branching ratios of the three transitions is computed with SuperIso v3.7 [196–198], and we apply the constraints shown in Table 3.4.

Observable	Experiment	SM prediction
$\mathrm{BR}(B_s \to \mu^+\mu^-) \times 10^9$	3.0 ± 0.65 [199]	3.54 ± 0.27
$\mathrm{BR}(B \to X_s\gamma) \times 10^4$	3.32 ± 0.15 [200]	3.34 ± 0.22
$\mathrm{BR}(B_u \to \tau\nu_\tau) \times 10^4$	1.06 ± 0.19 [200]	0.82 ± 0.29

Table 3.4: Experimental results and the corresponding SM values for the flavour physics observables used in this work. The experimental data represents the most recent measurements or official combinations.

Channel	Experimental value
$h \to \gamma\gamma$	1.14 ± 0.19
$h \to WW$	1.09 ± 0.18
$h \to ZZ$	1.29 ± 0.26
$h \to bb$	0.70 ± 0.29
$h \to \tau\tau$	1.11 ± 0.24

Table 3.5: List of the Higgs signal strengths used in this analysis [130].

3.2.3.3 Higgs constraints

Measurements in the Higgs sector can also bring significant constraints in the pMSSM. In this study, we will apply the constraints from the measurement of the light Higgs signal strength and from heavy Higgs decay.

Light Higgs signal strength The study of the light Higgs decay constrains in particular the Higgs mixing angles α and β, and thus the mass of the pseudoscalar. Other MSSM parameters are also concerned by the constraints, as the Higgs couplings can receive high-order corrections from the presence of supersymmetric particles. LHC experiments have measured the signal strengths of different channels of the light Higgs boson, *i.e.* the product of the production cross sections times branching ratios. We use these measurements in our analyses, as given in Table 3.5. The decays $h \to WW, ZZ, bb, \tau\tau$ provide direct constraints on the couplings and thus on the Higgs mixing angles. On the other hand, $h \to \gamma\gamma$ is a loop-level decay, in which the main contributions arise from top, stop, sbottom, chargino and charged Higgs loops [201]. Its measurement is therefore particularly important to constrain the MSSM.
The Higgs decay branching ratios and widths are computed using `HDECAY v6.51` [202]. The production cross sections are calculated using `Sushi 1.5.0` [203], `VV2H v1.10` and `V2HV v1.10` [204]. The constraints are obtained through a likelihood analysis using the experimental and theoretical correlations from [130] and [205], respectively. Constraints are applied at the 95% C.L.

Heavy Higgs decay Other relevant searches in the context of dark matter are searches for heavier Higgs bosons [185, 227–231]. In the limit when M_A is large, the light Higgs couplings are SM-like, and compatible with the current data. The heavier states are therefore expected to be heavy. Nevertheless, the couplings of the H/A to the b quarks and τ leptons are enhanced

Analysis	Target	8 TeV	13 TeV
2-6 jets + MET	$\tilde{g}$, $\tilde{q}$	20 fb^{-1} [206]	13.3 fb^{-1} [207], 36.1 fb^{-1} [208]
7-11 jets +MET	$\tilde{g}$, $\tilde{q}$	20 fb^{-1} [206]	18.2 fb^{-1} [209], 36.1 fb^{-1} [210]
2-6 jets + 1 lepton + MET	$\tilde{g}$, $\tilde{q}$	20 fb^{-1} [206]	14.8 fb^{-1} [211]
2, 3 leptons + MET	$\tilde{\chi}_2^0$, $\tilde{\chi}_1^\pm$, $\tilde{\ell}$	20 fb^{-1} [212]	13.3 fb^{-1} [213], 36.1 fb^{-1} [214]
jets + 0 lepton +MET	$\tilde{t}$	20 fb^{-1} [215]	13.3 fb^{-1} [216], 36.1 fb^{-1}, [217]
jets + 1 lepton + MET	$\tilde{t}$	20 fb^{-1} [215]	13.2 fb^{-1} [218], 36.1 fb^{-1} [214]
b-jets + 2 leptons + MET	$\tilde{t}$	20 fb^{-1} [215]	13.3 fb^{-1} [219], 36.1 fb^{-1} [220]
2 b-jets + MET	$\tilde{b}$, $\tilde{t}$	20 fb^{-1} [215]	3.2 fb^{-1} [221], 36.1 fb^{-1}, [222]
Monojet	MET	20.3 fb^{-1} [223]	3.2 fb^{-1} [224]
mono-Z,W	MET	20.3 fb^{-1} [225]	3.2 fb^{-1} [226]

Table 3.6: List of ATLAS searches implemented in this analysis.

by $\tan\beta$, so that it is possible to set strong limits in the small M_A and large $\tan\beta$ region when searching for $(pp)bb \to H/A \to \tau\tau$. We use the results of CMS with 12.9 fb^{-1} [232], and assess the exclusion by comparing the calculated cross section times branching ratio with the published tables. We note that it is sensitive to the same region which is probed by the branching ratio of $B_s \to \mu^+\mu^-$.

3.2.3.4 LHC direct search constraints

Direct searches from supersymmetric particles at the LHC provide amongst the most important constraints on the MSSM parameter space. We consider in our study the LHC searches presented in Table 3.6. Even if this list is not exhaustive, the most relevant searches for our study are considered, *i.e.* the channels with the highest sensitivity which are rather uncorrelated.

SUSY direct searches The SUSY direct searches correspond to final states with at least two SM particles and a large missing energy, carried by the invisible neutralinos. To assess the sensitivity of the LHC searches at 8 and 13 TeV, we generate inclusive samples of SUSY events with `PYTHIA 8.150` [233, 234], using the CTEQ6L1 parton distribution functions [235]. `Delphes 3.0` [236] is then used to simulate the detector response and obtain the physics objects of the signal events. For each of the analyses, the signal selection cuts are applied to the simulated events, and the SM background events are taken from experimental publications. The CLs method [237] is used to obtain the 95% confidence level (C.L.) exclusion in presence of background only.
As for the SUSY searches, we adopt the CTEQ6L1 parton distribution functions, hadronization is performed using PYTHIA 8.150, and detector simulation with DELPHES 3.0. The cuts, selection efficiencies, acceptances and backgrounds for the 8 and 13 TeV runs are taken from the experimental publications cited in Table 3.6. In addition, as the systematic uncertainties can have an important effect on these limits [238–240], we account for them by adding a 30% uncertainty to the cross sections.

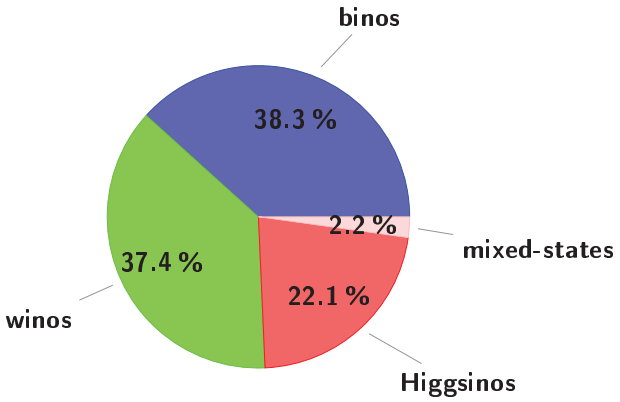

Figure 3.5: Fractions of neutralino 1 types in our scan after imposing only the light Higgs mass constraint.

Monojets and mono-W,Z Monojet and mono-W,Z searches on the other hand have been designed in order to detect invisible particles in the final states through the detection of a hard jet emitted by the initial states. The basic idea is to search for a jet with high p_T associated to a large missing E_T. The main background for monojet searches stems from Z or W-boson and a jet, with the Z-boson decaying to neutrinos and the W-boson decaying to leptons which are missed by the detector. Considering models in which a single mediator relates the dark matter particles to the SM particles reveals that the LHC can have a competitive or even superior reach compared to the dark matter detection experiments [241–244]. However, the simple description of dark matter production at the LHC based on a single mediator is not realistic with regard to concrete models such as the pMSSM, in which co-annihilations are favoured by the relic density constraints. Indeed, SUSY particles such as squarks or gluinos can be close in mass to the lightest neutralino, so that the production of two squarks or gluinos associated to a hard jet can still be seen as a monojet, because the jets produced in their decays would be soft enough to remain undetected [239, 245–248]. In addition, several mediators can be involved. As a consequence, the single mediator limits cannot be recast in the pMSSM in a simple way.
To study the exclusion by the monojet and mono-W,Z searches, we use MadGraph 5 [249] to compute the full $2 \to 3$ matrix elements for all the combinations of $pp \to \tilde{q}/\tilde{g} + \tilde{q}/\tilde{g} + j/W/Z$, $pp \to \tilde{\ell} + \tilde{\ell} + j/W/Z$ and $pp \to \tilde{\chi} + \tilde{\chi} + j/W/Z$, where $\tilde{q}$ refers to a squark of any type and generation, $\tilde{g}$ to the gluino, $\tilde{\ell}$ to any type of sleptons, $\tilde{\chi}$ to any electroweakino. j corresponds to a hard jet as required for the monojet searches, and W/Z for mono-W,Z searches.

3.3 Results

As a first step, we will impose the dark matter constraints individually on our sample of points and examine the effect of astrophysical uncertainties. Then, we will study the interplay between these constraints. Finally, we will combine dark matter and collider constraints and assess the the impact of astrophysical uncertainties on our exclusions in this context.
A particular care will be taken to identify the nature of the neutralinos that are excluded.
In the following, the neutralino 1 (denoted χ) will be said to be bino-/wino-/Higgsino-like if it is

composed of 90% of bino-/wino-/Higgsino component, respectively, or mixed state otherwise. In Fig. 3.5, the composition of our sample of pMSSM points after imposing the light Higgs mass interval is shown. Bino-like χ are the most represented points in our sample, followed by the winos and Higgsinos, with an almost equal share of each component. The fraction of mixed states is negligible.

3.3.1 Relic density constraints

We first consider the relic density constraint. The value of the neutralino relic density is computed with SuperIso Relic v3.4 [132, 133]. In Fig. 3.6, the relic density is shown as a function of the neutralino 1 mass, for the different types. Bino-like neutralinos 1 have in general large relic densities, above the Planck measurement. This can be explained by the smaller couplings of the binos with SM particles, which leads to smaller annihilation cross sections and therefore larger relic densities. On the other hand, the Higgsino-like χ give smaller relic densities which are close to the Planck measurements for χ masses around 1.3 TeV. The wino-like χ tend to have even smaller relic densities, and the Planck line is naturally reached for a mass of 2.7 TeV. The line at about 90 GeV in the figure corresponds to cross section enhancements through a Z-boson resonance, which lower the relic density.

Imposing both the upper and lower relic density bounds generally leads to a selection of scenarios with co-annihilations, for which the mass splitting of the neutralino 1 with the next-to-lightest supersymmetric particle is small, or of scenarios where χ annihilations are enhanced through a resonance of the Z-boson or one of the neutral Higgs bosons. This is demonstrated in Fig. 3.7. The valid points require in general small mass splitting, apart from some spread binos with larger mass splittings, which have a heavy Higgs boson or Z-boson resonance. For the case of winos, the small mass splitting is due to a chargino with a mass very close to the χ mass. For the Higgsino case, both the chargino 1 and the neutralino 2 have masses close to the neutralino 1 mass.
As discussed in Section 3.2.2.1, we consider only the upper bound of the Planck dark matter density interval, which favours light wino- and Higgsino-like χ, and bino-like χ with strong co-annihilations.

3.3.2 Indirect detection constraints

3.3.2.1 Constraints from AMS-02 and Fermi-LAT

We consider the constraints from AMS-02 antiproton and Fermi-LAT gamma ray data, which probe specific dark matter annihilation channels. For both sets of constraints, the most important parameters are the χ annihilation cross sections into specific channels. Annihilations to WW and $b\bar{b}$ are particularly interesting in the context of the pMSSM.
In Fig. 3.8, the total annihilation cross section times velocity $\langle\sigma v\rangle_{\text{tot}}$ is shown as a function of the neutralino 1 mass, for the different χ types. $\langle\sigma v\rangle_{\text{tot}}$ is the sum of all the σv of the different channels. The wino- and Higgsino-like neutralino 1 regions form two separate strips. The different types of neutralinos 1 have specific main decay channels: binos annihilate mainly into $t\bar{t}$, $b\bar{b}$, and in a lesser extent into Wh, Zh and $\tau\tau$, Higgsinos into WW and ZZ, and winos into WW,

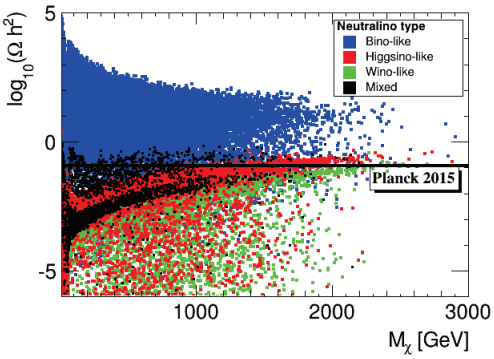

Figure 3.6: Neutralino relic density as a function of the neutralino 1 mass, for the different neutralino types. The central value of the Planck dark matter density is shown for comparison.

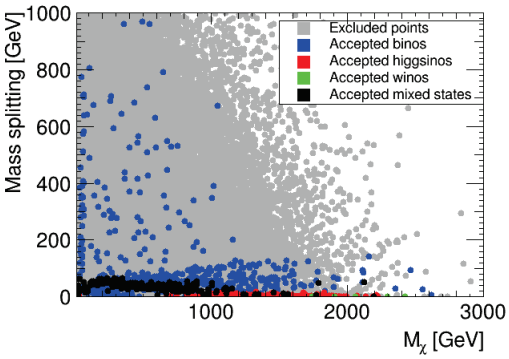

Figure 3.7: Points respecting both sides of the Planck 2015 relic dark matter density measurement in the mass splitting between the neutralino and the next lightest supersymmetric particle and the neutralino mass parameter plane.

when the decay channels are open. When the above-mentioned channels are closed because of a small neutralino 1 mass, the χ mostly decays to $b\bar{b}$ and $\tau\tau$, and less frequently into $c\bar{c}$ and $s\bar{s}$, independently from their type. As seen earlier, winos more strongly annihilate than the other χ types, followed by the Higgsinos. The binos, apart from the case of a resonant annihilation, are more weakly annihilating and are far below the experimental limits.

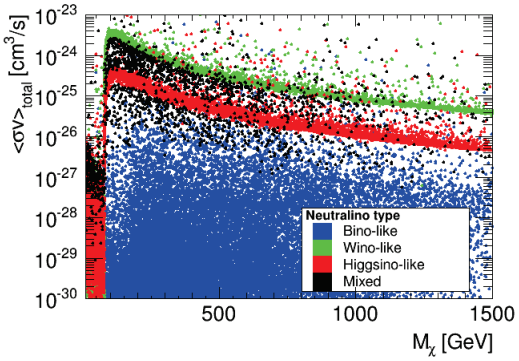

Figure 3.8: Total annihilation cross section as a function of the neutralino 1 mass for the different neutralino types.

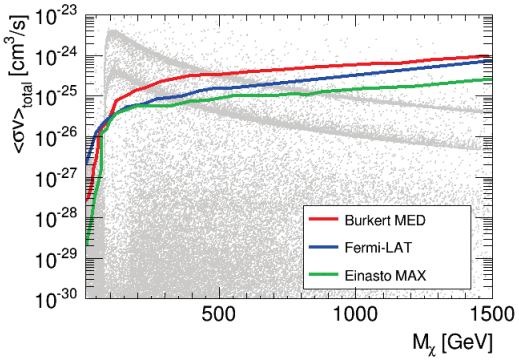

Figure 3.9: Lower limits of the points excluded by Fermi-LAT gamma ray and AMS-02 antiproton data in the total annihilation cross section vs. neutralino 1 mass parameter plane.

In Fig. 3.9, the exclusion by Fermi-LAT and AMS-02 is shown in the $\langle\sigma v\rangle_{\text{tot}}$ vs. neutralino 1 mass parameter plane. In order to quantify the uncertainties related to indirect detection, we consider separately the most conservative limits, *i.e.* obtained using Burkert profile and MED propagation model, and the most stringent ones, *i.e.* using Einasto profile and MAX propagation model. The

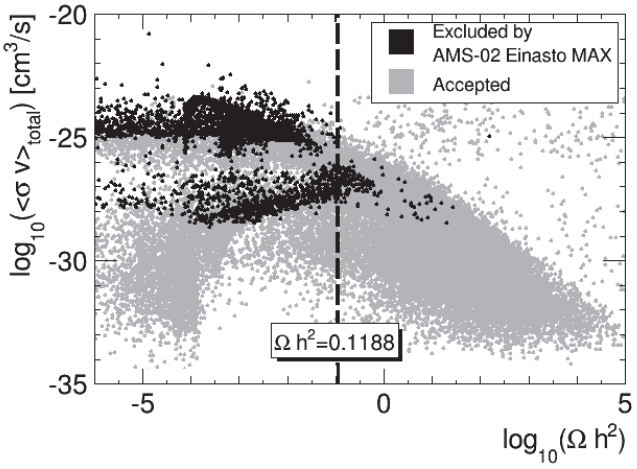

Figure 3.10: Total annihilation cross section as a function of the relic density. The vertical dashed line corresponds to the central value of the Planck dark matter density.

conservative limits lead to the exclusion of neutralinos 1 with masses between 90 and 550 GeV, which are mainly wino-like. The stringent limits exclude points with χ masses between 0 and 850 GeV. In the small mass region, as well as for masses above 90 GeV, the stringent exclusion limit is strengthened by one order of magnitude in comparison to the conservative case. The stringent case excludes large zones of the wino strip, and of the Higgsino one in a lesser extent. AMS-02 alone brings very strong constraints in the stringent case, beyond the Fermi-LAT limits.

3.3.2.2 Connections with relic density

Indirect detection constraints may be considered to be redundant with the relic density constraint. This is generally true for simplified dark matter models [244], because the relic density is directly related to the annihilation cross sections. However, in a complete model such as the MSSM, the value of the relic density is often led by the co-annihilations, especially when both the upper and lower bounds of the Planck dark matter density measurements are applied. This was already shown in Fig. 3.7.

Yet, there is a strong complementarity between indirect detection and relic density, as shown in Fig. 3.10. Considering the gray points, we see an anti-correlated region where the relic density increases when the annihilation cross section decreases, which is due to the relation between the relic density and the annihilation cross sections. This region is largely excluded by the upper Planck bound. The points with small relic density have in general efficient co-annihilations, which reduces the relic density. While these points are far from being excluded by the Planck upper bound, they can be probed by the stringent AMS-02 limits obtained using the Einasto profile and MAX propagation model. This clearly shows the complementarity between indirect detection and relic density constraints.

In Section 3.2.2.1, we discussed how the relic density constraint can be falsified. One of the possibilities is that the dark matter density measured by Planck is made only in part of neutralinos, the rest being made of other types of particles or more exotic objects. In such a case, galactic

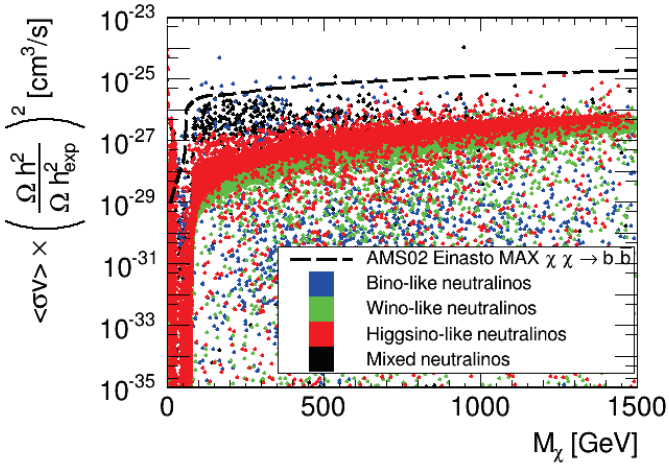

Figure 3.11: Points excluded by Fermi-LAT gamma ray and AMS-02 antiproton data in the total annihilation cross section vs. neutralino 1 mass parameter plane, where the total annihilation cross section is rescaled by the relic density. The AMS-02 upper limit with Einasto profile and MAX propagation model for the $b\bar{b}$ channel is plotted for comparison.

haloes would also be composed of different types of dark matters. Assuming that the mixture of dark matters is in the same proportion in galaxies as in the large scale Universe, the neutralino relic density is smaller than the measured dark matter density, and the dark matter density in galactic haloes has to be rescaled by the ratio of the neutralino relic density over the dark matter density, hence impacting the indirect detection limits. This is done in Fig. 3.11, in the total annihilation cross section vs. neutralino 1 mass parameter plane, where the total annihilation cross section is rescaled by the neutralino relic density over the measured dark matter density. Such a rescaling strongly weakens the indirect detection limits. Indeed, even using the most stringent AMS-02 constraints, only a very few points in the low mass region are still excluded, mostly in the $b\bar{b}$ channel. The large negative impact of the rescaling is due to the fact that the constraints from indirect detection scale as the squared density, leading to a strong loss of sensitivity.

3.3.3 Direct detection constraints

3.3.3.1 Constraints from XENON1T, LUX and PICO-60

Contrary to relic density and indirect detection, which mainly depend on the annihilation and co-annihilation cross sections, direct detection relies on the scattering cross section of neutralino 1 with nucleons. Direct detection is therefore complementary to indirect detection and relic density. In Fig. 3.12, the generalized spin-independent WIMP-nucleon cross section – which roughly corresponds to the χ-xenon scattering cross section normalized to one nucleon, and which applies to xenon-based experiments – is shown as a function of the neutralino mass, for the different neutralino 1 types. Higgsinos are in general more strongly interacting than the winos, leading to larger cross sections. In order to assess the consequences of the uncertainties on the obtained constraints, the recent limits of the XENON1T experiment are superimposed, for three values of the

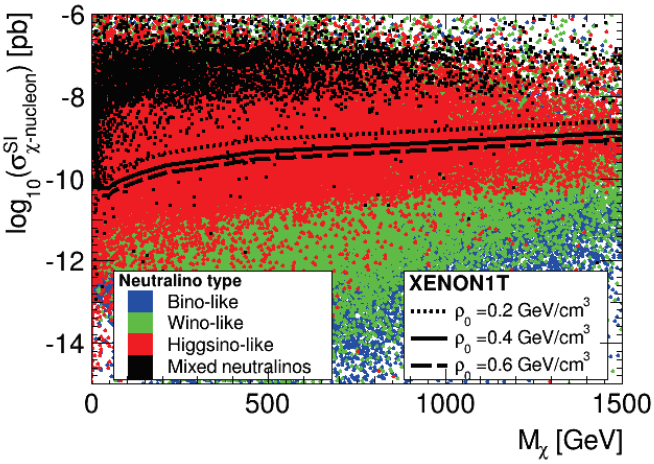

Figure 3.12: Generalized spin-independent neutralino scattering cross section as a function of the neutralino mass. The lines show the XENON1T 90% C.L. upper limit for three different values of the local dark matter density ρ_0.

local dark matter density, namely ρ_0 = 0.2, 0.4 and 0.6 GeV/cm^3. Between the conservative line corresponding to ρ_0 = 0.2 GeV/cm^3 and the most stringent limit obtained for ρ_0 = 0.6 GeV/cm^3, there is at most a factor 3 difference. While this is a large factor, in the context of pMSSM it does not change much the excluded region, which contains mainly Higgsino-like neutralinos 1. Depending on the value of the local DM density, we find that direct detection excludes between 25% and 40% of our points.

In Fig. 3.13 the exclusion by the XENON1T data with $\rho_0 = 0.4$ GeV/cm^3 is shown in the $(M_A, \tan\beta)$ parameter plane. For each bin, the fraction of excluded points is presented. This parameter plane is of interest since the neutral Higgs bosons can mediate the scattering, with couplings proportional to $\tan\beta$. About 100% of the points are excluded in a triangle region starting from the origin of the plot and up to $\tan\beta = 60$ and $M_A = 600$ GeV. A large fraction of the points with larger M_A can also be excluded. For comparison, the exclusion line from the CMS heavy Higgs searches for $H/A \to \tau\tau$ is also shown [232]. While the CMS limit extends beyond the 100% exclusion triangle and constitutes a well-defined and robust exclusion in this parameter plane, direct detection still adds complementary constraints for larger M_A and smaller $\tan\beta$ values.

LUX and PICO-60 also provide important constraints on the spin-dependent scattering cross section with protons and neutrons. This is shown in Fig. 3.14, for ρ_0 between 0.2 and 0.6 GeV/cm^3. The distribution of the points is different for the proton and neutron scatterings, because the wino-neutralino 1 mixing term in the neutralino-quark-squark coupling is proportional to the isospin. In both cases however, only the most strongly interacting Higgsinos are excluded, and the value of ρ_0 does not affect much the results.

Practically, LUX and PICO-60 spin-dependent constraints are redundant, since both exclude the same points. The spin-independent XENON1T results give quite stringent constraints, which exclude most of the points probed by LUX and PICO-60. After imposing the XENON1T constraints, the spin-dependent results exclude about 0.5% of the remaining points, with dominantly

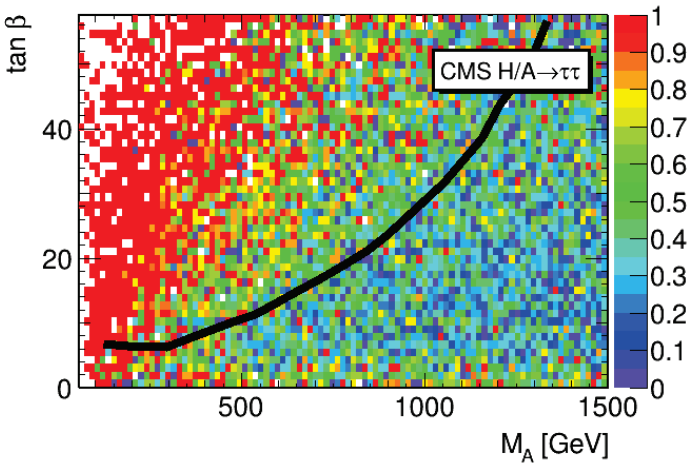

Figure 3.13: Fraction of points excluded by direct detection constraints in the $(M_A, \tan\beta)$ parameter plane. The CMS 13 TeV exclusion line from $H/A \to \tau\tau$ searches [232] is also plotted for comparison.

Higgsino-like χ.

3.3.3.2 Connections with relic density

Direct detection constraints are not related to the relic density through annihilation cross sections, as for indirect detection. They are nevertheless complementary, since they provide constraints on different pMSSM parameters.

The same paradigm as for indirect detection can apply: if the relic density is smaller than the observed dark matter density, it may be because the neutralino is not the sole component of dark matter, thus the local dark matter density has to be rescaled accordingly to obtain the local neutralino density. As a consequence, the limits become less constraining, since the effective scattering cross sections are lowered by a factor proportional to the relic density. In comparison

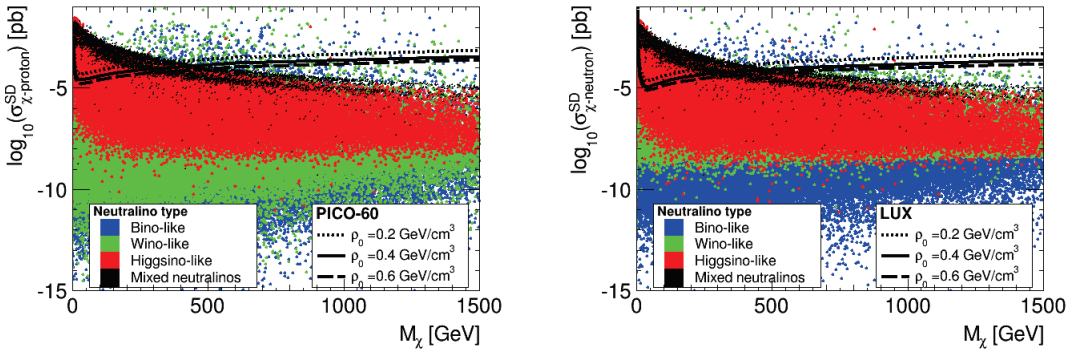

Figure 3.14: Spin-dependent neutralino scattering cross section with proton (left panel) and with neutron (right panel) as a function of the neutralino mass. The lines show the LUX and PICO-60 90% C.L. upper limits for three different values of the local dark matter density ρ_0.

Neutralino types	$\rho_0 = 0.2$ GeV/cm^3		$\rho_0 = 0.4$ GeV/cm^3		$\rho_0 = 0.6$ GeV/cm^3	
	No Rescale	With Rescale	No Rescale	With Rescale	No Rescale	With Rescale
Binos	33.5%	21.8%	38.8%	27.7%	42.6 %	31.9%
Winos	18.6%	1.7%	25.0%	2.9%	29.4 %	3.7%
Higgsinos	50.2%	12.1%	63.2%	18.1%	71.1 %	22.7%
Mixed	99.5%	80.0%	99.7%	87.0%	99.8 %	89.9%
All	33.5%	8.8%	42.2%	12.1%	47.7 %	14.3%

Table 3.7: Fraction of points, valid after imposing the relic density upper limit, that are excluded by direct detection limits, for the different neutralino types. The exclusions are set for different values of the local DM density, which is rescaled or not by the relic density.

with indirect detection, the impact of the rescaling is less pronounced, because the rescaling is proportional to the dark matter density for direct detection, whereas it is proportional to the density squared for indirect detection.
In Table 3.7, the fractions of excluded points are given for the different neutralino 1 types, with rescaling and without rescaling, for $\rho_0 = 0.2, 0.4, 0.6$ GeV/cm^3, after the upper limit of the relic density is applied. First, in absence of rescaling, even in the most conservative case corresponding to $\rho_0 = 0.2$ GeV/cm^3, direct detection imposes strong limits, and one third of the points are excluded. The Higgsinos are the most affected, followed by the binos and winos. The mixed states are almost completely excluded by direct detection, but their number is too small to draw statistically significant conclusions. When increasing the density to $\rho_0 = 0.6$ GeV/cm^3, the sensitivity is enhanced, with about half of the points excluded, and 70% of the Higgsinos. With the relic density rescaling, the exclusion power decreases strongly, as only 15% of the points remain excluded in the most favourable case. The exclusion hierarchy is also modified in presence of rescaling, with the binos being the most excluded neutralinos 1.

3.3.4 Combined dark matter constraints

We have seen that dark matter observables can lead to very strong constraints in the MSSM, despite the astrophysical uncertainties. Each kind of constraints seems to exclude a preferred nature of neutralino. The upper bound of dark matter density excludes mostly bino, while indirect detection excludes mostly winos and direct detection Higgsinos. In the following, we will examine more closely the interplay between these different constraints. We will focus only on the case where neutralinos constitute the whole dark matter.
We define three cases in order to estimate the impact of the astrophysical uncertainties:

- CONSERVATIVE: $\rho_0 = 0.2$ GeV/cm^3 for direct detection, Burkert dark matter profile and cosmic ray MED propagation model using AMS-02 data for indirect detection.
- STANDARD: $\rho_0 = 0.4$ GeV/cm^3 for direct detection, NFW dark matter profile using the combined analysis of the 19 confirmed dwarf spheroidal galaxies observed by Fermi-LAT

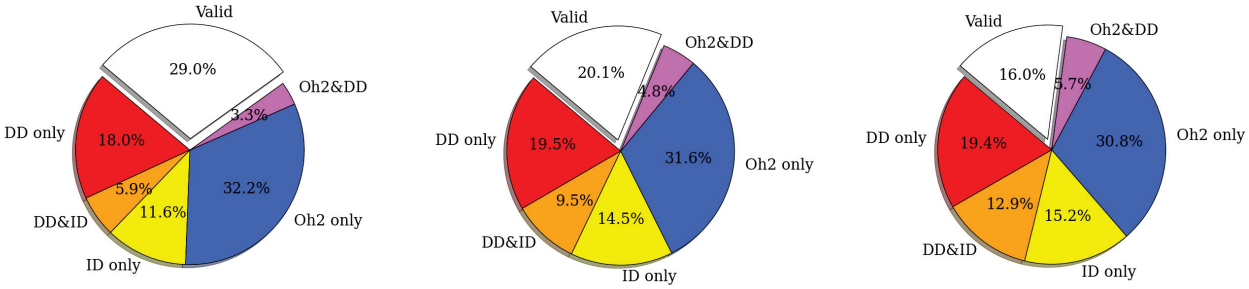

CONSERVATIVE STANDARD STRINGENT

Figure 3.15: Fraction of pMSSM points excluded by upper bound of the dark matter density, direct detection and indirect detection constraints.

for indirect detection.

- STRINGENT: $\rho_0 = 0.6$ GeV/cm^3 for direct detection, Einasto dark matter profile and cosmic ray MAX propagation model using AMS-02 data for indirect detection.

In Fig. 3.15, the fraction of pMSSM points initially satisfying the light Higgs mass constraint, which are excluded by the upper bound of the dark matter density, direct detection and indirect detection constraints, is shown for the three cases of astrophysical assumptions. The & symbol corresponds to the exclusive "and". Points excluded simultaneously by the relic density and indirect detection constraints represent less than 1% of the total number of points, and are not shown.
The relic density constraint excludes about 36% of the points. As already seen, direct detection constraints are relatively insensitive to the choice of the local density of dark matter, and direct detection excludes 25% of the points in the conservative case and 35% in the stringent case. Indirect detection is more sensitive to the choice of profile and propagation model and excludes less than 20% of the points in the conservative case and 30% in the stringent one. In all cases, the simultaneous application of the dark matter constraints is very important, and allows us to strongly reduce the number of valid points, even in the most conservative case.
In Fig. 3.16, the same analysis is performed for the different neutralino types separately. First, the bino-like neutralinos 1 have in general weaker couplings, leading to large relic densities and small annihilation and scattering cross sections. Thus, the bino-like points are strongly excluded by the relic density, slightly probed by direct detection, and negligibly by indirect detection. Therefore, the choice of the conservative or stringent constraints has a negligible effect, since the exclusion is dominated by the relic density. Second, wino-like neutralinos 1 are dominantly excluded by indirect detection, followed by direct detection. After these constraints, relic density only affects a negligible fraction of points, which is why the exclusion by relic density does not appear in the figure. For the winos, the choice of the conservative or stringent cases strongly affects the results, leaving 50% of the points valid in the conservative case, and 28% in the stringent case. Again, the standard case leads to results similar to the stringent case. Third, the Higgsino-like neutralinos 1 are mainly excluded by direct detection, which mildly depends on the astrophysical hypotheses. Indirect detection also excludes a number of points, even if a large fraction of them is already

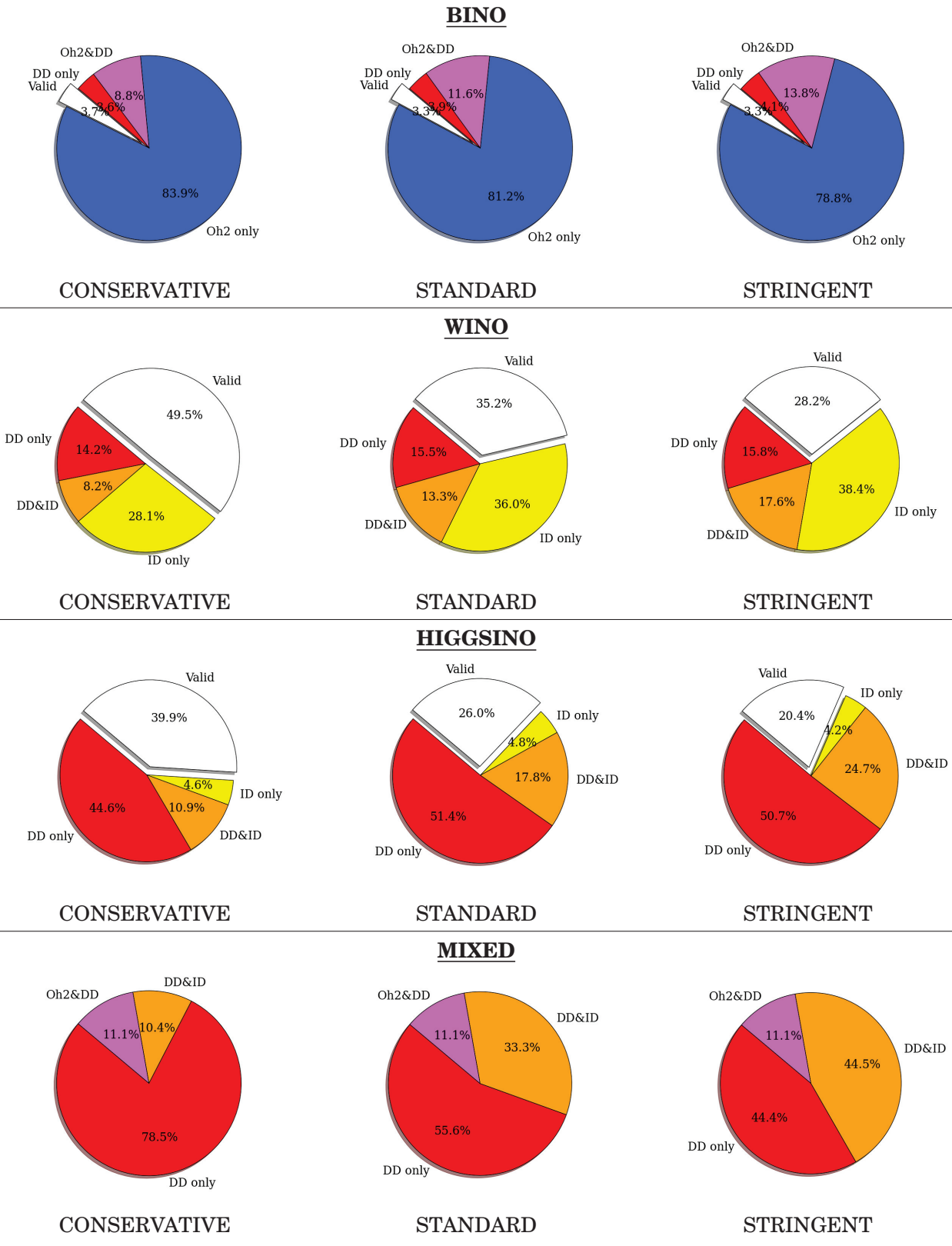

Figure 3.16: Fraction of pMSSM points excluded by the upper bound of the dark matter density, direct detection and indirect detection constraints for the different neutralino 1 types.

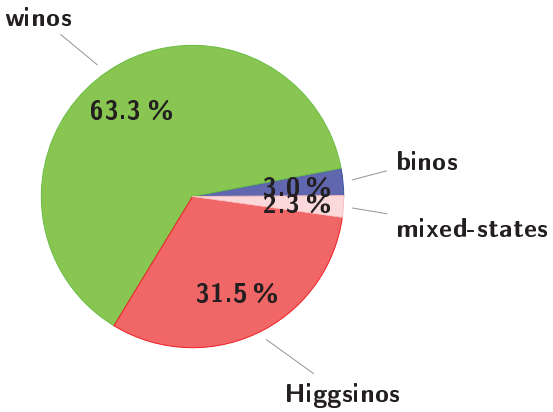

Figure 3.17: Fractions of neutralino 1 types in our scan after imposing the light Higgs mass limit, LEP and flavour constraints, and relic density upper bound.

excluded by direct detection. As for the winos, relic density only excludes a negligible fraction of points after the direct and indirect detection constraints. At the end, 40% of the Higgsinos remain valid in the conservative case, and 20% in the stringent case. Finally, the mixed-state neutralinos 1 are completely excluded independently from the astrophysical hypotheses, and predominantly by direct detection.

To summarise this section, dark matter constraints set strong constraints on the pMSSM parameter space. However, while direct detection leads to relatively robust constraints, indirect detection is more sensitive to the choice of galaxy halo profiles and cosmic ray propagation models.

3.3.5 Collider and Dark Matter constraints

In this section, the complementarity of collider and dark matter constraints will be studied. The LHC results requires the computation of numerous cross sections, generation of events and detector simulation, which are computationally heavy and CPU-time consuming. In order to gain CPU time, we perform the event generation and detector simulation only for model points which respect the light Higgs mass constraint, flavour physics, and LEP and Tevatron constraints, as well as the upper bound of the relic density. The points satisfying these constraints will be referred to as “Accepted points” in the following.
In Fig 3.17, we present the type of neutralinos 1 for the accepted points. A comparison with Fig. 3.5 showing the type of the points satisfying only the light Higgs mass limit, reveals that most of the binos have been excluded, but that the fraction of winos in comparison with the Higgsinos is unchanged. This is mainly due to the upper bound of the relic density, as explained in Section 3.3.1. The LEP and flavour constraints do not probe directly the neutralino 1, but can affect scenarios with light wino-like and Higgsino-like χ through the constraints on the charginos and heavier neutralinos. Nevertheless, the exclusion power of these constraints is limited in comparison to the relic density one.
In the Higgs sector, the light Higgs mass constraint favours the decoupling limit where the heavy Higgs bosons are heavy, and heavy stop masses with maximal mixing [185, 250–252]. Measure-

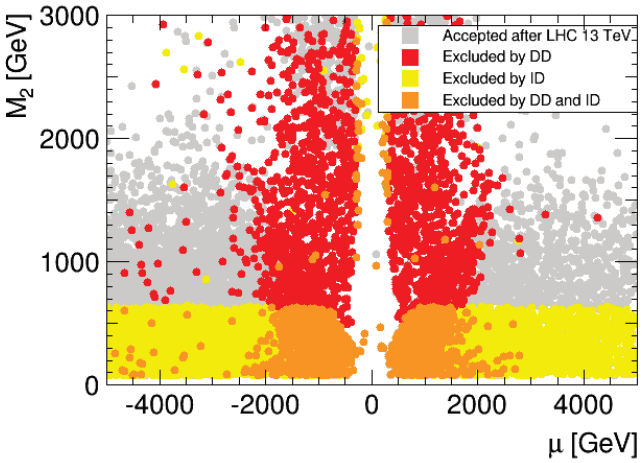

Figure 3.18: pMSSM points in the (μ, M_2) parameter plane. The accepted parameter points which are in agreement with the LHC 8 and 13 TeV data from Higgs and direct searches are shown in gray. The red points are in addition excluded by direct detection, the yellow points by indirect detection and the orange points by direct and indirect detections simultaneously.

ments of the light Higgs production and decay channels also point towards large heavy Higgs masses. In particular, the diphoton channel favours heavy charginos, stops and charged Higgs bosons [185, 186, 253–255]. In addition, light Higgs decays into supersymmetric particles are rather limited [185, 187–190]. These important limits provide strong constraints in the (μ, M_2) parameter plane. Indeed, both parameters are important for the neutralino and chargino mixings, and μ is also important for the third generation squark mixings. The limits obtained from the measurements of the light Higgs couplings are complemented by the electroweakino direct searches at LEP and the LHC. This is illustrated in Fig. 3.18, where the small μ values are excluded. The complementarity with dark matter constraints is rather clear. Direct detection excludes points spread over the plane. Indirect constraint severely excludes points with $M_2 \lesssim 600$ GeV and $|\mu| \lesssim 150$ GeV. One should however note that due to the multi-dimensional parameter space, there could be points below the coloured regions that still survive the dark matter and collider constraints.

The heavy Higgs searches, and in particular $H/A \to \tau\tau$ searches, impose strong constraints in the $(M_A, \tan\beta)$ parameter plane which is also relevant for direct detection as seen in Fig. 3.13. In Fig. 3.19, we superimpose over the points in agreement with the LHC constraints those which are excluded by direct detection. Similarly to direct detection, $H/A \to \tau\tau$ searches probe the large $\tan\beta$ and small M_A region (corresponding to the empty region in the upper right part in the figure). We can see from the figure that the exclusion by direct detection is not well defined and spread. Comparing with Fig. 3.13 reveals that the strongest and well defined exclusion by direct detection in this plane occurs below the $H/A \to \tau\tau$ limit. Both constraints are nevertheless complementary and allow us to exclude points beyond the large $\tan\beta$ and small M_A region.

As a hadron collider, LHC is more sensitive to strongly interacting particles. In particular, gluinos and squarks of the first and second generations are amongst the most actively searched particles,

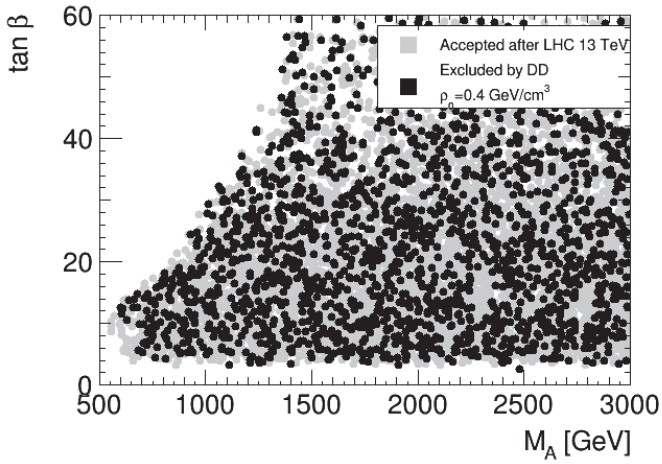

Figure 3.19: pMSSM points in the $(M_A, \tan\beta)$ parameter plane. The accepted model points which are in agreement with the LHC 8 and 13 TeV data from Higgs and direct searches are shown in gray. The black points are excluded by direct detection.

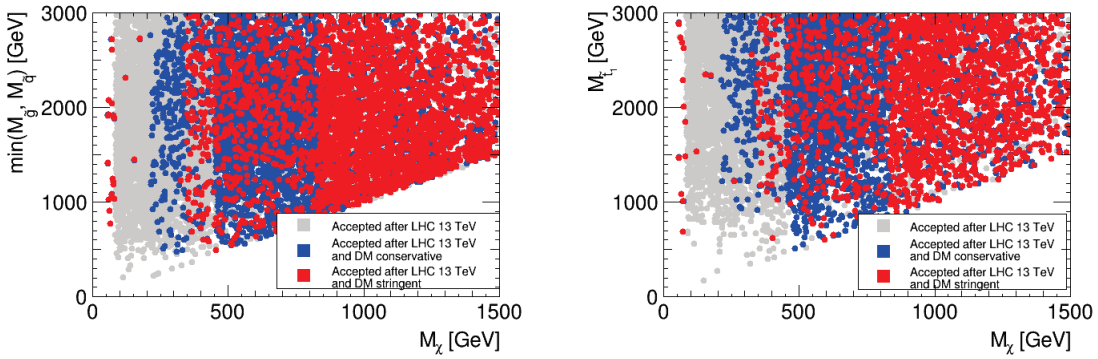

(a) (b)

Figure 3.20: (a) pMSSM points in the $(M_\chi, M_{\tilde{g},\tilde{q}})$ parameter plane. $M_{\tilde{g},\tilde{q}}$ is the lightest mass among the gluino and first and second generation squark masses. (b) pMSSM points in the $(M_\chi, M_{\tilde{t}_1})$ parameter plane. The accepted parameter points which are in agreement with the LHC 8 and 13 TeV data from Higgs and direct searches are shown in gray. The points which in addition agree with dark matter constraints with conservative astrophysical hypotheses are in blue, and with stringent hypotheses in red.

and LHC can probe masses as large as a few TeV in the most favourable scenarios. In Fig. 3.20, the accepted pMSSM points are plotted in the minimum mass amongst the gluino and first and second generation squark masses vs. neutralino 1 mass plane. We note that gluinos or squarks as light as a few hundred GeV can still escape LHC searches in a general scenario as the pMSSM. These points correspond mainly to compressed scenarios [256–259], where one or more supersymmetric particles have masses close-by, leading to decays with particles or jets in the final state which can leave the detectors undetected because of their small transverse energies. Dark mat-

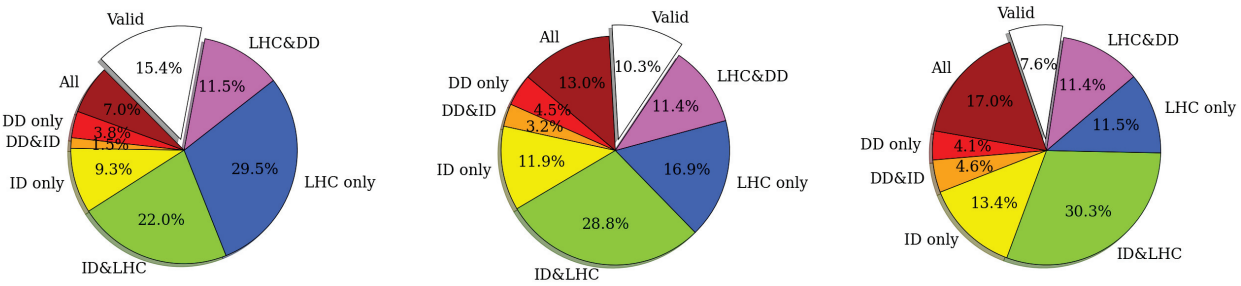

CONSERVATIVE STANDARD STRINGENT

Figure 3.21: Fraction of the pMSSM points satisfying the light Higgs mass, relic density, LEP and flavour constraints excluded by direct and indirect detections and LHC constraints.

ter searches can be very important in these cases and exclude points which are not probed at the LHC, as can be seen from the figure. Direct detection probes points spread over the plane. Indirect detection can probe neutralino 1 masses up to 450 GeV in the conservative case, 800 GeV in the stringent case, independently of the squark and gluino masses. We also see that after the LHC constraints, light squarks or gluinos of a few hundred GeV in compressed or complicated scenarios are still allowed, but after the dark matter constraints, they are less numerous and the surviving points correspond to very small squark/gluino-neutralino 1 mass splittings, and in the stringent case the squark and gluino masses are pushed beyond 450 GeV. So the complementarity is obvious, as dark matter experiments can probe parameter regions which are not accessible at the LHC, and vice versa.

Similar result for the lightest stop is presented in Fig 3.20. As for the gluino and squark case, light stops are still allowed by collider constraints in compressed scenarios, which can still be probed by dark matter detection experiments. Light stop scenarios which escape LHC detection are still allowed, but the stop 1 mass is pushed beyond 500 GeV in the conservative case and 600 GeV in the stringent case, after imposing the direct and indirect detection limits.

Finally, the interplay of the LHC and dark matter constraints is presented in a quantitative way in Fig. 3.21. It can be seen that the LHC has the major role in probing the pMSSM parameter space, but dark matter detection constraints further probe the parameter space. The combination of all constraints leads to an exclusion of between 85% and 92% of our sample.

Fig. 3.22 presents a more detailed view of the exclusion for the different neutralino 1 types. In particular, it reveals that LHC excludes more than 65% of the points independent of the neutralino 1 type. The role of dark matter constraints on the contrary is more type-dependent. As we showed earlier, binos, Higgsinos and mixed states are more strongly probed by direct detection, while indirect detection rather excludes winos. And whereas direct detection is mildly sensitive to the choice of the astrophysical parameters, indirect detection is more sensitive to it.

Finally, in Fig. 3.23, the fraction of neutralino 1 types after imposing all the constraints is shown. This figure is to be compared with Fig. 3.17, where only LEP, flavour and relic density constraints were applied. We can see that the final fractions are still similar after applying all constraints, with a larger proportion of winos, followed by a large proportion of Higgsino, and a small amount of binos. This shows that the relic density constraint is the most type-selecting constraint. How-

BINO

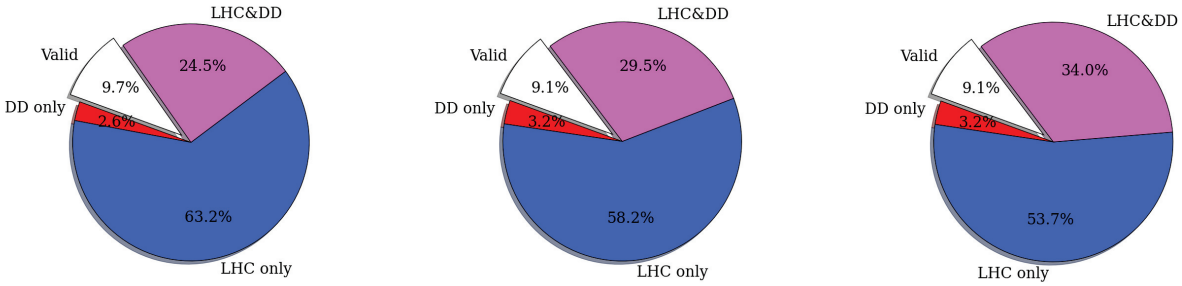

CONSERVATIVE STANDARD STRINGENT

WINO

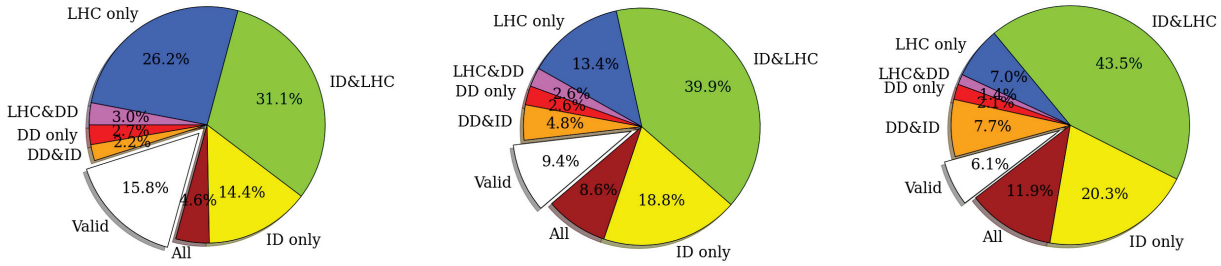

CONSERVATIVE STANDARD STRINGENT

HIGGSINO

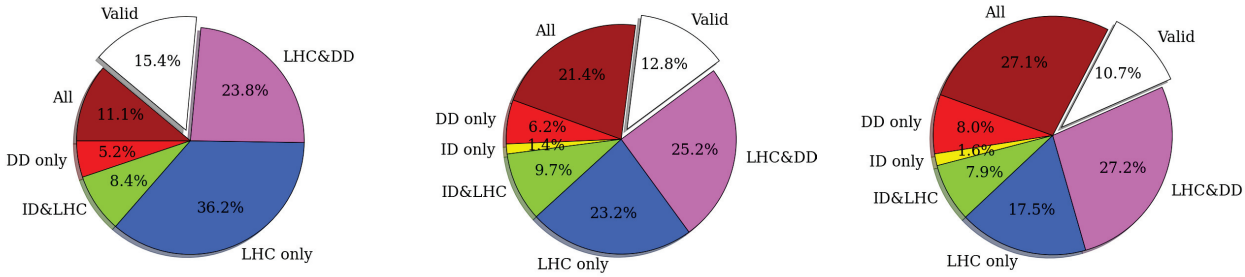

CONSERVATIVE STANDARD STRINGENT

MIXED

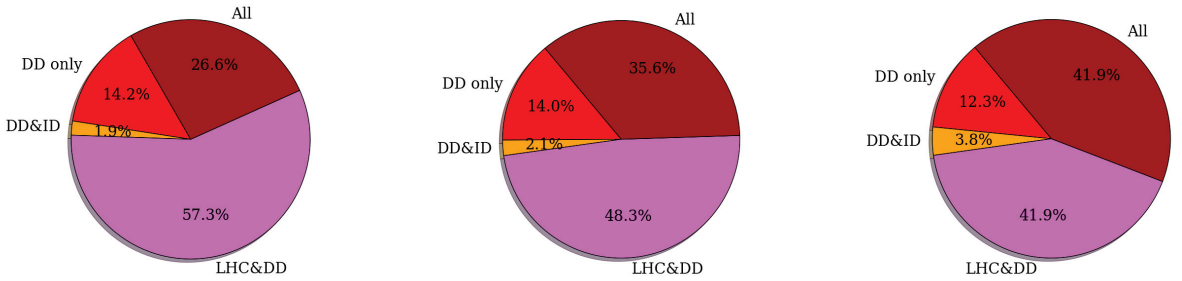

CONSERVATIVE STANDARD STRINGENT

Figure 3.22: Fraction of pMSSM points satisfying the light Higgs mass, relic density, LEP and flavour constraints, and excluded by direct and indirect detections and LHC constraints, for the different neutralino 1 types.

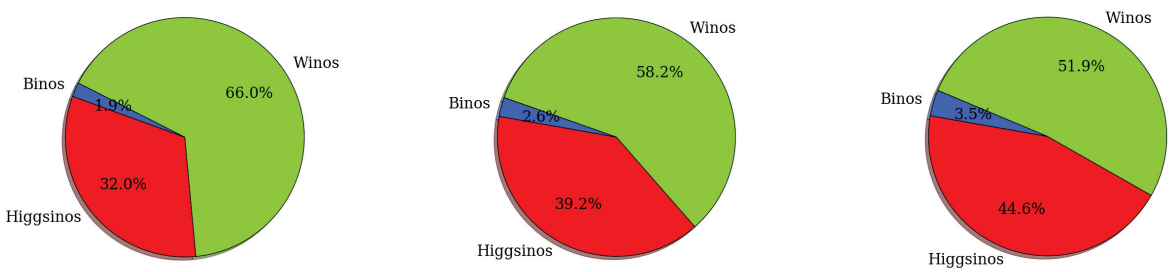

CONSERVATIVE STANDARD STRINGENT

Figure 3.23: Fractions of neutralino 1 types in our scan after imposing all the constraints (including only the upper bound for the relic density).

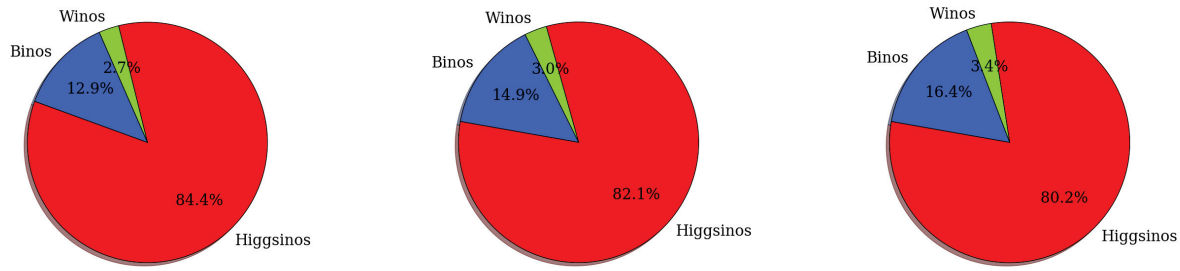

CONSERVATIVE STANDARD STRINGENT

Figure 3.24: Fractions of neutralino 1 types in our scan after imposing all the constraints, including also the lower relic density limit.

ever, we note that the proportion of winos is much larger in the conservative dark matter case than in the stringent case.

An important caveat here is in order. The fraction of points has no real statistical meaning, but rather shows the tendency of the constraints to select certain types. To illustrate this, we show in Fig. 3.24 the fraction of the types after applying all the constraints, including the Planck lower bound. In this case, the Higgsinos are now the dominant surviving species, followed by the binos, and the winos survive only in small proportion. It is interesting to note that in this case, the choice of conservative or stringent astrophysical hypotheses does not affect much the results.

Finally, it is worth mentioning that great improvements in the sensitivity of the direct and indirect detection experiments are expected in the coming years. Concerning direct detection, in the next few years XENONnT [78] and LZ [79] will push the XENON1T limit by two orders of magnitude, and within ten years DARWIN [80] will allow us to gain one extra order of magnitude. This is illustrated in Fig. 3.25. For comparison, the gray points correspond to a sample of our points which are in agreement with the current LHC 8 TeV and 13 TeV limits. Practically, XENONnT/LZ will exclude most of the Higgsino points, and DARWIN will be able to probe a

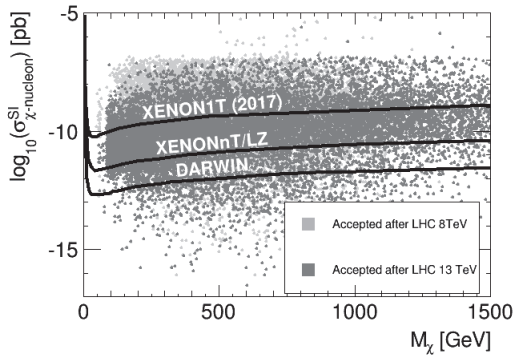

Figure 3.25: pMSSM points in the spin-independent scattering cross section vs. neutralino 1 mass parameter plane. The current XENON1T upper limit is superimposed together with the prospective limits of XENONnT/LZ and DARWIN.

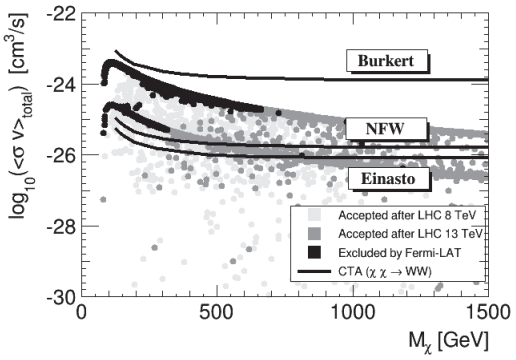

Figure 3.26: Total annihilation cross section as a function of the neutralino 1 mass. The CTA prospective upper limits are superimposed for the Einasto, NFW and Burkert profiles.

large part of the wino region. In addition, we have shown that the constraining power of direct detection is only mildly affected by the choice of the astrophysical assumptions, thus these limits will provide relatively robust constraints on the pMSSM parameter space. The DARWIN limit will however be close to the neutrino background, which constitutes a large obstacle to further improvements. Nevertheless, the remaining points after DARWIN will have mainly wino-like neutralinos 1, which will be probed by indirect detection.

For indirect detection, the Cherenkov Telescope Array (CTA) [260], dedicated to gamma rays, will use a Cherenkov imagery technique similar to HESS, VERITAS or MAGIC, and will be able to probe an energy range between a few tenths of GeV to above 100 TeV. Before 2030, CTA will also further push the indirect detection limits by observing gamma rays at the center of the Milky Way, as shown in Fig. 3.26. It is important to remark however, that contrary to the Fermi-LAT limits, which are obtained from the observations of spheroidal dwarves and which are therefore less affected by the dark matter profile, since CTA will focus on the galaxy center, it is subject to strong uncertainties from the dark matter profile. Since the question of the existence of cuspy profiles is unresolved [261], dark matter density distributions such as NFW or Einasto which incorporate cuspy profiles, will lead to fundamentally different exclusion limits than a Burkert profile with a core. This is illustrated in the figure, a Burkert profile will lead to limits which are two orders of magnitude less constraining than the NFW or Einasto profile. Therefore, CTA will be even more subject to astrophysical uncertainties, even if we can hope for an improvement of our knowledge of the galactic center within the next decade.

We will now describe the implementation of direct and indirect dark matter detection in further details.

CHAPTER 4

NEW EXTENSIONS AND FEATURES IN SUPERISO RELIC

The work on dark matter experimental limits in the MSSM required the development of numerical tools for the computation of direct and indirect detection constraints. The resulting code is integrated in the public program SuperIso Relic [132, 133, 262]. Several public codes already feature the calculation of direct and indirect detection observables in supersymmetric models, such as micrOmegas [150–152], DarkSUSY [263, 264] or MadDM [265]. However, they are most often used with default parameter sets, neglecting the astrophysical and nuclear uncertainties related to those constraints. In the DarkBit package [118], various sources of uncertainties are considered, but this program is most commonly used to perform best-fit calculations, whereas SuperIso Relic is rather used to test the validity of supersymmetric model points under experimental constraints. It was therefore useful to design the extensions of SuperIso Relic for direct and indirect detection as a continuation of our previous work. With this extension, it is possible to calculate a "conservative", "standard" or "stringent" constraints, according to the chosen set of uncertainties, for the latest experimental results of dark matter direct and indirect searches. This code works for model points in the MSSM and NMSSM with a neutralino LSP. It takes into account uncertainties from dark matter density and velocity profiles, as well as uncertainties from cosmic-ray propagation. In addition, we considered, the uncertainties on the nuclear form factors appearing in the calculation of direct detection observables.
The full description of the code can be found in the new SuperIso Relic manual which is submitted to Comput. Phys. Commun. [262].

4.1 SuperIso Relic

SuperIso Relic is a public program written in C and Fortran for the computation of flavour observables and the relic density in the MSSM and NMSSM. It is an extension of the program SuperIso [196–198] which computes, in particular, the Wilson coefficients and physical observables for the most severely constraining processes in flavour physics, namely $B \to X_s\gamma$, $B_s \to \mu^+\mu^-$, $B_u \to \tau\nu$ and for the inclusive and exclusive semileptonic decays, including the observables presenting

anomalies, namely $P_5^{'}$, R_{K,K^*}, R_{D,D^*}. The relic density module integrates the Boltzmann equation which describes the evolution of the density of the lightest supersymmetric particle. The program takes into account all annihilation and co-annihilation processes involved in the LSP thermal freeze-out. By default, this calculation is carried out within the frame of the standard model of cosmology, but the user also has the possibility of adding a dark source of density and entropy. The routines for the calculation of the annihilation and co-annihilation amplitudes are integrated in the SuperIso package. They were generated with a Mathematica [266] script which uses the LanHEP [267] Lagrangian in FeynArts format, and calls FeynArts and FormCalc [268–271]. The main routines in SuperIso Relic take in argument a SUSY LesHouches Accord file SLHA1 [272] or SLHA2 [273] which summarizes in a standardized form the soft-parameter numerical values of a given point. SLHA files can be generated by dedicated programs such as SOFTSUSY [123], ISAJET [274], SPheno [275] and SuSpect [276]. The Higgs decay width and branching ratios, relevant for the calculation of the relic density, are computed using HDECAY [202] or FeynHiggs [277]. A summary of Superiso Relic structure can be found in figure 4.1.
In order to complete the panel of constraints in SuperIso Relic, I implemented routines for dark matter direct and indirect detection rates for a neutralino LSP. In the following, I will detail this implementation, focusing more on the phenomenology than on technical details.

4.2 Direct detection

4.2.1 Generalities

The calculation of direct detection constraints requires the computation of the differential recoil rate per unit of target material mass $\frac{dR}{dE}$ which was described in section 3.2.2.3. We recall here the formula:

$$\frac{dR}{dE} = \underbrace{\frac{1}{2m_\chi \mu^2}\,\sigma(q)}_{\text{Particle physics}}\ \underbrace{\rho_\chi \eta(v_{min}(E),t)}_{Astrophysics}, \tag{4.1}$$

where μ is the reduced neutralino-nucleus mass, $\sigma(q)$ is an effective scattering cross section, ρ_χ the local DM density and $\eta(v_{min}(E),t)$ is the mean DM inverse speed.
In the general case where the target material is composed of more than one isotope, the total differential recoil rate is the sum of each isotope contribution weighted by the isotope mass fraction.

$$\frac{dR}{dE} = \sum_i \xi_i \frac{dR_i}{dE} \tag{4.2}$$

One can note that the first term on the right side of equation 4.1, in which appears the effective cross section, depends only on the particle model which is used. The main source of uncertainties in this term will come from nuclear form factors. The second term involves only astrophysical observables, namely dark matter local density and velocity profile. The calculation of each term will, therefore, be done separately.

The calculation of $\eta(v_{min},t)$ is performed with a Simpson method. The default velocity profile is the standard halo model with $v_{rot} = 220 \pm 20$ km/s, $v_{esc} = 544 \pm 50$ km/s and $\rho_\chi = 0.4 \pm 0.2$ GeV/cm^3. It is possible to calculate a “conservative”, “standard”, or “stringent” constraint in relation with

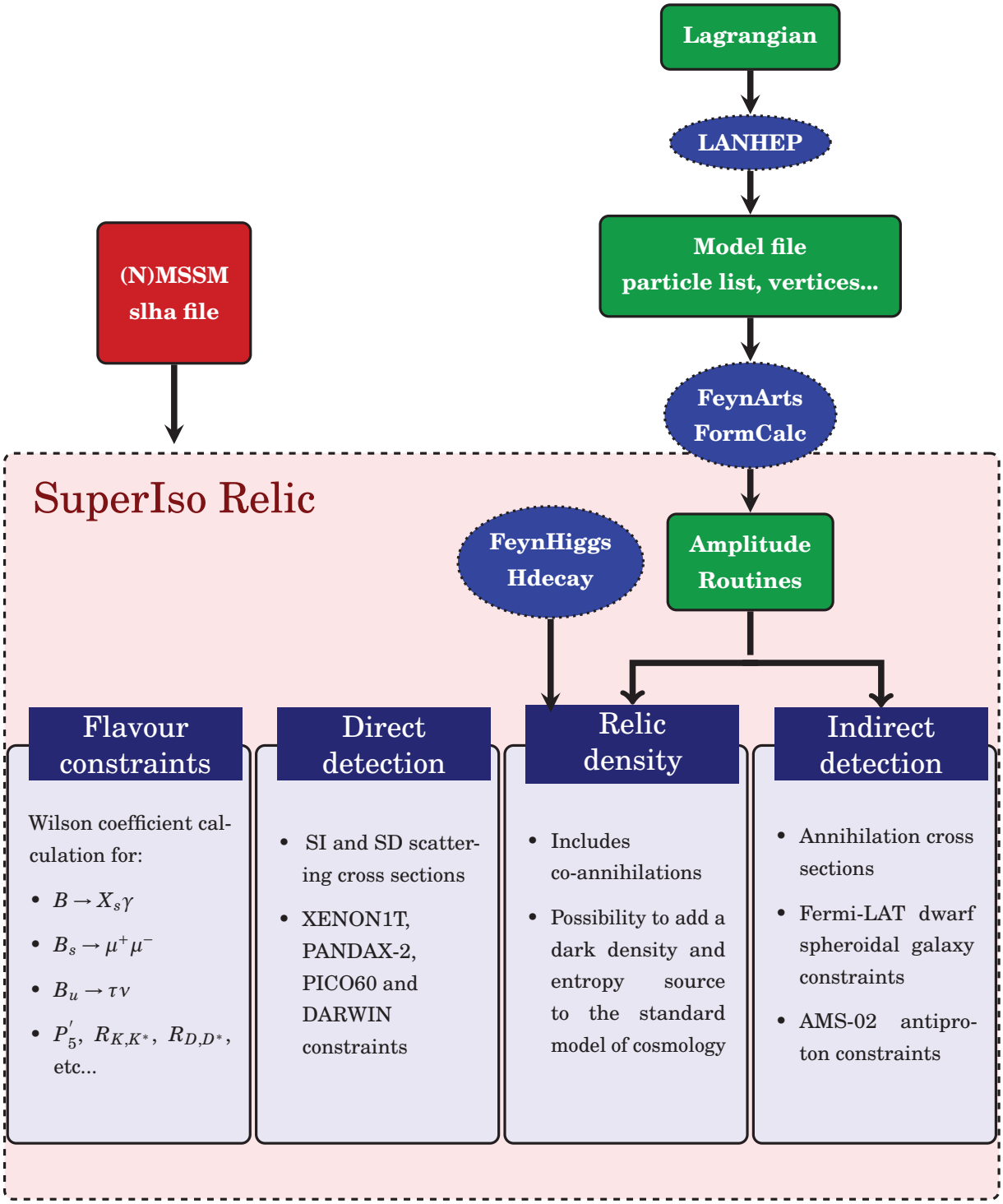

Figure 4.1: SuperIso Relic structure

the uncertainties of these three parameters. The effect of those uncertainties on XENON1T upper limit was already presented in chapter 3 (figure 3.4). The results were obtained by performing a variable substitution in equation 3.11. Here, a full computation will be presented. Results remain similar between the two methods, however it is possible in the new implementation to define another model of halo, beyond the standard model, which makes it much more powerful.
We will now focus only on the calculation of the effective cross section $\sigma_i(q)$ and on its related uncertainties.

4.2.2 Scattering cross sections

The effective WIMP/nucleus scattering cross section is commonly decomposed into a spin-dependent and spin-independent component $\sigma_i(q) = \sigma_i^{SI}(q) + \sigma_i^{SD}(q)$. Each component is the subject of a special treatment, but both need the calculation of effective neutralino-quark couplings which will be detailed, in the MSSM, in subsection 4.2.2.2.

4.2.2.1 SI and SD cross sections

The **spin-independent** term, in the case of a target nucleus composed of Z protons and $(A-Z)$ neutrons, can be written as:

$$\sigma_i^{SI}(q) = \frac{4\mu^2}{\pi} F_{SI}^2(q) \left[Z \times A_p^{SI} + (A-Z) \times A_n^{SI} \right]^2 \tag{4.3}$$

where F_{SI} is a nuclear form factor which probes the nucleon content of the nucleus and A_p^{SI}, A_n^{SI} are the proton/WIMP and neutron/WIMP effective scattering amplitudes. These amplitudes can be calculated from the WIMP/quark effective couplings λ_q^{SI} weighted by the quark form factors.

$$A_{p,n}^{SI} = \sum_{q=u,d,s} f_q^{p,n} \lambda_q^{SI} \,. \tag{4.4}$$

The quark form factors $f_q^{p,n}$ probe the mass content of the quarks in the nucleons:

$$f_q^N = \frac{m_q}{M_N} \langle N | \overline{\Psi}_q \Psi_q | N \rangle \,. \tag{4.5}$$

As for the **spin-dependent** counterpart, the effective cross section can be written as:

$$\sigma_i^{SD}(q) = \frac{16\mu^2}{2J+1} S(q) \,, \tag{4.6}$$

where J is the the total spin of the nucleus and

$$S(q) = a_0^2 S_{00}(q) + a_1^2 S_{11}(q) + a_0 a_1 S_{01}(q) \,. \tag{4.7}$$

S_{00}, S_{01} and S_{11} are structure factors which depend on the nature of the target isotope and a_0 and a_1 are defined as

$$a_0 = A_p^{SD} + A_n^{SD} \qquad a_1 = A_p^{SD} - A_n^{SD} \,, \tag{4.8}$$

where $A^{SD}_{p,n}$ are the WIMP/proton or neutron spin-dependent scattering amplitudes. In the same way as for the spin-independent amplitude, $A^{SD}_{p,n}$ are calculated as the sum of the WIMP/quark SD effective couplings λ^{SD}_q, weighted by quark form factors probing the spin content of the quarks in the nucleons $\Delta q^{p,n}$:

$$A^{SD}_{p,n} = \sum_{q=u,d,s} \Delta q^{p,n} \lambda^{SD}_q \ . \tag{4.9}$$

$\Delta q^{p,n}$ is defined as:

$$\Delta q^N = \frac{1}{2 s_\mu} \langle N | \overline{\Psi}_q \gamma_\mu \gamma^5 \Psi_q | N \rangle \ , \tag{4.10}$$

where s_μ is the nucleon spin.

4.2.2.2 Neutralino/quark effective couplings

An important step in the calculation of the scattering cross sections consists in computing the effective couplings λ^{SI}_q and λ^{SD}_q. This calculation could be done automatically from any Lagrangian. However, this method requires to separate the spin-dependent and spin-independent terms in the Lagrangian and then to generate the respective scattering amplitudes. Such a process necessitates a considerable modification of the way the amplitudes are generated in SuperIso Relic, which is currently under development. For the moment, we preferred the implementation of explicit analytical formulae for the calculation of the SI and SD effective couplings in the (N)MSSM based on the work by Drees & Nojiri [278].

The neutralino interacts with quarks at tree level by the exchange of CP-even Higgs bosons, Z bosons or squarks, according to the diagrams in figure 2.6. The neutralino interactions with these intermediate particles can be found in the following Lagrangians:

$$\begin{cases} \mathscr{L}_{\chi\chi Z} &= -\dfrac{1}{4}\dfrac{g}{cos\,\theta_W}\left(|N_{13}|^2 - |N_{14}|^2\right)\overline{\chi}\gamma^\mu\gamma^5\chi Z_\mu \\ \mathscr{L}_{\chi\chi H} &= \dfrac{g}{2}(N_{12} - tan\,\theta_W N_{11})\left[(cos\,\alpha N_{13} - sin\,\alpha N_{14})H^0 - (sin\,\alpha N_{13} + cos\,\alpha N_{14})h^0\right]\overline{\chi}\left(\dfrac{1+\gamma^5}{2}\right)\chi + h.c. \\ \mathscr{L}_{\chi q\tilde{q}} &= \sum_i \sum_{r=1}^{2} \overline{q}_{ir}(a_{ir} + b_{ir}\gamma^5)\chi\tilde{q}_{ir} + h.c. \end{cases} \tag{4.11}$$

where g is the SU(2) gauge coupling, θ_W the weak mixing angle and N is the neutralino mixing matrix. In the last Lagrangian, the subscript i stands for the type of quark $i = u, d, c, s, t, b$ and $r = 1, 2$ refers to the two squarks related to a given quark. The coupling constants a_{ir} and b_{ir} are calculated with

$$\begin{aligned} a_{i1} &= -\frac{1}{2}\left[cos\,\theta_{q_i}\left(X_i + Z^q_i\right) + sin\,\theta_{q_i}\left(Y_i + Z^q_i\right)\right] \\ b_{i1} &= -\frac{1}{2}\left[cos\,\theta_{q_i}\left(X_i - Z^q_i\right) + sin\,\theta_{q_i}\left(Y_i - Z^q_i\right)\right] \end{aligned} \tag{4.12}$$

where

$$\begin{aligned} X_i &= -g\sqrt{2}\left[t_i^3 N_{12} + (y_i/2) tan\,\theta_W N_{11}\right] & Y_i &= g\sqrt{2}\, q_i N_{11} tan\,\theta_W \\ Z_i^u &= \frac{g}{\sqrt{2}} \frac{m_{ui} N_{14}^*}{M_W sin\,\beta} & Z_i^d &= \frac{g}{\sqrt{2}} \frac{m_{di} N_{13}^*}{M_W cos\,\beta}\,. \end{aligned} \tag{4.13}$$

Here, t_i^3 and y_i are the quark weak isospin and hypercharge respectively and $\theta_{q,i}$ is the squark mixing angle. In order to obtain a_{i2} and b_{i2}, one only has to replace $cos\theta_{q_i}$ by $-sin\,\theta_{q_i}$ and $sin\,\theta_{q_i}$ by $cos\,\theta_{q_i}$ in equations 4.12.

In the non-relativistic limit, the solution of the Dirac equation takes the form $\Psi = \begin{pmatrix} \varphi \\ 0 \end{pmatrix}$ where φ is a two-component spinor field. Using Dirac representation for γ matrices:

$$\gamma^0 = \begin{pmatrix} 1 & 0 \\ 0 & -1 \end{pmatrix} \qquad \gamma^i = \begin{pmatrix} 0 & \sigma^i \\ -\sigma^i & 0 \end{pmatrix} \qquad \gamma^5 = \begin{pmatrix} 0 & 1 \\ 1 & 0 \end{pmatrix} \tag{4.14}$$

one can directly find that terms in $\overline{\Psi}\gamma^5\Psi$ vanish. Moreover, the terms in $\overline{\Psi}\gamma^\mu\Psi$ and $\overline{\Psi}\Psi$ can be reduced to a scalar (spin-independent) component $\varphi^\dagger\varphi$ while the terms in $\overline{\Psi}\gamma^\mu\gamma^5\Psi$ and $\overline{\Psi}\sigma^{\mu\nu}\Psi$ yield the vector (spin-dependent) interactions $\varphi^\dagger\sigma^i\varphi$. Furthermore, as the neutralino is a Majorana particle, the terms $\overline{\chi}\gamma^\mu\chi$ and $\overline{\chi}\sigma^{\mu,\nu}\chi$ also vanish.

The terms of the supersymmetric Lagrangian related to neutralino-quark scattering can thus be rewritten into an effective four-fermion Lagrangian composed of a spin-dependent (SD) and spin-independent (SI) part.

$$\mathscr{L}_{\text{eff}} = \sum_i [\underbrace{d_i \overline{\chi}\gamma^\mu\gamma^5\chi\overline{q}_i\gamma_\mu\gamma^5 q_i}_{\text{SD}} + \underbrace{f_i\overline{\chi}\chi\overline{q}_i q_i + g_i\overline{\chi}\gamma^\mu\partial^\nu\chi\left[\overline{q}\gamma_\mu\partial_\nu q - \partial_\nu\overline{q}\gamma_\mu q\right]}_{SI}] \tag{4.15}$$

The exchange of a CP-even Higgs yields straightforwardly a spin-independent term in this Lagrangian while the exchange of a Z boson yields a spin-dependent term. Concerning the exchange of squarks in the s or t-channel, a Fierz reordering of the gamma matrices is needed in order to separate the SI and SD terms.

The coupling constants d_i, f_i and g_i read (from Drees & Nojiri [278]):

$$d_i = \frac{1}{4}\left(\sum_{r=1,2} \frac{a_{ir}^2 + b_{ir}^2}{m_{\tilde{q}_{ir}}^2 - (m_\chi + m_{q_i})^2}\right) - \frac{g^2}{8M_W^2}\left(|N_{14}|^2 - |N_{13}|^2\right) t_i^3 \tag{4.16}$$

$$f_i = -\frac{1}{4}\left(\sum_{r=1,2} \frac{a_{ir}^2 - b_{ir}^2}{m_{\tilde{q}_{ir}}^2 - (m_\chi + m_{q_i})^2}\right) + m_{q_i}\left(\frac{c_\chi^{h^0} c_{q_i}^{h^0}}{m_{h^0}^2} + \frac{c_\chi^{H^0} c_{q_i}^{H^0}}{m_{H^0}^2}\right) \tag{4.17}$$

$$g_i = -\frac{1}{4}\sum_{r=1,2} \frac{a_{ir}^2 + b_{ir}^2}{\left[m_{\tilde{q}_{ir}}^2 - (m_\chi + m_{q_i})^2\right]^2} \tag{4.18}$$

where $c_\chi^{h^0,H^0}$, $c_q^{h^0,H^0}$ are terms defining the couplings of the neutralino and quarks with the CP-even Higgs bosons.

At leading order, $\lambda_i^{SD} = d_i$ and $\lambda_i^{SI} = f_i$. The term proportional to g_i in the effective Lagrangian is quadratically suppressed when the squark masses are large enough. However, in the specific case where the squark masses are close to the neutralino mass, this term needs full treatment. The

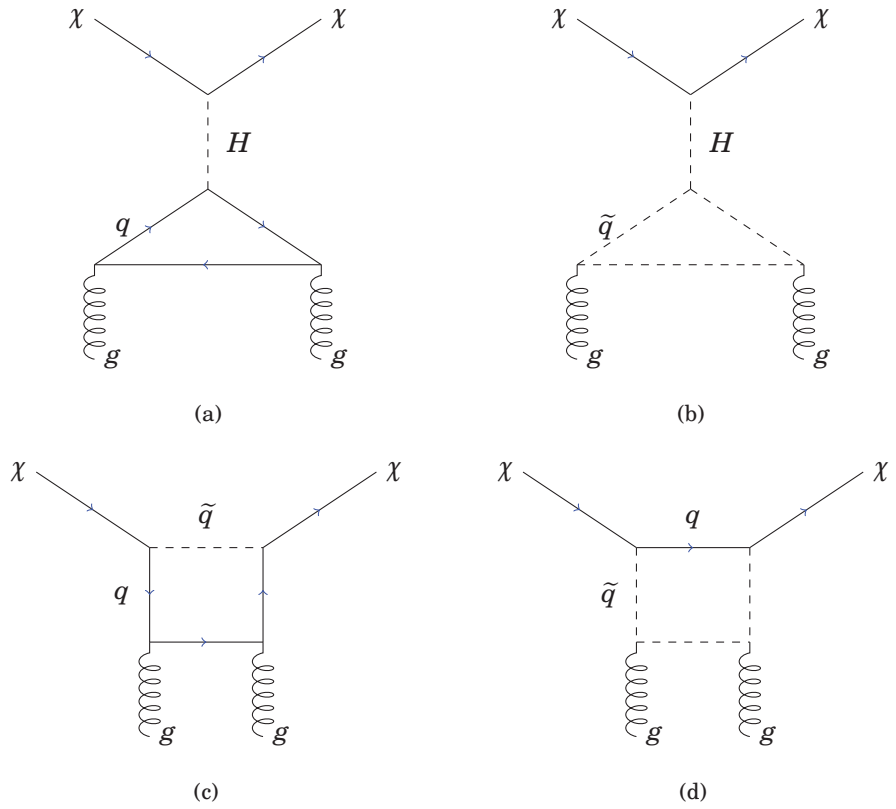

Figure 4.2: Loop diagrams involved in the spin-independent scattering amplitude

current $\overline{q}\gamma_\mu\partial_\nu q - \partial_\nu\overline{q}\gamma_\mu q$ can, in fact, be decomposed into a scalar and a twist-2 operator. The procedure to treat the twist-2 operator is explicitly described in Drees & Nojiri and was integrated in the code.

4.2.2.3 QCD and SUSY-QCD corrections

Additional higher-order corrections were implemented for the spin-independent amplitude. The neutralino can indeed interact with the gluon content of the nucleons via the diagrams including heavy quark or squark loops described in figure 4.2.
At first approximation, these diagrams can be treated as effective interactions between the neutralino and the heavy quarks and squarks, corrected by an appropriate form factor f_Q related to the gluon content of the nucleon. For heavy quarks, this form factor depends simply on the sum of the light quark form factors:

$$f_Q^{p,n} = \frac{2}{27}\left(1 - \sum_{q=u,d,s} f_q^{p,n}\right) \tag{4.19}$$

However, this form factor is enhanced in the case of a Higgs boson exchange (diagrams (a) and (b) in figure 4.2) due to QCD corrections. Diagram (a) requires to be corrected by a factor $\left(1+\frac{11\alpha_s(m_Q)}{4\pi}\right)$ while diagram (b) has a corrective factor of $\left(1+\frac{25\alpha_s(m_{\tilde{Q}})}{6\pi}\right)$ [279], where α_s is the strong coupling constant. Considering box diagrams (c) and (d), this kind of treatment is only

valid when $m_{\tilde{q}}^2 \gg (m_q + m_\chi)^2$, which is not necessarily true for top quarks. In more general cases, the box diagrams require a full calculation. Therefore, the loop integrals calculated in Drees & Nojiri for box diagrams were also implemented.

Finally, the bottom quark mass may receive significant correction from gluino-squark loop in SUSY scenarios. While down-type quarks couple normally only to the Higgs doublet H_d, this correction allows also a small coupling between the b-quark and H_u. This SUSY-QCD correction modifies the coupling of the b-quark to CP-even Higgs as described in [279]:

$$c_b^{h^0} = \frac{g}{2M_W}\left[-m_b^{\mathrm{SM}} cos(\alpha-\beta) + m_b^{\mathrm{MSSM}} sin(\alpha-\beta)\, tan\,\beta\right], \tag{4.20}$$

$$c_b^{H^0} = \frac{g}{2M_W}\left[m_b^{\mathrm{SM}} sin(\alpha-\beta) + m_b^{\mathrm{MSSM}} cos(\alpha-\beta)\, tan\,\beta\right]. \tag{4.21}$$

Using the pMSSM sample of points described in section 3.2.1, we compared the neutralino-nucleon amplitudes obtained with my code to the ones calculated with micrOMEGAs and DarkSUSY and found a good agreement, up to the order of the percent.

The implementation of the neutralino-nucleon scattering amplitudes in the NMSSM only required a small modification of the Higgs couplings, as the additional CP-even Higgs also participates to the scattering process. These couplings were calculated using FormCalc and are presented in Appendix B.

4.2.3 Uncertainties on the nucleon and nuclear form factors

The nucleon and nuclear form factors appearing in the calculation of the differential recoil rate suffer, in fact, from significant uncertainties. Depending on the type of target nuclei, this will impact differently the amount of expected nuclear recoil events. For this reason, I calculated the "conservative", "standard" and "stringent" expected number of events μ for our pMSSM sample of points, in the case of a xenon detector (XENON1T) and a fluorine detector (PICO60). μ is defined by

$$\mu = MT \int_0^\infty dE\, \phi(E) \frac{dR}{dE}(E), \tag{4.22}$$

where M is the total of target material, T is the time of exposure and $\phi(E)$ is the efficiency of the detector. Then, I studied the relative difference between the stringent and conservative case

$$\eta = \frac{\mu_{\mathrm{stringent}} - \mu_{\mathrm{conservative}}}{\mu_{\mathrm{standard}}}. \tag{4.23}$$

4.2.3.1 Nucleon form factors

Spin-independent interaction:

Starting with the spin-independent nucleon form factors, $f^{p,n}u$, $f^{p,n}d$ and $f^{p,n}s$ can be calculated from only two parameters namely the light and strange quark contents of the nucleon,

defined as

$$\sigma_l \equiv \frac{m_u + m_d}{2} \langle N|\overline{u}u + \overline{d}d|N\rangle \ , \tag{4.24}$$

$$\sigma_s \equiv m_s \langle N|\overline{s}s|N\rangle \, . \tag{4.25}$$

From these quantities, one can deduce:

$$\begin{cases} f_d^p = \dfrac{1}{m_p} \dfrac{2\sigma_l}{\frac{m_u}{m_d}(1+\alpha)} & f_d^n = \dfrac{m_p}{m_n} f_d^p \\ f_u^p = \alpha \dfrac{m_u}{m_d} f_d^p & f_u^n = \dfrac{m_p}{m_n} f_u^p \\ f_s^p = \dfrac{\sigma_s}{m_p} & f_s^n = \dfrac{\sigma_s}{m_n} \end{cases} \tag{4.26}$$

where α is defined as

$$\alpha = \frac{\langle N|\overline{u}u|\rangle}{\langle N|\overline{d}d|\rangle} = \frac{2z - (z-1)y}{2 + (z-1)y} \ , \tag{4.27}$$

with $y = \frac{1+\frac{m_u}{m_d}}{\frac{m_s}{m_d}} \frac{\sigma_s}{\sigma_l}$ and

$$z = \frac{\langle N|\overline{u}u|N\rangle - \langle N|\overline{s}s|N\rangle}{\langle N|\overline{d}d|N\rangle - \langle N|\overline{s}s|N\rangle}. \tag{4.28}$$

The light quark content of the nucleons is known from lattice QCD results [280–283] and from the analysis of pion-nucleon scattering [284–286]. As for the strange content of the nucleons, it is deduced from lattice QCD calculations [287]. We take the range of values of σ_l, σ_s and z from [288]:

$$\sigma_l = 46 \pm 11 \text{ MeV} \ , \tag{4.29}$$

$$\sigma_s = 35 \pm 16 \text{ MeV} \ , \tag{4.30}$$

$$z = 1.5 \pm 0.5 \tag{4.31}$$

We calculate the conservative, standard and stringent expected number of events for XENON1T and PICO60 experiments for our pMSSM sample of points, using a Powell method to minimize or maximize the SI scattering cross section according to σ_l and σ_s uncertainties. The results are shown in figure 4.3. The relative uncertainty is, in most cases, negligible for PICO60 experiment, which is more sensitive to spin-dependent interactions. However, the relative uncertainty for XENON1T is around 27%. This effect seems to be independent from the nature of the neutralino.

Spin-dependent interactions The nucleon SD form factors $\Delta_q^{(N)}$, can be computed from the combinations of two parameters:

$$a_3 = \Delta_u^{(p)} - \Delta_d^{(p)} \ , \tag{4.32}$$

$$a_8 = \Delta_u^{(p)} + \Delta_d^{(p)} - 2\Delta_s^{(p)}, \tag{4.33}$$

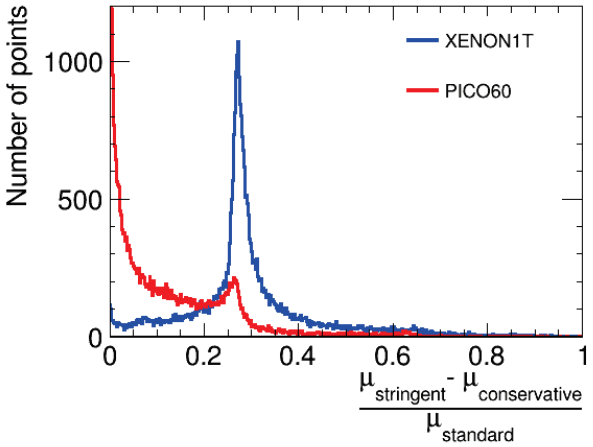

Figure 4.3: Relative uncertainty on the number of expected events for XENON1T and PICO60 experiments, in relation with the uncertainties on nucleon SI form factors.

and $\Delta_s^{(p)}$ itself. a_3 is known from neutron β decay measurements $a_3 = 1.2723 \pm 0.0023$ [289] and $a_8 = 0.585 \pm 0.023$ from hyperon β decay results [290]. The uncertainties on these two parameters are rather small compared to the error on $\Delta_s^{(p)} = -0.09 \pm 0.03$, which is deduced from measurement of the spin-dependent structure function of the deuteron from the COMPASS experiment [291]. Results on the relative uncertainty of the number of expected events are shown in figure 4.4. The uncertainties are globally negligible, especially for XENON1T. For PICO60, most of the points have a relative uncertainty of only 12 %.

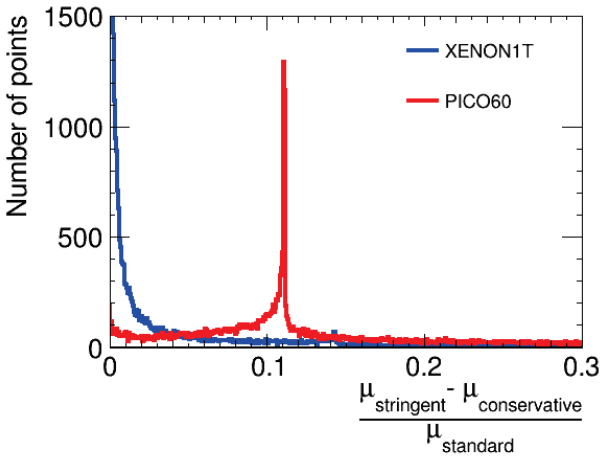

Figure 4.4: Relative uncertainty on the number of expected events for XENON1T and PICO60 experiments, in relation with the uncertainties on nucleon SD form factors.

4.2.3.2 Nuclear structure factors

Spin-independent interactions The SI form factor is essentially a Fourier transform of the mass distribution of the nucleus. A good approximation is the Helm form factor [292, 293]:

$$F(q) = 3e^{-q^2 s^2/2} \frac{\sin(qr_n) - qr_n \cos(qr_n)}{(qr_n)^3}, \tag{4.34}$$

where $s \simeq 0.9$ fm and $r_n^2 = c^2 + \frac{7}{3}\pi^2 a^2 - 5s^2$ is an effective nuclear radius with $a \simeq 0.52$ fm and $c \simeq 1.23A^{1/3} - 0.60$ fm. The uncertainties on the Helm form factors are expected to be rather low at small momentum exchange. However, the user may define its own SI form factor if desired.

Spin-dependent interactions Large uncertainties on S_{01} and S_{11} structure factors exist from long-range two-body currents due to pion exchange [294]. There is a correlation between S_{01} and S_{11} errors, so it is a priori not accurate to take the lower and upper bounds of S_{01} and S_{11} to assess the uncertainties on S. However, after a discussion with Javier Menéndez, co-author of the paper, we agreed that this method would be quite accurate in most cases and would in any cases just overestimate the uncertainties on $S(q)$, so that we would stay conservative.
The uncertainties are especially relevant for isospin violating models, since S_{01} and S_{11} are proportional to $A_p^{SD} - A_n^{SD}$. For XENON1T, the impact of those uncertainties are found to be negligible. However, the uncertainties may be significant for PICO60, in particular for Higgsino-like neutralinos (see figure 4.5). Indeed, the relative uncertainty on the expected number of events for higgsino-like neutralinos is around 42 %. This can be easily explained since the effective SD neutralino-quark coupling through a z boson exchange is proportional to the quark weak isospin t^3 and to the difference of the Higgsino mixing matrix elements $|N_{14}|^2 - |N_{13}|^2$.

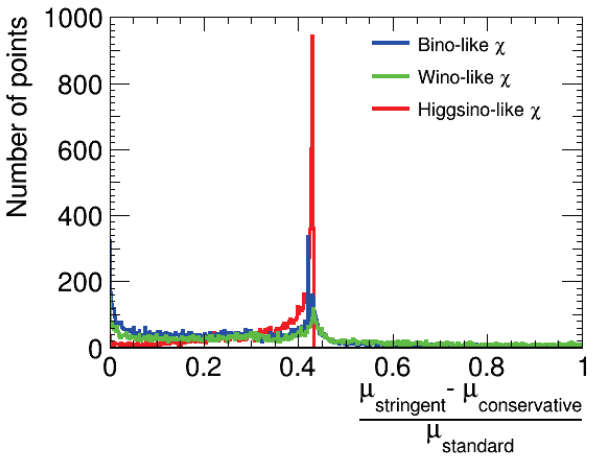

Figure 4.5: Relative uncertainty on the number of expected events for PICO60 experiments, in relation with the uncertainties on nuclear SD structure factors.

While the effects of all those uncertainties, considered altogether, may seem negligible in average when performing a scan over SUSY parameters, they may in fact be significant when studying a

given point. One should then preferably apply the conservative limits depending on the type of study.

4.2.4 Experimental limits

We present finally the constraints from experimental results. The analyses may vary significantly from an experiment to another. For instance, some collaborations chose to subtract the background noise from their data. This method necessitates to know extremely well the background spectrum, but is meant to draw severe constraints. However, the experiments of interest for us have not yet acquired a precise enough knowledge of their background. It is, nevertheless, possible to calculate good constraints without knowing the expected background. The most simple method is to use a *Poisson log-likelihood* defined by

$$\mathscr{L}\left(\mu|N_o\right) = \frac{(b+\mu)^{N_o} e^{-(b+\mu)}}{N_o!} \tag{4.35}$$

where μ is the total expected number of events from WIMP-nucleus scattering (equation4.22), N_o is the number of observed events and b is the expected background. We marginalize over b by chosing its value according to:

$$\begin{cases} b = N_o - \mu & \text{if } N_o > \mu \\ b = 0 & \text{otherwise} \end{cases} \tag{4.36}$$

A point will be excluded at 90% C.L. if the difference of its log-likelihoods respects

$$log\,\mathscr{L}(\mu = 0) - log\,\mathscr{L}(\mu) > \frac{2.71}{2} \tag{4.37}$$

This method, however, does not use the spectral information of the events. In the case where at least one event has been observed, it can be useful to use a more constraining method called the *maximum gap* [295]. If N_o events are observed at recoil energies E_1, E_2, ..., E_{N_o} , we divide the energy range over which the detector is sensitive into $N_o + 1$ intervals $[E_{\text{threshold}}, E_1]$, $[E_2, E_1]$,..., $\left[E_{N_o-1}, E_{N_o}\right]$, $\left[E_{N_o}, E_{\max}\right]$ and we calculate the expected number of events in each interval.

$$x_i = MT \int_{E_i}^{E_{i+1}} \phi(E) \frac{dR}{dE} dE \tag{4.38}$$

Accordingly to the way these intervals are built, no events are observed in each of them.
The maximum gap is defined as the interval where $x_i = x$ is maximum. x is proportional to the neutralino-nucleon cross-section, therefore for a strong coupling between the neutralino and ordinary matter, x may be very large while no event has been observed in this particular interval. Thus, if x is too large, the point can be excluded.
We define C_0, the probability of the maximum gap size being smaller than a particular value of x. This quantity depends only on x and on the total number of expected events μ:

$$C_0(x,\mu) = \sum_{k=0}^{m} \frac{(kx-\mu)^k e^{-kx}}{k!} \left(1 + \frac{k}{\mu - kx}\right) \tag{4.39}$$

where m is the greatest integer $\leq \mu/x$. A point will be excluded at 90% C.L. when $C_0 > 0.9$.

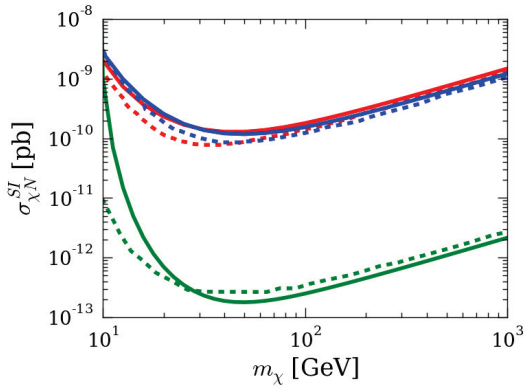

Figure 4.6: 90% C.L. spin-independent upper limit for XENON1T (red), PANDAX-2 (blue) and DARWIN (green). Official limits published by the collaborations are shown in dashed lines while the limits calculated from this work are in solid lines.

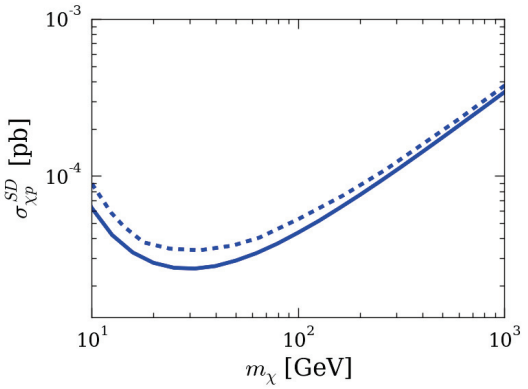

Figure 4.7: 90% C.L. spin-dependent upper limit for PICO60. Official limit published by the collaboration is shown in dashed lines while the limit calculated from this work is in solid line.

We implemented the constraints from the latest results of XENON1T, PANDAX-2 and PICO60, as well as the prospective limit at 200 t×year of DARWIN. No events were observed during the time of exposure of these experiments, except for PANDAX-2 who observed one event during RUN 9. However, the spectral information of this event is not publicly available. For this reason, we apply a Poisson log-likelihood method for all experiments.
The efficiencies are taken from the GAMBIT package DDCalc [118]. They were calculated using the TPCMC monte carlo [296] to model the detector response. TPCMC is Christopher Savage's private code which relies on NEST [297–299] for modeling the microphysics of a recoiling xenon atom.

The SI limits are shown in figure 4.6 for XENON1T, PANDAX-2 and DARWIN, while the SD limit for PICO 60 is shown in figure 4.6. These limits were obtained with the standard parameter values of the dark matter halo $\rho_\chi = 0.3$ GeV/cm^3, $v_{rot} = 220$ km/s and $v_{esc} = 544$ km/s, except for DARWIN prospective limit. In this last case, the constraints were marginalized over the astrophysical parameters and a conservative recoil energy threshold of 6.6 keV has been applied in order to reproduce the analysis of the collaboration.

4.3 Indirect detection

We will now turn to the calculation of the constraints from AMS-02 antiproton and Fermi-LAT gamma-ray data. These two types of constraint are derived from different kinds of analyses. However, they both require the calculation of the antiproton (or gamma-ray) flux produced from one dark matter annihilation. These two fluxes at production are computed following the same proce-

dure described below.

4.3.1 Fluxes at production

Dark matter annihilates into pairs of Standard Model particles which consecutively hadronize into high-energetic cosmic rays. In our case, we focus on the hadronization into antiprotons and gamma rays. The flux at production of antiprotons or gamma rays can be expressed as the sum over dark matter annihilation channels $\chi\chi \to p_3 p_4$ of the antiproton (γ-ray) flux resulting from the hadronization of particles p_3 and p_4 with an energy of E_{p_3} and E_{p_4} respectively, weighted by the channel branching ratio:

$$\frac{dN_{prod}}{dK}(K) = \sum_{\chi\chi\to p_3 p_4} BR(\chi\chi \to p_3 p_4)\left(\frac{dN_{p_3}}{dK}(E_{p_3},K) + \frac{dN_{p_4}}{dK}(E_{p_4},K)\right) , \tag{4.40}$$

where K is the kinetic energy of antiprotons (γ rays).

Noting that the center of mass energy of dark matter annihilation processes is $\sqrt{s} = 2m_\chi$, the energies E_{p_3} and E_{p_4} can be calculated from energy and momentum conservation:

$$\begin{cases} E_{p_3} + E_{p_4} = \sqrt{s} \ , \\ \overrightarrow{p_3} + \overrightarrow{p_4} = \overrightarrow{0} \ , \end{cases} \tag{4.41}$$

which gives

$$\begin{cases} E_{p_3} = \dfrac{\sqrt{s}}{2} + \dfrac{M_3^2 - M_4^2}{2\sqrt{s}} \ , \\ E_{p_4} = \dfrac{\sqrt{s}}{2} + \dfrac{M_4^2 - M_3^2}{2\sqrt{s}} \ , \end{cases} \tag{4.42}$$

where M_3 and M_4 are the outgoing particle masses. In the case $M_3 = M_4$, we retrieve the simple relation $E_{p_3} = E_{p_4} = \frac{\sqrt{s}}{2} = m_\chi$.

One can directly generate the spectra $\frac{dN_p}{dK}(E_p,k)$ using PYTHIA [233, 234]. This work was done in the PPPC4DMID [153, 300] in which one can find tabulated spectra $\frac{dN^{PPPC4DMID}_{\chi\chi\to p\overline{p}}}{dK}(m_\chi = E_p, K)$ giving the flux of antiprotons (γ rays) produced by one annihilation of dark matter particles of a given mass m_χ annihilating via one of the following channels:

$$\chi\chi \to e^+e^-,\ \mu^+\mu^-, \tau^+\tau^-, q\overline{q},\ c\overline{c},\ b\overline{b},,\ t\overline{t},\ W^+W^-,\ gg,\ \gamma\gamma,\ \nu_e\overline{\nu}_e,\ \nu_\mu\overline{\nu}_\mu,\ \nu_\tau\overline{\nu}_\tau \ ,$$

where q stands for light quarks u, d, s.
These channels do not cover all the possible annihilation processes in the MSSM, so they cannot be used directly. However, it is possible to deduce the fluxes produced by the hadronization of a SM particle p with energy E_p from these tabulated spectra.

$$\frac{dN_p}{dK}(E_p,k) = \frac{1}{2}\frac{dN^{PPPC4DMID}_{\chi\chi\to p\overline{p}}}{dK}(m_\chi = E_p, K) \ . \tag{4.43}$$

The spectra for the annihilation into light SM Higgs bosons of mass 125 GeV are also provided, however Higgs branching ratios may suffer from significant corrections in the MSSM. The hadronization spectra of the lightest Higgs boson is therefore re-calculated using the branching ratios computed with HDECAY [202] or FeynHiggs [277]

$$\frac{dN_h}{dK}(E_h,K) = \sum_{h\to p_3 p_4} BR(h\to p_3 p_4)\left(\frac{dN_{p_3}}{dK}(E_{p_3},K) + \frac{dN_{p_4}}{dK}(E_{p_4},K)\right), \tag{4.44}$$

where E_{p_3} and E_{p_4} are calculated from equation 4.42 with $\sqrt{s} = E_h$. The hadronization spectra of heavier Higgs bosons are then calculated in a similar way.

Finally, for the calculation of the neutralino annihilation branching ratios and cross section in the MSSM and NMSSM, we use the routines computing the amplitudes of the annihilations processes of the lightest neutralino into pairs of SM particles $\chi\chi \to p_3 p_4$. These routines were already present in SuperIso Relic package, as they were generated, in the first place, for the calculation of the relic density.
For a Majorana dark matter particle, at small velocity limit, the annihilation cross sections can easily be calculated from these amplitudes, following :

$$\langle\sigma v\rangle_{\chi\chi\to p_3 p_4} = \frac{|\mathscr{A}|^2_{\chi\chi\to p_3 p_4}}{128\pi m_\chi^2}\left[1 - \frac{M_3^2+M_4^2}{2m_\chi^2} + \frac{(M_3^2-M_4^2)^2}{16m_\chi^4}\right]^{\frac{1}{2}}. \tag{4.45}$$

These cross sections were compared to the ones calculated with micrOMEGAs. A very good agreement was found between the two programs when all the mass parameters were set to the same values. We notice, however, that the calculation of the amplitudes are quite sensitive to the value of the electroweak boson masses and of the Weinberg angle.

4.3.2 Constraints from Fermi-LAT dwarf spheroïdal galaxies

We base our analysis of Fermi-LAT dwarf spheroïdal galaxies (dSphs) on [170]. Fermi-LAT collaboration performs a binned Poisson maximum-likelihood analysis in order to deduce dark matter constraints. The energy range is seperated into 24 bins, logarithmically spaced from 500 MeV to 500 GeV. Tabulated log-likelihoods are provided by the collaboration for each dSph and energy bin [171]. These tables allow us to estimate the log-likelihood $\mathscr{L}_j^i$ for a dSph i and energy bin j as a function of the gamma-ray flux produced by dark matter annihilation.
The flux produced by the dark matter halo of a dSph i in the energy bin $\left[E^j_{\min}, E^j_{\max}\right]$ is calculated as

$$\Phi_j^i = \frac{1}{4\pi}\frac{\langle\sigma v\rangle}{2m_{DM}^2} \times J^i \times \int_{E^j_{min}}^{E^j_{max}} \left(\frac{dN_{\text{prod}}}{dE_\gamma}\right)_{\text{channel}} dE_\gamma\,, \tag{4.46}$$

where $\frac{dN_{\text{prod}}}{dE_\gamma}$ is the gamma-ray flux at production calculated as in subsection 4.3.1 and J^i is the J-factor of the dSph defined as $J = \int_{\Delta\Omega}\int_{l.o.s}\rho^2_{DM}(r(l))dl\,d\Omega$ with $\Delta\Omega$ the solid angle under which is seen the dSph. The J-factor of each dSph is either deduced from their observed kinematics or, when no measurements are available, from an empirical law which states that the J-factor scales as the inverse square of the distance of the dSph.

Confidence level / d.o.f.	1σ	80%	90%	95%	2σ	99%	3σ	99.9%	4σ	5σ
1	1	1.64	2.71	3.84	4.00	6.63	9.0	10.83	16.00	25.00
2	2.30	3.22	4.61	5.99	6.18	9.21	11.83	13.82	19.33	28.74
3	3.53	4.64	6.25	7.8	18.02	11.34	14.16	16.27	22.06	31.81
4	4.72	5.99	7.78	9.49	9.72	13.28	16.25	18.47	24.50	34.56
5	5.89	7.29	9.24	11.07	11.31	15.09	18.21	20.52	26.77	37.09

Table 4.1: χ^2 distribution table

In order to calculate the log-likelihood for a given dSph, we sum the log-likelihoods of every energy bins. Then, we add a corrective term to take into account the uncertainties on the J-factor:

$$\mathscr{L}^i(J_i) = \sum_j \mathscr{L}^i_j(J_i) - \frac{\left(log_{10}(J_i) - log_{10}(J_{obs,i})\right)^2}{2\sigma_i^2} \ , \tag{4.47}$$

where J_i is the true value of the J-factor, considered as a nuisance parameter, and $J_{obs,i}$ is the measured J-factor with error σ_i. For each dSph, a maximum log-likelihood is then calculated according to the nuisance parameters. Finally, we sum the maximum log-likelihood of every dSphs.

$$\mathscr{L} = \sum_i \max_{J_i} \mathscr{L}^i(J_i) \tag{4.48}$$

The statistical test we use to draw constraints on dark matter is then calculated by subtracting the log-likelihood in the case where no dark matter is assumed:

$$\mathrm{TS} = 2(\mathscr{L}_{\mathrm{DM}} - \mathscr{L}_{\mathrm{no\,DM}}) \ . \tag{4.49}$$

This quantity follows a normal distribution and we will exclude points with $\mathrm{TS} < \chi_0^2$, where χ_0^2 is a critical value which depends on the desired confidence level and on the number of degree of freedom. These critical values are listed in table 4.1. We chose the number of degree of freedom (d.o.f.) as the number of annihilation channels which contribute at least to 1% of the total annihilation cross section.

As already mentioned, the J-factor of some dSphs are calculated using an empirical relation. In order to assess the uncertainties on the log J-factor, we use 3 different values of σ_i = 0.4, 0.6 or 0.8 dex for the “stringent”, “standard” and “conservative” options.

In addition, three different samples of dSphs are defined in Fermi-LAT analysis: a "conservative", a "nominal" and an "inclusive" sample, depending on the ambiguity of the kinematics of the galaxies. The "conservative" sample does not necessarily leads to a weaker limit compared to the "inclusive" one, as some dSphs in the "nominal" and "inclusive" samples show slight but non-significant excesses. Therefore, the delta log-likelihood is calculated for each sample. Our “conservative” option use the largest delta log-likelihood, the “standard” option, the second largest and the “stringent” option, the smallest.

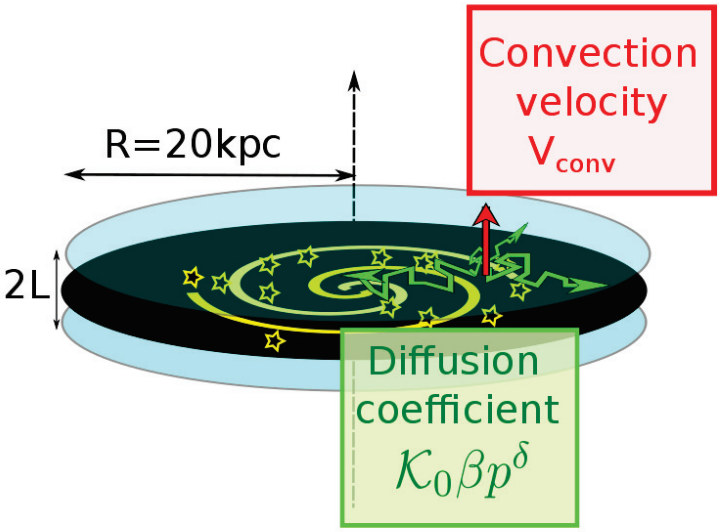

Figure 4.8: Model of propagation: the galactic medium is a thin disk of radius 20 kpc and cosmic rays diffuse within a cylinder of half-height L.

4.3.3 Constraints from AMS-02 antiprotons

Contrary to gamma rays, antiprotons are diffused by turbulent magnetic fields in the galaxy. Therefore, it is necessary to describe the propagation of cosmic rays in the galactic medium in order to deduce the antiproton flux reaching Earth. To this end, I integrated in SuperIso Relic, a code developed by Pierre Salati and Mathieu Boudaud, which is detailed in [154]. The propagation model used in this code is shortly described below. We use a two-zone diffusion model where the galactic medium is a thin disk of $R = 20$ kpc radius and cosmic rays are diffused in a cylinder of half-height $L =$ and radius R (see figure 4.8).
The antiproton spectrum respects the differential equation of propagation:

$$\frac{\partial f}{\partial t} - \mathcal{K}(K)\cdot\nabla^2 f + \frac{\partial}{\partial z}\{\mathrm{sign}(z)\, f\, V_{\mathrm{conv}}\} + \frac{\partial}{\partial E}\left\{b(K,\vec{x})f - \mathcal{K}_{\mathrm{EE}}(K)\frac{\partial f}{\partial E}\right\} = Q\,, \tag{4.50}$$

where $f = \frac{dN}{dK}(r,z,E)$ is the antiproton spectrum at radius r and height z . We assume cylindrical symmetry, which allows us to decompose f into Bessel transforms

$$f(r,z,E) = \sum_{i=1}^{+\infty} F_i(z,E)\, J_0(\alpha_i\, r/R)\,. \tag{4.51}$$

J_0 is the Bessel function of zeroth-order and α_i its i^{th} zero, so that $f(r=R,z,E)=0$. This method allows us to solve semi-analytically the equation of transport, which reduces significantly computation time compared to programs which adopt a full numerical approach such as GALPROP [301].

The first term in the equation of transport 4.50 is set to zero since we only focus on steady-state solutions.

Model	δ	$\mathcal{K}_0$ [kpc^2/Myr]	L [kpc]	V_{conv} [km/s]	V_a [km/s]
MIN	0.85	0.0016	1	13.5	22.4
MED	0.70	0.0112	4	12	52.9
MAX	0.46	0.0765	15	5	117.6

Table 4.2: Benchmark MIN, MED, and MAX sets of propagation parameters [155].

Space diffusion: The second term describes antiproton space diffusion with a coefficient

$$\mathcal{K}(K) = \mathcal{K}_0 \beta p^{\delta}, \tag{4.52}$$

where $\beta = \frac{v}{c}$ is the antiproton beta factor and p its momentum. $\mathcal{K}_0$ and δ are free parameters of the model which set the normalization and momentum dependence of the diffusion coefficient. The third term stands for convection processes, with a characteristic velocity V_{conv} on the outside of the galactic disk. These processes tend to push antiprotons vertically outside the disk.

Energy losses: Then, the term in $b(K,\vec{x})$ accounts for energy losses. Antiprotons undergo energy losses according to three main processes: through the ionization of the interstellar neutral medium, through the scattering off thermal electrons in interstellar ionized matter, and through convective processes. In addition, the inelastic but non-annihilating interactions of antiprotons with the interstellar medium (tertiary component) are treated as in [154].

Diffusive re-acceleration: Finally, the last term on the left-hand side of equation 4.50 describes diffusive re-acceleration. The knots of the turbulent magnetic field can, in fact, drift with a characteristic velocity v_a, which results in a second order Fermi acceleration of antiprotons.

This model presents in total five free parameters whose values can be defined at the convenience of the user. However, the three benchmark propagation models MIN, MED and MAX, which give a minimum, median and maximum antiproton flux at Earth, are directly provided (table 4.2). The term on the right-hand side of equation 4.50 stands for the sources of antiprotons and will be detailed below.

4.3.3.1 Source terms

Secondary antprotons: The astrophysical antiproton background, so-called *secondary antiprotons*, is mostly created through the interaction of proton and helium cosmic rays produced by supernovae with hydrogen and helium atoms in the interstellar medium. This type of antiproton accounts for one part of the source term in the equation of transport 4.50 :

$$Q_{\bar{p}}^{\mathrm{II}}(\mathbf{x},K_{\bar{p}}) = 4\pi(1+N_{\mathrm{IS}}(K_{\bar{p}}))\sum_{i=\mathrm{p,He}}\sum_{j=\mathrm{H,He}} \times \int_{K_i^0}^{+\infty} dT_i \frac{d\sigma_{ij\to\bar{p}X}}{dK_{\bar{p}}}(K_i\to K_{\bar{p}}) n_j(\mathbf{x})\Phi_i(\mathbf{x},K_i)\,, \tag{4.53}$$

where K_i is the kinetic energy of the nucleon i. The differential cross section $d\sigma_{ij\to\bar{p}X}/dK_{\bar{p}}$ is computed from the proton-proton differential cross section taken from [302] and the threshold K_p^0 of this reaction is taken to be $7m_p$.
The factor N_{IS} accounts for the fact that antineutrons are also produced, along with antiprotons, in the interaction of cosmic rays with the interstellar medium. Antineutron consecutively decay into antiprotons and contribute to the source term. Most of the antiprotons are, however, produced in proton-proton reactions.
The flux of proton and helium cosmic rays, at position $\mathbf{x}$, $\Phi_i(\mathbf{x})$ are deduced from the fluxes measured at Earth position through a retropropagation technique.

Primary antiprotons: The production rate $Q_{\bar{p}}^{\mathrm{I}}$ of primary antiprotons produced by the annihilation of two dark matter particles into the channel j is given by the expression (4.54)

$$Q_{\bar{p}}^{\mathrm{I}}(\mathbf{x},K_{\bar{p}}) = \eta\left(\frac{\rho(\mathbf{x})}{m_{\mathrm{DM}}}\right)^2\langle\sigma v\rangle\frac{dN_{prod}}{dK_{\bar{p}}}\,, \tag{4.54}$$

where $\langle\sigma v\rangle$ is the thermal average annihilating cross section, and η is equal to 1/2 (1/4) for a Majorana (Dirac) type particle. $\frac{dN_{prod}}{dK_{\bar{p}}}$ is the flux at production of antiprotons which is calculated as in subsection 4.3.1.

4.3.3.2 Calculation of the constraints

We calculate the total antiproton spectrum at the Earth position as the sum of primary and secondary antiproton contributions.

$$\Phi_{\mathrm{tot}}^{\oplus}(K,\phi_F,A) = \Phi_{\mathrm{I}}^{\oplus}(K,\phi_F) + \Phi_{\mathrm{II}}^{\oplus}(K,\phi_f,A)\,.$$

The parameters A and ϕ_F are nuisance parameters over which we marginalize. They are related respectively to the uncertainties on the antineutron production cross section and to the solar modulation.

Uncertainties on the antineutron production cross section: The parameter N_{IS} which accounts for antineutron production in equation 4.53 is energy-dependent and suffers from large uncertainties [302]. For this reason, we calculate the secondary antiproton spectra for the lower and upper bound of N_{IS}. The real secondary antiproton spectrum takes values between these two bounds, according to a nuisance parameter $A\in[0,1]$

$$\Phi_{\mathrm{II}}(A) = (1-A)\times\Phi_{\mathrm{II}}^{lower} + A\times\Phi_{\mathrm{II}}^{upper}\,. \tag{4.55}$$

Solar modulation: As antiprotons reach the sun vicinity, they enter the sphere of influence of the sun magnetic field and of its cosmic-ray wind. It has for effect to decrease the kinetic energy of antiprotons, especially for low-energetic particles ($\lesssim 10$ GeV). It is therefore necessary to modify the spectrum at the Earth position calculated from the equation of transport. A simple way to do this is to use a force-field approximation parametrized by the Fisk potential ϕ_F [303, 304]:

$$\Phi^{\oplus}(K) = \Phi^0(K + |e|\phi_F) \cdot \frac{K(K+2m_p)}{(K+m_p+|e|\phi_F)^2 - m_p^2}. \tag{4.56}$$

where $\Phi^{\oplus}$ is the antiproton spectrum at Earth and Φ^0 the antiproton spectrum at the end of the propagation but before entering into the solar influence. For AMS-02 data, we take $\phi_F \in [0.1, 1]$.

In order to quantify the deviation of the theoretical spectrum from the antiproton spectrum measured by AMS-02, we calculate a χ^2 as:

$$\chi^2(\Phi^{\oplus}_{\text{tot}}) = \sum_i \left(\frac{\Phi^{\oplus}_{\text{tot}}(E_i) - \Phi^{\oplus}_{AMS-02}(E_i)}{\Delta\Phi^{\oplus}_{AMS-02}(E_i))} \right)^2 , \tag{4.57}$$

where we sum over AMS-02 energy bins, with central values E_i. AMS-02 flux measurement $\Phi^{\oplus}_{AMS-02}$ is given with an error $\Delta\Phi^{\oplus}_{AMS-02}$ [305, 306].
We minimize the χ^2 with respect to the nuisance parameters A and ϕ_F and we compare it to the χ^2 in the case where no dark matter is assumed.

$$\Delta\chi^2 = \min_{A,\phi_F} \{\chi^2(\Phi^{\oplus}_{\text{tot}})\} - \min_{A,\phi_F} \{\chi^2(\Phi^{\oplus}_{\text{noDM}})\} \ . \tag{4.58}$$

The $\Delta\chi^2$ thus obtained follows a normal distribution. For instance, if only one annihilation channel is dominant (1 d.o.f.), a point will be excluded at 2 σ if $\Delta\chi^2 > 4$.

The computation of antiproton primary and secondary spectra can be time-consuming when performing large scans. This is the reason why we also provide tabulated spectra for the benchmark sets of propagation parameters MIN, MED, MAX, and the three DM halo profiles used in chapter 3: Burkert, Einasto and NFW. Following our previous study, the "conservative" constraint is given by Burkert MED, the "standard" by Einasto MED and the "stringent" Einasto MAX.
However, the user is completely free to define its own propagation parameters and DM density profile, as long as it respects axisymmetry. The constraints can, in this way, be calculated directly for the new sets of parameters. If the user wishes to perform large scans, we advise, nevertheless, to generate tabulated spectra of primary and secondary antiprotons using the dedicated function in SuperIso Relic.

Part III

Relic density in alternative cosmological scenario

CHAPTER 5

DARK MATTER CASTS LIGHT ON THE EARLY UNIVERSE

5.1 Introduction

In this chapter, we show that the discovery of new particles at colliders could allow us to probe the content of the Universe at an epoch which is currently beyond observational reach. Indeed, before BBN, the Universe is assumed to be radiation dominated in the standard cosmological model. However, this assumption is not well justified, and it is possible to consider alternative scenarios which alter the dark matter relic density. In this study, we consider two alternative scenarios involving the presence of a scalar field before BBN and show their influence on different new physics scenarios. We focus on scenarios including a WIMP which has a relic density calculated in the standard cosmological model either too small or too large. We show that, in order to obtain the correct relic density, strong constraints must be imposed on the scalar field properties. Two benchmark points in the MSSM will be considered for this analysis and we will use a pMSSM-19 sample of points to assess the dependence of the scalar field constraints on the WIMP properties. This work was carried out in collaboration with Prof. Alexandre Arbey, Prof. John Ellis and Prof. Nazila Mahmoudi and is submitted to JHEP [307].

5.2 Relic density calculation

The relic density calculation is generally performed in the standard cosmological model, in which the expansion rate of the Universe is given by the Friedmann equation. In the early Universe when the radiation density dominates this reduces to:

$$H^2 = \left(\frac{\dot{a}}{a}\right)^2 = \frac{8\pi G}{3}\rho_{rad} \,, \tag{5.1}$$

where a is the cosmological scale factor and H the Hubble parameter. The radiation density reads

$$\rho_{rad}(T) = g_{\text{eff}}(T)\frac{\pi^2}{30}T^4 \,, \tag{5.2}$$

where $g_{\rm eff}$ is the effective number of degrees of freedom of radiation, which is given by the particle content of the Standard Model and the QCD equation of state (see, for example, [137, 139]).
Assuming that, in a given BSM scenario, only the lightest BSM particle is stable, and constitutes a suitable dark matter candidate that was originally in thermal equilibrium, the number of relic particles is obtained by solving the Boltzmann evolution equation [308, 309]:

$$dn/dt = -3Hn - \langle\sigma_{\rm eff} v\rangle (n^2 - n_{\rm eq}^2) \,, \tag{5.3}$$

where n is the number density of BSM particles, $n_{\rm eq}$ is their equilibrium density, and $\langle\sigma_{\rm eff} v\rangle$ is the thermal average of the annihilation rate of pairs of BSM particles to SM particles.
To define $\langle\sigma_{\rm eff} v\rangle$, it is useful to define first the annihilation rate of BSM particles i and j into SM particles k and l:

$$W_{ij\to kl} = \frac{p_{kl}}{16\pi^2 g_i g_j S_{kl}\sqrt{s}} \sum_{\text{internal d.o.f.}} \int |\mathscr{M}(ij\to kl)|^2 \, d\Omega \,, \tag{5.4}$$

where $\mathscr{M}$ is the transition amplitude, s is the centre-of-mass energy squared, g_i is the number of degrees of freedom of the particle i, p_{kl} is the final centre-of-mass momentum, given by

$$p_{kl} = \frac{\left[s-(m_k+m_l)^2\right]^{1/2}\left[s-(m_k-m_l)^2\right]^{1/2}}{2\sqrt{s}} \,, \tag{5.5}$$

and S_{kl} is a symmetry factor equal to 2 for identical final particles and to 1 otherwise.
The thermal average of the effective cross section is given by:

$$\langle\sigma_{\rm eff} v\rangle = \frac{\displaystyle\int_0^\infty dp_{\rm eff} p_{\rm eff}^2 W_{\rm eff}(\sqrt{s}) K_1\left(\frac{\sqrt{s}}{T}\right)}{m_{relic}^4 T\left[\displaystyle\sum_i \frac{g_i}{g_{LSP}}\frac{m_i^2}{m_1^2} K_2\left(\frac{m_i}{T}\right)\right]^2} \,, \tag{5.6}$$

where K_1 and K_2 are the modified Bessel functions of the second kind of order 1 and 2 respectively, and $W_{\rm eff}$ is an effective annihilation rate:

$$W_{\rm eff} \equiv \frac{1}{g_{relic}^2 p_{\rm eff}} \sum_{ij} g_i g_j p_{ij} W_{ij} \,, \tag{5.7}$$

with

$$p_{\rm eff}(\sqrt{s}) = \frac{1}{2}\sqrt{(\sqrt{s})^2 - 4m_{relic}^2} \,, \tag{5.8}$$

In order to solve the Boltzmann equation, it is necessary to have a link between time and temperature, which is given under the assumption of adiabaticity by

$$\frac{ds_{rad}}{dt} = -3Hs_{rad} \,, \tag{5.9}$$

where the radiation entropy density is given by

$$s(T) = h_{\rm eff}(T)\frac{2\pi^2}{45}T^3 \,, \tag{5.10}$$

with $h_{\rm eff}$ the effective number of entropic degrees of freedom of radiation.

To solve this set of equations, one defines the ratio of the number density of BSM particles to the radiation entropy density $Y(T) \equiv n(T)/s_{rad}(T)$, and the ratio of the relic particle mass to the temperature, $x \equiv m_{relic}/T$, and combines them into [308, 309]:

$$\frac{dY}{dx} = -\sqrt{\frac{\pi}{45G}} \frac{g_*^{1/2} m_{relic}}{x^2} \langle \sigma_{\text{eff}} v \rangle (Y^2 - Y_{\text{eq}}^2) \,, \tag{5.11}$$

with

$$g_*^{1/2} = \frac{h_{\text{eff}}}{\sqrt{g_{\text{eff}}}} \left(1 + \frac{T}{3h_{\text{eff}}} \frac{dh_{\text{eff}}}{dT} \right) . \tag{5.12}$$

The freeze-out temperature T_f is the temperature at which the relic particle leaves the initial thermal equilibrium, which is expected to happen at $\sim m_{relic}/10 \sim 10 - 100$ GeV in many BSM WIMP scenarios.

Solving the equations down to the present temperature T_0, we find that Y approaches a constant asymptotic value and the relic density so obtained is [308, 309]:

$$\Omega_{relic} h^2 = \frac{m_{relic} s(T_0) Y(T_0) h^2}{\rho_c^0} \approx 2.755 \times 10^8 \frac{m_{relic}}{1 \text{ GeV}} Y(T_0) \,, \tag{5.13}$$

where ρ_c^0 is the critical density of the Universe, given by

$$H_0^2 = \frac{8\pi G}{3} \rho_c^0 \,, \tag{5.14}$$

and H_0 is the Hubble constant. The relic density can then be compared to the measurements of the dark matter density by the Planck Collaboration [22] to set constraints on the BSM scenarios. In the following, we use `SuperIso Relic v4.0` [132, 133, 262] to compute the relic density. Since it was shown that the theoretical uncertainties due to the cross section calculation at tree level and to the uncertainties in the QCD equation of state are of the order of a tenth [134, 136, 137, 139, 144, 149], we add a 10% theoretical error to the Planck measurements and obtain the following 95% C.L. interval:

$$0.095 < \Omega h^2 < 0.1428 \,. \tag{5.15}$$

5.3 Cosmological scenarios

The standard relic density calculation can be modified by the presence of scalar fields in the early Universe, which can affect the expansion rate by adding a new energy density, generate non-thermal relic particles, or inject entropy and affect the relation between time and temperature. In the following, we consider the case of a decaying pressureless scalar field and of quintessence as realistic examples of cosmological models affecting the early Universe. Since the freeze-out occurs at $\sim 10 - 100$ GeV, a large deviation from the standard model of cosmology at this temperature could modify strongly the results, without having other consequences for the observable Universe. The strongest constraints that can be set on such cosmological scenarios are those from BBN. In the following, we compute BBN constraints for the scenarios of interest using `AlterBBN v2.0` [310, 311] and the conservative limits on the abundances of the elements given in [312].

5.3.1 Decaying primordial scalar field

We consider a pressureless scalar field ϕ of mass m_ϕ that decays into radiation with a width Γ_ϕ, and into BSM particles with a branching ratio b [148, 313]. The evolution in time of the scalar field density ρ_ϕ and the WIMP density $n = \rho_\chi/m_\chi$ can be determined from the following equations:

$$\frac{d\rho_\Phi}{dt} = -3H\rho_\Phi - \Gamma_\Phi\rho_\Phi \,, \tag{5.16}$$

$$\frac{dn}{dt} = -3Hn - \langle\sigma v\rangle\left(n^2 - n_{eq}^2\right) + \frac{b}{m_\phi}\Gamma_\Phi\rho_\Phi \,, \tag{5.17}$$

where $\langle\sigma v\rangle$ is the thermally-averaged WIMP annihilation cross section, n_{eq} is the WIMP equilibrium density, and H is the Hubble parameter, which depends on the total energy density in the Universe:

$$H^2 = \frac{8\pi}{3M_p^2}\left(\rho_\phi + \rho_{rad} + \rho_\chi\right) \,. \tag{5.18}$$

We assume that the thermalisation of the decay products of the scalar field occurs instantaneously*. In order to obtain a relation between the time and the temperature, one may use the following equation for the evolution of the radiation entropy density [316]:

$$\frac{ds_{rad}}{dt} = -3Hs_{rad} + \frac{\Gamma_\Phi\rho_\Phi}{T} = -3H\left(1 - \widetilde{\Sigma}^*\right)s_{rad} \,, \tag{5.19}$$

with

$$\widetilde{\Sigma}^* \equiv \frac{\Gamma_\Phi\rho_\Phi}{3HTs_{rad}} \,. \tag{5.20}$$

The energy and entropy densities of radiation can be determined from the temperature according to:

$$\begin{cases} \rho_{rad} = \dfrac{\pi^2}{30}g_{eff}(T)T^4 \,, \\ s_{rad} = \dfrac{2\pi^2}{45}h_{eff}(T)T^3 \,, \end{cases} \tag{5.21}$$

where g_{eff} and h_{eff} are the number of degrees of freedom of radiation energy and the entropy, respectively. We use the QCD equation of state "B" of Ref. [137] in our analysis.
The decay width may conveniently be expressed as a function of the reheating temperature T_{RH} [148, 313], which is the temperature at which the scalar field density starts to be significantly reduced:

$$\Gamma_\phi = \sqrt{\frac{4\pi^3 g_{eff}(T_{RH})}{45}}\,\frac{T_{RH}^2}{M_p} \,. \tag{5.22}$$

We also define $\tilde{\rho}_\phi \equiv \rho_\phi/\rho_{rad}$ and the initial condition $\kappa_\phi \equiv \rho_\phi(T_{init})/\rho_\gamma(T_{init})$.
In the following we assume that the period of interest for the relic density occurs when the radiation entropy density decreases with time, which corresponds to $\widetilde{\Sigma}^* < 1$. This imposes a maximal temperature $T_{\max}$ for the validity of the following discussion, which corresponds to the temperature at which $\widetilde{\Sigma}^* = 1$. The above equations can be re-written as derivatives of $Y_\Phi = \rho_\phi/s_{\rm rad}$ and

*Discussions of the effect of other thermalisation assumptions can be found in [314, 315].

$Y = n/s_{\rm rad}$:

$$\frac{dY_\Phi}{dx} = -\frac{\alpha_0}{x}\frac{\widetilde{\Sigma}^*}{1-\widetilde{\Sigma}^*}\left(Y_\Phi + \frac{m_\chi}{x}\right) , \tag{5.23}$$

$$\frac{dY}{dx} = -\frac{\alpha_0}{x}\frac{s_{\rm rad}}{1-\widetilde{\Sigma}^*}\frac{1}{3H}\langle\sigma v\rangle\left(Y^2 - Y_{eq}^2\right) - \frac{\alpha_0}{x}\frac{\widetilde{\Sigma}^*}{1-\widetilde{\Sigma}^*}\left(Y - \frac{b}{m_\phi}\frac{m_\chi}{x}\right) , \tag{5.24}$$

with

$$\alpha_0 = \frac{3g_*^{1/2}g_{eff}^{1/2}}{h_{eff}} \approx 3 , \tag{5.25}$$

where $x = m_\chi/T$.

Eqs. (5.23) and (5.24) are controlled by the parameter $\widetilde{\Sigma}^*$ defined in Eq. (5.20). In order to understand its role, we consider the entropy time-derivative equation (5.19) in the case where $\widetilde{\Sigma}^*$ is constant. If $T \propto t^\alpha$ and the scale factor $a \propto t^\beta$, then $H = \beta t^{-1}$ and we obtain:

$$3\alpha = -3\beta(1-\widetilde{\Sigma}^*) . \tag{5.26}$$

Thus, $\beta = -\alpha/(1-\widetilde{\Sigma}^*)$ and $a \propto t^{-\alpha/(1-\widetilde{\Sigma}^*)} \propto T^{-1/(1-\widetilde{\Sigma}^*)}$. After freeze-out, the WIMP density verifies $\rho_\chi \propto a^{-3}$, so $\rho_\chi \propto T^{3/(1-\widetilde{\Sigma}^*)}$. The WIMP density will therefore be diluted very fast as $\widetilde{\Sigma}^* \to 1$. In fact, one can derive a maximum value for $\widetilde{\Sigma}^*$ where $d\log(\widetilde{\Sigma}^*)/d\log(x) = 0$. In the limit $\rho_\phi \gg \rho_{\rm rad}$, $\widetilde{\Sigma}^* \propto x^{5/2}Y_\Phi^{1/2}$ according to Eq. (5.22). Thus the maximum value of $\widetilde{\Sigma}^*$ is reached when $d\log(Y_\Phi)/d\log(x) = -5$. Using Eq. (5.23) we obtain the condition

$$-\alpha_0\frac{\widetilde{\Sigma}^*_{\rm MAX}}{1-\widetilde{\Sigma}^*_{\rm MAX}}\left(1+\frac{T}{Y_\Phi}\right) = \frac{d\log(Y_\Phi)}{d\log(x)} = -5 , \tag{5.27}$$

from which it follows that

$$\frac{\widetilde{\Sigma}^*_{\rm MAX}}{1-\widetilde{\Sigma}^*_{\rm MAX}} = \frac{5}{\alpha_0}\frac{1}{1+\frac{T}{Y_\Phi}} < \frac{5}{\alpha_0} \lesssim 1.66 , \tag{5.28}$$

which leads to

$$\widetilde{\Sigma}^* < \frac{5}{\alpha_0}\frac{1}{1+\frac{5}{\alpha_0}} \approx 0.625 . \tag{5.29}$$

This prevents any singularities in the term $\widetilde{\Sigma}^*/1-\widetilde{\Sigma}^*$, but limits the strength of the dilution.
We have seen that the scalar field density can decrease in two ways: either by decay, or by dilution. Thus, the presence of the scalar field may modify the WIMP relic density from that calculated in the standard model of cosmology in three different ways. First, WIMPs can be diluted in the same way as the scalar field. As this phenomenon only changes the evolution of the temperature with time, it does not affect the WIMP density at a given temperature during thermal equilibrium, since the equilibrium density is determined by the temperature alone. Secondly, if the scalar field decays into BSM particles, the WIMP density may increase. If the decay happens before freeze-out, however, the decay products will annihilate and there would be no consequence on the relic density.
Thirdly, if the scalar field density is large enough, it will change significantly the Hubble parameter and the freeze-out will occur sooner, thus increasing the density at freeze-out compared to the standard calculation. However, as we shall see, this last case corresponds also to that where dilution is important. Therefore, the only way to increase the relic density is if the scalar field decays also into BSM particles.

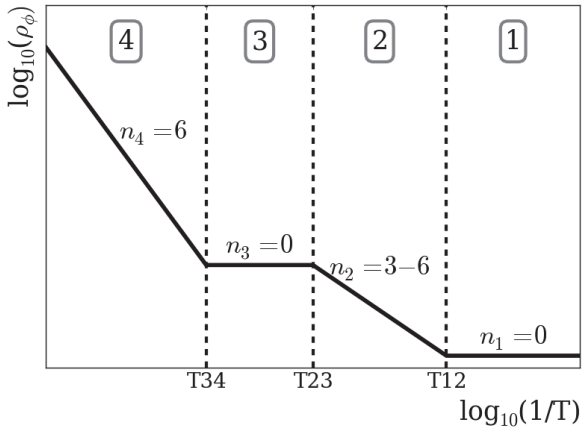

Figure 5.1: *Evolution with temperature of the scalar field density in representative power-law models of quintessence.*

5.3.2 Quintessence

As an alternative, we also consider a quintessence field[†], which satisfies the continuity equation:

$$\frac{d\rho_\Phi}{dt} = 3H(\rho_\Phi + P_\phi)\,, \tag{5.30}$$

where the pressure and the energy density of the scalar field are $P_\phi = \dot{\phi}^2/2 - V(\phi)$ and $\rho_\Phi = \dot{\phi}^2/2 + V(\phi)$, respectively.

We have computed the scalar field density evolution with the temperature for three different standard quintessence potentials $V(\phi)$ [317]: a double exponential [318], an inverse power law [319], and a pseudo-Nambu-Goldstone boson potential [320]. We find that the scalar field density can be well approximated for the three potentials with a power law of slope 6 at high temperatures (zone 4 of Figure 5.1) and of slope 0 at low temperatures coinciding with the measured dark energy density (zone 1). In the case of the double exponential potential, two additional power-law changes occur: the first to a slope 0 (zone 3) and then to a slope ranging from 3 to 6 (zone 2). Hence, we consider a simplified model whose free parameters are the temperatures T_{34}, T_{23}, T_{12} at which the power-law changes occur, together with the slope in zone 2, n_2.

In this model, there is no way to reduce the relic density compared to the standard cosmological model. The only possible influence of the scalar field is the WIMP density at freeze-out. If the scalar field density is large enough while the WIMP is in thermal equilibrium, the Hubble parameter can be enhanced compared to the standard cosmological model. This would have the effect of advancing freeze-out and thereby increasing the relic WIMP density.

5.4 New physics scenarios

In order to illustrate the possible implications of such cosmological scenarios, we consider variants of the minimal supersymmetric extension of the Standard Model (MSSM) with CP and R-

[†]See, for example, [317] for a review of quintessence models.

parity conservation, which is representative of a large class of WIMP models. The lightest neutralino is a well-motivated candidate for dark matter [321], and we assume in the following that 100% of cold dark matter is composed of neutralinos. The neutralino can be bino-like, wino-like, higgsino-like or a mixed state. These candidates are weakly-interacting, and in conventional calculations bino-like neutralinos have in general a too large a relic density, apart in cases where they are associated with near-degenerate supersymmetric particles with which they can coannihilate, or if annihilations are enhanced by resonances such as heavy Higgs bosons. Winos and Higgsinos can reach a relic density close to the observed dark matter abundance via coannihilations with charginos and/or neutralinos that are nearly degenerate with the lightest neutralino. On the other hand, light winos and Higgsinos generally have too small a relic density.

In the following we first choose as specific examples one MSSM scenario which would yield overdense DM according to the standard cosmological calculation, and one that would yield underdense DM. We also consider a sample of points in the phenomenological MSSM (pMSSM) with 19 free parameters specified at a low energy scale (the pMSSM19).

5.4.1 Benchmark Point A

We first consider a point with a relic density that would be too large (Point A) according to the standard cosmological calculation. For this we modify the parameters of the best-fit point of the pMSSM with 11 free parameters specified at a low energy scale (the pMSSM11), which was found in [322] taking into account the constraints from ~ 36 fb^{-1} of LHC data at 13 TeV, including those from direct searches for supersymmetric (SUSY) particles at the LHC, measurements of the Higgs boson mass and signal strengths, LHC searches for the heavier MSSM Higgs bosons, precision electroweak observables, the measurement of $(g-2)_\mu$ [323], and flavour physics constraints from B- and K-physics observables. In addition, the constraints from the direct dark matter detection experiments PICO60 [72], XENON1T [63] and PandaX-II [68] were taken into account, together with the previous accelerator and astrophysical measurements. The cosmological constraint on the cold dark matter density measured by Planck [22] was also considered. The relic density at this point is therefore close to the measured dark matter density, but it is possible to increase the relic density while respecting the other constraints. This point has a bino-like neutralino of mass 381 GeV. As commented above, binos tend to have a relic density that is too large. However, thanks to the small mass splittings with the sleptons of the first and second generations, the relic density of this points is very close to the measured dark matter density. In order to obtain a larger relic density, we increase the mass parameter $M_{\tilde{l}_{1,2}}$ of the sleptons of first and second generation, taking $M_{\tilde{l}_{1,2}} = 400$ GeV. The mass of the lightest neutralino is 381 GeV and the next-to-lightest supersymmetric particles are the right-handed selectron and smuon of mass 423 GeV. The mass splitting is large enough so that the impact of the co-annihilations is limited. We obtain a relic density $\Omega h^2 = 1.27$ according to the standard cosmological calculation, and a freeze-out temperature $T_{\rm fo} \approx 16$ GeV. The parameters of Point A are given in Table 5.1 and the spectrum is generated with `SOFTSUSY` [123].

M_1	M_2	M_3	μ	M_{A^0}	$\tan\beta$
-391	1240	-1714	-5739	4221	18.8

$M_{\tilde{q}_{1,2}}$	$M_{\tilde{q}_3}$	$M_{\tilde{l}_{1,2}}$	$M_{\tilde{l}_3}$	A_0
1996	4058	400	1365	5372

Table 5.1: *The pMSSM11 parameter values (in GeV) of Point A.*

5.4.2 Benchmark Point B

In this case we modify the best-fit point in the constrained MSSM (CMSSM) found in [322]. This point has a higgsino-like neutralino and a relic density close to the dark matter density measured by Planck. We decrease M_{12} to 3872 GeV in order to get a lower value of the relic density: $\Omega h^2 = 5.907 \times 10^{-3}$ and use `SOFTSUSY` [123] to calculate the spectrum. The parameters of point B are given in Table 5.2.

M_0	M_{12}	$\tan\beta$	A_0	sign(μ)
10931	3872	52.9	9188	+1

Table 5.2: *The CMSSM parameter values (in GeV when applicable) of Point B.*

5.4.3 Sample of pMSSM19 Points

We consider in addition a sample of points in the pMSSM19 generated using `SOFTSUSY` [123] with a flat random sampling over the ranges given in Table 5.3 for the 19 parameters. After checking the theoretical validity of each point, we require it to have a light Higgs boson with mass between 122 and 128 GeV. We also require the lightest neutralino to be the lightest supersymmetric particle that constitutes dark matter, using the set-up presented in [120, 124, 125]. As the neutralino can be bino-like, wino-like, Higgsino-like or a mixed state, this approach allows considerable flexibility, making our analysis sufficiently general that it can indicate the possibilities also in other dark matter models.

5.5 Results

5.5.1 Decaying primordial scalar field

We consider first the cosmological scenario with a scalar field decaying into radiation and SUSY particles. We perform a scan over the reheating temperature T_{RH} and the initial scalar field density parametrised as the ratio between the scalar field density and the photon density at $T = T_{\rm init}$, $\kappa_\phi = \frac{\rho_\phi}{\rho_\gamma}(T = T_{\rm init})$, and calculate the relic density of Points A and B specified in Section 4. We consider different values of the parameter $\eta = b\left(\frac{1\ \text{GeV}}{m_\phi}\right)$, in order to study the effect of non-thermal production of SUSY particles on the relic density. In each case we derive constraints on the scalar field parameters for our sample of pMSSM19 points so as to investigate the influence of the neutralino properties on the limits derived from the relic DM density.

Parameter	Range (in GeV)
M_A	[50, 2000]
M_1	[-3000, 3000]
M_2	[-3000, 3000]
M_3	[50, 3000]
$A_d = A_s = A_b$	[-10000, 10000]
$A_u = A_c = A_t$	[-10000, 10000]
$A_e = A_\mu = A_\tau$	[-10000, 10000]
μ	[-3000, 3000]
$M_{\tilde{e}_L} = M_{\tilde{\mu}_L}$	[0, 3000]
$M_{\tilde{e}_R} = M_{\tilde{\mu}_R}$	[0, 3000]
$M_{\tilde{\tau}_L}$	[0, 3000]
$M_{\tilde{\tau}_R}$	[0, 3000]
$M_{\tilde{q}_{1L}} = M_{\tilde{q}_{2L}}$	[0, 3000]
$M_{\tilde{q}_{3L}}$	[0, 3000]
$M_{\tilde{u}_R} = M_{\tilde{c}_R}$	[0, 3000]
$M_{\tilde{t}_R}$	[0, 3000]
$M_{\tilde{d}_R} = M_{\tilde{s}_R}$	[0, 3000]
$M_{\tilde{b}_R}$	[0, 3000]
$\tan\beta$	[1, 60]

Table 5.3: *The pMSSM19 parameter ranges used in our scan.*

We start integrating the Boltzmann equations at a temperature $T_{\rm init}$ = 40 GeV for point A and $T_{\rm init}$ = 20 GeV for point B. For our sample of pMSSM19 points, we use $T_{\rm init} = 1.5 \times T_{\rm fo}$, where $T_{\rm fo}$ is the freeze-out temperature in the standard cosmological model. These choices were made in order to reduce the computation time while starting the calculation sufficiently long before freeze-out and the decay of the scalar field.

5.5.1.1 Point with a large relic density

We first investigate the case where the neutralino has a relic density that is too large in the standard cosmological model, illustrated by Point A. The results of the scan over the reheating temperature T_{RH} and the initial scalar field density κ_ϕ are shown in Figure 5.2, assuming that the scalar field does not decay into SUSY particles ($\eta = 0$). We can distinguish two zones in this figure: a zone at large initial scalar field density and small reheating temperature, where the relic density is strongly reduced, and the complementary zone where the presence of the scalar field does not modify the relic density. On the one hand, the dependence on κ_ϕ of the dilution is rather clear: the larger κ_ϕ is, the larger $\widetilde{\Sigma}^*$ is initially, and the dilution is stronger. On the other hand, the value of the reheating temperature affects more the duration of the dilution than its strength. As illustrated in Figure 5.3, when T_{RH} is small, $\widetilde{\Sigma}^*$ can remain at its maximum during a large

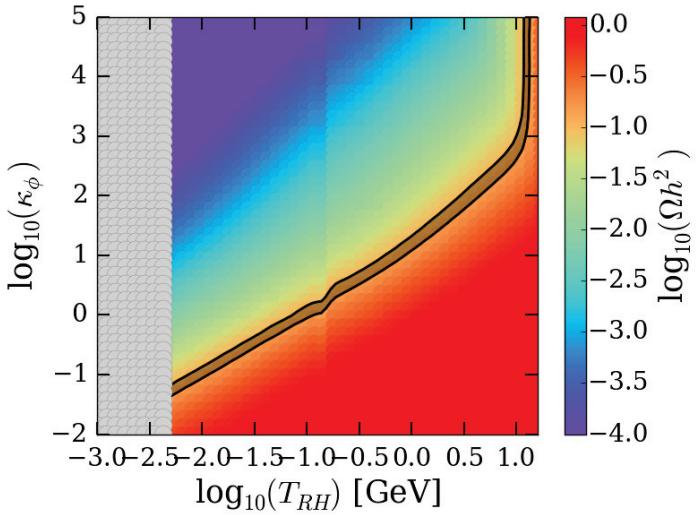

Figure 5.2: *The relic density* $\log_{10}(\Omega h^2)$ *of Point A, indicated by the colour code in the legend, as a function of* T_{RH} *and* κ_ϕ*. Parameter sets consistent with the Planck constraints lie along the darker shaded strip. The grey zone at small* T_{RH} *is excluded by BBN constraints.*

range of temperatures before its decrease due to the decay of the scalar field. The neutralino and scalar field densities decrease during this period with a slope −5, as expected when $\widetilde{\Sigma}^*$ is at its maximum. For a large value of T_{RH}, however, the fields are diluted over a smaller range of temperatures and the total decrease is reduced.

Points respecting the Planck constraints, which we will refer to as *accepted points*, lie along a thin line in the $\log_{10}(\kappa_\phi)$/$\log_{10}(T_{RH})$ plane. They follow a line of slope ~ 1 at small T_{RH} that changes slightly at $T_{RH} \sim 150$ MeV to a slope 1.5. This transition is the result of the quark/hadronic phase transition, which lowers the number of radiation degrees of freedom. In particular, below $T \sim 150$ MeV, pions become non-relativistic and no longer contribute to the radiation density. This feature is independent of the WIMP and scalar field properties, and is present in all the following results. The line of accepted points becomes vertical at $T_{RH} \sim T_{\rm fo}$, which is to be expected when the scalar field decays completely during neutralino thermal equilibrium, as there is no possible modification of the relic density. Thus, we can derive a maximum value of the reheating temperature $T_{RH} \lesssim T_{\rm fo}$. One can also note that if $T_{RH} < T_{RH}^{\rm BBN\,lim} \sim 6$ MeV, the scalar field density is too large during BBN, and the model is therefore excluded. This constraint is very general, as it is also independent of the WIMP properties, and thus applicable to any WIMP model. This limit gives us a lower bound for the reheating temperature, as well as a minimum value for the initial scalar field density κ_ϕ using $T_{RH} = T_{RH}^{\rm BBN\,lim}$. For Point A, we can deduce $\kappa_\phi \gtrsim 0.1$, but this minimum value will depend on the nature of the WIMP.

No enhancement of the relic density is possible when $\eta = 0$. At small T_{RH} and large κ_ϕ, where the scalar field density could have increased the freeze-out temperature via its relation with the Hubble parameter, and thereby increased the relic density, the densities are in fact already significantly reduced by dilution. Therefore, in order to increase the relic density, it is necessary to consider non-thermal production of the WIMP, i.e., $\eta > 0$. In the case of Point A, the region of

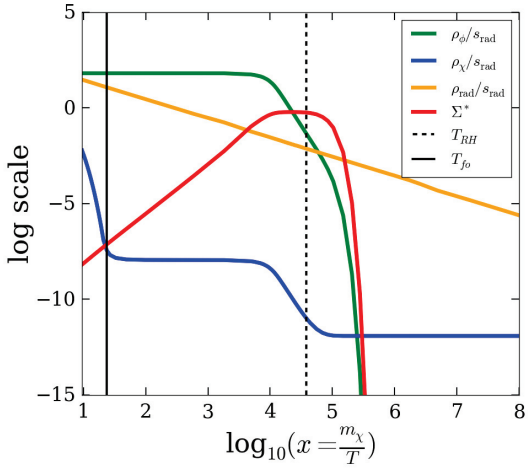

[$T_{RH} = 0.01$ GeV, $\kappa_\phi = 100$, $T_{\rm init} = 40$

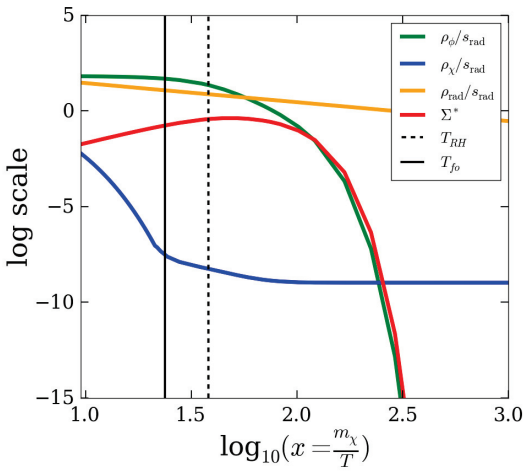

[$T_{RH} = 10$ GeV, $\kappa_\phi = 100$, $T_{\rm init} = 40$ GeV]

Figure 5.3: *The evolution of the scalar field, neutralino and radiation densities normalised to the radiation entropy density, and of the injection of entropy $\widetilde{\Sigma}^*$, as a function of $x = m_\chi/T$.*

interest will be at small T_{RH} and large κ_ϕ, where the relic density is strongly reduced by dilution. The scalar field decay into SUSY particles provides an additional contribution to the relic density, and the DM density measured by Planck may be reached with the appropriate value of η. We test four different values of η in Figure 5.4, and notice that the larger η is, the more the line of accepted points is shifted towards small T_{RH}.

We observe in Figure 5.5 that in the region of interest the relic density increases linearly with η and T_{RH}, which explains the observed feature. Similarly to what happens with the dilution, the parameter η impacts the strength of the non-thermal production of neutralinos, while T_{RH} impacts the time between the freeze-out and the scalar field decay, during which the relic density can benefit from this new contribution.

In the limit of large κ_ϕ and small T_{RH}, we find that the evolution of the relic density with respect to η and T_{RH} can be approximated by:

$$\Omega h^2 \approx \eta\,(\alpha\, T_{RH} + \beta)\,, \tag{5.31}$$

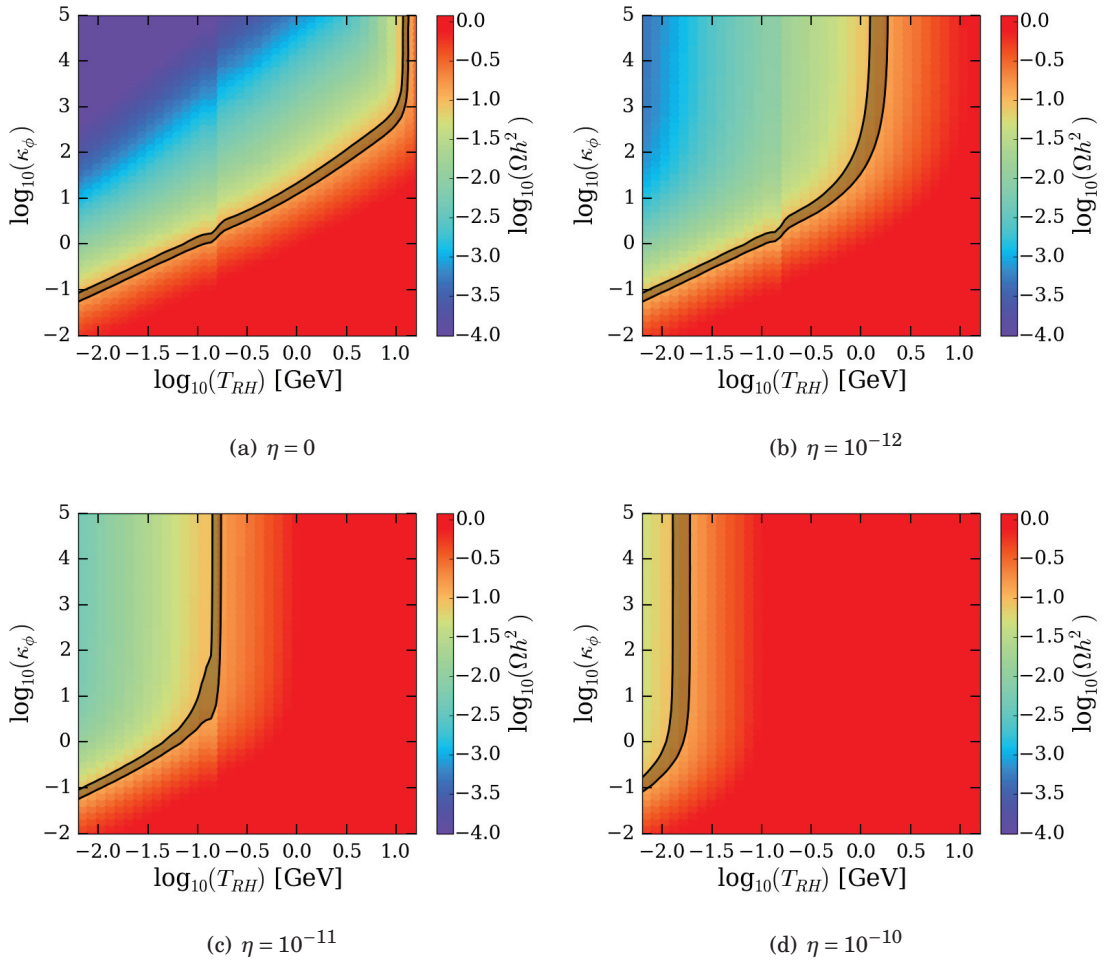

(a) $\eta = 0$ (b) $\eta = 10^{-12}$

(c) $\eta = 10^{-11}$ (d) $\eta = 10^{-10}$

Figure 5.4: *The effect of varying* η *on* $\log_{10}(\Omega h^2)$ *for Point A, indicated by the colour code in the legend.*

where α and β are numerical factors that depend, *a priori*, on the WIMP properties. When η goes to zero, the relic density vanishes, which is expected since, in this region of the parameter space, the dilution due to the entropy injection is dominant in absence of non-thermal production. One can also note that the effects of the dilution and of the non-thermal production equilibrate in such a way that the above expression does not depend on κ_ϕ. For Point A, we find that $\alpha \approx 7.68 \times 10^{10}$ GeV^{-1} and $\beta \approx 2.62 \times 10^{7}$. This parametrisation enables us to find the value of η required to get the correct relic density for a given reheating temperature. On the other hand, a maximum value of η can be calculated by considering the reheating temperature where the BBN constraints start excluding the model ($T_{RH}^{\rm lim} \approx 6 \times 10^{-3}$ GeV):

$$\eta_{\rm Max} = \frac{\Omega h^{2\,\rm upper\,lim}_{\rm DM}}{\alpha T_{RH}^{\rm lim} + \beta} \,. \tag{5.32}$$

For our benchmark point, we calculate $\eta_{\rm Max} \approx 2.93 \times 10^{-10}$. Thus, in this scenario the branching ratio into SUSY particles must be very small, which can be traced back to our choice of a scalar field with a substantial initial density. We note also that the variation in η does not modify the

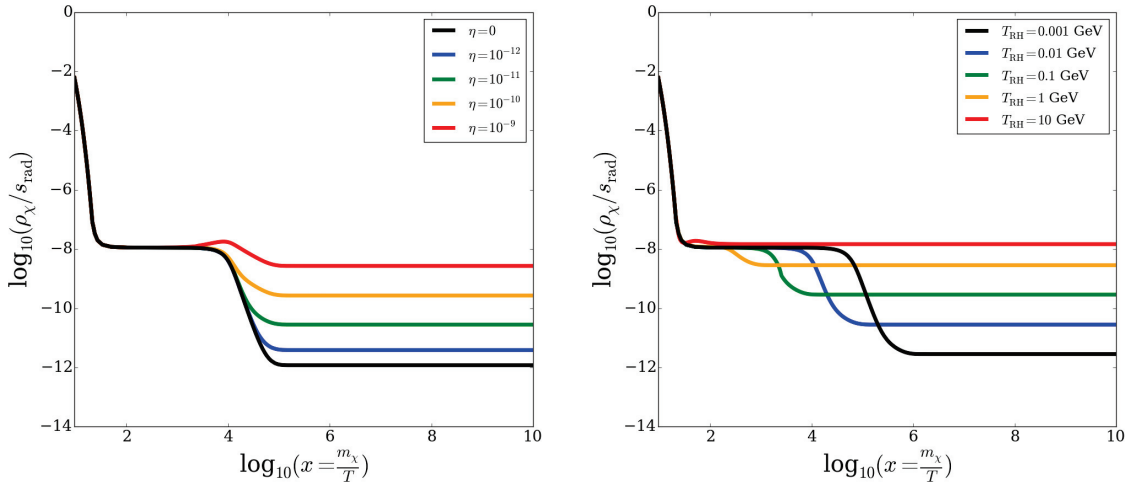

(a) (b)

Figure 5.5: *The variation of the relic density normalised to the radiation entropy density as a function of the temperature, for* $T_{\rm init} = 40$ *GeV and* $\kappa_\phi = 100$*, when (a) varying the value of* η *with fixed* $T_{RH} = 0.01$ *GeV, and (b) varying the value of* T_{RH} *with fixed* $\eta = 10^{-11}$.

constraints on κ_ϕ and T_{RH} that we derived in the case $\eta = 0$. Strong constraints on the scalar field parameters can therefore be derived, namely 6 MeV $\lesssim T_{RH} \lesssim T_{\rm fo}$, $\kappa_\phi \gtrsim 0.1$ and $\eta \lesssim 2.93 \times 10^{-10}$.

5.5.1.2 Point with a small relic density

As discussed previously, no enhancement of the relic density is possible when only entropy injection is considered. Therefore, one needs to allow the scalar field to decay into BSM particles. We show in Figure 5.6 the result of scans over T_{RH} and κ_ϕ for Point B with four different values of η. In each scenario, the region of accepted points forms a U shape in the κ_ϕ /T_{RH} plane. The vertical right limit corresponds to $T_{RH} \sim T_{\rm fo}$, and does not move significantly as η increases. The vertical left limit, however, is shifted to the left along the T_{RH} axis and the horizontal limit is shifted downwards towards lower values of κ_ϕ. The constraints on T_{RH} that we deduced for point A hold also in this case: $T_{RH}^{\rm BBN\,lim} \lesssim T_{RH} \lesssim T_{\rm fo}$. However, it is difficult to find limits on κ_ϕ and η as stringent as the ones we found for point A.
The largest effect is in the case where the scalar field decays entirely into BSM particles and not into radiation. Thus, if a decay produces two SUSY particles, for example, $b = 2$ and $m_\phi > 2m_\chi$, so $\eta < 1/m_\chi$. In such a case, all the SUSY particles produced by the scalar field decay, starting from the neutralino freeze-out, constitute an overall contribution to the relic density that has to be added to the value of the relic density in the standard model, i.e., $Y = Y_{\rm stand} + Y_\phi^{\rm T=T_{fo}}/m_\chi$. Therefore, one has a constraint on the scalar field density at freeze-out.

5.5.1.3 pMSSM19 sample

In the following, we study how the constraints on the scalar field depend on the WIMP properties disregarding the case of a relic density that is too small, as the constraints deduced in this case

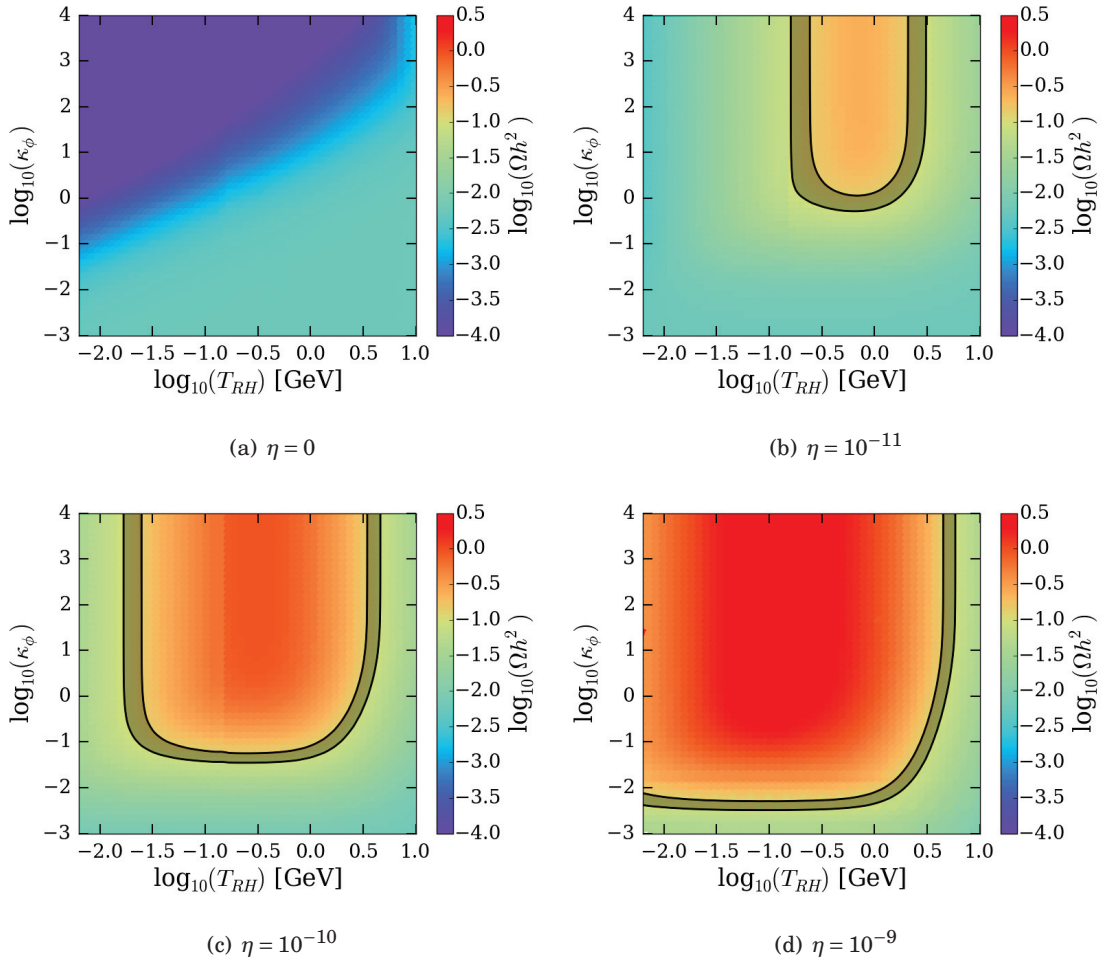

(a) $\eta = 0$

(b) $\eta = 10^{-11}$

(c) $\eta = 10^{-10}$

(d) $\eta = 10^{-9}$

Figure 5.6: *The effect of varying* η *on* $\log_{10}(\Omega h^2)$ *for Point B, indicated by the colour code in the legend.*

already showed an explicit dependence on the freeze-out temperature and the relic density at freeze-out.

We focus on the points in our pMSSM19 sample that have a relic density that is too large in the standard cosmological model, which leaves us almost exclusively with bino-like neutralinos. We calculated the values of κ_ϕ that give the correct relic density at $T_{RH} = T_{RH}^{\mathrm{BBN\,lim}}$, as shown in Figure 5.7, and find a very good correlation between the relic density calculated in the standard model and $\kappa_{\phi_{\min}}$.

The points in Figure 5.7 follow a line of slope ~ 1. Thus, the minimum value of the initial scalar field density increases with the value of the relic density in the standard model. This can be understood because the larger the relic density at freeze-out is, the stronger must be the dilution for a given reheating temperature. The small scatter of the points at low relic density is due to numerical uncertainties alone, but we note a departure from this line at large $\Omega h^2_{\mathrm{stand}}$, when $\kappa_{\phi_{\min}} \gtrsim 1$. With a scalar field density of this order of magnitude, there is also a modification of the Hubble parameter, which advances freeze-out. This mechanism tends to increase the relic density, while the entropy injection decreases it. Overall, the dilution has a stronger effect, but

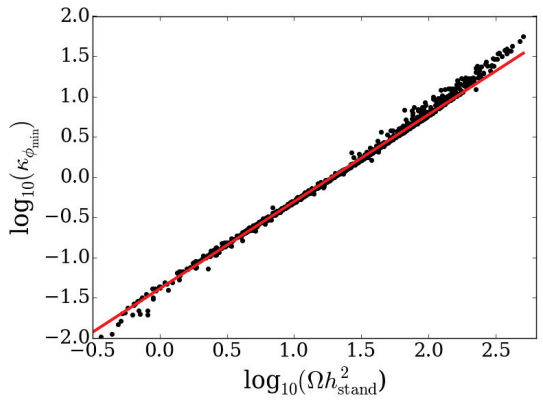

Figure 5.7: *The values of κ_ϕ required to reduce the relic density to the measured DM density with $T_{RH} = T_{RH}^{\text{BBN lim}}$ and $T_{\text{init}} = 40$ GeV as a function of the relic density calculated in the standard model of cosmology. The calculations were done for the sample of points in the pMSSM19 characterised in Table 2.1.*

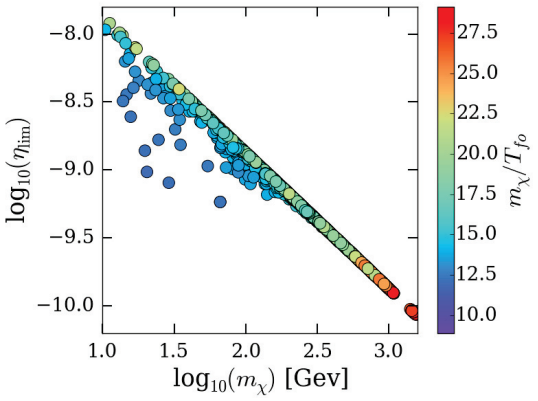

Figure 5.8: *The maximum value of the parameter η for the pMSSM19 sample of points as a function of the neutralino mass. The values of m_χ/T_{fo} are colour-coded as indicated in the legend.*

a larger scalar field density is required to decrease the relic density down to the measured DM density.

Next, we calculate the maximum value of η and find a clear dependence on the WIMP mass, as seen in Figure 5.8. Indeed, the scalar field produces a fraction b of SUSY particles, which contributes as $m_\chi \times b$ to the WIMP mass density. Therefore, the larger m_χ is, the more the relic density will be increased for a given value of η, and the smaller will be the maximum value of η. At first approximation, the maximum value of η is inversely proportional to the WIMP mass. However, another mechanism is at play: for the same neutralino mass, the larger T_{fo} is, the larger the neutralino density at the freeze-out temperature is, and thus the smaller η must be in order to reach the correct relic density. As $T_{\text{fo}_{\text{stand}}} \approx m_\chi/20$, we can express a linear relation between η_{lim} and m_χ. However, as shown in Figure 5.8, when T_{fo} departs from this approximation towards larger values, the second mechanism becomes more important, and we see a departure from the linear relation between m_χ and η_{lim}. This happens for neutralino masses smaller than ~ 100 GeV in our sample of points. In any case, η must be very small, of the order of $\sim 10^{-10} - 10^{-9}$.

5.5.2 Quintessence

We now turn to the study of the quintessence model. This scenario only has the power to increase the relic density by advancing freeze-out. Therefore, we disregard the case of a standard relic density that is too large.

5.5.2.1 Point with a small relic density

We have scanned over the three temperature parameters such that $T_0 < T_{12} < T_{23} < T_{34}$ with $T_0 = 2 \times 10^{-13}$ GeV, the temperature of the CMB at present time. We performed the scans for the two

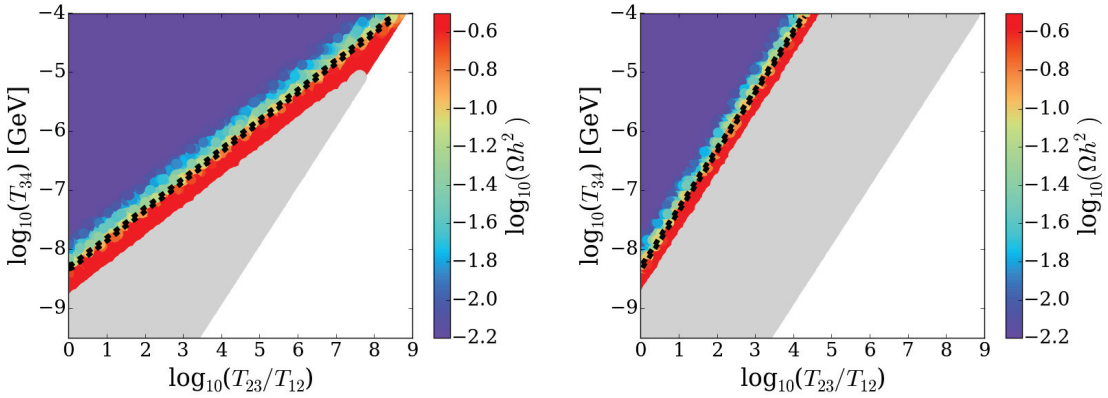

(a) $n_2 = 3$ (b) $n_2 = 6$

Figure 5.9: *The value of* $\log_{10}(\Omega h^2)$*, colour-coded as indicated in the legend, in the* T_{34}*,* T_{23}/T_{12} *parameter plane of the quintessence model. The accepted parameter sets lie between the two dashed lines, the grey region is excluded by BBN and the white region is not accessible in this model.*

extreme values of the slope in zone 2 of Figure 5.1, namely $n_2 = 3$ and $n_2 = 6$. We have calculated the relic density of our benchmark CMSSM point for each set of quintessence parameters, and show the results in Figure 5.9.

The relevant parameters are T_{34} and the ratio T_{23}/T_{12}. The smaller T_{34} is, and the greater T_{23}/T_{12} is, the larger is the relic density. This can easily be understood as the larger the scalar field density is around freeze-out, the larger will be the increase of the relic density, and a small value of T_{34} and a large difference between T_{12} and T_{23} helps in obtaining a large scalar field density at large temperatures. In the case $n_2 = 3$, the accepted parameter sets follow a line of slope ~ 0.5, and we find a limit at $T_{23}/T_{12} \sim 6 \times 10^8$ and $T_{34} \sim 10^{-4}$ GeV, where the line reaches the limiting case $T_{34} = T_{23}$. A minimum value of T_{34} can be found when $T_{12} = T_{23}$, where we find $T_{34} \gtrsim 2 \times 10^{-9}$ GeV. In the case where $n_2 = 6$, the same minimal value can be found. However, the accepted parameter sets follow a line of slope 1, parallel to the limit $T_{23} = T_{34}$. There are, therefore, no maximum values for the temperature parameters.

In both cases, we note also that the accepted parameter sets are very close to the limit imposed by BBN, which mainly depends on the density of the scalar field at a temperature $T \sim 1$ MeV.

When T_{34} is smaller than 1 MeV, which must be the case for values of n_2 close to 3, it is possible to find simpler constraints on the scalar field properties. In this case, freeze out and BBN both occur during phase 4 of the scalar field evolution in the model. The scalar field density can thus be specified simply by its value at freeze-out, and determined at other temperatures according to the slope $n_4 = 6$. We can therefore disregard what happens in phases 1, 2 and 3. We show in Figure 5.10 the evolution of the relic density for Point B with the ratio of the scalar field density to the radiation density at freeze-out, $\widetilde{\rho}_\phi = \frac{\rho_\phi}{\rho_{rad}}(T = T_{\rm fo})$ when we consider only phase 4 of the model.

The scalar field starts having an effect on the relic density when its density is comparable to the radiation density at freeze-out. The Hubble parameter is thus significantly modified and freeze-out is advanced. The relic density then increases with a slope ~ 0.48. In addition, we note that

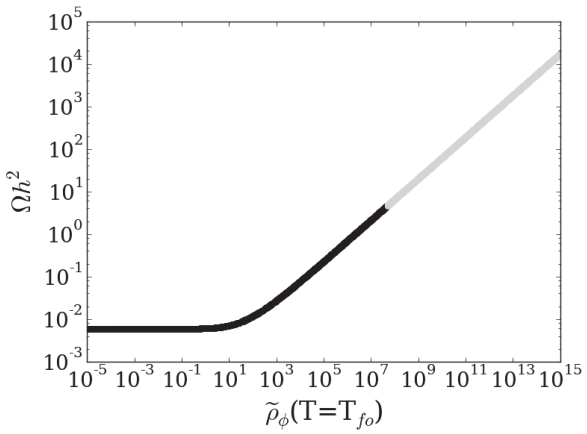

Figure 5.10: *The increase in the relic density for Point B as a function of the ratio of the scalar density and the radiation density at 1 MeV. The grey region is excluded by BBN.*

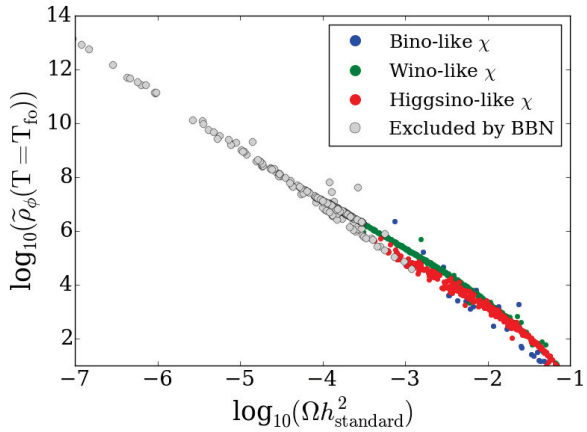

Figure 5.11: *The value of the scalar field density at freeze-out that is required to increase the relic density up to the observed DM density for our sample of pMSSM19 points. The neutralino mass is shown in colour and parameter sets excluded by BBN are shown in grey.*

points are excluded by BBN if $\frac{\rho_\phi}{\rho_{rad}}(\mathrm{T}{=}T_{\mathrm{fo}}) \gtrsim 10^8$, which corresponds to $\frac{\rho_\phi}{\rho_{rad}}(1\ \mathrm{MeV}) \gtrsim 1$.

5.5.2.2 pMSSM19 sample

In addition, we have calculated the value of $\widetilde{\rho}_\Phi(T = T_{\mathrm{fo}})$ required to obtain the correct relic density in our sample of pMSSM19 points. The result is presented in Figure 5.11, which shows the dependence of $\widetilde{\rho}_\Phi(T = T_{\mathrm{fo}})$ on the standard relic density.

In a first approximation, $\widetilde{\rho}_\Phi(T = T_{\mathrm{fo}})$ scales as a power of the standard relic density, with an exponent ~ -2. The smaller the standard relic density is, the larger the scalar field density must be around freeze-out in order to increase the relic density up to the DM density. The exponent -2 can be understood from a simple calculation. Freeze-out occurs when the annihilation rate equals

the expansion rate, in the standard cosmological model:

$$n_{eq}(T_{\rm fo}^{stand})\langle\sigma v\rangle_{T_{fo_{stand}}} \sim H \sim H_0\rho_{rad}^{1/2}(T = T_{fo_{stand}}) \,, \tag{5.33}$$

with $H_0 = \sqrt{8\pi/3M_p^2}$. The comoving neutralino density Y_{stand} can then be expressed as:

$$Y_{stand} = \frac{n_{eq}(T_{fo_{stand}})}{s_{rad}(T_{fo_{stand}})} \,, \tag{5.34}$$

which can be re-expressed using Eq. (5.33) as

$$Y_{stand} = \frac{H_0\rho_{rad}^{1/2}(T_{fo_{stand}})}{\langle\sigma v\rangle_{T_{fo_{stand}}} s_{rad}(T_{fo_{stand}})} \,. \tag{5.35}$$

When the scalar field density is very large in the quintessence model, compared to the radiation density, we obtain similar equations:

$$n_{eq}(T_{\rm fo})\langle\sigma v\rangle_{T=T_{\rm fo}} \sim H \sim H_0\rho_\Phi^{1/2}(T = T_{\rm fo}) = H_0\rho_\Phi^{1/2}(T = T_{fo_{stand}}) \times \left(\frac{T_{\rm fo}}{T_{fo_{stand}}}\right)^3 \,, \tag{5.36}$$

and

$$Y = \frac{n_{eq}(T_{\rm fo})}{s_{rad}(T_{\rm fo})} \,, \tag{5.37}$$

where we have used in Eq. (5.36) the fact that the scalar field density evolves as T^{n_4} with $n_4 = 6$. The relic comoving density Y in this scenario can then be re-written using Eq. (5.36) as:

$$Y = \frac{H_0\rho_\Phi^{1/2}(T = T_{fo_{stand}}) \times \left(\frac{T_{\rm fo}}{T_{fo_{stand}}}\right)^3}{\langle\sigma v\rangle_{T_{\rm fo}} s_{rad}(T_{\rm fo})} = \frac{H_0\rho_\Phi^{1/2}(T = T_{fo_{stand}})}{\langle\sigma v\rangle_{T_{\rm fo}} s_{rad}(T_{fo_{stand}})} \,. \tag{5.38}$$

Finally, we can combine Eqs. (5.38) and (5.35) to obtain:

$$Y = Y_{stand}\frac{\langle\sigma v\rangle_{T_{fo_{stand}}}}{\langle\sigma v\rangle_{T_{\rm fo}}}\frac{\rho_\Phi^{1/2}(T = T_{fo_{stand}})}{\rho_{rad}^{1/2}} \,. \tag{5.39}$$

This gives us the ratio between the scalar field density and the radiation density at the standard freeze-out temperature that is required to increase the relic density to the measured dark matter density:

$$\begin{aligned}\widetilde{\rho}_\Phi(T_{fo_{stand}}) &= \left(\frac{Y}{Y_{stand}}\right)^2 \times \left(\frac{\langle\sigma v\rangle_{T_{\rm fo}}}{\langle\sigma v\rangle_{T_{fo_{stand}}}}\right)^2 \\ &= \left(\frac{\Omega h^2_{DM}}{\Omega h^2_{stand}}\right)^2 \times \left(\frac{Y(T = T_{\rm fo})/Y(T = present)}{Y_{stand}(T = T_{fo_{stand}})/Y_{stand}(T = present)}\right)^2 \times \left(\frac{\langle\sigma v\rangle_{T_{\rm fo}}}{\langle\sigma v\rangle_{T_{fo_{stand}}}}\right)^2 \,.\end{aligned} \tag{5.40}$$

We retrieve here the slope -2. We note, however, that this particular value appears only because $n_4 = 6$, and thus depends on the quintessence model. Residual annihilations occurring after freeze-out are taken into account by the factor

$$\xi = \left(\frac{Y(T = T_{\rm fo})/Y(T = present)}{Y_{stand}(T = T_{fo_{stand}})/Y_{stand}(T = present)}\right)^2 \,,$$

which takes a value ~ 10 in our sample of pMSSM19 points. It was indeed already noted in [324] that the residual annihilations, so-called *relentless annihilations*, can be particularly important when $H \propto T^{2+\frac{n}{2}}$, with $n \geq 2$. In the case of the quintessence model, $n = 2$, which corresponds well to this regime. The value of ξ is model-dependent, however, and we show in Figure 5.11 that wino-like neutralinos, for instance, require a larger scalar field density than higgsino-like neutralinos.
Finally, we note that for neutralinos with a standard relic density $\lesssim 3 \times 10^{-4}$, the scalar field density is too large at 1 MeV and our scenario is ruled out by BBN.

5.6 Conclusion

In this work, we showed that dark matter could be used as a powerful tool to probe the content of the Universe at an epoch which is beyond observational reach. Assuming that a weakly interacting massive particle is discovered at colliders and that the measurements of its annihilation and co-annihilation cross sections are precise enough, it would be possible to calculate its relic density in the standard scenario where the Universe is radiation dominated before BBN and also to constrain alternative models. As an example, we considered the case of a WIMP that would yield a relic density either too small or too large in the standard cosmological model and constrained the parameters of two cosmological models which present typical mechanisms to modify the relic density: a primordial scalar field decaying into radiation and SUSY particles and a quintessence model. Model points in the MSSM were taken in this analysis, but we showed that the constraints were very general and would stand for most WIMP models. The detection of a dark matter particle would therefore be an important step in the understanding of the early Universe and would constitute a new pillar of the cosmology, along with the Big Bang nucleosynthesis and the Cosmic Microwave Background.

General Conclusion

In this thesis, we have shown the importance of the uncertainties related to dark matter searches. First we have presented a study of the constraints derived from dark matter searches and SUSY searches at colliders applied to the Minimal Supersymmetric extension of the Standard Model, focusing on neutralino dark matter. It showed that the various types of dark matter constraints, namely from the relic density, direct and indirect detections, are very complementary, as they exclude neutralinos of different natures. More precisely, the upper bound of the relic density excludes mostly bino-like neutralinos, whereas direct and indirect detection rather excludes Higgsinos and winos respectively. Concerning direct detection, the constraints are limited, in particular, by the uncertainties on the local dark matter density. As for indirect detection, the constraints suffer from our poor knowledge of the dark matter density profile and of the propagation of charged cosmic rays through the galactic medium. When combined with collider constraints, which are obtained in an environment under control, direct detection constraints become quite robust with respect to the mentioned uncertainties. This is not the case for indirect detection, whose constraints are still undermined by cosmic ray propagation uncertainties. Nevertheless, even in the most conservative case, indirect detection excludes compressed scenarios which evade collider constraints.

In a second part, we have presented the development of numerical tools in the public code SuperIso Relic designed to take into account correctly the astrophysical and nuclear uncertainties on direct and indirect detection constraints. We implemented constraints from AMS-02, Fermi-LAT, PANDAX-2, XENON1T and PICO60 and showed the importance of nuclear uncertainties on direct detection limits.

In the last part, we showed that the content of the Universe could be constrained from the discovery of new particles at colliders. We considered two alternative cosmological scenarios involving the presence of a scalar field in the primordial Universe and showed that the discovery of a WIMP with a standard relic density either too small or too large would allow us to set strong constraints on the scalar field properties.

Appendices

APPENDIX A

RELIC DENSITY CALCULATION

A.1 Relic density without co-annihilation

A.1.1 General Solution

The evolution in time of a WIMP density in an expanding Universe is given by the Boltzmann equation

$$\frac{dn}{dt} = -3Hn - \langle\sigma_{ann}v\rangle(n^2 - n_{eq}^2) \,, \tag{A.1}$$

where $\langle\sigma_{ann}v\rangle$ is the average dark matter annihilation cross-section times the relative velocity of the two particles annihilating and n_{eq} is the equilibrium density, which follows Fermi-Dirac or Bose-Einstein statistics depending if the WIMP is a fermion or a boson

$$n_{eq} = \frac{g}{(2\pi)^3}\int \frac{1}{e^{-\frac{E}{T}} \pm 1} d^3\mathbf{p} \,, \tag{A.2}$$

with g, the number of internal degrees of freedom of the WIMP, $\mathbf{p}$ its four-momentum and $E = \sqrt{p^2 + m^2}$, its energy . In the non-relativistic limit,

$$n_{eq} = g\left(\frac{mT}{2\pi}\right)^{3/2} exp\left(-\frac{m}{T}\right) \,. \tag{A.3}$$

As we want to calculate the temperature at which the WIMP density freezes-out, an additional relation is necessary to relate the evolution of the temperature to time. This relation can be calculated under the assupmtion of adiabaticity from the conservation of entropy

$$\frac{ds}{dt} = -3Hs \,. \tag{A.4}$$

Assuming that entropy is dominated by radiation, it is known as a function of the temperature

$$s = \frac{2\pi^2}{45} h_{eff}(T)T^3 \,, \tag{A.5}$$

where $h_{eff}(T)$ is the effective number of entropic degrees of freedom of radiation.
Instead of using directly the temperature, it is more convenient to use the parameter $x = \frac{m}{T}$ with m, the mass of the WIMP. Then,

$$\frac{dn}{dx} = \frac{dn}{dt}\frac{dt}{dx} . \tag{A.6}$$

The first term on the right side of equation (A.6) can be replaced by equation (A.1) and the second term by

$$\frac{dt}{dx} = \frac{dt}{ds}\frac{ds}{dx} = \frac{-1}{3Hs}\frac{ds}{dx} .$$

Equation (A.6) becomes

$$\begin{aligned}\frac{dn}{dx} &= \left[-3Hn - \langle\sigma_{ann}v\rangle(n^2 - n_{eq}^2)\right]\left[\frac{-1}{3Hs}\frac{ds}{dx}\right] \\ &= \frac{n}{s}\frac{ds}{dx} - \langle\sigma_{ann}v\rangle(n^2 - n_{eq}^2)\left[\frac{-1}{3Hs}\frac{ds}{dx}\right]\end{aligned}$$

which, divided by the entropy gives

$$\frac{dY}{dx} = \langle\sigma_{ann}v\rangle(Y^2 - Y_{eq}^2)\left[\frac{1}{3H}\frac{ds}{dx}\right] , \tag{A.7}$$

with $Y = \frac{n}{s}$.

From equation (A.5) one can deduce that

$$\begin{aligned}\frac{ds}{dx} &= \frac{-T^2}{m}\frac{ds}{dT} \\ &= \frac{-T^2}{m} \times \left[\frac{2\pi^2}{45}\left(3T^2 h_{eff} + T^3\frac{dh_{eff}}{dT}\right)\right] \\ &= \frac{-6\pi^2}{45}\frac{T^4}{m}h_{eff}\left(1 + \frac{1}{3}\frac{T}{h_{eff}}\frac{dh_{eff}}{dT}\right) .\end{aligned} \tag{A.8}$$

We also know that for a radiation-dominated Universe, $H^2 = \frac{8\pi}{3M_p^2}\rho_{rad}$, with $\rho_{rad} = \frac{\pi^2}{30}g_{eff}(T)T^4$, and $g_{eff}(T)$ being the effective number of degrees of freedom of radiation.
Therefore,

$$H = \sqrt{\frac{8\pi^3}{90M_p^2}}\, g_{eff}^{1/2} T^2 \tag{A.9}$$

and equation (A.8) becomes

$$\boxed{\frac{dY}{dx} = -\sqrt{\frac{\pi M_p^2}{45}}\,\frac{g_*^{1/2} m}{x^2}\langle\sigma_{ann}v\rangle(Y^2 - Y_{eq}^2)} , \tag{A.10}$$

with

$$g_*^{1/2} = \frac{heff}{g_{eff}^{1/2}}\left(1 + \frac{1}{3}\frac{T}{h_{eff}}\frac{dh_{eff}}{dT}\right) . \tag{A.11}$$

In order to calculate the WIMP relic density at present time

$$\Omega_\chi^0 = \frac{\rho_\chi^0}{\rho_c} = \frac{8\pi}{3M_p^2}\frac{ms_0Y_0}{H_0^2} \,, \tag{A.12}$$

one should integrate equation (A.10) from $x = 0$ to $x = \frac{m_\chi}{T_0}$, with a background temperature $T_0 =$ 2.7K.

A.1.2 The WIMP miracle

After freeze-out, n_{eq} will continue to decrease as $e^{-m/T}$ so that eventually, $Y_{eq} \ll Y$. In this context, equation (A.10) can be rewritten as

$$\frac{dY}{dx} = \frac{-\lambda(x)}{x^2}Y^2 \,, \tag{A.13}$$

with $\lambda(x) = \sqrt{\frac{\pi M_p^2}{45}}\, g_*^{1/2} m\langle\sigma_{ann}v\rangle$. When only s-waves are considered, $\langle\sigma_{ann}v\rangle$ is constant, and so is $\lambda(x)$. One can easily integrate equation (A.13) between freeze-out and today as

$$\frac{1}{Y_0} - \frac{1}{Y_f} = \lambda\left(\frac{1}{x_f} - \frac{1}{x_0}\right) \,, \tag{A.14}$$

which can be simplified, noticing that $x_0 \gg x_f$ and $Y_0 \ll Y_f$,

$$Y_0 \approx \frac{x_f}{\lambda} \,. \tag{A.15}$$

Freeze-out corresponds to the moment when WIMP annihilation rate equals the rate of expansion of the Universe. Thus, x_f can be obtained by resolving the equation

$$n_{eq}(x_f)\langle\sigma_{ann}v\rangle = H(x_f) \,. \tag{A.16}$$

Using equations (A.3) and (A.9), one obtains at first order approximation

$$x_f = \ln\left(0.038\frac{g}{g_{eff}^{1/2}} mM_p\langle\sigma_{ann}v\rangle\right) \,. \tag{A.17}$$

Thanks to the logarithm in the expression of x_f, its value depends poorly on the exact value of the WIMP mass or on its annihilation cross section. Taking $m \approx 100$ GeV and a typical value for weak interactions $\langle\sigma_{ann}v\rangle \approx 10^{-26}$ cm^3/s, one obtains $x_f \approx 20$.
Replacing Y_0 in equation (A.12),

$$\Omega_\chi^0 = \frac{\rho_\chi^0}{\rho_c} = \frac{8\pi}{3M_p^2}\frac{ms_0x_f}{H_0^2\lambda} \,, \tag{A.18}$$

and then

$$\Omega_\chi^0 h^2 = \frac{16\pi^{5/2}T_0^3}{9\sqrt{5}M_p^3}\frac{h_{eff}(T_0)}{g_*^{1/2}}\frac{x_f}{\langle\sigma_{ann}v\rangle} \,. \tag{A.19}$$

Finally, replacing with numerical values,

$$\boxed{\Omega_\chi^0 h^2 \sim \frac{3\times 10^{-27}\mathrm{cm}^3\mathrm{s}^{-1}}{\langle\sigma_{ann}v\rangle}}. \tag{A.20}$$

The "miracle" in this last equation is that if $\langle\sigma v\rangle \sim 3\times 10^{-26}\mathrm{cm}^3\mathrm{s}^{-1}$, which is a typical value for weak interaction processes, one obtains the measured dark matter density $\Omega_\chi^0 h^2 \approx 0.1$.

APPENDIX B

NMSSM COUPLINGS FOR DIRECT DETECTION

We present here the couplings, in the NMSSM, between the neutral CP-even Higgs bosons and the quarks, squarks and neutralino 1.
The couplings with the quarks differ for down-type and up-type quarks:

$$c_q^i = \frac{g}{2M_W}\left(m_q r_q^i\right) , \tag{B.1}$$

(B.2)

where g is the SU(2) gauge coupling, M_W is the W boson mass, m_q is the quark mass and r_q^i depends on the type of the quark:

$$r_d^i = \frac{H_{i1}}{cos\,\beta} \qquad r_u^i = \frac{H_{21}}{sin\,\beta} \tag{B.3}$$

with H the Higgs mixing matrice. The subscript $i = 1,2,3$ stands for the three CP-even neutral Higgs bosons ordered by ascending masses.
The couplings with the squarks also depend on the type of the related quark, but also on the squark number $j = 1,2$, defined so that $m_{\tilde{q}_1} < m_{\tilde{q}_2}$:

$$\begin{aligned} c_{\tilde{q}_j}^i = & \frac{g}{M_W}\left(H_{i1}cos\,\beta - H_{i2}sin\,\beta\right) \times \alpha_j \\ & + \frac{g}{M_W} m_q^2 r_q^i \\ & - \frac{g}{M_W}\frac{sin(2\theta_q)}{2}\left(A_q \times r_q^i + \mu \times r_{\tilde{q}}^i\right) \\ & + \lambda\, tan\,\beta H_{i3}\frac{sin(2\theta_q)}{\sqrt{2}} m_q , \end{aligned} \tag{B.4}$$

where θ_q is the squark mixing angle and A_q is the quark trilinear coupling. λ is a term appearing in the NMSSM superpotential :

$$W = \tilde{u}_R^* y_u\left(\tilde{Q}^T \epsilon H_u\right) - \tilde{d}_R^* y_d\left(\tilde{Q}^T \epsilon H_d\right) - \tilde{e}_R^* y_e\left(\tilde{L}^T \epsilon H_d\right) + \lambda S\left(H_u^T \epsilon H_d\right) + \frac{1}{3}\kappa S^3 , \tag{B.5}$$

where S is the NMSSM singlet.
The coefficients α_j read:

$$\alpha_1 = t^3 cos(\theta_q)^2 - q\, sin(\theta_W)^2 cos(2\theta_q) \tag{B.6}$$

$$\alpha_2 = t^3 sin(\theta_q)^2 + q\, sin(\theta_W)^2 cos(2\theta_q)\ , \tag{B.7}$$

where t^3 stands for the third-component weak isospin and q the electric charge.
Finally, the coefficient $r^i_{\tilde{q}}$ is defined as:

$$r^i_{\tilde{d}} = \frac{H_{i2}}{cos\,\beta} \qquad r^i_{\tilde{u}} = \frac{H_{i1}}{sin\,\beta}\ . \tag{B.8}$$

We end by giving the couplings between the neutralino 1 and the Higgs:

$$\begin{aligned} c^i_\chi =& \frac{g}{2}\left(N_{12} - \frac{sin\,\theta_W}{cos\,\theta_W} N_{11}\right) \times (H_{i1}N_{13} - H_{i2}N_{14}) \\ &+ \sqrt{2}\,\lambda\,(H_{i3}N_{13}N_{14} + H_{i2}N_{13}N_{15} + H_{i1}N_{14}N_{15}) \\ &- \sqrt{2}\,\kappa H_{i3}N^2_{15}\ , \end{aligned} \tag{B.9}$$

where N_{ij} is the neutralino mixing matrix.

Bibliography

[1] B. Kelvin, "Baltimore lectures on molecular dynamics and the wave theory of light," 1904.

[2] H. Poincare, "The Milky Way and the Theory of Gases," *Popular Astronomy* **14** (Oct., 1906) 475–488.

[3] E. Opik, "Selective absorption of light in space, and the dynamics of the universe," *Bull. de la Soc. Astr. de Russie* **21** no. 150, (1915) 5.

[4] J. C. Kapteyn, "First Attempt at a Theory of the Arrangement and Motion of the Sidereal System," *ApJ* **55** (May, 1922) 302.

[5] J. H. Jeans, "The Motions of Stars in a Kapteyn Universe," *mnras* **82** (Jan., 1922) 122–132.

[6] J. H. Oort, "The force exerted by the stellar system in the direction perpendicular to the galactic plane and some related problems," *Bull. of Astron. Inst. of the Netherlands* **6** (Aug., 1932) 249.

[7] J. I. Read, "The Local Dark Matter Density," *J. Phys.* **G41** (2014) 063101, arXiv:1404.1938 [astro-ph.GA].

[8] F. Zwicky, "Die Rotverschiebung von extragalaktischen Nebeln," *Helv. Phys. Acta* **6** (1933) 110–127. [Gen. Rel. Grav.41,207(2009)].

[9] S. Smith, "The Mass of the Virgo Cluster," *ApJ* **83** (Jan., 1936) 23.

[10] F. D. Kahn and L. Woltjer, "Intergalactic Matter and the Galaxy.," *ApJ* **130** (Nov., 1959) 705.

[11] D. Clowe, A. Gonzalez, and M. Markevitch, "Weak lensing mass reconstruction of the interacting cluster 1E0657-558: Direct evidence for the existence of dark matter," *Astrophys. J.* **604** (2004) 596–603, arXiv:astro-ph/0312273 [astro-ph].

[12] H. W. Babcock, "The rotation of the Andromeda Nebula," *Lick Observatory Bulletin* **19** (1939) 41–51.

[13] J. H. Oort, "Some Problems Concerning the Structure and Dynamics of the Galactic System and the Elliptical Nebulae NGC 3115 and 4494.," *ApJ* **91** (Apr., 1940) 273.

[14] H. C. van de Hulst, E. Raimond, and H. van Woerden, "Rotation and density distribution of the Andromeda nebula derived from observations of the 21-cm line," *Bull. of Astron. Inst. of the Netherlands* **14** (Nov., 1957) 1.

[15] M. S. Roberts, "A High-Resolution 21-CM Hydrogen-Line Survey of the Andromeda Nebula," *ApJ* **144** (May, 1966) 639.

[16] V. C. Rubin and W. K. Ford, Jr., "Rotation of the Andromeda Nebula from a Spectroscopic Survey of Emission Regions," *ApJ* **159** (Feb., 1970) 379.

[17] M. S. Roberts and A. H. Rots, "Comparison of Rotation Curves of Different Galaxy Types," *Astron. & Astrophys.* **26** (Aug., 1973) 483–485.

[18] R. A. Alpher, H. Bethe, and G. Gamow, "The origin of chemical elements," *Phys. Rev.* **73** (1948) 803–804.

[19] A. A. Penzias and R. W. Wilson, "A Measurement of Excess Antenna Temperature at 4080 Mc/s.," *ApJ* **142** (July, 1965) 419–421.

[20] **COBE** Collaboration, G. F. Smoot *et al.*, "Structure in the COBE differential microwave radiometer first year maps," *Astrophys. J.* **396** (1992) L1–L5.

[21] **WMAP** Collaboration, G. Hinshaw *et al.*, "Nine-Year Wilkinson Microwave Anisotropy Probe (WMAP) Observations: Cosmological Parameter Results," *Astrophys. J. Suppl.* **208** (2013) 19, arXiv:1212.5226 [astro-ph.CO].

[22] **Planck** Collaboration, P. A. R. Ade *et al.*, "Planck 2015 results. XIII. Cosmological parameters," *Astron. Astrophys.* **594** (2016) A13, arXiv:1502.01589 [astro-ph.CO].

[23] M. Davis, J. Huchra, D. W. Latham, and J. Tonry, "A survey of galaxy redshifts. II - The large scale space distribution," *ApJ* **253** (Feb., 1982) 423–445.

[24] S. D. M. White, C. S. Frenk, and M. Davis, "Clustering in a Neutrino Dominated Universe," *Astrophys. J.* **274** (1983) L1–L5.

[25] **Planck** Collaboration, N. Aghanim *et al.*, "Planck 2015 results. XI. CMB power spectra, likelihoods, and robustness of parameters," *Astron. Astrophys.* **594** (2016) A11, arXiv:1507.02704 [astro-ph.CO].

[26] B. Paczynski, "Gravitational microlensing by the galactic halo," *ApJ* **304** (May, 1986) 1–5.

[27] R. J. Nemiroff, "Prediction and analysis of basic gravitational microlensing phenomena,".

[28] **MACHO** Collaboration, C. Alcock *et al.*, "The MACHO project: Microlensing results from 5.7 years of LMC observations," *Astrophys. J.* **542** (2000) 281–307, arXiv:astro-ph/0001272 [astro-ph].

[29] **EROS-2** Collaboration, P. Tisserand *et al.*, "Limits on the Macho Content of the Galactic Halo from the EROS-2 Survey of the Magellanic Clouds," *Astron. Astrophys.* **469** (2007) 387–404, arXiv:astro-ph/0607207 [astro-ph].

[30] H. Reeves, J. Audouze, W. A. Fowler, and D. N. Schramm, "On the Origin of Light Elements," *ApJ* **179** (Feb., 1973) 909–930.

[31] S. Burles and D. Tytler, "The Deuterium abundance towards Q1937-1009," *Astrophys. J.* **499** (1998) 699, arXiv:astro-ph/9712108 [astro-ph].

[32] S. Burles and D. Tytler, "The Deuterium abundance toward QSO 1009+2956," *Astrophys. J.* **507** (1998) 732–744, arXiv:astro-ph/9712109 [astro-ph].

[33] S. Burles, K. M. Nollett, and M. S. Turner, "Big bang nucleosynthesis predictions for precision cosmology," *Astrophys. J.* **552** (2001) L1–L6, arXiv:astro-ph/0010171 [astro-ph].

[34] M. Fukugita, C. J. Hogan, and P. J. E. Peebles, "The Cosmic baryon budget," *Astrophys. J.* **503** (1998) 518, arXiv:astro-ph/9712020 [astro-ph].

[35] J. M. O'Meara, D. Tytler, D. Kirkman, N. Suzuki, J. X. Prochaska, D. Lubin, and A. M. Wolfe, "The Deuterium to hydrogen abundance ratio towards a fourth QSO: HS 0105 + 1619," *Astrophys. J.* **552** (2001) 718–730, arXiv:astro-ph/0011179 [astro-ph].

[36] **Virgo, LIGO Scientific** Collaboration, B. P. Abbott *et al.*, "Observation of Gravitational Waves from a Binary Black Hole Merger," *Phys. Rev. Lett.* **116** no. 6, (2016) 061102, arXiv:1602.03837 [gr-qc].

[37] B. Carr, F. Kuhnel, and M. Sandstad, "Primordial Black Holes as Dark Matter," *Phys. Rev.* **D94** no. 8, (2016) 083504, arXiv:1607.06077 [astro-ph.CO].

[38] G. Steigman and M. S. Turner, "Cosmological Constraints on the Properties of Weakly Interacting Massive Particles," *Nucl. Phys.* **B253** (1985) 375–386.

[39] J. L. Feng, "Dark Matter Candidates from Particle Physics and Methods of Detection," *Ann. Rev. Astron. Astrophys.* **48** (2010) 495–545, arXiv:1003.0904 [astro-ph.CO].

[40] L. Randall and R. Sundrum, "A Large mass hierarchy from a small extra dimension," *Phys. Rev. Lett.* **83** (1999) 3370–3373, arXiv:hep-ph/9905221 [hep-ph].

[41] G. G. Raffelt, "Astrophysical axion bounds," *Lect. Notes Phys.* **741** (2008) 51–71, arXiv:hep-ph/0611350 [hep-ph]. [,51(2006)].

[42] S. Borsanyi *et al.*, "Calculation of the axion mass based on high-temperature lattice quantum chromodynamics," *Nature* **539** no. 7627, (2016) 69–71, arXiv:1606.07494 [hep-lat].

[43] **ADMX** Collaboration, S. J. Asztalos *et al.*, "A SQUID-based microwave cavity search for dark-matter axions," *Phys. Rev. Lett.* **104** (2010) 041301, arXiv:0910.5914 [astro-ph.CO].

[44] **H.E.S.S.** Collaboration, H. Abdallah *et al.*, "Search for dark matter annihilations towards the inner Galactic halo from 10 years of observations with H.E.S.S," *Phys. Rev. Lett.* **117** no. 11, (2016) 111301, arXiv:1607.08142 [astro-ph.HE].

[45] J. Aleksić *et al.*, "Optimized dark matter searches in deep observations of Segue 1 with MAGIC," *JCAP* **1402** (2014) 008, arXiv:1312.1535 [hep-ph].

[46] **VERITAS** Collaboration, E. Aliu *et al.*, "VERITAS Deep Observations of the Dwarf Spheroidal Galaxy Segue 1," *Phys. Rev.* **D85** (2012) 062001, arXiv:1202.2144 [astro-ph.HE]. [Erratum: Phys. Rev.D91,no.12,129903(2015)].

[47] **HAWC** Collaboration, A. Albert *et al.*, "Dark Matter Limits From Dwarf Spheroidal Galaxies with The HAWC Gamma-Ray Observatory," *Astrophys. J.* **853** no. 2, (2018) 154, arXiv:1706.01277 [astro-ph.HE].

[48] D. Hooper and L. Goodenough, "Dark Matter Annihilation in The Galactic Center As Seen by the Fermi Gamma Ray Space Telescope," *Phys. Lett.* **B697** (2011) 412–428, arXiv:1010.2752 [hep-ph].

[49] D. Hooper and T. Linden, "On The Origin Of The Gamma Rays From The Galactic Center," *Phys. Rev.* **D84** (2011) 123005, arXiv:1110.0006 [astro-ph.HE].

[50] T. Daylan, D. P. Finkbeiner, D. Hooper, T. Linden, S. K. N. Portillo, N. L. Rodd, and T. R. Slatyer, "The characterization of the gamma-ray signal from the central Milky Way: A case for annihilating dark matter," *Phys. Dark Univ.* **12** (2016) 1–23, arXiv:1402.6703 [astro-ph.HE].

[51] K. N. Abazajian, N. Canac, S. Horiuchi, and M. Kaplinghat, "Astrophysical and Dark Matter Interpretations of Extended Gamma-Ray Emission from the Galactic Center," *Phys. Rev.* **D90** no. 2, (2014) 023526, arXiv:1402.4090 [astro-ph.HE].

[52] T. Lacroix, C. Boehm, and J. Silk, "Fitting the Fermi-LAT GeV excess: On the importance of including the propagation of electrons from dark matter," *Phys. Rev.* **D90** no. 4, (2014) 043508, arXiv:1403.1987 [astro-ph.HE].

[53] F. Calore, I. Cholis, C. McCabe, and C. Weniger, "A Tale of Tails: Dark Matter Interpretations of the Fermi GeV Excess in Light of Background Model Systematics," *Phys. Rev.* **D91** no. 6, (2015) 063003, arXiv:1411.4647 [hep-ph].

[54] S. K. Lee, M. Lisanti, and B. R. Safdi, "Distinguishing Dark Matter from Unresolved Point Sources in the Inner Galaxy with Photon Statistics," *JCAP* **1505** no. 05, (2015) 056, arXiv:1412.6099 [astro-ph.CO].

[55] J. Petrović, P. D. Serpico, and G. Zaharijaš, "Galactic Center gamma-ray "excess" from an active past of the Galactic Centre?," *JCAP* **1410** no. 10, (2014) 052, arXiv:1405.7928 [astro-ph.HE].

[56] O. Adriani *et al.*, "Measurement of the flux of primary cosmic ray antiprotons with energies of 60-MeV to 350-GeV in the PAMELA experiment," *JETP Lett.* **96** (2013) 621–627. [Pisma Zh. Eksp. Teor. Fiz.96,693(2012)].

[57] **AMS** Collaboration, M. Aguilar *et al.*, "Antiproton Flux, Antiproton-to-Proton Flux Ratio, and Properties of Elementary Particle Fluxes in Primary Cosmic Rays Measured with the Alpha Magnetic Spectrometer on the International Space Station," *Phys. Rev. Lett.* **117** no. 9, (2016) 091103.

[58] A. Cuoco, M. Krämer, and M. Korsmeier, "Novel Dark Matter Constraints from Antiprotons in Light of AMS-02," *Phys. Rev. Lett.* **118** no. 19, (2017) 191102, arXiv:1610.03071 [astro-ph.HE].

[59] M.-Y. Cui, Q. Yuan, Y.-L. S. Tsai, and Y.-Z. Fan, "Possible dark matter annihilation signal in the AMS-02 antiproton data," *Phys. Rev. Lett.* **118** no. 19, (2017) 191101, arXiv:1610.03840 [astro-ph.HE].

[60] **AMS** Collaboration, M. Aguilar *et al.*, "Electron and Positron Fluxes in Primary Cosmic Rays Measured with the Alpha Magnetic Spectrometer on the International Space Station," *Phys. Rev. Lett.* **113** (2014) 121102.

[61] **IceCube** Collaboration, M. G. Aartsen *et al.*, "Search for annihilating dark matter in the Sun with 3 years of IceCube data," *Eur. Phys. J.* **C77** no. 3, (2017) 146, arXiv:1612.05949 [astro-ph.HE].

[62] **Super-Kamiokande** Collaboration, K. Choi *et al.*, "Search for neutrinos from annihilation of captured low-mass dark matter particles in the Sun by Super-Kamiokande," *Phys. Rev. Lett.* **114** no. 14, (2015) 141301, arXiv:1503.04858 [hep-ex].

[63] **XENON** Collaboration, E. Aprile *et al.*, "First Dark Matter Search Results from the XENON1T Experiment," *Phys. Rev. Lett.* **119** no. 18, (2017) 181301, arXiv:1705.06655 [astro-ph.CO].

[64] **EDELWEISS** Collaboration, E. Armengaud *et al.*, "Constraints on low-mass WIMPs from the EDELWEISS-III dark matter search," *JCAP* **1605** no. 05, (2016) 019, arXiv:1603.05120 [astro-ph.CO].

[65] **CDMS** Collaboration, R. Agnese *et al.*, "Silicon Detector Dark Matter Results from the Final Exposure of CDMS II," *Phys. Rev. Lett.* **111** no. 25, (2013) 251301, arXiv:1304.4279 [hep-ex].

[66] **CRESST** Collaboration, G. Angloher *et al.*, "Results on light dark matter particles with a low-threshold CRESST-II detector," *Eur. Phys. J.* **C76** no. 1, (2016) 25, arXiv:1509.01515 [astro-ph.CO].

[67] **LUX** Collaboration, D. S. Akerib *et al.*, "Results from a search for dark matter in the complete LUX exposure," *Phys. Rev. Lett.* **118** no. 2, (2017) 021303, arXiv:1608.07648 [astro-ph.CO].

[68] **PandaX-II** Collaboration, X. Cui *et al.*, "Dark Matter Results From 54-Ton-Day Exposure of PandaX-II Experiment," *Phys. Rev. Lett.* **119** no. 18, (2017) 181302, arXiv:1708.06917 [astro-ph.CO].

[69] **DarkSide** Collaboration, P. Agnes *et al.*, "Results from the first use of low radioactivity argon in a dark matter search," *Phys. Rev.* **D93** no. 8, (2016) 081101, arXiv:1510.00702 [astro-ph.CO]. [Addendum: Phys. Rev. D95, no.6, 069901 (2017)].

[70] **LUX** Collaboration, D. S. Akerib *et al.*, "Limits on spin-dependent WIMP-nucleon cross section obtained from the complete LUX exposure," *Phys. Rev. Lett.* **118** no. 25, (2017) 251302, arXiv:1705.03380 [astro-ph.CO].

[71] **PandaX-II** Collaboration, C. Fu *et al.*, "Spin-Dependent Weakly-Interacting-Massive-ParticleâĂŞNucleon Cross Section Limits from First Data of PandaX-II Experiment," *Phys. Rev. Lett.* **118** no. 7, (2017) 071301, arXiv:1611.06553 [hep-ex]. [Erratum: Phys. Rev. Lett.120,no.4,049902(2018)].

[72] **PICO** Collaboration, C. Amole *et al.*, "Dark Matter Search Results from the PICO-60 C_3F_8 Bubble Chamber," *Phys. Rev. Lett.* **118** no. 25, (2017) 251301, arXiv:1702.07666 [astro-ph.CO].

[73] **DAMA** Collaboration, R. Bernabei *et al.*, "First results from DAMA/LIBRA and the combined results with DAMA/NaI," *Eur. Phys. J.* **C56** (2008) 333–355, arXiv:0804.2741 [astro-ph].

[74] **DAMA, LIBRA** Collaboration, R. Bernabei *et al.*, "New results from DAMA/LIBRA," *Eur. Phys. J.* **C67** (2010) 39–49, arXiv:1002.1028 [astro-ph.GA].

[75] D. Hooper, J. I. Collar, J. Hall, D. McKinsey, and C. Kelso, "A Consistent Dark Matter Interpretation For CoGeNT and DAMA/LIBRA," *Phys. Rev.* **D82** (2010) 123509, arXiv:1007.1005 [hep-ph].

[76] **CoGeNT** Collaboration, C. E. Aalseth *et al.*, "Results from a Search for Light-Mass Dark Matter with a P-type Point Contact Germanium Detector," *Phys. Rev. Lett.* **106** (2011) 131301, arXiv:1002.4703 [astro-ph.CO].

[77] J. H. Davis, C. McCabe, and C. Boehm, "Quantifying the evidence for Dark Matter in CoGeNT data," *JCAP* **1408** (2014) 014, arXiv:1405.0495 [hep-ph].

[78] **XENON** Collaboration, E. Aprile *et al.*, "Physics reach of the XENON1T dark matter experiment," *JCAP* **1604** no. 04, (2016) 027, arXiv:1512.07501 [physics.ins-det].

[79] **LZ** Collaboration, D. S. Akerib *et al.*, "LUX-ZEPLIN (LZ) Conceptual Design Report," arXiv:1509.02910 [physics.ins-det].

[80] **DARWIN** Collaboration, J. Aalbers *et al.*, "DARWIN: towards the ultimate dark matter detector," *JCAP* **1611** (2016) 017, arXiv:1606.07001 [astro-ph.IM].

[81] F. Mayet *et al.*, "A review of the discovery reach of directional Dark Matter detection," *Phys. Rept.* **627** (2016) 1–49, arXiv:1602.03781 [astro-ph.CO].

[82] P. Binetruy, *Supersymmetry*.
Oxford Graduate Texts. Oxford University Press, 2012.

[83] S. P. Martin, "A Supersymmetry primer," arXiv:hep-ph/9709356 [hep-ph]. [Adv. Ser. Direct. High Energy Phys.18,1(1998)].

[84] F. Englert and R. Brout, "Broken Symmetry and the Mass of Gauge Vector Mesons," *Phys. Rev. Lett.* **13** (1964) 321–323. [,157(1964)].

[85] P. W. Higgs, "Broken symmetries, massless particles and gauge fields," *Phys. Lett.* **12** (1964) 132–133.

[86] P. W. Higgs, "Broken Symmetries and the Masses of Gauge Bosons," *Phys. Rev. Lett.* **13** (1964) 508–509. [,160(1964)].

[87] G. S. Guralnik, C. R. Hagen, and T. W. B. Kibble, "Global Conservation Laws and Massless Particles," *Phys. Rev. Lett.* **13** (1964) 585–587. [,162(1964)].

[88] P. W. Higgs, "Spontaneous Symmetry Breakdown without Massless Bosons," *Phys. Rev.* **145** (1966) 1156–1163.

[89] T. W. B. Kibble, "Symmetry breaking in nonAbelian gauge theories," *Phys. Rev.* **155** (1967) 1554–1561. [,165(1967)].

[90] **CMS** Collaboration, S. Chatrchyan *et al.*, "Observation of a new boson at a mass of 125 GeV with the CMS experiment at the LHC," *Phys. Lett.* **B716** (2012) 30–61, arXiv:1207.7235 [hep-ex].

[91] **ATLAS** Collaboration, G. Aad *et al.*, "Observation of a new particle in the search for the Standard Model Higgs boson with the ATLAS detector at the LHC," *Phys. Lett.* **B716** (2012) 1–29, arXiv:1207.7214 [hep-ex].

[92] J.-L. Gervais and B. Sakita, "Field Theory Interpretation of Supergauges in Dual Models," *Nucl. Phys.* **B34** (1971) 632–639. [,154(1971)].

[93] Yu. A. Golfand and E. P. Likhtman, "Extension of the Algebra of Poincare Group Generators and Violation of p Invariance," *JETP Lett.* **13** (1971) 323–326. [Pisma Zh. Eksp. Teor. Fiz.13,452(1971)].

[94] J. Wess and B. Zumino, "Supergauge Transformations in Four-Dimensions," *Nucl. Phys.* **B70** (1974) 39–50. [,24(1974)].

[95] D. V. Volkov and V. P. Akulov, "Is the Neutrino a Goldstone Particle?," *Phys. Lett.* **46B** (1973) 109–110.

[96] D. Z. Freedman, P. van Nieuwenhuizen, and S. Ferrara, "Progress Toward a Theory of Supergravity," *Phys. Rev.* **D13** (1976) 3214–3218.

[97] P. Van Nieuwenhuizen, "Supergravity," *Phys. Rept.* **68** (1981) 189–398.

[98] S. Deser and B. Zumino, "Consistent Supergravity," *Phys. Lett.* **B62** (1976) 335. [,335(1976)].

[99] G. R. Farrar and P. Fayet, "Phenomenology of the Production, Decay, and Detection of New Hadronic States Associated with Supersymmetry," *Phys. Lett.* **76B** (1978) 575–579.

[100] P. Fayet, "Supersymmetry and Weak, Electromagnetic and Strong Interactions," *Phys. Lett.* **64B** (1976) 159.

[101] P. Fayet and S. Ferrara, "Supersymmetry," *Phys. Rept.* **32** (1977) 249–334.

[102] P. Fayet, "Spontaneously Broken Supersymmetric Theories of Weak, Electromagnetic and Strong Interactions," *Phys. Lett.* **69B** (1977) 489.

[103] T. Falk, K. A. Olive, and M. Srednicki, "Heavy sneutrinos as dark matter," *Phys. Lett.* **B339** (1994) 248–251, arXiv:hep-ph/9409270 [hep-ph].

[104] G. L. Kane, C. F. Kolda, L. Roszkowski, and J. D. Wells, "Study of constrained minimal supersymmetry," *Phys. Rev.* **D49** (1994) 6173–6210, arXiv:hep-ph/9312272 [hep-ph].

[105] **MSSM Working Group** Collaboration, A. Djouadi *et al.*, "The Minimal supersymmetric standard model: Group summary report," in *GDR (Groupement De Recherche) - Supersymetrie Montpellier, France, April 15-17, 1998*.
arXiv:hep-ph/9901246 [hep-ph].
https://inspirehep.net/record/481987/files/arXiv:hep-ph_9901246.pdf.

[106] **ATLAS** Collaboration, M. Aaboud *et al.*, "Search for resonances in diphoton events at $\sqrt{s}$=13 TeV with the ATLAS detector," *JHEP* **09** (2016) 001, arXiv:1606.03833 [hep-ex].

[107] **CMS** Collaboration, V. Khachatryan *et al.*, "Search for Resonant Production of High-Mass Photon Pairs in Proton-Proton Collisions at $\sqrt{s}$ =8 and 13 TeV," *Phys. Rev. Lett.* **117** no. 5, (2016) 051802, arXiv:1606.04093 [hep-ex].

[108] B. Mellado Garcia, P. Musella, M. Grazzini, and R. Harlander, "CERN Report 4: Part I Standard Model Predictions,". https://cds.cern.ch/record/2150771.

[109] **LHCb** Collaboration, R. Aaij *et al.*, "Angular analysis of the $B^0 \to K^{*0}\mu^+\mu^-$ decay using 3 fb^{-1} of integrated luminosity," *JHEP* **02** (2016) 104, arXiv:1512.04442 [hep-ex].

[110] **LHCb** Collaboration, R. Aaij *et al.*, "Test of lepton universality using $B^+ \to K^+\ell^+\ell^-$ decays," *Phys. Rev. Lett.* **113** (2014) 151601, arXiv:1406.6482 [hep-ex].

[111] **LHCb** Collaboration, R. Aaij *et al.*, "Test of lepton universality with $B^0 \to K^{*0}\ell^+\ell^-$ decays," *JHEP* **08** (2017) 055, arXiv:1705.05802 [hep-ex].

[112] L. Roszkowski, E. M. Sessolo, and A. J. Williams, "Prospects for dark matter searches in the pMSSM," *JHEP* **02** (2015) 014, arXiv:1411.5214 [hep-ph].

[113] M. Cahill-Rowley, J. L. Hewett, A. Ismail, and T. G. Rizzo, "Lessons and prospects from the pMSSM after LHC Run I," *Phys. Rev.* **D91** no. 5, (2015) 055002, arXiv:1407.4130 [hep-ph].

[114] A. Arbey, M. Battaglia, and F. Mahmoudi, "The Higgs boson, Supersymmetry and Dark Matter: Relations and Perspectives," *Annalen Phys.* **528** (2016) 179–186, arXiv:1504.05091 [hep-ph].

[115] **ATLAS** Collaboration, G. Aad *et al.*, "Summary of the ATLAS experiment's sensitivity to supersymmetry after LHC Run 1 ? interpreted in the phenomenological MSSM," *JHEP* **10** (2015) 134, arXiv:1508.06608 [hep-ex].

[116] G. Bertone, F. Calore, S. Caron, R. Ruiz, J. S. Kim, R. Trotta, and C. Weniger, "Global analysis of the pMSSM in light of the Fermi GeV excess: prospects for the LHC Run-II and astroparticle experiments," *JCAP* **1604** no. 04, (2016) 037, arXiv:1507.07008 [hep-ph].

[117] **GAMBIT** Collaboration, P. Athron *et al.*, "GAMBIT: The Global and Modular Beyond-the-Standard-Model Inference Tool," arXiv:1705.07908 [hep-ph].

[118] **GAMBIT Dark Matter Workgroup** Collaboration, T. Bringmann *et al.*, "DarkBit: A GAMBIT module for computing dark matter observables and likelihoods," arXiv:1705.07920 [hep-ph].

[119] **GAMBIT** Collaboration, P. Athron *et al.*, "A global fit of the MSSM with GAMBIT," arXiv:1705.07917 [hep-ph].

[120] A. Arbey, M. Boudaud, F. Mahmoudi, and G. Robbins, "Robustness of dark matter constraints and interplay with collider searches for New Physics," *JHEP* **11** (2017) 132, arXiv:1707.00426 [hep-ph].

[121] A. Chakraborty, B. Das, J. L. Diaz-Cruz, D. K. Ghosh, S. Moretti, and P. Poulose, "125 GeV Higgs signal at the LHC in the CP-violating MSSM," *Phys. Rev.* **D90** no. 5, (2014) 055005, arXiv:1301.2745 [hep-ph].

[122] A. Arbey, J. Ellis, R. M. Godbole, and F. Mahmoudi, "Exploring CP Violation in the MSSM," *Eur. Phys. J.* **C75** no. 2, (2015) 85, arXiv:1410.4824 [hep-ph].

[123] B. C. Allanach, "SOFTSUSY: a program for calculating supersymmetric spectra," *Comput. Phys. Commun.* **143** (2002) 305–331, hep-ph/0104145.

[124] A. Arbey, M. Battaglia, and F. Mahmoudi, "Implications of LHC Searches on SUSY Particle Spectra: The pMSSM Parameter Space with Neutralino Dark Matter," *Eur. Phys. J.* **C72** (2012) 1847, arXiv:1110.3726 [hep-ph].

[125] A. Arbey, M. Battaglia, and F. Mahmoudi, "Constraints on the MSSM from the Higgs Sector: A pMSSM Study of Higgs Searches, $B_s^0 -> \mu^+\mu^-$ and Dark Matter Direct Detection," *Eur. Phys. J.* **C72** (2012) 1906, arXiv:1112.3032 [hep-ph].

[126] A. Arbey, M. Battaglia, and F. Mahmoudi, "Light Neutralino Dark Matter in the pMSSM: Implications of LEP, LHC and Dark Matter Searches on SUSY Particle Spectra," *Eur. Phys. J.* **C72** (2012) 2169, arXiv:1205.2557 [hep-ph].

[127] G. Belanger, G. Drieu La Rochelle, B. Dumont, R. M. Godbole, S. Kraml, and S. Kulkarni, "LHC constraints on light neutralino dark matter in the MSSM," *Phys. Lett.* **B726** (2013) 773–780, arXiv:1308.3735 [hep-ph].

[128] C. Boehm, P. S. B. Dev, A. Mazumdar, and E. Pukartas, "Naturalness of Light Neutralino Dark Matter in pMSSM after LHC, XENON100 and Planck Data," *JHEP* **06** (2013) 113, arXiv:1303.5386 [hep-ph].

[129] A. Arbey, M. Battaglia, and F. Mahmoudi, "Supersymmetry with Light Dark Matter confronting the recent CDMS and LHC Results," *Phys. Rev.* **D88** (2013) 095001, arXiv:1308.2153 [hep-ph].

[130] **ATLAS, CMS** Collaboration, G. Aad *et al.*, "Measurements of the Higgs boson production and decay rates and constraints on its couplings from a combined ATLAS and CMS analysis of the LHC pp collision data at $\sqrt{s} = 7$ and 8 TeV," *JHEP* **08** (2016) 045, arXiv:1606.02266 [hep-ex].

[131] B. C. Allanach, A. Djouadi, J. L. Kneur, W. Porod, and P. Slavich, "Precise determination of the neutral Higgs boson masses in the MSSM," *JHEP* **09** (2004) 044, hep-ph/0406166.

[132] A. Arbey and F. Mahmoudi, "SuperIso Relic: A Program for calculating relic density and flavor physics observables in Supersymmetry," *Comput. Phys. Commun.* **181** (2010) 1277–1292, arXiv:0906.0369 [hep-ph].

[133] A. Arbey and F. Mahmoudi, "SuperIso Relic v3.0: A program for calculating relic density and flavour physics observables: Extension to NMSSM," *Comput. Phys. Commun.* **182** (2011) 1582–1583.

[134] N. Baro, F. Boudjema, and A. Semenov, "Full one-loop corrections to the relic density in the MSSM: A Few examples," *Phys. Lett.* **B660** (2008) 550–560, arXiv:0710.1821 [hep-ph].

[135] N. Baro, F. Boudjema, G. Chalons, and S. Hao, "Relic density at one-loop with gauge boson pair production," *Phys. Rev.* **D81** (2010) 015005, arXiv:0910.3293 [hep-ph].

[136] J. Harz, B. Herrmann, M. Klasen, K. Kovarik, and Q. Le Boulc'h, "Neutralino-stop coannihilation into electroweak gauge and Higgs bosons at one loop," *Phys. Rev.* **D87** no. 5, (2013) 054031, arXiv:1212.5241 [hep-ph].

[137] M. Hindmarsh and O. Philipsen, "WIMP dark matter and the QCD equation of state," *Phys. Rev.* **D71** (2005) 087302, arXiv:hep-ph/0501232 [hep-ph].

[138] M. Laine and Y. Schroder, "Quark mass thresholds in QCD thermodynamics," *Phys. Rev.* **D73** (2006) 085009, hep-ph/0603048.

[139] M. Drees, F. Hajkarim, and E. R. Schmitz, "The Effects of QCD Equation of State on the Relic Density of WIMP Dark Matter," *JCAP* **1506** no. 06, (2015) 025, arXiv:1503.03513 [hep-ph].

[140] M. Kamionkowski and M. S. Turner, "THERMAL RELICS: DO WE KNOW THEIR ABUNDANCES?," *Phys. Rev.* **D42** (1990) 3310–3320.

[141] P. Salati, "Quintessence and the relic density of neutralinos," *Phys. Lett.* **B571** (2003) 121–131, astro-ph/0207396.

[142] S. Profumo and P. Ullio, "SUSY dark matter and quintessence," *JCAP* **0311** (2003) 006, hep-ph/0309220.

[143] D. J. H. Chung, L. L. Everett, K. Kong, and K. T. Matchev, "Connecting LHC, ILC, and Quintessence," *JHEP* **10** (2007) 016, arXiv:0706.2375 [hep-ph].

[144] A. Arbey and F. Mahmoudi, "SUSY constraints from relic density: High sensitivity to pre-BBN expansion rate," *Phys. Lett.* **B669** (2008) 46–51, arXiv:0803.0741 [hep-ph].

[145] T. Moroi and L. Randall, "Wino cold dark matter from anomaly mediated SUSY breaking," *Nucl. Phys.* **B570** (2000) 455–472, hep-ph/9906527.

[146] G. F. Giudice, E. W. Kolb, and A. Riotto, "Largest temperature of the radiation era and its cosmological implications," *Phys. Rev.* **D64** (2001) 023508, hep-ph/0005123.

[147] N. Fornengo, A. Riotto, and S. Scopel, "Supersymmetric dark matter and the reheating temperature of the universe," *Phys. Rev.* **D67** (2003) 023514, hep-ph/0208072.

[148] G. Gelmini, P. Gondolo, A. Soldatenko, and C. E. Yaguna, "The Effect of a late decaying scalar on the neutralino relic density," *Phys. Rev.* **D74** (2006) 083514, hep-ph/0605016.

[149] A. Arbey and F. Mahmoudi, "SUSY Constraints, Relic Density, and Very Early Universe," *JHEP* **05** (2010) 051, arXiv:0906.0368 [hep-ph].

[150] G. Belanger, F. Boudjema, A. Pukhov, and A. Semenov, "MicrOMEGAs: A Program for calculating the relic density in the MSSM," *Comput. Phys. Commun.* **149** (2002) 103–120, hep-ph/0112278.

[151] G. Belanger, F. Boudjema, A. Pukhov, and A. Semenov, "MicrOMEGAs 2.0: A Program to calculate the relic density of dark matter in a generic model," *Comput. Phys. Commun.* **176** (2007) 367–382, hep-ph/0607059.

[152] G. Belanger, F. Boudjema, A. Pukhov, and A. Semenov, "micrOMEGAs 3: A program for calculating dark matter observables," *Comput. Phys. Commun.* **185** (2014) 960–985, arXiv:1305.0237 [hep-ph].

[153] M. Cirelli, G. Corcella, A. Hektor, G. Hutsi, M. Kadastik, P. Panci, M. Raidal, F. Sala, and A. Strumia, "PPPC 4 DM ID: A Poor Particle Physicist Cookbook for Dark Matter Indirect Detection," *JCAP* **1103** (2011) 051, arXiv:1012.4515 [hep-ph]. [Erratum: JCAP 1210, E01 (2012)].

[154] M. Boudaud, M. Cirelli, G. Giesen, and P. Salati, "A fussy revisitation of antiprotons as a tool for Dark Matter searches," *JCAP* **1505** no. 05, (2015) 013, arXiv:1412.5696 [astro-ph.HE].

[155] F. Donato, N. Fornengo, D. Maurin, and P. Salati, "Antiprotons in cosmic rays from neutralino annihilation," *Phys. Rev.* **D69** (2004) 063501, astro-ph/0306207.

[156] G. Di Bernardo, C. Evoli, D. Gaggero, D. Grasso, and L. Maccione, "Cosmic Ray Electrons, Positrons and the Synchrotron emission of the Galaxy: consistent analysis and implications," *JCAP* **1303** (2013) 036, arXiv:1210.4546 [astro-ph.HE].

[157] T. Bringmann, F. Donato, and R. A. Lineros, "Radio data and synchrotron emission in consistent cosmic ray models," *JCAP* **1201** (2012) 049, arXiv:1106.4821 [astro-ph.GA].

[158] E. Orlando and A. Strong, "Galactic synchrotron emission with cosmic ray propagation models," *Mon. Not. Roy. Astron. Soc.* **436** (2013) 2127, arXiv:1309.2947 [astro-ph.GA].

[159] N. Fornengo, R. A. Lineros, M. Regis, and M. Taoso, "The isotropic radio background revisited," *JCAP* **1404** (2014) 008, arXiv:1402.2218 [astro-ph.CO].

[160] M. Di Mauro, F. Donato, N. Fornengo, R. Lineros, and A. Vittino, "Interpretation of AMS-02 electrons and positrons data," *JCAP* **1404** (2014) 006, arXiv:1402.0321 [astro-ph.HE].

[161] **Fermi-LAT** Collaboration, M. Ackermann *et al.*, "Fermi-LAT Observations of the Diffuse Gamma-Ray Emission: Implications for Cosmic Rays and the Interstellar Medium," *Astrophys. J.* **750** (2012) 3, arXiv:1202.4039 [astro-ph.HE].

[162] J. Lavalle, D. Maurin, and A. Putze, "Direct constraints on diffusion models from cosmic-ray positron data: Excluding the minimal model for dark matter searches," *Phys. Rev.* **D90** (2014) 081301, arXiv:1407.2540 [astro-ph.HE].

[163] M. Boudaud, E. F. Bueno, S. Caroff, Y. Genolini, V. Poulin, V. Poireau, A. Putze, S. Rosier, P. Salati, and M. Vecchi, "The pinching method for Galactic cosmic ray positrons: implications in the light of precision measurements," *Astron. Astrophys.* **605** (2017) A17, arXiv:1612.03924 [astro-ph.HE].

[164] P. J. McMillan, "Mass models of the Milky Way," *Mon. Not. Roy. Astron. Soc.* **414** (2011) 2446–2457, arXiv:1102.4340 [astro-ph.GA].

[165] R. Catena and P. Ullio, "A novel determination of the local dark matter density," *JCAP* **1008** (2010) 004, arXiv:0907.0018 [astro-ph.CO].

[166] F. Nesti and P. Salucci, "The Dark Matter halo of the Milky Way, AD 2013," *JCAP* **1307** (2013) 016, arXiv:1304.5127 [astro-ph.GA].

[167] J. F. Navarro, C. S. Frenk, and S. D. M. White, "The Structure of cold dark matter halos," *Astrophys. J.* **462** (1996) 563–575, astro-ph/9508025.

[168] J. F. Navarro, A. Ludlow, V. Springel, J. Wang, M. Vogelsberger, S. D. M. White, A. Jenkins, C. S. Frenk, and A. Helmi, "The Diversity and Similarity of Cold Dark Matter Halos," *Mon. Not. Roy. Astron. Soc.* **402** (2010) 21, arXiv:0810.1522 [astro-ph].

[169] A. Burkert, "The Structure of dark matter halos in dwarf galaxies," *IAU Symp.* **171** (1996) 175, astro-ph/9504041. [Astrophys. J. 447, L25 (1995)].

[170] **DES, Fermi-LAT** Collaboration, A. Albert *et al.*, "Searching for Dark Matter Annihilation in Recently Discovered Milky Way Satellites with Fermi-LAT," *Astrophys. J.* **834** no. 2, (2017) 110, arXiv:1611.03184 [astro-ph.HE].

[171] **Fermi-LAT** Collaboration. https://www-glast.stanford.edu/pub_data/1203/.

[172] **Fermi-LAT** Collaboration, M. Ackermann *et al.*, "Searching for Dark Matter Annihilation from Milky Way Dwarf Spheroidal Galaxies with Six Years of Fermi Large Area Telescope Data," *Phys. Rev. Lett.* **115** no. 23, (2015) 231301, arXiv:1503.02641 [astro-ph.HE].

[173] G. Belanger, F. Boudjema, A. Pukhov, and A. Semenov, "Dark matter direct detection rate in a generic model with micrOMEGAs 2.2," *Comput. Phys. Commun.* **180** (2009) 747–767, arXiv:0803.2360 [hep-ph].

[174] P. J. McMillan, "The mass distribution and gravitational potential of the Milky Way," *Mon. Not. Roy. Astron. Soc.* **465** (Feb., 2017) 76–94, arXiv:1608.00971.

[175] K. Freese, J. A. Frieman, and A. Gould, "Signal Modulation in Cold Dark Matter Detection," *Phys. Rev.* **D37** (1988) 3388–3405.

[176] A. K. Drukier, K. Freese, and D. N. Spergel, "Detecting Cold Dark Matter Candidates," *Phys. Rev.* **D33** (1986) 3495–3508.

[177] M. J. Reid *et al.*, "Trigonometric Parallaxes of Massive Star Forming Regions: VI. Galactic Structure, Fundamental Parameters and Non-Circular Motions," *Astrophys. J.* **700** (2009) 137–148, arXiv:0902.3913 [astro-ph.GA].

[178] P. J. McMillan and J. J. Binney, "The uncertainty in Galactic parameters," *Mon. Not. Roy. Astron. Soc.* **402** (2010) 934, arXiv:0907.4685 [astro-ph.GA].

[179] J. Bovy, D. W. Hogg, and H.-W. Rix, "Galactic masers and the Milky Way circular velocity," *Astrophys. J.* **704** (2009) 1704–1709, arXiv:0907.5423 [astro-ph.GA].

[180] M. C. Smith *et al.*, "The RAVE Survey: Constraining the Local Galactic Escape Speed," *Mon. Not. Roy. Astron. Soc.* **379** (2007) 755–772, astro-ph/0611671.

[181] I. R. King, "The structure of star clusters. III. Some simple dynamical models," *Astron. J.* **71** (Feb., 1966) 64.

[182] S. Chaudhury, P. Bhattacharjee, and R. Cowsik, "Direct detection of WIMPs : Implications of a self-consistent truncated isothermal model of the Milky Way's dark matter halo," *JCAP* **1009** (2010) 020, arXiv:1006.5588 [astro-ph.CO].

[183] N. W. Evans, C. M. Carollo, and P. T. de Zeeuw, "Triaxial haloes and particle dark matter detection," *Mon. Not. Roy. Astron. Soc.* **318** (2000) 1131, astro-ph/0008156.

[184] **Particle Data Group** Collaboration, C. Patrignani *et al.*, "Review of Particle Physics," *Chin. Phys.* **C40** no. 10, (2016) 100001.

[185] A. Djouadi, "The Anatomy of electro-weak symmetry breaking. II. The Higgs bosons in the minimal supersymmetric model," *Phys. Rept.* **459** (2008) 1–241, hep-ph/0503173.

[186] A. Arbey, M. Battaglia, A. Djouadi, and F. Mahmoudi, "The Higgs sector of the phenomenological MSSM in the light of the Higgs boson discovery," *JHEP* **09** (2012) 107, arXiv:1207.1348 [hep-ph].

[187] A. Arbey, M. Battaglia, A. Djouadi, and F. Mahmoudi, "An update on the constraints on the phenomenological MSSM from the new LHC Higgs results," *Phys. Lett.* **B720** (2013) 153–160, arXiv:1211.4004 [hep-ph].

[188] A. Djouadi, "Precision Higgs coupling measurements at the LHC through ratios of production cross sections," *Eur. Phys. J.* **C73** (2013) 2498, arXiv:1208.3436 [hep-ph].

[189] M. Chakraborti, U. Chattopadhyay, A. Choudhury, A. Datta, and S. Poddar, "The Electroweak Sector of the pMSSM in the Light of LHC - 8 TeV and Other Data," *JHEP* **07** (2014) 019, arXiv:1404.4841 [hep-ph].

[190] M. Chakraborti, U. Chattopadhyay, and S. Poddar, "How light a higgsino or a wino dark matter can become in a compressed scenario of MSSM," *JHEP* **09** (2017) 064, arXiv:1702.03954 [hep-ph].

[191] C.-S. Huang, W. Liao, and Q.-S. Yan, "The Promising process to distinguish supersymmetric models with large tan Beta from the standard model: B —> X(s) mu+ mu-," *Phys. Rev.* **D59** (1999) 011701, hep-ph/9803460.

[192] K. S. Babu and C. F. Kolda, "Higgs mediated $B^0 \to \mu^+\mu^-$ in minimal supersymmetry," *Phys. Rev. Lett.* **84** (2000) 228–231, hep-ph/9909476.

[193] J. R. Ellis, K. A. Olive, and V. C. Spanos, "On the interpretation of $B_s \to \mu^+\mu^-$ in the CMSSM," *Phys. Lett.* **B624** (2005) 47–59, hep-ph/0504196.

[194] D. Eriksson, F. Mahmoudi, and O. Stal, "Charged Higgs bosons in Minimal Supersymmetry: Updated constraints and experimental prospects," *JHEP* **11** (2008) 035, arXiv:0808.3551 [hep-ph].

[195] A. Arbey, M. Battaglia, F. Mahmoudi, and D. Martìnez Santos, "Supersymmetry confronts $B_s \to \mu^+\mu^-$: Present and future status," *Phys. Rev.* **D87** no. 3, (2013) 035026, arXiv:1212.4887 [hep-ph].

[196] F. Mahmoudi, "SuperIso: A Program for calculating the isospin asymmetry of B —> K* gamma in the MSSM," *Comput. Phys. Commun.* **178** (2008) 745–754, arXiv:0710.2067 [hep-ph].

[197] F. Mahmoudi, "SuperIso v2.3: A Program for calculating flavor physics observables in Supersymmetry," *Comput. Phys. Commun.* **180** (2009) 1579–1613, arXiv:0808.3144 [hep-ph].

[198] F. Mahmoudi, "SuperIso v3.0, flavor physics observables calculations: Extension to NMSSM," *Comput. Phys. Commun.* **180** (2009) 1718–1719.

[199] **LHCb** Collaboration, R. Aaij *et al.*, "Measurement of the $B_s^0 \to \mu^+\mu^-$ branching fraction and effective lifetime and search for $B^0 \to \mu^+\mu^-$ decays," *Phys. Rev. Lett.* **118** no. 19, (2017) 191801, arXiv:1703.05747 [hep-ex].

[200] Y. Amhis *et al.*, "Averages of b-hadron, c-hadron, and τ-lepton properties as of summer 2016," arXiv:1612.07233 [hep-ex].

[201] U. Haisch and F. Mahmoudi, "MSSM: Cornered and Correlated," *JHEP* **01** (2013) 061, arXiv:1210.7806 [hep-ph].

[202] A. Djouadi, J. Kalinowski, and M. Spira, "HDECAY: A Program for Higgs boson decays in the standard model and its supersymmetric extension," *Comput. Phys. Commun.* **108** (1998) 56–74, hep-ph/9704448.

[203] R. V. Harlander, S. Liebler, and H. Mantler, "SusHi: A program for the calculation of Higgs production in gluon fusion and bottom-quark annihilation in the Standard Model and the MSSM," *Comput. Phys. Commun.* **184** (2013) 1605–1617, arXiv:1212.3249 [hep-ph].

[204] M. Spira. http://tiger.web.psi.ch/proglist.html.

[205] A. Arbey, S. Fichet, F. Mahmoudi, and G. Moreau, "The correlation matrix of Higgs rates at the LHC," *JHEP* **11** (2016) 097, arXiv:1606.00455 [hep-ph].

[206] **ATLAS** Collaboration, G. Aad *et al.*, "Summary of the searches for squarks and gluinos using $\sqrt{s} = 8$ TeV pp collisions with the ATLAS experiment at the LHC," *JHEP* **10** (2015) 054, arXiv:1507.05525 [hep-ex].

[207] **ATLAS** Collaboration, "Further searches for squarks and gluinos in final states with jets and missing transverse momentum at $\sqrt{s}$=13 TeV with the ATLAS detector," ATLAS-CONF-2016-078.

[208] **ATLAS** Collaboration, "Search for squarks and gluinos in final states with jets and missing transverse momentum using 36 fb^{-1} of $\sqrt{s} = 13$ TeV pp collision data with the ATLAS detector," ATLAS-CONF-2017-022.

[209] **ATLAS** Collaboration, "Pursuit of new phenomena in final states with high jet multiplicity, high jet masses and missing transverse momentum with ATLAS at $\sqrt{s} = 13$ TeV," ATLAS-CONF-2016-095.

[210] **ATLAS** Collaboration, "Search for new phenomena with large jet multiplicities and missing transverse momentum using large-radius jets and flavour-tagging at ATLAS in 13 TeV pp collisions," ATLAS-CONF-2017-033.

[211] **ATLAS** Collaboration, "Search for squarks and gluinos in events with an isolated lepton, jets and missing transverse momentum at $\sqrt{s} = 13$ TeV with the ATLAS detector," ATLAS-CONF-2016-054.

[212] **ATLAS** Collaboration, G. Aad *et al.*, "Search for the electroweak production of supersymmetric particles in $\sqrt{s}$=8 TeV pp collisions with the ATLAS detector," *Phys. Rev.* **D93** no. 5, (2016) 052002, arXiv:1509.07152 [hep-ex].

[213] **ATLAS** Collaboration, "Search for supersymmetry with two and three leptons and missing transverse momentum in the final state at $\sqrt{s} = 13$ TeV with the ATLAS detector," ATLAS-CONF-2016-096.

[214] **ATLAS** Collaboration, "Search for electroweak production of supersymmetric particles in the two and three lepton final state at $\sqrt{s} = \mathbf{13}$ TeV with the ATLAS detector," ATLAS-CONF-2017-039.

[215] **ATLAS** Collaboration, G. Aad *et al.*, "ATLAS Run 1 searches for direct pair production of third-generation squarks at the Large Hadron Collider," *Eur. Phys. J.* **C75** no. 10,

(2015) 510, arXiv:1506.08616 [hep-ex]. [Erratum: Eur. Phys. J. C76, no.3, 153 (2016)].

[216] **ATLAS** Collaboration, "Search for the Supersymmetric Partner of the Top Quark in the Jets+Emiss Final State at sqrt(s) = 13 TeV," ATLAS-CONF-2016-077.

[217] **ATLAS** Collaboration, "Search for a Scalar Partner of the Top Quark in the Jets+ETmiss Final State at $\sqrt{s}$ = 13 TeV with the ATLAS detector," ATLAS-CONF-2017-020.

[218] **ATLAS** Collaboration, "Search for top squarks in final states with one isolated lepton, jets, and missing transverse momentum in $\sqrt{s}$ = 13 TeV pp collisions with the ATLAS detector," ATLAS-CONF-2016-050.

[219] **ATLAS** Collaboration, "Search for direct top squark pair production and dark matter production in final states with two leptons in $\sqrt{s}$ = 13 TeV pp collisions using 13.3 fb^{-1} of ATLAS data," ATLAS-CONF-2016-076.

[220] **ATLAS** Collaboration, "Search for direct top squark pair production in final states with two leptons in $\sqrt{s}$ = 13 TeV pp collisions with the ATLAS detector," ATLAS-CONF-2017-034.

[221] **ATLAS** Collaboration, M. Aaboud *et al.*, "Search for bottom squark pair production in proton/proton collisions at $\sqrt{s}$ = 13 TeV with the ATLAS detector," *Eur. Phys. J.* **C76** no. 10, (2016) 547, arXiv:1606.08772 [hep-ex].

[222] **ATLAS** Collaboration, "Search for Supersymmetry in events with b-tagged jets and missing transverse energy in pp collisions at $\sqrt{s}$ = 13 TeV with the ATLAS detector," ATLAS-CONF-2017-038.

[223] **ATLAS** Collaboration, G. Aad *et al.*, "Search for new phenomena in final states with an energetic jet and large missing transverse momentum in pp collisions at $\sqrt{s}$ =8 TeV with the ATLAS detector," *Eur. Phys. J.* **C75** no. 7, (2015) 299, arXiv:1502.01518 [hep-ex]. [Erratum: Eur. Phys. J. C75, no.9, 408 (2015)].

[224] **ATLAS** Collaboration, M. Aaboud *et al.*, "Search for new phenomena in final states with an energetic jet and large missing transverse momentum in pp collisions at $\sqrt{s}$ = 13 TeV using the ATLAS detector," *Phys. Rev.* **D94** no. 3, (2016) 032005, arXiv:1604.07773 [hep-ex].

[225] **ATLAS** Collaboration, G. Aad *et al.*, "Search for dark matter in events with a hadronically decaying W or Z boson and missing transverse momentum in pp collisions at $\sqrt{s}$ = 8 TeV with the ATLAS detector," *Phys. Rev. Lett.* **112** no. 4, (2014) 041802, arXiv:1309.4017 [hep-ex].

[226] **ATLAS** Collaboration, "Search for dark matter produced in association with a hadronically decaying vector boson in pp collisions at $\sqrt{s}$ = 13 TeV with the ATLAS detector at the LHC," ATLAS-CONF-2015-080.

[227] L. Maiani, A. D. Polosa, and V. Riquer, "Probing Minimal Supersymmetry at the LHC with the Higgs Boson Masses," *New J. Phys.* **14** (2012) 073029, arXiv:1202.5998 [hep-ph].

[228] A. Arbey, M. Battaglia, and F. Mahmoudi, "Supersymmetric Heavy Higgs Bosons at the LHC," *Phys. Rev.* **D88** no. 1, (2013) 015007, arXiv:1303.7450 [hep-ph].

[229] N. D. Christensen, T. Han, and S. Su, "MSSM Higgs Bosons at The LHC," *Phys. Rev.* **D85** (2012) 115018, arXiv:1203.3207 [hep-ph].

[230] T. Han, T. Li, S. Su, and L.-T. Wang, "Non-Decoupling MSSM Higgs Sector and Light Superpartners," *JHEP* **11** (2013) 053, arXiv:1306.3229 [hep-ph].

[231] P. Bechtle, S. Heinemeyer, O. Stål, T. Stefaniak, and G. Weiglein, "Probing the Standard Model with Higgs signal rates from the Tevatron, the LHC and a future ILC," *JHEP* **11** (2014) 039, arXiv:1403.1582 [hep-ph].

[232] **CMS** Collaboration, "Search for a neutral MSSM Higgs boson decaying into $\tau\tau$ with 12.9 fb^{-1} of data at $\sqrt{s} = 13$ TeV," CMS-PAS-HIG-16-037.

[233] T. Sjostrand, S. Mrenna, and P. Z. Skands, "PYTHIA 6.4 Physics and Manual," *JHEP* **05** (2006) 026, hep-ph/0603175.

[234] T. Sjostrand, S. Mrenna, and P. Z. Skands, "A Brief Introduction to PYTHIA 8.1," *Comput. Phys. Commun.* **178** (2008) 852–867, arXiv:0710.3820 [hep-ph].

[235] J. Pumplin, D. R. Stump, J. Huston, H. L. Lai, P. M. Nadolsky, and W. K. Tung, "New generation of parton distributions with uncertainties from global QCD analysis," *JHEP* **07** (2002) 012, hep-ph/0201195.

[236] **DELPHES 3** Collaboration, J. de Favereau, C. Delaere, P. Demin, A. Giammanco, V. Lemaître, A. Mertens, and M. Selvaggi, "DELPHES 3, A modular framework for fast simulation of a generic collider experiment," *JHEP* **02** (2014) 057, arXiv:1307.6346 [hep-ex].

[237] A. L. Read, "Presentation of search results: The CL(s) technique," *J. Phys.* **G28** (2002) 2693–2704. [,11(2002)].

[238] H. Dreiner, M. Krämer, and J. Tattersall, "Exploring QCD uncertainties when setting limits on compressed supersymmetric spectra," *Phys. Rev.* **D87** no. 3, (2013) 035006, arXiv:1211.4981 [hep-ph].

[239] A. Arbey, M. Battaglia, and F. Mahmoudi, "Combining monojet, supersymmetry, and dark matter searches," *Phys. Rev.* **D89** no. 7, (2014) 077701, arXiv:1311.7641 [hep-ph].

[240] H. Baer, A. Mustafayev, and X. Tata, "Monojets and mono-photons from light higgsino pair production at LHC14," *Phys. Rev.* **D89** no. 5, (2014) 055007, arXiv:1401.1162 [hep-ph].

[241] J. Goodman, M. Ibe, A. Rajaraman, W. Shepherd, T. M. P. Tait, and H.-B. Yu, "Constraints on Dark Matter from Colliders," *Phys. Rev.* **D82** (2010) 116010, arXiv:1008.1783 [hep-ph].

[242] J. Goodman, M. Ibe, A. Rajaraman, W. Shepherd, T. M. P. Tait, and H.-B. Yu, "Constraints on Light Majorana dark Matter from Colliders," *Phys. Lett.* **B695** (2011) 185–188, arXiv:1005.1286 [hep-ph].

[243] **LHC New Physics Working Group** Collaboration, D. Alves, "Simplified Models for LHC New Physics Searches," *J. Phys.* **G39** (2012) 105005, arXiv:1105.2838 [hep-ph].

[244] J. Abdallah *et al.*, "Simplified Models for Dark Matter Searches at the LHC," *Phys. Dark Univ.* **9-10** (2015) 8–23, arXiv:1506.03116 [hep-ph].

[245] B. C. Allanach, S. Grab, and H. E. Haber, "Supersymmetric Monojets at the Large Hadron Collider," *JHEP* **01** (2011) 138, arXiv:1010.4261 [hep-ph]. [Erratum: JHEP09,027(2011)].

[246] M. Drees, M. Hanussek, and J. S. Kim, "Light Stop Searches at the LHC with Monojet Events," *Phys. Rev.* **D86** (2012) 035024, arXiv:1201.5714 [hep-ph].

[247] G. Cullen, N. Greiner, and G. Heinrich, "Susy-QCD corrections to neutralino pair production in association with a jet," *Eur. Phys. J.* **C73** no. 4, (2013) 2388, arXiv:1212.5154 [hep-ph].

[248] A. Arbey, M. Battaglia, and F. Mahmoudi, "Monojet Searches for MSSM Simplified Models," *Phys. Rev.* **D94** no. 5, (2016) 055015, arXiv:1506.02148 [hep-ph].

[249] J. Alwall, R. Frederix, S. Frixione, V. Hirschi, F. Maltoni, O. Mattelaer, H. S. Shao, T. Stelzer, P. Torrielli, and M. Zaro, "The automated computation of tree-level and next-to-leading order differential cross sections, and their matching to parton shower simulations," *JHEP* **07** (2014) 079, arXiv:1405.0301 [hep-ph].

[250] A. Arbey, M. Battaglia, A. Djouadi, F. Mahmoudi, and J. Quevillon, "Implications of a 125 GeV Higgs for supersymmetric models," *Phys. Lett.* **B708** (2012) 162–169, arXiv:1112.3028 [hep-ph].

[251] P. Bechtle, S. Heinemeyer, O. Stal, T. Stefaniak, G. Weiglein, and L. Zeune, "MSSM Interpretations of the LHC Discovery: Light or Heavy Higgs?," *Eur. Phys. J.* **C73** no. 4, (2013) 2354, arXiv:1211.1955 [hep-ph].

[252] M. W. Cahill-Rowley, J. L. Hewett, A. Ismail, and T. G. Rizzo, "The Higgs Sector and Fine-Tuning in the pMSSM," *Phys. Rev.* **D86** (2012) 075015, arXiv:1206.5800 [hep-ph].

[253] M. Carena, S. Gori, N. R. Shah, and C. E. M. Wagner, "A 125 GeV SM-like Higgs in the MSSM and the $\gamma\gamma$ rate," *JHEP* **03** (2012) 014, arXiv:1112.3336 [hep-ph].

[254] M. Carena, S. Gori, N. R. Shah, C. E. M. Wagner, and L.-T. Wang, "Light Stau Phenomenology and the Higgs $\gamma\gamma$ Rate," *JHEP* **07** (2012) 175, arXiv:1205.5842 [hep-ph].

[255] R. Benbrik, M. Gomez Bock, S. Heinemeyer, O. Stal, G. Weiglein, and L. Zeune, "Confronting the MSSM and the NMSSM with the Discovery of a Signal in the two Photon Channel at the LHC," *Eur. Phys. J.* **C72** (2012) 2171, arXiv:1207.1096 [hep-ph].

[256] T. J. LeCompte and S. P. Martin, "Large Hadron Collider reach for supersymmetric models with compressed mass spectra," *Phys. Rev.* **D84** (2011) 015004, arXiv:1105.4304 [hep-ph].

[257] T. J. LeCompte and S. P. Martin, "Compressed supersymmetry after 1/fb at the Large Hadron Collider," *Phys. Rev.* **D85** (2012) 035023, arXiv:1111.6897 [hep-ph].

[258] B. Bhattacherjee and K. Ghosh, "Degenerate SUSY search at the 8 TeV LHC," arXiv:1207.6289 [hep-ph].

[259] H. K. Dreiner, M. Kramer, and J. Tattersall, "How low can SUSY go? Matching, monojets and compressed spectra," *Europhys. Lett.* **99** (2012) 61001, arXiv:1207.1613 [hep-ph].

[260] **CTA** Collaboration, J. Carr *et al.*, "Prospects for Indirect Dark Matter Searches with the Cherenkov Telescope Array (CTA)," *PoS* **ICRC2015** (2016) 1203, arXiv:1508.06128 [astro-ph.HE].

[261] J. Silk, "Challenges in Cosmology from the Big Bang to Dark Energy, Dark Matter and Galaxy Formation," *JPS Conf. Proc.* **14** (2017) 010101, arXiv:1611.09846 [astro-ph.CO].

[262] A. Arbey, F. Mahmoudi, and G. Robbins, "SuperIso Relic v4: A program for calculating dark matter and flavour physics observables in Supersymmetry," arXiv:1806.11489 [hep-ph].

[263] P. Gondolo, J. Edsjo, P. Ullio, L. Bergstrom, M. Schelke, and E. A. Baltz, "DarkSUSY: Computing supersymmetric dark matter properties numerically," *JCAP* **0407** (2004) 008, arXiv:astro-ph/0406204 [astro-ph].

[264] T. Bringmann, J. Edsjö, P. Gondolo, P. Ullio, and L. Bergström, "DarkSUSY 6 : An Advanced Tool to Compute Dark Matter Properties Numerically," arXiv:1802.03399 [hep-ph].

[265] F. Ambrogi, C. Arina, M. Backovic, J. Heisig, F. Maltoni, L. Mantani, O. Mattelaer, and G. Mohlabeng, "MadDM v.3.0: a Comprehensive Tool for Dark Matter Studies," arXiv:1804.00044 [hep-ph].

[266] S. Wolfram, *The mathematica book*.
Wolfram Media, 2000.

[267] A. Semenov, "LanHEP — A package for automatic generation of Feynman rules from the Lagrangian. Version 3.2," *Comput. Phys. Commun.* **201** (2016) 167–170, arXiv:1412.5016 [physics.comp-ph].

[268] T. Hahn, "Generating Feynman diagrams and amplitudes with FeynArts 3," *Comput. Phys. Commun.* **140** (2001) 418–431, arXiv:hep-ph/0012260 [hep-ph].

[269] T. Hahn and C. Schappacher, "The Implementation of the minimal supersymmetric standard model in FeynArts and FormCalc," *Comput. Phys. Commun.* **143** (2002) 54–68, arXiv:hep-ph/0105349 [hep-ph].

[270] T. Hahn and M. Rauch, "News from FormCalc and LoopTools," *Nucl. Phys. Proc. Suppl.* **157** (2006) 236–240, arXiv:hep-ph/0601248 [hep-ph]. [,236(2006)].

[271] T. Hahn and M. Perez-Victoria, "Automatized one loop calculations in four-dimensions and D-dimensions," *Comput. Phys. Commun.* **118** (1999) 153–165, arXiv:hep-ph/9807565 [hep-ph].

[272] P. Z. Skands *et al.*, "SUSY Les Houches accord: Interfacing SUSY spectrum calculators, decay packages, and event generators," *JHEP* **07** (2004) 036, arXiv:hep-ph/0311123 [hep-ph].

[273] B. C. Allanach *et al.*, "SUSY Les Houches Accord 2," *Comput. Phys. Commun.* **180** (2009) 8–25, arXiv:0801.0045 [hep-ph].

[274] F. E. Paige, S. D. Protopopescu, H. Baer, and X. Tata, "ISAJET 7.69: A Monte Carlo event generator for pp, anti-p p, and e+e- reactions," arXiv:hep-ph/0312045 [hep-ph].

[275] W. Porod, "SPheno, a program for calculating supersymmetric spectra, SUSY particle decays and SUSY particle production at e+ e- colliders," *Comput. Phys. Commun.* **153** (2003) 275–315, arXiv:hep-ph/0301101 [hep-ph].

[276] A. Djouadi, J.-L. Kneur, and G. Moultaka, "SuSpect: A Fortran code for the supersymmetric and Higgs particle spectrum in the MSSM," *Comput. Phys. Commun.* **176** (2007) 426–455, arXiv:hep-ph/0211331 [hep-ph].

[277] T. Hahn, S. Heinemeyer, W. Hollik, H. Rzehak, and G. Weiglein, "FeynHiggs 2.7," *Nucl. Phys. Proc. Suppl.* **205-206** (2010) 152–157, arXiv:1007.0956 [hep-ph].

[278] M. Drees and M. Nojiri, "Neutralino - nucleon scattering revisited," *Phys. Rev.* **D48** (1993) 3483–3501, arXiv:hep-ph/9307208 [hep-ph].

[279] A. Djouadi and M. Drees, "QCD corrections to neutralino nucleon scattering," *Phys. Lett.* **B484** (2000) 183–191, arXiv:hep-ph/0004205 [hep-ph].

[280] L. Alvarez-Ruso, T. Ledwig, J. Martin Camalich, and M. J. Vicente-Vacas, "Nucleon mass and pion-nucleon sigma term from a chiral analysis of lattice QCD data," *Phys. Rev.* **D88** no. 5, (2013) 054507, arXiv:1304.0483 [hep-ph].

[281] **RQCD** Collaboration, G. S. Bali, S. Collins, D. Richtmann, A. Schäfer, W. Söldner, and A. Sternbeck, "Direct determinations of the nucleon and pion σ terms at nearly physical quark masses," *Phys. Rev.* **D93** no. 9, (2016) 094504, arXiv:1603.00827 [hep-lat].

[282] **ETM** Collaboration, A. Abdel-Rehim, C. Alexandrou, M. Constantinou, K. Hadjiyiannakou, K. Jansen, C. Kallidonis, G. Koutsou, and A. Vaquero Aviles-Casco, "Direct Evaluation of the Quark Content of Nucleons from Lattice QCD at the Physical Point," *Phys. Rev. Lett.* **116** no. 25, (2016) 252001, arXiv:1601.01624 [hep-lat].

[283] P. E. Shanahan, "Chiral Effective Theory Methods and their Application to the Structure of Hadrons from Lattice QCD," *J. Phys.* **G43** no. 12, (2016) 124001, arXiv:1606.08812 [hep-lat].

[284] M. M. Pavan, I. I. Strakovsky, R. L. Workman, and R. A. Arndt, "The Pion nucleon Sigma term is definitely large: Results from a G.W.U. analysis of pi nucleon scattering data," *PiN Newslett.* **16** (2002) 110–115, arXiv:hep-ph/0111066 [hep-ph].

[285] J. M. Alarcon, J. Martin Camalich, and J. A. Oller, "The chiral representation of the πN scattering amplitude and the pion-nucleon sigma term," *Phys. Rev.* **D85** (2012) 051503, arXiv:1110.3797 [hep-ph].

[286] J. Ruiz de Elvira, M. Hoferichter, B. Kubis, and U.-G. MeiSSner, "Extracting the σ-term from low-energy pion-nucleon scattering," *J. Phys.* **G45** no. 2, (2018) 024001, arXiv:1706.01465 [hep-ph].

[287] H.-W. Lin, "Lattice QCD for Precision Nucleon Matrix Elements," arXiv:1112.2435 [hep-lat].

[288] J. Ellis, N. Nagata, and K. A. Olive, "Uncertainties in WIMP Dark Matter Scattering Revisited," arXiv:1805.09795 [hep-ph].

[289] **Particle Data Group** Collaboration, K. A. Olive *et al.*, "Review of Particle Physics," *Chin. Phys.* **C38** (2014) 090001.

[290] **Asymmetry Analysis** Collaboration, Y. Goto *et al.*, "Polarized parton distribution functions in the nucleon," *Phys. Rev.* **D62** (2000) 034017, arXiv:hep-ph/0001046 [hep-ph].

[291] **COMPASS** Collaboration, V. Yu. Alexakhin *et al.*, "The Deuteron Spin-dependent Structure Function g1(d) and its First Moment," *Phys. Lett.* **B647** (2007) 8–17, arXiv:hep-ex/0609038 [hep-ex].

[292] R. H. Helm, "Inelastic and Elastic Scattering of 187-Mev Electrons from Selected Even-Even Nuclei," *Phys. Rev.* **104** (1956) 1466–1475.

[293] J. D. Lewin and P. F. Smith, "Review of mathematics, numerical factors, and corrections for dark matter experiments based on elastic nuclear recoil," *Astropart. Phys.* **6** (1996) 87–112.

[294] P. Klos, J. Menéndez, D. Gazit, and A. Schwenk, "Large-scale nuclear structure calculations for spin-dependent WIMP scattering with chiral effective field theory currents," *Phys. Rev.* **D88** no. 8, (2013) 083516, arXiv:1304.7684 [nucl-th]. [Erratum: Phys. Rev. D89, no.2, 029901 (2014)].

[295] S. Yellin, "Finding an upper limit in the presence of an unknown background," *Phys. Rev.* **D66** no. 3, (Aug, 2002) 032005, physics/0203002.

[296] C. Savage, "Tpcmc: a time projection chamber monte carlo for dark matter searches." Private code.

[297] M. Szydagis, N. Barry, K. Kazkaz, J. Mock, D. Stolp, M. Sweany, M. Tripathi, S. Uvarov, N. Walsh, and M. Woods, "NEST: A Comprehensive Model for Scintillation Yield in Liquid Xenon," *JINST* **6** (2011) P10002, arXiv:1106.1613 [physics.ins-det].

[298] M. Szydagis, A. Fyhrie, D. Thorngren, and M. Tripathi, "Enhancement of NEST Capabilities for Simulating Low-Energy Recoils in Liquid Xenon," *JINST* **8** (2013) C10003, arXiv:1307.6601 [physics.ins-det].

[299] "Nest,". http://nest.physics.ucdavis.edu/site/.

[300] P. Ciafaloni, D. Comelli, A. Riotto, F. Sala, A. Strumia, and A. Urbano, "Weak Corrections are Relevant for Dark Matter Indirect Detection," *JCAP* **1103** (2011) 019, arXiv:1009.0224 [hep-ph].

[301] A. E. Vladimirov, S. W. Digel, G. Johannesson, P. F. Michelson, I. V. Moskalenko, P. L. Nolan, E. Orlando, T. A. Porter, and A. W. Strong, "GALPROP WebRun: an internet-based service for calculating galactic cosmic ray propagation and associated photon emissions," *Comput. Phys. Commun.* **182** (2011) 1156–1161, arXiv:1008.3642 [astro-ph.HE].

[302] M. di Mauro, F. Donato, A. Goudelis, and P. D. Serpico, "New evaluation of the antiproton production cross section for cosmic ray studies," *Phys. Rev.* **D90** no. 8, (2014) 085017, arXiv:1408.0288 [hep-ph].

[303] L. J. Gleeson and W. I. Axford, "Cosmic Rays in the Interplanetary Medium," *Astrophys. J.* **149** (1967) L115–L118.

[304] L. J. Gleeson and W. I. Axford, "Solar Modulation of Galactic Cosmic Rays," *Astrophys. J.* **154** (1968) 1011.

[305] **AMS** Collaboration, M. Aguilar *et al.*, "Precision Measurement of the Proton Flux in Primary Cosmic Rays from Rigidity 1 GV to 1.8 TV with the Alpha Magnetic Spectrometer on the International Space Station," *Phys. Rev. Lett.* **114** (2015) 171103.

[306] **AMS** Collaboration, M. Aguilar *et al.*, "Precision Measurement of the Helium Flux in Primary Cosmic Rays of Rigidities 1.9 GV to 3 TV with the Alpha Magnetic Spectrometer on the International Space Station," *Phys. Rev. Lett.* **115** no. 21, (2015) 211101.

[307] A. Arbey, J. Ellis, F. Mahmoudi, and G. Robbins, "Dark Matter Casts Light on the Early Universe," arXiv:1807.00554 [hep-ph].

[308] P. Gondolo and G. Gelmini, "Cosmic abundances of stable particles: Improved analysis," *Nucl. Phys.* **B360** (1991) 145–179.

[309] J. Edsjo and P. Gondolo, "Neutralino relic density including coannihilations," *Phys. Rev.* **D56** (1997) 1879–1894, hep-ph/9704361.

[310] A. Arbey, "AlterBBN: A program for calculating the BBN abundances of the elements in alternative cosmologies," *Comput. Phys. Commun.* **183** (2012) 1822–1831, arXiv:1106.1363 [astro-ph.CO].

[311] A. Arbey, J. Auffinger, K. P. Hickerson, and E. S. Jenssen, "AlterBBN v2: A public code for calculating Big-Bang nucleosynthesis constraints in alternative cosmologies," arXiv:1806.11095 [astro-ph.CO].

[312] K. Jedamzik, "Big bang nucleosynthesis constraints on hadronically and electromagnetically decaying relic neutral particles," *Phys. Rev.* **D74** (2006) 103509, arXiv:hep-ph/0604251 [hep-ph].

[313] G. B. Gelmini and P. Gondolo, "Neutralino with the right cold dark matter abundance in (almost) any supersymmetric model," *Phys. Rev.* **D74** (2006) 023510, arXiv:hep-ph/0602230 [hep-ph].

[314] R. Allahverdi and M. Drees, "Thermalization after inflation and production of massive stable particles," *Phys. Rev.* **D66** (2002) 063513, arXiv:hep-ph/0205246 [hep-ph].

[315] K. Mukaida and M. Yamada, "Thermalization Process after Inflation and Effective Potential of Scalar Field," *JCAP* **1602** (2016) 003, arXiv:1506.07661 [hep-ph].

[316] E. W. Kolb and M. S. Turner, "The Early Universe," *Front. Phys.* **69** (1990) 1–547.

[317] S. Tsujikawa, "Quintessence: A Review," *Class. Quant. Grav.* **30** (2013) 214003, arXiv:1304.1961 [gr-qc].

[318] T. Barreiro, E. J. Copeland, and N. J. Nunes, "Quintessence arising from exponential potentials," *Phys. Rev.* **D61** (2000) 127301, arXiv:astro-ph/9910214 [astro-ph].

[319] P. G. Ferreira and M. Joyce, "Cosmology with a primordial scaling field," *Phys. Rev.* **D58** (1998) 023503, arXiv:astro-ph/9711102 [astro-ph].

[320] J. A. Frieman, C. T. Hill, A. Stebbins, and I. Waga, "Cosmology with ultralight pseudo Nambu-Goldstone bosons," *Phys. Rev. Lett.* **75** (1995) 2077–2080, arXiv:astro-ph/9505060 [astro-ph].

[321] G. Jungman, M. Kamionkowski, and K. Griest, "Supersymmetric dark matter," *Phys. Rept.* **267** (1996) 195–373, hep-ph/9506380.

[322] E. Bagnaschi *et al.*, "Likelihood Analysis of the pMSSM11 in Light of LHC 13-TeV Data," *Eur. Phys. J.* **C78** (2018) 256, arXiv:1710.11091 [hep-ph].

[323] **Muon g-2** Collaboration, G. W. Bennett *et al.*, "Final Report of the Muon E821 Anomalous Magnetic Moment Measurement at BNL," *Phys. Rev.* **D73** (2006) 072003, arXiv:hep-ex/0602035 [hep-ex].

[324] F. D'Eramo, N. Fernandez, and S. Profumo, "When the Universe Expands Too Fast: Relentless Dark Matter," *JCAP* **1705** (2017) 012, arXiv:1703.04793 [hep-ph].